NOVA SCHOOL OF SCIENCE & TECHNOLOGY

DEPARTAMENT OF MATERIALS SCIENCE

SUSTAINABLE MATERIALS APPLIED TO FLEXIBLE ELECTRONICS USING A LASER-INDUCED MODULAR PLATFORM

SARA ISABEL LAIGINHA SILVESTRE

Master in Micro and Nanotechnologies Engineering

DOCTORATE IN NANOTECHNOLOGIES AND NANOSCIENCES

NOVA University of Lisbon

September, 2024

DEPARTAMENT OF MATERIALS SCIENCE

SUSTAINABLE MATERIALS APPLIED TO FLEXIBLE ELECTRONICS USING A LASER-INDUCED MODULAR PLATFORM

SARA ISABEL LAIGINHA SILVESTRE

Master in Micro and Nanotechnologies Engineering

Adviser: João Carlos Mesquita Coelho
Researcher, Sevilla University Faculty of Physics

Co-advisers: Luís Miguel Nunes Pereira
Invited Assistant Professor, NOVA School of Science and Technology, NOVA University of Lisbon

Examination Committee:

Chair: José Júlio Alves Alferes,
Full Professor, NOVA School of Science and Technology, NOVA University of Lisbon

Rapporteurs: Neri Alves,
Full Professor, School of Science and Technology, São Paulo State University
Clara Isabel Barbosa Rodrigues Pereira,
Assistant Professor, Faculty of Sciences, University of Porto

Adviser: João Carlos Mesquita Coelho,
Researcher, Sevilla University Faculty of Physics

Members: Thiago Regis Longo Cesar da Paixão,
Full Professor, Institute of Chemistry, University of São Paulo
Elvira Maria Correia Fortunato,
Full Professor, NOVA School of Science and Technology, NOVA University of Lisbon
Ana Catarina Bernardino Baptista,
Assistant Professor, NOVA School of Science and Technology, NOVA University of Lisbon

DOCTORATE IN NANOTECHNOLOGIES AND NANOSCIENCES
NOVA University of Lisbon
September, 2024

Sustainable Materials Applied To Flexible Electronics Using A Laser-Induced Modular Platform

AGRADECIMENTOS

Começo por agradecer ao meu orientador, Doutor João Coelho, à Professora Elvira Fortunato, e ao meu coorientador, Professor Luís Pereira, pelo apoio e orientação ao longo destes últimos anos.

De forma mais informal, quero usar estes parágrafos para agradecer individualmente a cada um deles.

O João merecia uma página inteira de agradecimentos, mas o espaço não seria suficiente. Para além de orientador, tornou-se um amigo — daqueles chatos, mas que nunca nos largam. Foi o meu "pai emprestado da ciência" e fez de tudo para que eu chegasse até aqui, mesmo nos dias em que eu própria não acreditei. Um agradecimento especial a ti.

À Professora Elvira, por ter sido um exemplo ao longo da sua carreira, especialmente como mulher e engenheira. Não só me abriu portas desde a tese de mestrado, como acompanhou o meu trabalho como investigadora e desafiou-me a seguir este caminho do doutoramento.

Ao Professor Luís, quero agradecer por ter sido meu professor durante o curso. Foi dos melhores que encontrei. Sem dúvida cativou o meu interesse pela ciência, e como coorientador, esteve sempre pronto a oferecer novas perspetivas, ideias e feedback.

Agradeço à FCT pelo financiamento da bolsa de doutoramento, à bolsa Fulbright, ao I3N pelo financiamento e acesso aos laboratórios para a realização do trabalho experimental, bem como à NOVA FCT por todas as condições fornecidas.

À Professora Carmen e ao Professor Claussen, por me terem recebido na sua equipa de investigação durante o período nos EUA, e aos amigos que fiz e à família que ganhei do outro lado do mundo. Ao Gustavo, Raquel, Jéssica, Víctor S., Víctor C., Gustavo do Víctor, Bruna, Maria, Pris, Chris, Isabella, Ana Paula, Cícero (perdoem-me se esqueci de alguém), vocês serão sempre o melhor sentimento de nostalgia que guardo.

À Sam e à Jayde, vocês serão sempre as melhores colegas de casa de sempre, obrigada por terem sido as minhas âncoras ao longo daqueles curtos 6 meses.

Também agradeço a todos os colegas/amigos do I3N: Alexandra, Joana Neto, Joana Pinto, Inês Cunha, Sofia Ferreira, Tiago Mateus, Ricardo, Jonas, Ana Pimentel, Daniela, Diana, Henrique, João Resende, e equipa de secretariado.

Aos amigos do Open Space, Mariana, Guilherme, Luna, David, Catarina, Rui, Douglas, Raquel, Zulema, obrigada por terem feito parte desta jornada. Hoje sou eu, amanhã serão vocês — estamos juntos!

Ao Rafael Resende, agradeço toda a ajuda incansável nesta última fase da tese, és um investigador incrível. Os nossos TENG sobreviveram!

À equipa Virinha (Carolina, Manu, Tomás e Maria Morais), obrigada pelo vosso suporte, pela troca de ideias e pela amizade ao longo destes últimos anos. Um especial obrigado à Maria Morais — foste uma amiga, uma irmã mais velha (embora mais nova!), o meu filtro de ideias, a minha companhia fora de horas, o meu chatGPT humano, e muito mais. Não há palavras para descrever toda a tua ajuda ao longo destes anos. “Quero ser como tu quando for grande.”

À Maria, Cátia e Inês, um agradecimento especial por me aturarem dentro e fora do trabalho, nos meus melhores e piores dias. O vosso apoio incondicional foi imprescindível.

Ao meu tortuga Bruno, obrigada pela amizade, pelos pores do sol depois do trabalho, pelas escapadinhas de surf, por me desafiares a ir ao mar, mesmo quando não podia, e por todas as vezes que precisei de alinhar os chakras. Prometo que esta semana volto ao mar.

À Inês, Cheila, Lilas, Pimpim e Lucas, vocês são amigos para a vida. Teria tanto para dizer e tão pouco espaço para descrever, obrigada por estarem sempre presentes!

Aos meus pais, por terem feito de mim quem sou hoje — deram-me asas para voar e eu voei alto.

Ao meu melhor amigo e irmão, és o meu braço direito, o meu ponto de equilíbrio, o meu maior confidente e suporte. És o maior exemplo de pessoa, profissional, amigo e tantas outras coisas boas que existem no mundo. Obrigada por estares ao meu lado todos os segundos da minha vida. Amo-te muito.

Um especial obrigado a quem mais deu voltas comigo durante esta jornada. Aprendi tanto contigo e continuo a aprender todos os dias. Tornaste esta etapa da minha vida muito mais interessante. Obrigada por tudo e por tanto ;)

Por fim, quero agradecer a mim mesma por todo este trabalho árduo, e por nunca desistir.

"Here's to the crazy ones, the misfits, the rebels, the troublemakers... because the ones who are crazy enough to think they can change the world, are the ones who do." — Steve Jobs

ABSTRACT

Wearable electronics and miniaturized devices have become integral to modern life. The next step is scaling these innovations for larger systems while maintaining efficiency, flexibility, and energy performance, especially as smart cities expand and demand eco-friendly solutions to reduce electronic waste and environmental impact.

This thesis bridges advanced electronics and sustainability by using renewable materials and low-cost, eco-friendly methods for large-scale applications. Through a one-step direct laser writing (DLW) technique, three-dimensional porous green laser-induced graphene (gLIG) is produced. Optimization strategies, including precursor selection, substrate pretreatment, and laser parameter tuning, yield robust, thin, and flexible conductive patterns of high quality with low sheet resistances: 55.4 ohm sq^{-1} (for paper), 45.5 ohm sq^{-1} (for lignin-enriched paper), and 10.6 ohm s^{-1} (for cork). These properties make gLIG suitable for applications such as energy storage devices, sensors, and energy harvesting systems. Micro-supercapacitors (MSCs) developed in this work achieved capacitance values of 1.35–10 mF cm^{-2} and energy densities of 0.13–0.85 μWh cm^{-2}, with power densities up to 80 μW cm^{-2}. Stability tests revealed a capacitance retention of ≈80–85% over extended charge-discharge cycles, highlighting their reliability during prolonged operation. Additionally, these devices maintained stable performance under mechanical deformation, demonstrating their versatility for dynamic applications. Cork-based piezoresistive sensors further enhance this work, showcasing exceptional pressure sensitivity (0.38 mV Pa^{-1} at 15–35 kPa and 0.286 mV Pa^{-1} at ≥35 kPa) and functionality as triboelectric nanogenerators (TENGs), efficiently charging 0.47 and 4.7 μF capacitors. These results highlight their potential for powering small electronics and supporting sustainable energy solutions. Finally, this work underscores the importance of integrating sustainable, high-performance technologies into future infrastructure, paving the way for eco-friendly, self-sustaining platforms in smart cities and beyond.

Keywords: Sustainability, Renewable Materials, Direct Laser Writing, Laser-Induced Graphene, Sensors, Energy Storage Devices, Energy Harvesting Systems, Self-Sustaining Platforms.

RESUMO

Eletrónica vestível e dispositivos miniaturizados tornaram-se parte integrante da vida moderna. O próximo passo é escalar essas inovações para sistemas de maior dimensão, mantendo a eficiência, flexibilidade e desempenho energético, especialmente à medida que as cidades inteligentes se expandem e demandam soluções ecológicas para reduzir o desperdício eletrónico e o impacto ambiental.

Esta tese conecta a eletrónica avançada e sustentabilidade, utilizando materiais renováveis e métodos de baixo custo e ecológicos para aplicações em larga escala. Através de uma técnica de escrita direta a laser (DLW) de um único passo, é produzido grafeno verde induzido por laser (gLIG) com uma estrutura tridimensional porosa. Estratégias de otimização, incluindo a seleção do precursor, o pré-tratamento do substrato e o ajuste dos parâmetros do laser, resultam em padrões condutores robustos, finos e flexíveis, de alta qualidade e com baixas resistências de folha: 55.4 Ω sq^{-1} (para papel), 45.5 Ω sq^{-1} (para papel enriquecido com lignina) e 10.6 Ω sq^{-1} (para cortiça). Essas propriedades tornam o gLIG adequado para aplicações como dispositivos de armazenamento de energia, sensores e sistemas de colheita de energia. Os micro-supercondensadores (MSCs) desenvolvidos neste trabalho alcançaram valores de capacitância de 1.35–10 mF cm^{-2} e densidades de energia de 0.13–0.85 µWh cm^{-2}, com densidades de potência de até 80 µW cm^{-2}. Testes de estabilidade revelaram uma retenção de capacitância de ≈80–85% ao longo de ciclos prolongados de carga e descarga, destacando a sua fiabilidade durante operações de longa duração. Além disso, esses dispositivos mantiveram desempenho estável sob deformação mecânica, demonstrando a sua versatilidade para aplicações dinâmicas. Sensores piezoresistivos à base de cortiça reforçam ainda mais este trabalho, apresentando uma sensibilidade excecional à pressão (0.38 mV Pa^{-1} entre 15–35 kPa e 0.286 mV Pa^{-1} para ≥35 kPa) e funcionalidade como nanogeradores triboelétricos (TENGs), carregando de forma eficiente condensadores de 0.47 e 4.7 µF. Esses resultados destacam o seu potencial para alimentar pequenos dispositivos eletrónicos e apoiar soluções energéticas sustentáveis.

Por fim, este trabalho sublinha a importância de integrar tecnologias sustentáveis e de alto desempenho nas infraestruturas futuras, abrindo caminho para plataformas ecológicas e autossustentáveis em cidades inteligentes e além.

Palavras-chave: Eletrónica Vestível, Sustentabilidade, Materiais Renováveis, Escrita Direta a Laser, Grafeno Induzido Por Laser, Sensores, Dispositivos de Armazenamento de Energia, Sistemas de Colheita de Energia, Plataformas Autossustentáveis.

CONTENTS

LIST OF FIGURES

LIST OF TABLES

LIST OF EQUATIONS

xxx

ACRONYMS AND ABBREVIATIONS

2D	Two-Dimensional
3D	Three-Dimensional
BC-LIG	Borax-Cork Laser-Induced Graphene
BC-LIG-Flix	Borax-Cork Laser-Induced Graphene-Fixomull
BC-LIG/ZnO-Flix	Borax-Cork Laser-Induced Graphene-Zinc Oxide-Fixomull
BLEP-LIG	Borax-Lignin-Enriched Paper Laser-Induced Graphene
BP-LIG	Borax-Paper Laser-Induced Graphene
CEMOP	Centre of Excellence in Microelectronics Optoelectronics and Processes
CENIMAT	Centro de Investigação de Materiais
cLIG	Cork Laser-Induced Graphene
CV	Cyclic Voltammetry
DLW	Direct Laser Writing
EDLC	Electrical Double-Layer Capacitors
EDLs	Electrical Double-Layers
EDS	Energy Dispersive X-Ray Spectroscopy
EIS	Electrochemical Impedance Spectroscopy
FL	Focal Length
GCD	Galvanostatic Charge-Discharge
gLIG	Green Laser-Induced Graphene

IoT	Internet-Of-Things
IR	Infrared
LCA	Life Cycle Assessment
LDW	Laser Direct-Writing
LEDs	Light-Emitting Diodes
LIG	Laser-Induced Graphene
MSCs	Micro-Supercapacitors
SEM	Scanning Electron Microscopy
SS	Spot Size
TENG	Triboelectric Nanogenerator
UV	Ultraviolet
Vis	Visible
w-cLIG	Waxed-Cork Laser-Induced Graphene
XPS	X-Ray Photoelectron Spectroscopy
XRD	X-Ray Diffraction
ZnO	Zinc Oxide

SYMBOLS

A	Area
C_A	Areal Capacitance
C_{dl}	Double-Layer Capacitance
C_V	Volumetric Capacitance
E_A	Areal Energy Density
ESR	Equivalent Series Resistance
E_V	Volumetric Energy Density
f	Frequency
I	Current Intensity
I_{sc}	Short-circuit Current
P_A	Areal Power Density
P_V	Volumetric Power Density
R	Electrical Resistance
R_{ct}	Charge-Transfer Resistance
R_o	Initial Electrical Resistance
R_s	Sheet Resistance
R_s	Series Resistance
t	Time
V	Potential
V_{oc}	Open-circuit Voltage

$\boldsymbol{Z_W}$	Warburg element
$\boldsymbol{\varepsilon}$	Electrical Permittivity

1

THESIS MOTIVATION AND OBJECTIVES

1.1 Motivation

In the modern era, the boundaries of technological innovation are continually expanded by global research efforts. As we approach what may come next, the field of the Internet of Things (IoT) and smart cities stands out as a key area of progress, significantly improving human well-being and enhancing life quality worldwide[1,2]. Toward what can be introduced in the future, the demand for advanced systems that combine high efficiency, flexibility, durability, and low-power consumption, while supporting scalable manufacturing processes, is becoming increasingly important[3]. These technologies will be essential for building interconnected and sustainable cities, incorporating high-performance sensors, capacitors, light-emitting diodes (LEDs), and radio frequency identification (RFID) antennas, among others. Such innovations will enable a wide range of applications, from biological and environmental monitoring to energy harvesting and storage, intelligent robotics, electronic paper, and smart healthcare devices[4]. A significant focus of recent research efforts has been on carbon-based materials such as graphite, active carbon, carbon nanotubes, and notably graphene[2,5,6]. These materials present unique properties such as excellent electrical conductivity, thermal and chemical stability, high strength, and outstanding flexibility. They also offer ease of functionalization, making them ideal for integration into sensors as well as storage devices for various smart technologies. As mentioned, it is essential to select and develop proper materials to be mass-produced in a reproducible, eco-friendly, and inexpensive fabrication process[7]. Graphene is the one that stands out from this family of carbon materials, a one-atom-thick layer of graphite arranged in a honeycomb lattice[8]. Currently, the graphene fabrication and patterning processes are mostly based on screen-printing, stamp-imprinting, inkjet-printing, slow-flow assisted assembly, photolithography, chemical etching, and vacuum coating technology.

Those conventional techniques generally introduce complexity and high costs[9]. Moreover, they may rely as well on toxic chemicals or produce large quantities of waste.

This thesis explores the laser-direct writing technique, a promising method that allows for precise and controlled production of laser-induced graphene (LIG) under various atmospheric conditions, significantly simplifying the manufacturing process and supporting an environmentally friendly outcome[10,11]. The versatility of LIG production in natural, renewable, and abundant materials, its capacity for rapid production, and its potential to significantly reduce costs make it an excellent candidate for developing the next generation of green electronics.

The objective of this research is to develop robust, thin, and conformable discrete sensors and energy storage devices that can be seamlessly integrated into smart and sustainable systems. A particular emphasis is placed on the study of micro-supercapacitors, as energy storage systems remain a significant obstacle to the further advancement of flexible technologies. This dissertation aims to not only contribute to the understanding and development of these technologies but also to offer practical solutions that address current manufacturing challenges, thereby pushing the boundaries of what is possible in electronics and IoT applications.

1.2 Research objetives

The main goal of this thesis is to demonstrate the potential of adapting current technologies with the development of green technologies toward the preservation of our planet for future generations.

This thesis aims to address the following relevant key points:

- **Exploring natural carbon materials** like paper, lignin-enriched paper, cork, and others, to discover their potential as environmentally friendly substrates for electrode fabrication;
- **Use a simple, direct, low-cost, and scalable electrode fabrication method** toward the development of sustainable platforms;
- **Design and develop green discrete devices**, such as supercapacitors, piezoresistive sensors, and a harvesting component, as well as optimizing each one independently, giving them an open-source application;
- **Validating a self-sustaining system** by integrating the developed discrete devices to prove their effectiveness and reliability.

1.3 Thesis outline

The thesis consists of 6 chapters divided as below:

- **Chapter 1** presents the motivation and main objectives of the thesis;
- **Chapter 2** provides an in-depth introduction to graphene, covering the most common synthesis methods along with their respective advantages and disadvantages. This chapter also discusses the need for alternative methodologies for the future development of graphene-based electronics. It focuses on the direct laser writing technique as a promising solution for electrode production. Furthermore, the chapter highlights the LIG's versatility as both an active and sensing electrode material, emphasizing its potential for applications in smart platforms.
- **Chapter 3** explores the synthesis of green laser-induced graphene (gLIG) from bioderived precursors, detailing substrate preparation, experimental methods for optimizing gLIG structures on paper, lignin-enriched paper, and cork materials, and the characterization techniques used to evaluate graphitization outcomes throughout this research endeavor;
- **Chapter 4** underscores the demand for a technological transition towards a more environmentally friendly and sustainable era by exploring the direct conversion of the bioderived materials used in this thesis into gLIG. The chapter also includes the investigation and optimization of laser parameters for each material and compares the conversion process with that of a commercial polymer. The characterization of gLIG, using techniques such as Raman spectroscopy, X-ray photoelectron spectroscopy (XPS), scanning electron microscopy (SEM), and Hall Effect measurements, supports its potential application as an electrode material, which will be further explored in Chapter 5;
- **Chapter 5** focuses on the application of materials prepared in Chapter 3 and fully optimized in Chapter 4, with an emphasis on their suitability for energy storage applications. The green electrodes' potential was successfully demonstrated through the fabrication of planar and sandwiched LIG-based micro-supercapacitors. Electrochemical characterization demonstrated that these electrodes can be implemented in flexible and environmentally friendly energy storage devices, thus opening a novel route for the development of sustainable platforms;
- **Chapter 6** will explore the development of potential applications of green LIG, including piezoresistive sensors and energy harvesting components. The independent optimization of each component will be demonstrated, culminating in their integration

to validate a self-sustaining system. This chapter aims to prove the effectiveness and reliability of the integrated discrete devices fabricated throughout the thesis.

- **Chapter 7** presents the main conclusions of the thesis and suggests future developments.

1.4 Research Impact

1.4.1 List of scientific publications

- **Silvestre, S. L.**, Morais, M., Soares, R. R. A., Johnson, Z. T., Benson, E., Ainsley, E., Pham, V., Claussen, J. C., Gomes, C. L., Martins, R., Fortunato, E., Pereira, L., & Coelho, J. (2024). Green Fabrication of Stackable Laser-Induced Graphene Micro-Supercapacitors under Ambient Conditions: Toward the Design of Truly Sustainable Technological Platforms. *Advanced Materials Technologies*, 2400261.
DOI:10.1002/ADMT.20240026

- **Silvestre, S. L.**, Pinheiro, T., Marques, A. C., Deuermeier, J., Coelho, J., Martins, R., Pereira, L., & Fortunato, E. (2022). Cork derived laser-induced graphene for sustainable green electronics. *Flexible and Printed Electronics*, *7*.
DOI:10.1088/2058-8585/ac8e7b

1.4.2 Contributions to other publications

- Pinheiro, T., Morais, M., **Silvestre, S.**, Carlos, E., Coelho, J., Almeida, H. v., Barquinha, P., Fortunato, E., & Martins, R. (2024). Direct Laser Writing: From Materials Synthesis and Conversion to Electronic Device Processing. *Advanced Materials*.
DOI:10.1002/ADMA.202402014

- Coelho, J., Correia, R. F., **Silvestre, S.**, Pinheiro, T., Marques, A. C., Correia, M. R. P., Pinto, J. V., Fortunato, E., & Martins, R. (2023). Paper-based laser-induced graphene for sustainable and flexible microsupercapacitor applications. *Microchimica Acta*, *190* (1).
DOI:10.1007/s00604-022-05610-0

- C. Claro, P. I., Pinheiro, T., **Silvestre, S. L.**, Marques, A. C., Coelho, J., Marconcini, J. M., Fortunato, E., C. Mattoso, L. H., & Martins, R. (2022). Sustainable carbon sources for green laser-induced graphene: A perspective on fundamental principles, applications, and challenges. *Applied Physics Reviews*, *9*(4).
  DOI:10.1063/5.0100785

- Pinheiro, T., **Silvestre, S.**, Coelho, J., Marques, A. C., Martins, R., Sales, M. G. F., & Fortunato, E. (2021). Laser-Induced Graphene on Paper toward Efficient Fabrication of Flexible, Planar Electrodes for Electrochemical Sensing. *Advanced Materials Interfaces*, *8*(22).
  DOI:10.1002/admi.202101502

- Kulyk, B., Silva, B. F. R., Carvalho, A. F., **Silvestre, S.**, Fernandes, A. J. S., Martins, R., Fortunato, E., & Costa, F. M. (2021). Laser-Induced Graphene from Paper for Mechanical Sensing. *ACS Applied Materials & Interfaces*, *13*(8).
  DOI:10.1021/acsami.0c20270

1.4.3 Oral/Poster presentations

- Silvestre, S. *et al*., Laser-Induced Graphene-Based Structures Derived from Cellulosic Materials for Flexible and Green Electronics Applications. MRS Spring Meeting & Exhibit, San Francisco, CA, USA - 2023. (Poster)

- Silvestre, S. *et al.*, Cork derived laser-induced graphene for sustainable micro-supercapacitors fabrication, XX Brazil MRS Meeting, Foz de Iguazu, Brasil -2022. (Oral)

- Silvestre, S. et al., Cork derived laser-induced graphene for sustainable green electronics, Summer School Materials for Energy Transition, Sociedade Portuguesa de Materiais, Ordem dos Engenheiros, INL, LNEG e DGEG, Lisbon, Portugal - 2022. (**Best poster award**)

- Silvestre, S., Sustainable materials applied to flexible electronics using a laser induced modular platform, 8th European Nanoanalysis Symposium, European Materials Research Society (E-MRS) - 2020. (Poster)

1.4.4 List of courses, schools, congresses, and seminars

- 9th European School for Young Materials Scientists. International PhD Meeting/Seminar - European Advanced Training DGM Course "Laboratory x-ray techniques for materials development and process control". (2020)
- 8th International Summer School "Trends and new developments in Laser Technology". One-week summer school for students and PhD students to have the opportunity to study basic and applied aspects of laser technology. Location: Fraunhofer-*Institut für Werkstoff-und Strahltechnik* (IWS). (2020)

2

INTRODUCTION

This chapter provides a comprehensive overview of the topics related to this thesis. It includes the state of the art regarding graphene and its derivatives, as well as a summary of the most common graphene synthesis methods, such as chemical vapor deposition, epitaxial growth, chemical exfoliation, electrochemical exfoliation, and others. Following this, the direct laser writing technique is introduced as a simple, inexpensive, and environmentally friendly method for the preparation of laser-induced graphene electrodes. The advantages of the laser-induced graphene process compared to conventional methodologies for the development of innovative electrodes for a variety of applications are highlighted. Particularly, LIG has demonstrated exceptional utility as an active and sensing electrode material, underscoring its versatility and promise for smart platforms applications.

This chapter was adapted from:

- C. Claro, P. I., Pinheiro, T., **Silvestre, S. L.**, Marques, A. C., Coelho, J., Marconcini, J. M., Fortunato, E., C. Mattoso, L. H., & Martins, R. (2022). Sustainable carbon sources for green laser-induced graphene: A perspective on fundamental principles, applications, and challenges. *Applied Physics Reviews*, *9*(4). **DOI**:10.1063/5.0100785

- Pinheiro, T., Morais, M., **Silvestre, S.**, Carlos, E., Coelho, J., Almeida, H. v., Barquinha, P., Fortunato, E., & Martins, R. (2024). Direct Laser Writing: From Materials Synthesis and Conversion to Electronic Device Processing. *Advanced Materials*. **DOI**:10.1002/ADMA.202402014

2. INTRODUCTION

Throughout the years, technology has revolutionized and enhanced our daily existence through the advent of smart devices. Within these systems, a myriad of functional materials has been explored, with graphene emerging as one of the most popular and prominent choices in recent years.

2.1 From Graphite to Graphene

Graphite, a naturally occurring form of carbon, was introduced in the world with the invention of the first pencil in the 1560s, setting the beginning of a series of events and discoveries. Throughout the 19th and mid-20th centuries, the graphite oxide (GO) synthesis was explored by many researchers with noteworthy contributions of Schafhaeutl, Brodie, Staudenmaier, Hummers, Wallace, and others. These early investigations laid a foundation for further exploration in this field[12–14].

In the 1970s, a significant breakthrough emerged when carbon monolayer graphite was observed segregating on the surface of nickel, offering the possibility of isolating single-layer carbon atoms on top of other materials. Another significant milestone occurred in 1975 when the preparation of monolayer graphite through silicon sublimation was demonstrated. This achievement marked the first-time that researchers achieved graphene's epitaxial growth on isolating substrates, particularly silicon carbide (SiC)[15]. In 1986, chemists Hans-Peter Boehm, Ralph Setton, and Eberhard Stamp introduced the term "graphene" to describe it as individual graphite sheets[16]. The name derived from the word "graphite" combined with a suffix "-ene", denoting polycyclic aromatic hydrocarbons[17,18]. Furthermore, in 1997, the International Union of Pure and Applied Chemistry (IUPAC) formalized the definition of graphene, specifying that "the term graphene should be used only when discussing the reactions, structural relations, or other properties of individual layers"[19,20].

The pivotal year of 1999 was marked by the work of Ruoff and colleagues, who successfully exfoliated graphite into thin lamellae composed of multiple layers of graphene using a

micromechanical approach. Finally, in 2004, Andre Geim and Konstantin Novoselov made history by synthesizing graphene through the micromechanical cleavage method, popularly known as the “Scotch tape method”[21]. Their approach involved using sellotape to delicately peel off a single layer of graphene from a graphite block and then chemically dissolving the tape, resulting in the successful isolation of graphene. A chronological arrangement of events in the history of graphene is summarized in Figure 1.

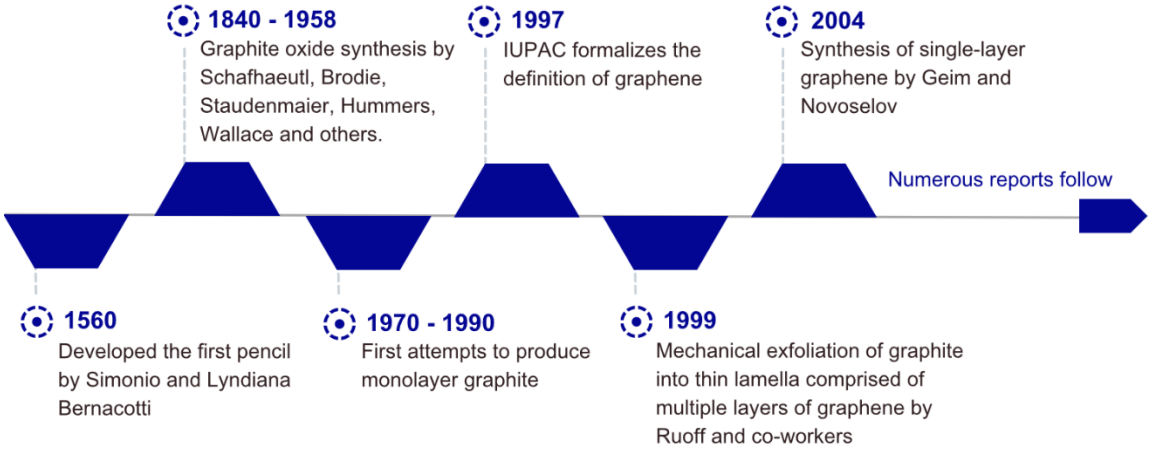

Figure 1. Timeline of events in the graphite and graphene history[16,23].

Geim and Novoselov were rewarded in 2010 with the Nobel Prize in Physics for their pioneering work that revolutionized the field of graphene research[22]. These milestones have propelled graphite and graphene to the forefront of materials science, sparking a “graphene gold rush” and expanding the knowledge of these extraordinary carbon-based materials with diverse and promising applications[17]. Therefore, graphene has undergone a significant transformation, evolving from a laboratory curiosity to a transformative material with diverse applications. The introduction of collaborative initiatives like the Graphene Flagship project in 2013 accelerated graphene research and innovation. This period also witnessed the onset of commercial-scale graphene production, which enabled the development of high-performance batteries with graphene electrodes, crucial for advancing energy storage technologies. By 2015, researchers developed ultra-sensitive graphene-based magnetic field sensors, paving the way for advanced sensing applications[23]. Graphene's versatility was showcased in subsequent years as it found its way into aircraft components, mobile phone screens, batteries, and coding systems, highlighting its broad industrial potential.

In 2017, pioneering experiments with graphene in zero-gravity conditions provided insights into its behavior in space, in collaboration with the European Space Agency. By 2018, graphene-based ultrahigh-capacity transmitters and receivers enhanced telecommunication networks, improving performance and efficiency. The adoption of graphene in automotive technologies

accelerated in 2019 when Ford Motor embraced graphene-enhanced materials in production vehicles. Additionally, graphene-based bioelectronic retinal implants emerged as a promising frontier in vision restoration technology, demonstrating graphene's potential in healthcare[24]. In 2020, the achievement of industrial-scale graphene production laid the groundwork for widespread adoption across industries[8].

2.2 Structure and properties of graphene

The basic unit structure of graphene comprises six carbon atoms tightly bonded together, forming a hexagonal arrangement. Each atom shares three in-plane σ-bonds with its neighboring atoms and forms an out-of-plane π-bond, with an average interatomic separation of 0.14 nm[25]. Essentially, graphene is a one-atom-thick planar sheet of sp^2 hybridized carbon atoms. This hybridization combines s, p_x, and p_y orbitals[26]. Arranged in a two-dimensional honeycomb lattice within a single plane, graphene is known as the thinnest material, yet it boasts an exceptionally large surface area (~ 2630 $m^2\ g^{-1}$). Due to the combination of unique electronic and crystallographic structures, graphene demonstrates outstanding mechanical strength (1 TPa, making it 100-300 times stronger than steel), flexibility, chemical stability, high transmittance (~ 98 %), electrical conductivity (~ 1.0×10^8 S m^{-1}), excellent thermal conductivity (~ 5000 W $m^{-1}\ K^{-1}$), and high-carrier electron mobility (~ 250 000 $cm^2\ V^{-1}\ s^{-1}$)[27,28].

Over the past two decades, researchers have dedicated considerable effort to uncovering these extraordinary properties, presenting clear advantages over conventional electronic materials, and enabling the development of next-generation electronics with unprecedented capabilities. Since its first isolation in 2004 by Geim an Novoselov et al., graphene has been recognized as the building block and “the mother of all graphitic forms”. Therefore, its versatility prompted the development of other dimensionalities of graphene.

These include zero-dimensional (0D) fullerenes buckyballs, one-dimensional (1D) nanotubes, or even three-dimensional (3D) materials (Figure 2)[29].

Furthermore, thorough extensive research into the physical and chemical properties of graphene allowed its categorization based on the number of carbon layers (from 1 to 10 or more), lateral flake or crystal size (varying from sub-micron to tens of microns across), and the presence as well as quantity of impurities. According to Barkan et. al, discussions on 2D graphene span from a monolayer or “pure” single-layer carbon (1 layer) to multilayer graphene (3-10 layers)[30]. Additionally, the ongoing development and exploration of graphene with topological defects, functional groups, dopants, and disordered structures, have broadened its applicability for electronic devices. These graphene-based materials are also categorized under the umbrella of 2D graphene materials within the global research community.

Regarding 3D graphene materials, researchers have engineered 3D graphene structures and smart layer arrangements to render higher surface areas while maintaining other distinctive properties of the 2D-graphene materials as high mobility and mechanical stability, directly impacting its performance.

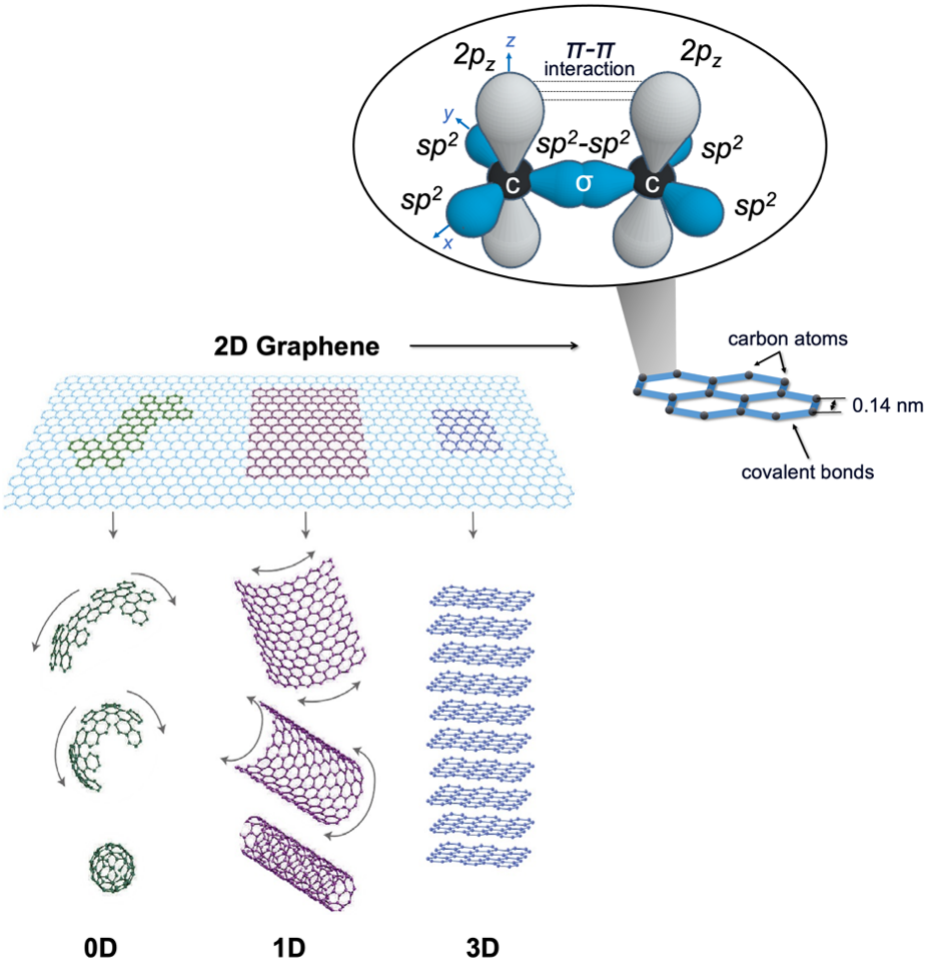

Figure 2. Graphene as the origin of all graphitic forms. 2D building material wrapped into 0D buckyballs, rolled into 1D nanotubes or stacked into 3D material. Illustration of the honeycomb lattice structure of graphene and sp^2 hybridization, adapted with permission from [17,31]. Copyright (2007) Springer Nature.

Accordingly, these can be clearly defined as non-graphite 3D structured graphene materials, with walls consisting of less than 10 graphene layers. Structures with more than 10 graphene layers are considered as thin films of graphite [32]. This clarifies the relationships among graphene, 2D graphene materials, 3D graphene materials and graphite, as demonstrated in Figure 3.

Graphene extends its presence into other forms, often as derivatives. These include graphene oxide (GO), graphene nano-platelets (GNPs), graphene nanoribbons (GNRs), reduced

graphene oxide (rGO), graphene quantum dots (GQDs), and other graphene-based products, such as graphene inks.

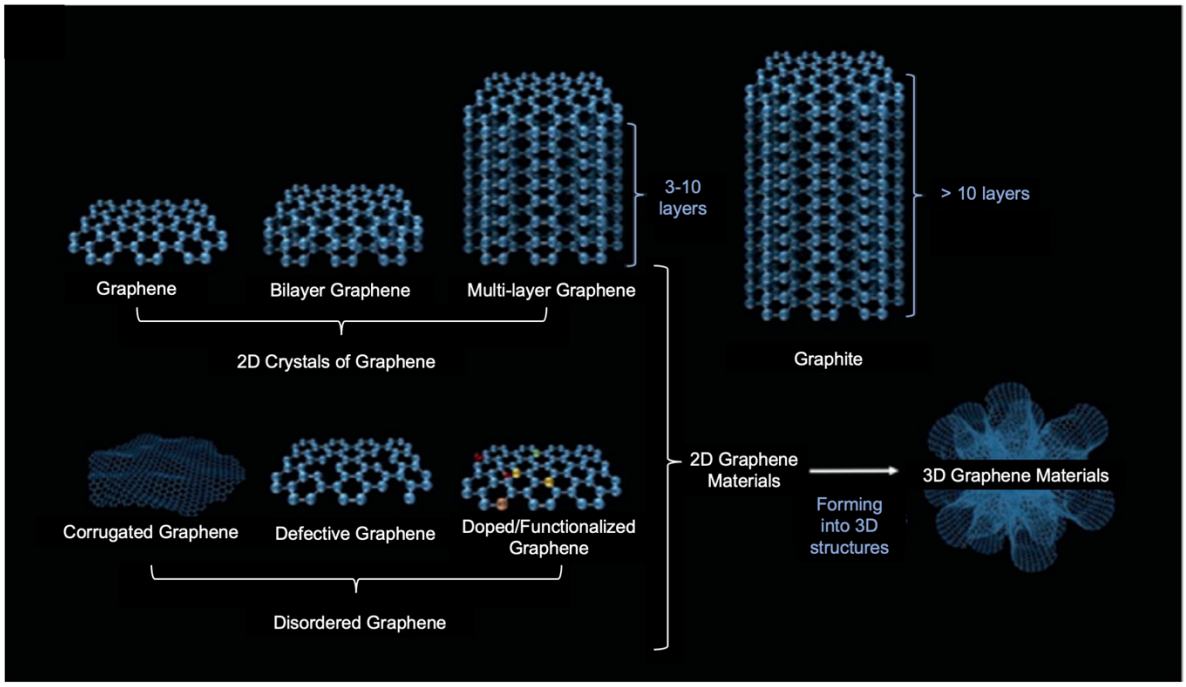

Figure 3. Illustration of the relationships between graphite and graphene materials, reproduced with permission from [29]. Copyright (2020) American Chemical Society.

Among these derivatives, GO consists of a layered carbon structure with oxygen-containing functional groups (=O, -OH, -O-, -COOH) along its edges and surfaces. Despite its reduced electrical conductivity and mechanical properties compared to pristine graphene, owing to sp^3 hybridization and defects introduced during oxidation processes, GO maintains remarkable versatility across various applications. It finds utility in fields such as energy storage, sensing, and biomedical systems.

In attempts to revitalize graphene's pristine properties, scientists have pursued reduction strategies, resulting in the creation of reduced graphene oxide (rGO). While rGO shares structural similarities with graphene, it retains defects, additional carbon ring domains, and residual oxygen-functional groups. Nonetheless, rGO exhibits improved electronic and mechanical properties compared to GO, offering attractive advantages such as high yield and low production costs[33]. Structure of these materials are shown in Figure 4.

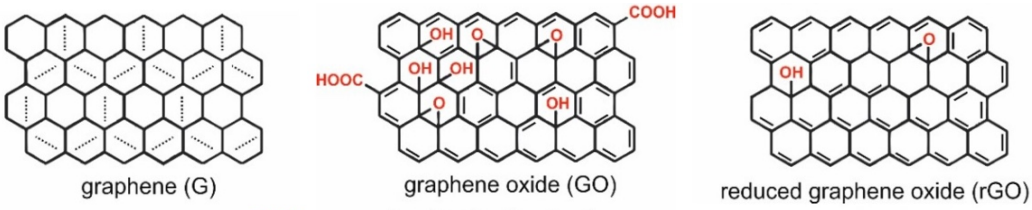

Figure 4. Structure diagram of graphene and other forms, as graphene oxide (GO) and reduced graphene oxide (rGO), reproduced from [34]. CC BY 4.0 license, https://creativecommons.org/licenses/by/4.0/.

2.3 General methods of graphene synthesis

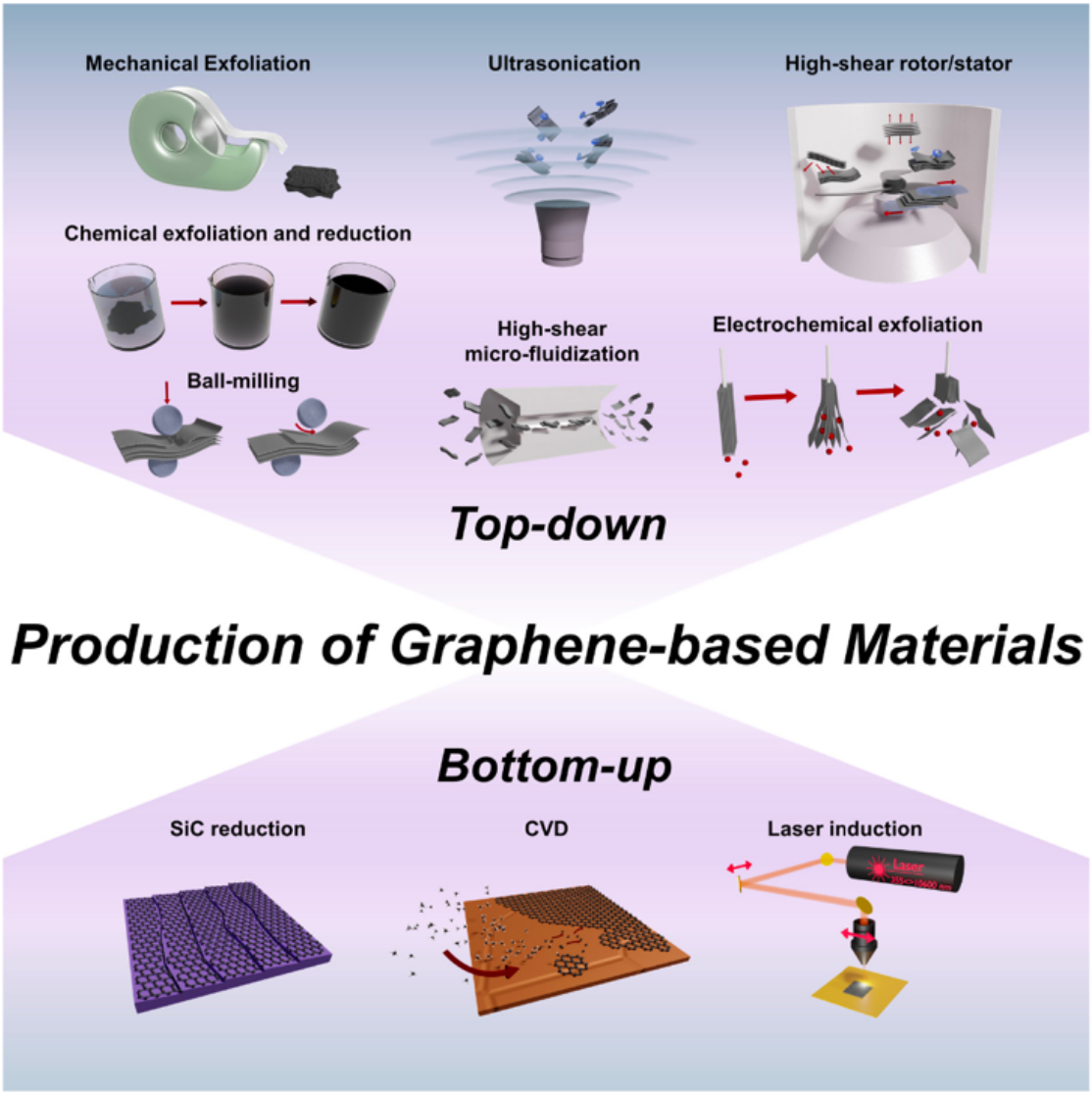

Figure 5. Overview of some graphene synthesis methods, with top-down and bottom-up synthesis, reproduced with permission from [35]. Copyright (2021) Wiley - VCH GmbH.

Since the discovery of graphene, several synthesis methods have been developed to achieve its mass production and meet specific requirements imposed by various applications while also

keep production costs low [36]. This has led to a diversity of methods that can be broadly categorized into two approaches: top-down and bottom-up synthesis, as depicted in Figure 5. These strategies will be reviewed briefly in the sub-sections below.

2.3.1 Top-Down Methods

The fundamental principle of top-down methods involves transforming or exfoliating a bulk or starting material, such as graphite or its derivatives (such as graphite oxide), into its smallest constituents to produce graphene. The core idea behind these methods is to overcome the Van der Waals forces between the graphene layers, resulting in the formation of few-layer or monolayer flakes. Among the most used top-down methods are mechanical exfoliation, chemical exfoliation and reduction and electrochemical exfoliation[9,37].

2.3.1.1 Mechanical exfoliation (Micromechanical Cleavage Method)

Mechanical exfoliation, also known as micromechanical cleavage, and often referred to as the "Scotch tape method", was the first traditional method used for the graphene production[21]. Geim and Novoselov peeled-off layers of highly oriented pyrolytic graphite (HOPG) using adhesive tape until one-atom-thick flakes were able to be identified[38]. Their groundbreaking research on graphene earned them the Nobel Prize in Physics. The optimization of this process resulted in the production of high structural quality and single-layer graphene with more than 100 μm^2 in size[39]. Remarkable properties that pristine graphene is known for, such as outstanding charge carrier mobility and ambipolar field-effect, among others, were identified. Although this unconventional method was essential for studying the properties of graphene, opening the door toward a multitude of applications and proof-of-concept devices, it is described as slow and imprecise, making it unsuitable for large-scale commercial production[40].

2.3.1.2 Chemical oxidative-exfoliation and reduction

Approaches based on the methods of Brodie, Staudenmaier, and Hummer use oxidizing agents, such as sulfuric acid, nitric acid, and potassium permanganate to introduce oxygen groups between the layers of graphene, leading to the production of graphite oxide.

The chemical composition and structure of resulting graphite oxide are influenced by the chosen oxidizing agents, graphite precursor, reaction conditions, and the selected synthesis procedure[41]. This process increases the interlayer spacing between the graphite sheets and reduces the Van der Waals forces, thereby allowing the exfoliation of graphite oxide into few layers of graphene oxide (GO).

Furthermore, reduced graphene oxide (rGO) can be obtained from GO through various reduction methods, such as thermal, chemical, electrochemical, hydrothermal, microwave, and photoreduction methods (Figure 6)[41]. While these methods provide scalability and the capability to functionalize graphene, the use of hazardous chemicals and the resulting inferior quality require further developments towards eco-friendly alternatives. Additionally, both graphene oxide and reduced graphene oxide exhibit low electrical conductivity and structural defects, which hinder their practical applications[42,43].

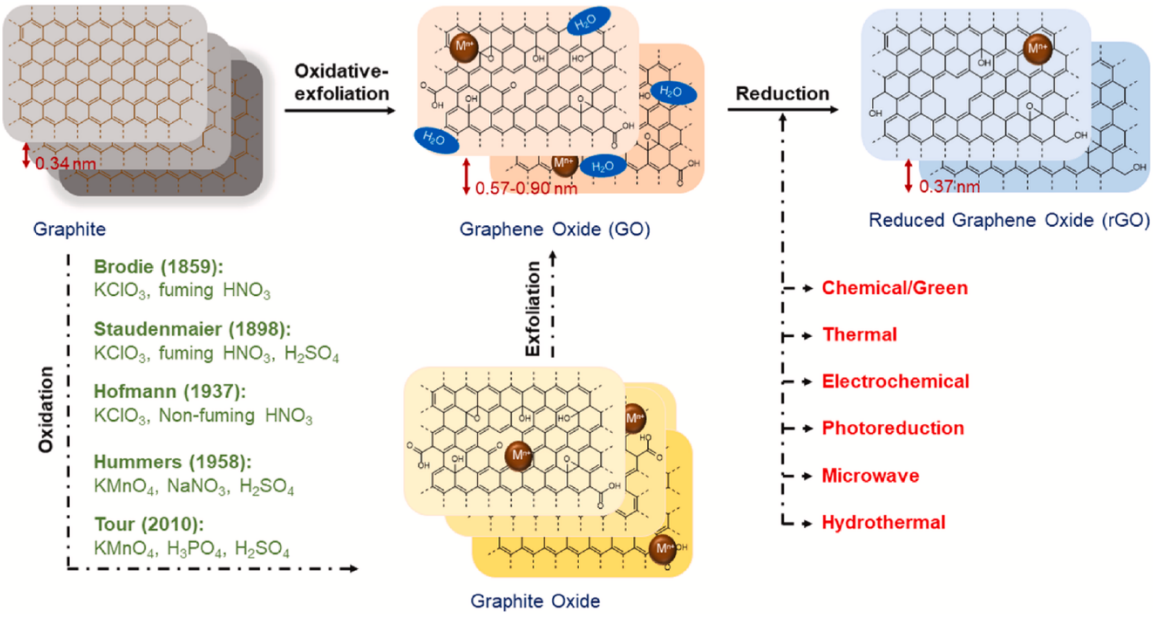

Figure 6. Schematic summary of the chemical oxidative-exfoliation and reduction method used to prepare GO and rGO from graphite, reproduced with permission from [41]. Copyright (2021) Elsevier B.V.

2.3.1.3 Liquid-phase exfoliation

An alternative method to synthesizing graphene is through liquid-phase exfoliation (LPE). In this method, a graphite precursor is introduced into either an aqueous solution or an organic solvent, such as N-methylpyrrolidone (NMP). The solvent plays a crucial role in reducing the Van der Waals attraction forces between the graphene interlayers, facilitating their exfoliation[38]. This exfoliation process can occur naturally or with mechanical assistance.

By subjecting the 2D material to an external driving force, such as shear mixing, sonication, or ball milling, the Van der Waals forces between the graphene layers are overcome, resulting in the exfoliation of graphene flakes[44].

During ball milling, solid graphite is rapidly ground in a sealed rotating jar containing steel balls. The resulting graphene flakes are then dispersed into a liquid medium. Alternatively, shear mixing and sonication involve treating graphite in a solution. This process can be further

enhanced by intercalating the layers using chemicals like ferric chloride, sulfuric acid, among other ionic species [42]. Some of the shearing methods are described below[45]:

(a) LPE via **sonication** uses either a sonication probe or bath to agitate liquid solution, leading to the formation of cavitation bubbles. Upon collapse, these bubbles generate shockwaves, which are transmitted through the graphite, creating tensile stress. The presence of multiple cavities results in the peeling off graphene layers from the graphite. The efficiency of the process and the quantity of graphene produced depend on the geometry of the vessel exposed to the sound energy, the volume of dispersion and solvent type.

(b) LPE via **high-shear mixing** is a method that uses either a rotor-stator or rotating blade to rapidly move the solution containing graphite. This movement generates shear stress, effectively peeling off layers of graphene. In rotor-stator mixing, the production rate is influenced by the volume of the solution as well as its composition.

This straightforward process enables the production of single and few-layer graphene stabilized in various solvents, including organic solvents, ionic liquids, water/polymer or surfactant solutions, and some other green dispersants, such as water[46]. LPE is recognized for its simplicity, scalability, and eco-friendly approach, offering significant potential for the mass production of graphene and, consequently, bolstering its broader market presence[46].

However, LPE has its downsides. Particularly, it faces limitations such as the production and concentration of monolayers, inhomogeneous distribution of graphene flakes, and its highly energy-intensive, costly, and time-consuming nature. These factors anticipate the necessity for further research and innovation to refine the LPE process, addressing these challenges and fully exploit its potential[47].

2.3.1.4 Solid-phase exfoliation

Solid-phase exfoliation (SPE), as the name indicates, involves exfoliating graphene layers from graphite within a solid state. This can be achieved through methods as ball milling or using rollers with a reducing agent[9,38].

(a) SPE via **ball milling**: graphite is placed in a rotating container along with balls. As the container rotates, the balls collide with the graphite, causing the layers of graphene to exfoliate or fragment from the graphite.

(b) SPE via **three-roll milling**: a a mixture of an adhesive (such as dioctyl phthalate and polyvinyl chloride) and graphite is fed through rollers. These rollers force the graphite to exfoliate into graphene and disperse within the adhesive. The final mixture is then added to alcohol and heated to 500 °C to remove the adhesive.

While this process enables the exploration of mixing and functionalizing graphene with other materials, it tends to yield non-uniform and defective few-layer graphene nanosheets[42].

2.3.1.5 Electrochemical exfoliation

Another top-down method for graphene production is electrochemical exfoliation. In this process, a graphite rod working electrode is submerged in an electrolyte (usually a solution containing ionic species, such as ammonium sulfate, sodium sulfate, ammonium oxalate, hydrogen peroxide, ammonium persulfate, among others) along with a counter electrode. When a current is applied to the electrodes, the electrolyte intercalates between the graphene layers[48]. This promotes an increase in the interlayer distance and weakens the van der Waals interactions, resulting in the effective exfoliation of graphene layers. This method commonly employs aqueous solutions or ionic liquids, enabling the application of positive or negative voltage to the graphite electrode. This process allows for simultaneous exfoliation at both electrodes[49]. Despite its potential for large-scale graphene production with minimal defects, challenges remain, particularly the need for more environmentally friendly chemicals, a concern shared across various liquid exfoliation techniques[35].

2.3.2 Bottom-Up Methods

On the other hand, bottom-up approach starts out with the decomposition of carbon-containing percursors (both gaseous and liquid) followed by the formation of graphene layers. Chemical vapor deposition (CVD), epitaxial growth (SiC), and pyrolysis are some of the most frequently used bottom-up techniques for the graphene production. Furthermore, a promising and environmentally friendly technique known as direct laser writing has emerged. This method was further studied through this thesis, offering precise fabrication capabilities while also being eco-conscious, representing a notable advancement in graphene synthesis methodologies[8,49].

2.3.2.1 Graphene Epitaxial Growth

Among the highly acclaimed methods of graphene synthesis, epitaxial growth stands out as a prominent technique for developing single-layer or multilayer graphene on a single-crystalline silicon carbide (SiC) substrate[47].

Through thermal decomposition at temperatures greater than 1000 °C under an ultrahigh vacuum environment, SiC crystal decomposes into its constituents: silicon and carbon. During this process, silicon vaporizes from the crystal surface, while carbon atoms arrange into graphene layers[50]. The epitaxial graphene growth method represents a highly promising approach for large-scale production of high-quality graphene, characterized by well-ordered films and minimal wrinkles, presenting excellent properties that are especially attractive for

electronics applications. Even though, the major drawbacks are the elevated temperatures required to decompose SiC and the challenge of achieving a high production rate, which makes the widespread adoption of this method a less favorable consideration[9,38].

2.3.2.2 Chemical Vapor Deposition (CVD)

Chemical Vapor Deposition stands out as leading bottom-up synthesis technique known for producing large-area, high-quality graphene films[51]. Thermal CVD and plasma-enhanced CVD are two variant systems used to grow graphene layer-by-layer with high purity and precise structure. Despite the development of various CVD types, the fundamental process remains similar, comprising common elementary steps (Figure 7)[52]. The process starts with the injection of gaseous carbon-based precursors into a reactor chamber. Under varying conditions and gas-phase reactions, the reactant gases adsorb onto the heated substrate surface and diffuse across it. Subsequent heterogeneous reactions at the gas-solid interface led to the continuous thin film formation. The gas-phase reactions occur due to the introduction of sufficiently high temperature or additional energy in the form of plasma[49]. The growth of graphene can be precisely controlled by adjusting critical parameters, including the precursor gas flow rate, temperature, plasma discharges, pressure, growth duration, among others. This level of control allows the tailoring of graphene films with the desired number of layers and other properties to suit specific applications. Furthermore, Plasma CVD is an alternative to thermal CVD, providing a low-temperature approach to graphene synthesis. This method leverages controlled plasma discharges to activate and facilitate precursor gas reactions, expanding the range of applicable substrates, including those that may not withstand the extreme conditions of thermal CVD[53].

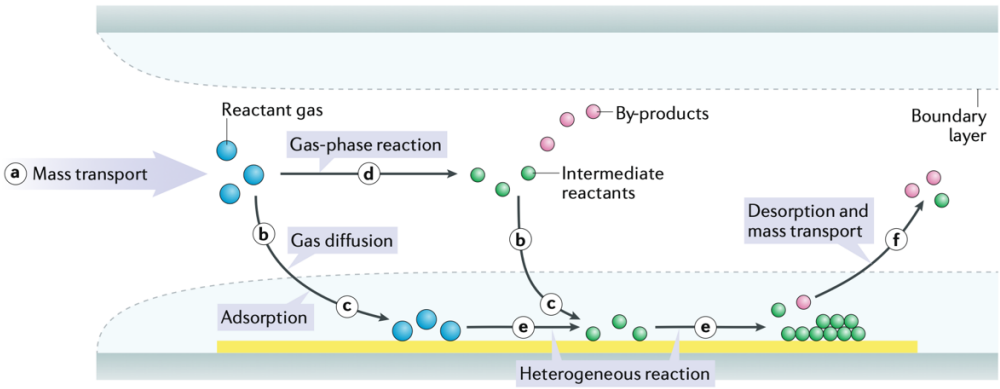

Figure 7. Schematic of typical CVD process steps: (a) Reactant gases are introduced into the reactor. These gases can either directly diffuse (b) and adsorb onto the substrate (c), or they may participate in gas-phase reactions before being deposited onto the substrate. Surface diffusion and heterogeneous reactions (e) occur after thin film formation. Finally, (f) by-products and unreacted species desorb from the surface and

are carried out away from the reactor, reproduced with permission from [52]. Copyright (2021) Springer Nature Limited.

For instance, through the CVD method, well-ordered graphene films with a few layers were synthesized on Ni substrates. However, the use of Ni as a catalyst has some limitations, leading to the formation of single and few-layered graphene over a confined region of a few to tens of microns. This process lacks precise control over the number of layers and exhibits poor homogeneity throughout the entire substrate. On the other hand, using polycrystalline copper foils as a substrate allows for the mass production of high-quality single-layered graphene. This behavior can arise from the different solubilities of C in Cu and Ni. Ni can dissolve more carbon atoms, leading to extra C being precipitated, resulting in non-homogeneous films with worse properties[54]. Nevertheless, this method is not cost-effective and straightforward[38].

2.3.2.3 Direct laser writing (DLW)

Direct laser writing (DLW), also known as laser direct write (LDW), was initially introduced by Tour's group in 2014. They demonstrated that certain polymers, such as polyimide (PI) and polyetherimide (PEI), could be directly and photothermally converted into carbonaceous products using a CO_2 laser system with a wavelength of 10.6 µm, as illustrated in Figure 8. Throughout this process, when laser beam irradiates the PI substrate, it thermally induces lattice vibrations onto the substrate, resulting in high localized temperatures (exceeding 2500 °C) capable of breaking the C-O, C=O, and the N-C bonds. Consequently, the sp^3-carbon are rearranged into sp^2-carbon atoms, indicating the formation of graphitic structures. The remaining small molecules are released in the form of gases [28]. The first results revealed the presence of foam-like 3D graphene stacked structures, termed laser-induced graphene (LIG) [55]. Alternative terms found in the literature include laser-engraved graphene (LEG)[56] or laser-scribed graphene (LSG)[57], however LIG is the most used term. Lin *et al.* demonstrated the production of LIG with a porous structure and exceptionally high specific surface area (Figure 8b-d).

Since the initial discovery of LIG, considerable efforts have been made toward expanding the range of LIG precursors beyond PI substrates. Nowadays, LIG can be synthesized from an impressive variety of materials, including thermoplastic polymers, phenolic resins, biopolymers like lignin, as well as textiles, cellulose, wood, cork, or even food (e.g., potato skins, bread, and coconut shells)[25].

These developments highlight the vast potential applications of LIG across various applications fields, particularly with the emerging need for environmentally friendly production methods using natural, bio-based sources.

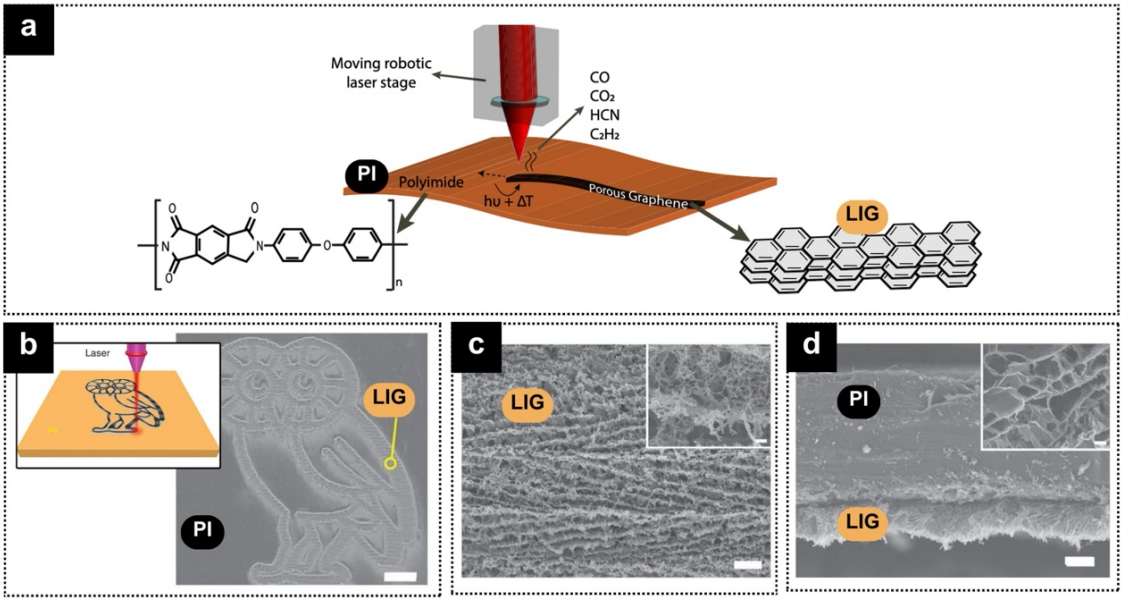

Figure 8.(a) Schematic representation of the porous 3D LIG synthesis in polyimide (PI) substrate, adapted with permission from [58]. Copyright (2018) Institute of Physics Publishing Ltd. (b) SEM image of LIG patterned into PI; scale, 1mm. Bright contrast corresponds to LIG. (c) SEM image of the LIG obtained in (b); scale bar, 10 µm. Inset correspond to higher magnification; scale bar, 1 µm. (d) Cross-section SEM image of the LIG onto PI substrate; scale bar, 20 µm. Inset image correspond to a higher magnification, showing the porous morphology of LIG; scale bar, 1 µm, adapted with permission from [55,58]. Copyright (2014) Springer Nature Limited.

Furthermore, various laser systems with different characteristics, such as wavelength, pulse duration, and repetition rate, have been explored and successfully utilized to produce LIG[27]. These systems include ultraviolet (UV), visible, and infrared (IR) light, and involve distinct irradiation processes (e.g., photothermal, photochemical, or a combination of both). Additionally, by adjusting the laser parameters, the process can be fine-tuned to produce LIG-based materials with improved properties. This technique, controlled by computer software, allows precise LIG patterning without direct substrate contact, and rapid production of high-quality LIG with exceptional electrical conductivity and mechanical properties under ambient conditions[58].

In contrast to conventional synthesis methods, which are often complex, time-consuming, and hazardous, the groundbreaking technique of DLW emerges as a rapid, safe, cost-effective alternative[10,59]. Its potential to drive innovation is evident, particularly in the realm of flexible and smart devices, sensors, and energy storage systems. A summary of the commonly used top-down and bottom-up synthesis methods of graphene is presented in Table 1, along with their respective advantages and disadvantages.

Table 1. Summary of some examples of bottom-up and top-down graphene synthesis methods[42,49,50].

Type	Method	No. of layers	Advantages	Limitations
Top-down	Mechanical exfoliation	Monolayer to few layers	Uniform, large size of layers, low-cost, high structural and electronic quality	Delicate, time-consuming, poor reproducibility, low yield, low scalability
	Chemical oxidative-exfoliation and reduction	Few layers, and multilayer	Scalable, functionalized graphene	Time-consuming, low quality, large number of defects, hazardous chemicals
	Liquid-phase exfoliation	Few layers and multilayer	Low cost, scalable	Low yield, time-consuming, inhomogeneous flakes, small size
	Solid-phase exfoliation	Few layers, and multilayer	Enables functionalization	Impurities, complex, time-consuming, non-uniform flake size
	Electrochemical exfoliation	Monolayer, few layers, and multilayer	Scalable, functionalized graphene	Expensive ionic liquids, non-uniform, time-consuming
Bottom-up	Graphene epitaxial growth	Few layers	High-quality large-area graphene	Expensive, energy intensive process
	Chemical vapor deposition (CVD)	Monolayer and few layers	High quality, large size	Expensive, high energy required, complex, low scalability
	Direct laser writing (DLW)	Few layers and multilayer	Direct, single-step, low-cost, large scale-production	Limited in achieving high aspect ratios, material compatibility

Each of these synthesis techniques have their distinctive advantages and limitations that influence their respective applications. Figure 9 shows the evolution of graphene synthesis methodologies over the past decade and provides insights into future directions. As shown in Figure 9, CVD stands out as the most extensively researched and employed technique compared to other methods. This preference is attributable to the fact that CVD can yield high-quality graphene with minimal defects and large dimensions, thereby allowing precise control over the number of graphene layers. The graphene production by CVD has seen a sustained growth until 2017, followed by a slight decline over the years. This decline may be due to the search for alternative, environmentally friendly synthesis approaches.

It is anticipated that future research will prioritize the cost-effective and environmentally friendly synthesis of graphene to enhance its appeal for commercial applications. Thus, it is expected that in future years there will be a shift towards investment in greener and sustainable techniques currently used, as well as the development of novel production processes.

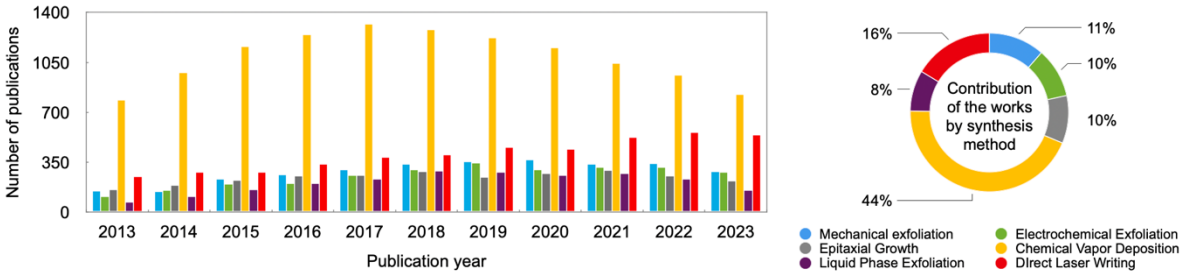

Figure 9. Number of publications in the Web of Science database by the search of the synthesis method term and the word "graphene" from 2013 to 2023. (Source: Web of Science database, searched on September 2, 2024).

In the realm of conventional graphene synthesis, there are numerous challenges to address, including cost-effectiveness, safety, repeatability, workability, and ensuring consistent quality. Over the past decade, there has been a rush to optimize graphene production methods, aiming to minimize costs while mitigating environmental impacts[60].

Notably, the European Union launched the Graphene Flagship, a consortium of 150 partners with a budget of €1 billion, covering various research areas from fundamental studies to the commercialization of graphene-based materials[25,41,42]. Similar endeavors are underway globally to unlock graphene's full potential across energy storage, environmental, biomedical, and other applications. Despite significant investments and intense research activity, several shortcomings hinder the full commercialization of graphene[32]. Beyond cost reduction and production capacity expansion, at a more fundamental level, graphene industry faces a lack of a bandgap and unavoidable defects which limits its applications; lack of suitable sustainable production methods and "standard-grade" graphene in the market; and the inexistence of prototypes to boost and demonstrate its potential[41].

These aspects are interlinked with other relevant questions, namely, the perception of technological maturity among potential investors and customers, regulatory hurdles regarding graphene's toxicity and biocompatibility. Usually, new technologies have difficulties entering new markets as they are not being validated by consumers. As such, unless there is an obvious advantage, investment may be difficult to come by. In the same note, the lack of investment impairs technological development towards higher TRLs, which in turn further difficult market penetration. And of course, no devices can be commercialized without being properly regulated and proven to be safe, which are processes which can take years. Regarding safety and toxicity, most reports do not deem graphene as a toxic substance, but more conclusive data is still required. These commercialization issues have been mostly addressed by optimizing and standardizing production methods[25]. In this context, direct laser writing emerges as a promising technique for producing laser-induced graphene. Although LIG does not

necessarily imply a single sheet or a few layers of sp^2 carbon lattice and may not match the properties of monolayer graphene, 3D porous graphene is preferred for many applications that do not require optimal graphene properties due to its ease preparation and low production cost (549 € per kilogram for biomass based LIG)[61].

The microstructure, functionality, and defect density of LIG electrodes can be manipulated. Additionally, the structural defects on graphene sheets provide opportunities for further material doping and functionalization. The oxygen content in LIG can also be controlled, allowing for tunability of surface wettability from superhydrophilicity to super hydrophobicity[62,63].

LIG enables the simple, cost-effective, and scalable production of technological components, leading to the development of sensors, supercapacitors, and resistors, among other applications. Moreover, the production of LIG is environmentally friendly, requiring no controlled environments, expensive chemicals, or specialized equipment. It generates minimal waste and can utilize biocompatible and biodegradable precursors[27,59,64]. Additionally, LIG's one-step manufacturing process does not require the need for slurry preparation or other deposition methods, reducing production time and costs.

Of particular interest is the recent rise in the synthesis of LIG from natural, bio-based substrates, expanding its use in various electronic applications[25,65]. Green LIG (gLIG) represents a promising and interesting approach to address, or at least reduce, the problems associated with the toxic and e-waste. Moreover, offering compatibility with well-established production methods like roll-to-roll processing, which poses quick implementation at industrial level[66].

Nevertheless, it is not common for new and emerging technologies to become available on the market if they do not surpass the current state of the art (SOTA) or if they do not follow the “ten times cheaper or ten times better” rule[67]. Therefore, despite the advantages of gLIG-based devices, it is highly unlikely that they will quickly replace existing mature technologies, which can be manufactured on a large scale at relatively low costs. Nanomaterials, such as graphene, offer clear advantages for the production and scale-up of emerging flexible and smart devices. Due to its compatibility with flexible substrates and low-cost fabrication, gLIG-based electronics can bring electronic functionality to markets that are unfit for rigid and expensive silicon electronics[68].

The increasing demand for Internet-of-Things (IoT) smart devices is projected to drive the growth of the global wearable market from an estimated value of USD 116.2 billion in 2021 to USD 265.4 billion by 2026. This represents a compound annual growth rate of 18.0% for the period in question [25]. From this perspective, LIG could become a fundamental material for

device fabrication, based on a trade-off between high performance and fast device patterning. Nevertheless, one of the key advantages of gLIG processing is its sustainable nature, which fosters the promotion of a greener, circular economy[69].

In 2024, the graphene market reached $445 million, with studies estimating graphene prices ranging $50 to $1k per kilogram. These estimates primarily account for graphene nanoplatelets (GNPs) and similar top-down graphene materials, such as graphene oxide (GO) and reduced graphene oxide (rGO), which incur higher costs due to additional processing steps. Similarly, graphene produced via CVD commands higher prices due to the need for a controlled environment and specialized equipment.

Laser-induced graphene, on the other hand, requires an initial investment in a laser cutter- $25k for industrial-grade equipment, though commercial options are available for under $5k. Beyond this, production costs should be considerably low, owing to inexpensive substrates and minimal power consumption. However, direct cost comparisons are challenging, as LIG production is better measured in terms of cost per meter (or square meter) rather than by mass. Such distinctions also apply when comparing other properties given the plethora of systems where graphene from different sources have been implemented. In the graphene market, a “one-size-fits all” approach is unlikely to succeed, and different processing techniques will find their niche. Nevertheless, the development of scalable, versatile, eco-friendly, and single step methods for carbon-based electrode patterning is crucial. In this context, direct laser writing stands out as a promising technique. This thesis uses DLW to fabricate LIG-based structures, enabling their integration into sustainable platforms.

2.4 Laser-induced graphene: Fundamental principles and applications

This subsection provides an in-depth exploration of the formation mechanism underlying laser-induced graphene. It provides a comprehensive overview of the key factors that significantly impact the fabrication of LIG by direct laser writing. These factors include the type of laser system used, operating parameters, processing atmosphere, and doping strategies, among others. It also briefly discusses how these parameters influence the morphology, as well as the chemical, electrical and mechanical properties of the prepared LIG. In addition, strategies for achieving tailorable material properties, precise writing resolutions, and functional material designs are explored in this subsection. Furthermore, potential applications of LIG as an active electrode and sensing material are explored, highlighting its versatility and potential in various fields.

2.4.1 Laser system setup

LIG production process uses a laser source to generate a beam that is coupled to an adjustable-intensity control system, with a specific setup and motors capable of directing the laser beam through a mirror system and a focusing lens to a specific location on the substrate, while the computer-controlled design determines when the laser beam is turned on or off.

The position and speed of the laser beam are controlled by a movable X-Y axis, while the focal distance is regulated by the specifications of the focusing lens and a movable stage (Z axis), where the substrates are placed, as illustrated in Figure 10. These laser setups can be operated in either vector or raster mode. In vector mode, the laser system's X-Y axis motion system simultaneously moves in two dimensions along the line or path to match the shape being processed. In raster mode, a bitmap image with a specific pulse density, given in dots per inch (DPI) or pulses per inch (PPI), is rasterized on a millisecond timescale. This mode is preferred for 2D patterning of LIG.

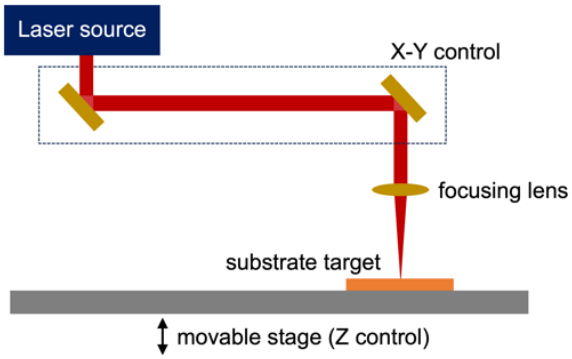

Figure 10. Schematic illustration of the working principle of a processing laser.

2.4.1 Formation mechanism of LIG

The interactions between lasers and materials involve intricate physical and chemical processes that depend on the multiparametric characteristics of the laser beam and the properties of the irradiated materials[70]. An understanding of the mechanism behind the production of LIG provides a theoretical basis for laser processing of carbon materials, the preparation of 3D porous laser-induced graphene structures, and the development of graphene-based devices.

Lasers are primarily used as a source of light and provide photonic energy. In the DLW technique, when a laser beam irradiates a target material, a portion of the photonic energy is absorbed, while the remaining energy is reflected and/or scattered. The absorbed energy can induce different phenomena[71]. According to the mechanism of laser-induced graphene, the

photophysical process can be divided into two main processes, photothermal and photochemical, as illustrated in Figure 11a[72].

During the **photothermal process**, photonic energy is absorbed by the carbon source materials and transformed into lattice vibrations, leading to a high energy accumulation and exceptionally high temperatures (above 2000°C) in the irradiated area. The promotion of photons with high vibrational energies induces the decomposition of several lower energy and weak chemical bonds, such as -COOH and -OH, while allowing rapid reorganization of strong C-C bonds and structural transitions within irradiated chemical structures during thermal accumulation and subsequent thermal relaxation[73,74]. Consequently, photothermal effects instigate bond cleavage and the rearrangement of bonds from sp^3 to sp^2, culminating in the formation of LIG. In instances of prolonged or excessive exposure, complete ablation of the irradiated material may occur. Regarding **photochemical conversion**, when the photonic energy of the laser exceeds the dissociation energy of the substrate's chemical bonds, the carbon source material absorbs this energy, which can lead to direct bond isomerization, forming, and breaking. This process enables the rearrangement and formation of LIG structures without heating the substrate[72]. The localized reactions that occur during the light absorption of the substrate for conversion to LIG depend on several processing parameters. For example, photochemical bond breaking depends primarily on the wavelength of the laser photons and their interaction with specific bonds within the chemical framework of the precursor material. Conversely, photothermal effects depend on a set of operational parameters, including laser power, scanning speed, pulse width, pulse frequency, among others, which control the optical fluence and the resulting induced temperatures[27,75]. Thus, the next subsection provides an overview of the interdependencies between the laser system characteristics, variable operating parameters, carbon precursors, and strategies to enhance LIG formation.

2.4.1.1 Laser processing parameters

2.4.1.1.1 Laser source wavelength, pulse width and pulse repetition rate

Laser systems are commonly categorized according to the laser's gain medium, which refers to the matter stimulated within the laser cavity to generate the laser beam. This medium can be solid-state, gaseous, dye, and semiconductor[71]. Beyond the laser gain medium, laser beams can have diverse characteristics, such as wavelengths, energy levels, and temporal propagation.

Laser wavelength for LIG formation mostly range from infrared (IR, >780 nm)[76–78], to visible (Vis, 400 – 780 nm)[79,80], and ultraviolet (UV, < 400 nm)[81–84](Figure 11a).

During laser light generation the energy of a photon depends on the energy levels of the atom involved in its generation through transitions. This energy can be determined according to Planck's equation, $E = h \cdot v$, where E represents the energy in Joules, h is Planck's constant (6.626×10^{-34} Joule-seconds), and v is frequency in Hertz.

Lower frequency light corresponds to longer wavelengths, while higher frequency light is associated with shorter wavelengths, corresponding to light that carries more energy per photon.

The morphology of the LIG structure can be significantly influenced by the laser wavelength. Hence, LIG formation induced by IR wavelengths is more likely to occur through a photothermal process due to the longer wavelength and lower energy, thereby enabling the carbon precursor materials to efficiently absorb energy and convert it into heat. The rapid increase in temperature leads to the breaking and reformation of chemical bonds within the material. Consequently, this process facilitates the formation of micrometer sized LIG pores and flakes. In contrast, lower wavelengths and higher energy lasers mainly trigger a photochemical conversion, which allows photons to carry energy greater than the dissociation energy required for breaking chemical bonds within the material. Thereby, UV lasers can be used to prepare LIG with better uniformity in pore generation from the nano-to micrometer sized pores[82,85]. Visible lasers offer the potential for a combination of both photothermal and photochemical reactions, contributing to the formation of LIG[79]. Notably, the surface size of LIG obtained through visible laser processing has been shown to be considerably smaller than that achieved with IR lasers[28]. In addition to photophysical processes, the choice of operating wavelength also plays a pivotal role in determining the laser spot size, thus influencing the ultimate patterning resolution.

Laser spot size at the focal plane depends on two main components, namely the wavelength of laser photons and the optics system employed for beam shaping [86].

It is important to note that at a focused position, the spot size is minimal, resulting in the most condensed interaction of the beam with the material. The optical diffraction limit dictates a direct proportionality between the spot size and wavelength. Thus, laser sources emitting shorter wavelengths are preferred for achieving high-resolution patterning. While typical IR CO_2 lasers present spot sizes in the hundreds of micrometer range, visible and UV lasers can achieve much higher spatial resolution[55,80].

This characteristic renders UV lasers particularly advantageous over IR lasers in facilitating the miniaturization of LIG-based devices[28,86].

In the time domain, an important laser feature to consider when categorizing a laser system is its operation mode, which can be divided into continuous wave (CW) and pulsed modes.

A CW laser emits steady beams with consistent energy regardless of time, while a pulsed laser emits photon energy for a set duration, namely **pulse width** or pulse duration (PW), at a fixed repetition rate, known as **pulse repetition rate** or pulse repetition frequency (PRF).

Pulse width and pulse repetition rate are two main variables that have a great influence on the photon flux and the resulting energy and heat accumulation of single pulses or subsequent pulse trains[71].

PW can vary depending on the laser type, for example the most common CO_2 lasers are very limited ranging from milliseconds (ms, 10^{-3} s) to microseconds (µs, 10^{-6}), while other configurations allow for ultra-short laser pulses, with duration from picoseconds (ps, 10^{-12}) to femtoseconds (fs, 10^{-15}).

An overview of the most widely used lasers for LIG production, categorized by wavelengths and pulse duration, is provided Figure 11b[27,87].

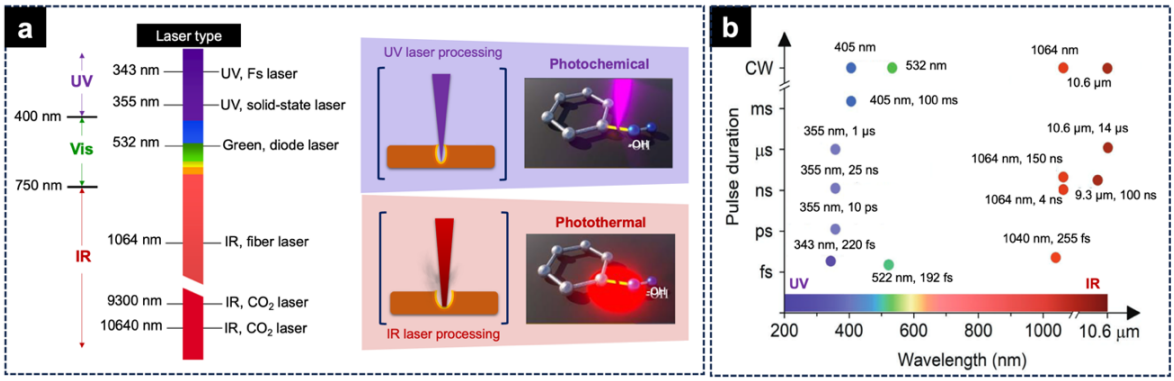

Figure 11. (a) Type of lasers used for LIG production and correspondent photophysical processes, adapted from [72,85]. (b) Summary of lasers used in LIG fabrication, categorized by wavelengths and pulse durations, reproduced with permission from [27]. Copyright (2022) Wiley - VCH GmbH.

Ultrashort laser pulses (fs lasers) have been introduced to DLW to achieve higher patterning resolution and finer control of heat accumulation compared to longer pulse duration lasers [27]. This results in a significant reduction of the thermal energy impact on the material, preventing unexpected thermal effects in nearby irradiated regions and minimizing the heat-affected zone (HAZ), as illustrated in Figure 12a. This enables the creation of narrower pattern linewidths, even beyond the limits of optical diffraction. Hence, to minimize the HAZ and improve the spatial resolution of LIG patterning, ultrafast lasers with shorter pulse durations are preferred. Despite the effectiveness of fs lasers, a portion of photon energy can still be converted into heat, contributing to a mechanism that remains incompletely understood. It is hypothesized that fs lasers involve a combination of photochemical and photothermal processes with the prevalence of each reaction determined by the pulse-to-pulse time spacing, which is inversely related to the pulse repetition rate [88].

Figure 12b shows the correlation between femtosecond pulses and the photothermal response[87,88]. By reducing the interval between pulses (e.g., at high repetition rates of several kHz or higher), the energy transfer rate is increased. While higher efficiency material processing through heat accumulation is possible, this may also result in thermal side effects, similar to those observed with CW lasers[89,90].

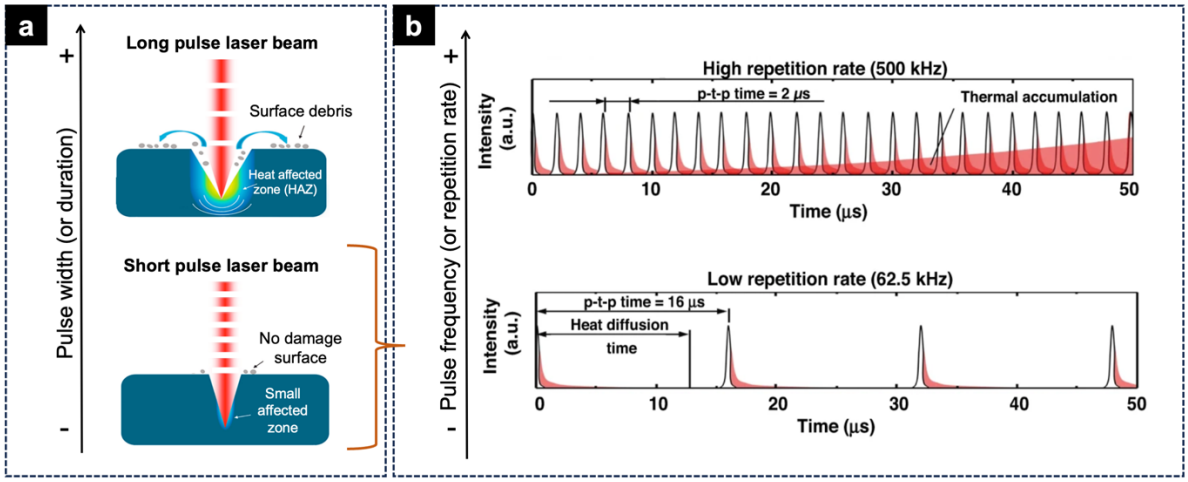

Figure 12. (a) Illustration of laser–material interaction characteristics, of long pulse and short pulse (the gradient color represents the heat affected zones), adapted from [91]. CC BY 4.0 license, https://creativecommons.org/licenses/by/4.0/. (b) Pulse repetition rate effects on heat accumulation in femtosecond DLW, adapted from [86]. CC BY 4.0 license, https://creativecommons.org/licenses/by/4.0/.

Another key factor, besides the type of laser system used, that contributes to the graphitization of the substrate is ensuring that the power supply exceeds the threshold energy required for LIG formation[28]. This is achieved by controlling the laser fluence over the substrate.

Fluence (F), defined as the optical energy delivered per unit area to the substrate in joules per square centimeter (J cm^{-2}), is the most suitable metric for characterizing the interaction between the laser and the material. The impact of the fluence is substantial as it dictates the energy dynamics involved in carbonization and graphitization processes. This parameter will be further explored later in this section.

At lower fluences, photochemical reactions predominate, while at higher fluences, marked by extended exposure of each unit area, the influence of photothermal effects becomes more pronounced[71].

Thus, the selection of an appropriate laser source is important, considering various factors, including the substrate light absorption to facilitate efficient photon-induced heating at suitable fluence levels, as well as considerations regarding laser spot size.

2.4.1.1.2 Laser power, scanning speed and beam focus

The input energy onto the substrate is controlled by the **laser power**. Depending on the selected laser system and its maximum power output, adjusting the irradiation power allows to control the energy delivered to the substrate surface and the resulting irradiation temperature. This tunning should promote bond cleavage and subsequent reorganization, while minimizing excessive degradation and ablation. However, the selection of optimized laser power and understanding its impact over the graphitization is not an isolated variable.

The **scanning speed** enters directly into the equation of the exposed energy density and is therefore a critical parameter, as it determines the reaction time. For synthesis and patterning of LIG, the scanning speed impacts the distribution of irradiation energy in both CW and pulsed type of lasers[11].

The relationship between laser power and scanning speed is of paramount importance in the graphitization process, as it determines the amount of energy delivered to the carbon atoms, which in turn influences the quality of the graphene produced.

To ensure sufficient energy for effective graphitization, it is necessary to increase the laser power at higher scan speeds. This results in the formation of higher quality LIG with improved structural and electronic properties.

In addition, increasing the laser power leads to an increase in the thickness of the LIG as a result of the conversion of a greater number of carbon atoms into graphene, thereby improving mechanical strength and durability. The formation of more graphene domains improves material's electrical conductivity. Thus, increased power results in a greater amount of gas being released, with the formation of more pores, thereby enhancing the porosity of the LIG.

It is important to note that excessively high laser power can degrade the LIG quality and introduce defects. Therefore, the optimal combination of laser power and scan speed is critical for high-quality LIG synthesis with desired properties. This entails balancing improvements in structural and electronic properties, thickness, electrical conductivity, and porosity while avoiding the detrimental effects associated with excessive power levels[55].

In addition to adjusting the power and scan speed variables, another method of manipulating the pulse profile and irradiation effects is by varying the **beam focus** parameter.

The laser spot size at the focal plane is primarily determined by the laser wavelength and the optical system used for beam shaping, as discussed previously. Meanwhile, the spot size can also be directly adjusted by changing the relative position of the optical system and the substrate surface. Following a Gaussian beam profile, the laser spot size radius (ω) can be calculated using the expression: $\omega(z) = \omega_o\sqrt{1 + (\lambda \cdot z/\pi \cdot {\omega_o}^2)^2}$, where ω_o is the spot size radius at the focal point and z is the relative distance to the focal point (Figure 13a).

Furthermore, defocusing the laser beam increases the spot radius, which affects the energy density of a laser pulse and promotes greater overlap between successive laser pulses, as shown in Figure 13b.

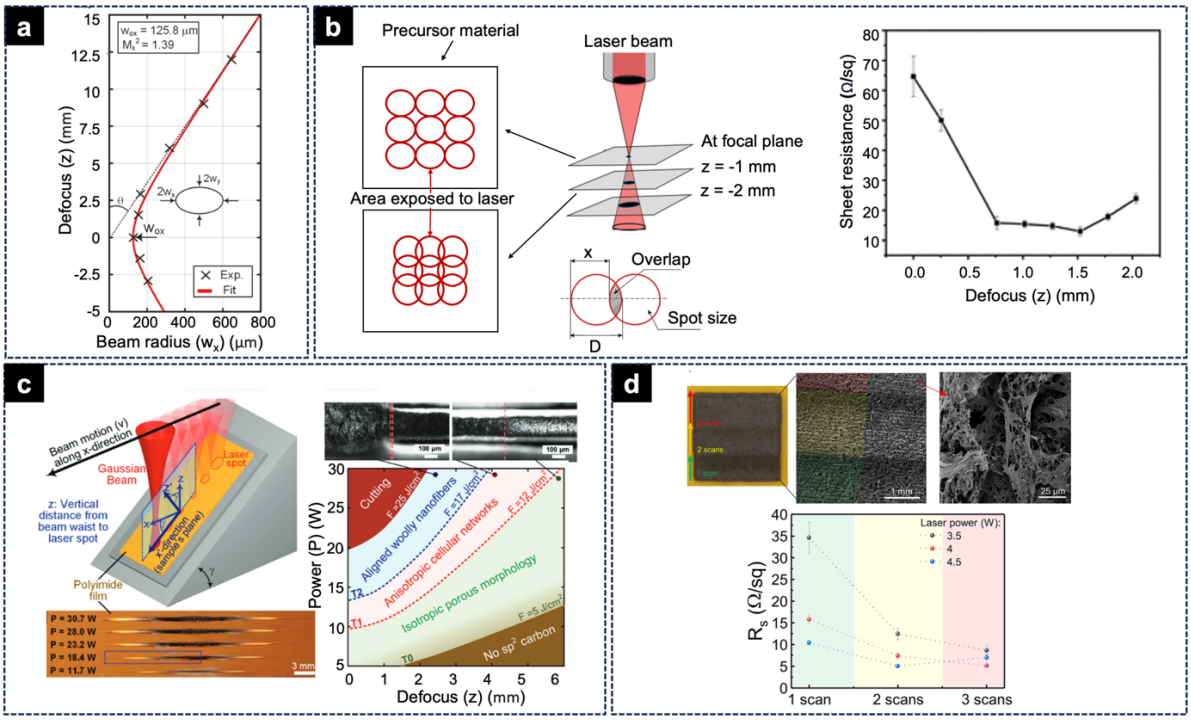

Figure 13. (a) Estimated gaussian beam profile, illustrating the divergence of the beam radius *vs* defocus distance (z), reproduced with permission from [92]. (b) spot size effect *vs* defocus, and correspondent effect in sheet resistance values at various level of defocus, adapted with permission from [93]. Copyright (2018) American Chemical Society. (c) dependency on laser power and defocus distance toward morphological transition levels and laser beam defocus *vs* laser fluence selection, reproduced from [92], Copyright (2021) American Chemical Society. (d) sheet resistance values of LIG produced by one to three lasing scans and varying laser powers over substrate, reproduced with permission from [94]. CC BY 4.0 license, https://creativecommons.org/licenses/by/4.0/.

In this sequential process, graphitization is initiated by the first pulse, followed by overlapping irradiation in subsequent pulses to induce the desired graphitization. This approach enhances conversion efficiency within a single raster line, and the overlapping regions of individual laser lines undergo multiple exposures, resulting in improved electrical sheet conductivity of LIG films[93].

Additionally, defocusing the laser beam can reduce the effective fluence on the precursor, as shown in Figure 13c, which directly affects the LIG morphology[92].

In Figure 13d, similar improvements in graphitization potential and efficiency have been demonstrated through multiple laser scans for conversion, leading to improvements in electrical sheet conductivity[94]. However, careful control of the laser's operating parameters enables single-scan irradiation conversion. This is achieved by tuning the input power and its

distribution to create superposition pulse patterns that mimic the effects of multiple patterning cycles.

Researchers have explored the manipulation of pulse energy distribution as a strategic approach to complement the effects of the laser power, scan speed, and beam defocus in LIG production.

In the realm of pulsed laser systems, control of the pulse density over irradiated areas can be achieved by adjusting the pulse width and pulse repetition rates, as discussed previously.

Variable parameters such as pulses-per-inch (PPI), dots-per-inch (DPI), or switching frequencies provide adaptive control over fabrication conditions. Pulse density can also be described in SI units, as pulses-per-centimeter (PPc) or dots-per-centimeter (DPc) (see Figure 14a).

Higher PPI values lead to greater overlap of pixels and higher image density. This enhanced density results in higher resolution and precision during the synthesis process, allowing for detailed and intricate patterns to be formed in the graphitization process. This finer resolution enables the creation of LIG films with well-defined features and uniformity, crucial for achieving superior electronic properties compared to LIG produced with lower PPI values. To produce high-quality LIG films, a PPI value of 1000 is commonly used to maximize the number of laser pulses per inch and optimize pixel overlap[11].

When manipulating pulse density while examining power and scan speed variables, pulse selection is a relevant variable. Pulse repetition rate or frequency (PRF) can be calculated as follows: $PRF = Speed \cdot Maximum\ Speed \cdot PPI$. Depending on the power and scan speed parameters, the energy output of the laser beam pulses can be adjusted to match the desired power by changing the pulse width, given by: $PW(s) = (1/PRF) \cdot Power$. This determines the duty cycle and how long the laser pulse is active during each pulse, as shown in Figure 14b.

The strategy of defocusing is another effective method for adjusting laser fluence, which can be quantified by the equation: $F = (Power \cdot PW)/(\pi \cdot {\omega_z}^2)$, where ω_z represents the radius of the laser spot size.

Defocusing the laser beam, along with modifications to the PPIs, DPIs, or repetition rate/frequency, facilitates manipulation of the pulse profile. This manipulation is crucial as it enhances the graphitization potential and improves conversion efficiency[95].

Furthermore, defining these parameters enables precise control over the laser fluence, determined by the power and scanning speed as well, as shown in Figure 14b[96,97].

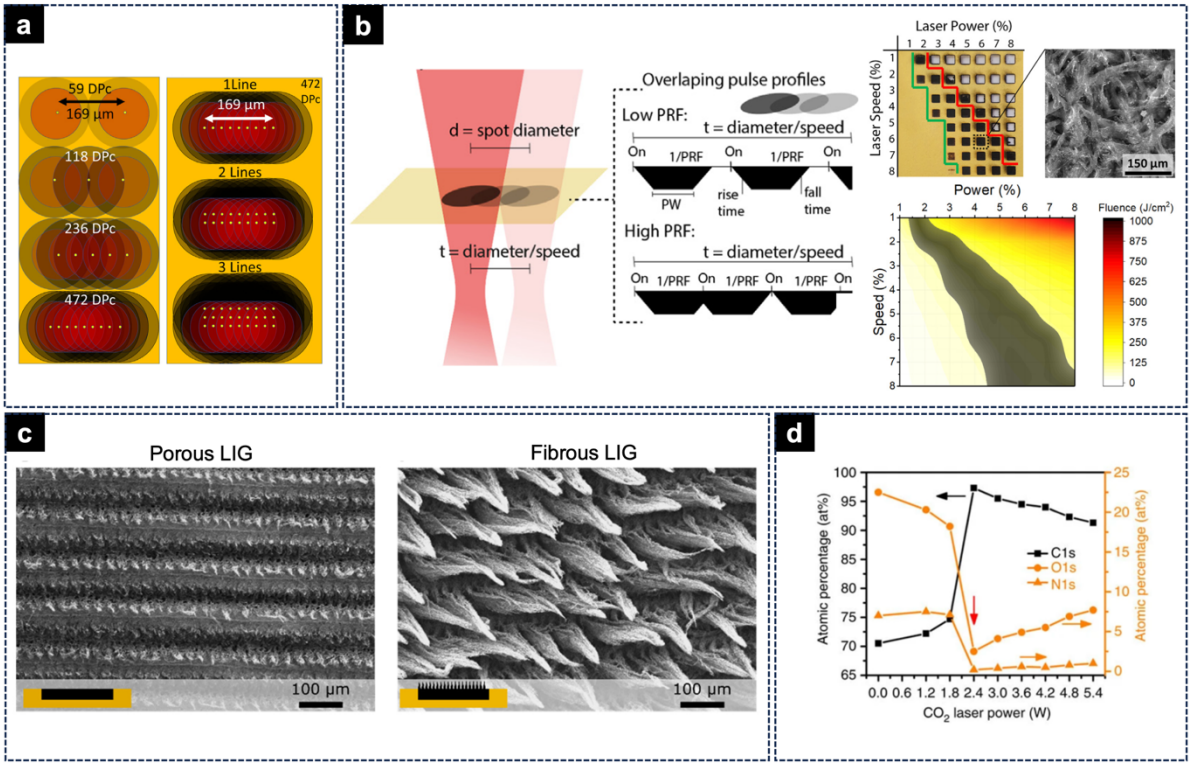

Figure 14. (a) Engraving LIG lines at different DPc (dots per centimeter) and overlap effect between pulses, reproduced with permission from [98]. Copyright (2021) Elsevier Ltd. (b) Pulse profiles according to defocus and PRF variable and LIG film matrix and fluence heatmap identifying graphitization region and its distribution in different fluence levels, reproduced from [95]. CC BY NC-ND 4.0 license, https://creativecommons.org/licenses/by-nc-nd/4.0/. (c) SEM images of porous and fibrous LIG, and (d) X-ray photoelectron spectroscopy (XPS) of LIG scribed with different laser power showing the conversion of PI into LIG, reproduced with permission from [99]. CC BY 4.0 license, https://creativecommons.org/licenses/by/4.0/.

The laser energy applied during LIG production can also be calculated using the formula: $F = (Power)/(Speed \cdot \omega_z \cdot PPI)$. Duy et al. calculated a critical fluence, F_{crit}= 5 J cm^{-2}, necessary for initiating LIG formation. By adjusting the laser fluence, the LIG morphology can be tailored. For instance, it was observed that surpassing a specific fluence threshold during a set scribing resolution causes a shift from a flat, porous LIG to a structure featuring bundles of carbon fibers, as observed in Figure 14c[100]. High scribing resolutions yield a flat LIG, whereas lower resolutions lead to the formation of fibers. In cases of high resolution, overlapping laser spots tend to disrupt the growth of emerging fibers, whereas at lower resolutions, these fibers are allowed to develop. Moreover, laser fluence also impact the chemical composition of the LIG. Once the conversion threshold is reached, the carbon content reaches a maximum and then decreases with higher fluence values, as shown in Figure 14d. Simultaneously, the oxygen content increases with higher fluence values, resulting in a lower-grade LIG. Nonetheless,

increasing the fluence also deepens the conversion, thereby converting more material into LIG. This process ultimately leads to increased sheet resistance up to a certain fluence value[55].

2.4.1.2 Carbon precursors

The selection of the precursor material is a crucial factor in determining the properties and structure of LIG. Researchers have conducted numerous studies regarding the significant influence of the precursor material on the morphology, electrical conductivity, and surface area of the resulting LIG product.

In the early days of LIG discovery, only a few materials, such as PI and polyetherimide (PEI), could be successfully converted into graphene.

Since then, a variety of material precursors have been explored for laser graphitization, including both polymer-based materials and renewable sources. Polymer-based materials including polyetherimide (PEI), sulfone polyether ether ketone (SPEEK), polyarylsulfone (PES), polyphenylsulfone (PPSU), and polyphenylene sulfide (PPS), which share structural similarities with PI, have been employed as precursors for laser graphitization according to various studies[55,101–103]

It is crucial to acknowledge that these polymer precursors may undergo thermal deformation when subjected to high-temperature laser treatment, which could result in structural alterations and compromise the material's overall quality. Among polymer-based precursors, PI stands out for laser graphitization due to its thermal stability, chemical resistance, and excellent mechanical flexibility.

Moreover, the presence of aromatic sp^2 carbons in PIs facilitates the formation of hexagonal graphene more effectively compared to other precursors. The distinctive chemical structure of PIs, characterized by highly conjugated aromatic rings, offers a plentiful supply of sp^2 carbon atoms that readily engage in the graphitization process. These aromatic sp^2 carbons exhibit a high degree of planarity, which promotes the formation of hexagonal graphene structures.

A few years after the initial report on LIG generation from synthetic precursors, researchers demonstrated that LIG could also be directly produced using bioderived materials like bread, potato peel, or coconut shells[93].

This transition from synthetic to bioderived LIG sparked interest in understanding the conversion mechanism and exploring new applications enabled by these natural precursors.

Bio-based substrates include readily available and abundant raw materials like wood, leaves, cork, husks, coal, food, among others. In recent years, there has been a notable increase in exploring these environmentally friendly materials for LIG production. Their versatile chemical compositions and potential to be transformed into valuable products make them an exciting

field of study. This topic will be explored further in the following chapter. Thus, tailoring the chemical composition and mechanical properties of these precursor substrates allows for optimal irradiation and graphitization outcomes[25]. The advantage of using bioderived precursors includes the reduction of carbon footprint and upcycling of waste materials, aligning with the principles of the circular economy. Another intriguing aspect is the potential for developing transient electronics using these materials. Bioderived precursors can be engineered to control their biodegradability, thereby minimizing end-of-life electronic waste. This research on bioderived LIG aligns with the United Nations' Sustainable Development Goals (SDGs), particularly SDG 9 (Industry, Innovation, and Infrastructure), SDG 11 (Sustainable Cities and communities), SDG 12 (Responsible Consumption and Production), SDG 13 (Climate Action) and SDG 15 (Life On Land) contributing to a more sustainable future)[65].

2.4.1.3 LIG functionalization

One strategy for broadening the use of LIG in electronic devices is to modify its properties or introduce new ones to enhance LIG's performance and introduce functionalities that it inherently lacks.

From an engineering perspective, the tunable characteristics of LIG are beneficial for expanding its range of applications. Various doping methods, including pre-treatment of carbon precursors, post-treatment of LIG, and producing LIG in different atmospheres, have been employed to modify LIG properties (e.g., hydrophilicity/hydrophobicity and electrical/electrochemical characteristics)[59].

Two distinct methodologies can be used to modify LIG: in situ and post-treatment modification.

2.4.1.3.1 In situ

Typically, in situ modification involves: (a) modifying either the substrate composition or (b) the laser atmosphere during the laser ablation process.

(a) Substrate pre-treatment

Pre-treatment involves incorporating additional materials into carbon sources prior to lasing. This approach can induce LIG formation and modulate the hydrophilic/hydrophobic and electrical/electrochemical properties of LIG, depending on the added material.

Researchers have employed a variety of chemical pre-treatments on precursor materials that typically have poorer thermal stability compared to high-performance synthetic polymers. One such approach involves using fire-retardants. These treatments increase the thermal stability of substrates by introducing functional groups or external molecules, such as phosphate and boron moieties. These compounds undergo endothermic decomposition and act as chemical

heat sinks, allowing laser-induced reactions to occur at the molecular level without igniting or ablating the precursor materials[104].

In the absence of such pretreatments, substrates rich in aliphatic compounds typically undergo pyrolytic decomposition processes, resulting in the formation of volatile compounds and complete substrate ablation[25,105]. Although fire retardants are commonly used as additives for pre-treating precursors in LIG synthesis, their specific role and chemical pathways in this process are not always well understood. Most research employs these additives without investigating the underlying mechanisms. There is more knowledge available about fire retardants themselves, even if they are not specifically studied in the context of LIG synthesis. Phosphate-based fire retardants are the most frequently used in bioderived substrates. When heated during laser irradiation, these compounds react and turn into polymeric phosphoric acid, creating a char layer. This char layer prevents further burning of the material and may contribute to the formation of LIG[106]. Another example is pre-treating substrates with certain functional elements, such as fluorine, can result in fluorine doped LIG. During this process, the high temperature of the laser causes decomposed atoms to be incorporated into the LIG, making it hydrophobic. For instance, incorporating metal nanoparticles (e.g., copper, cobalt, nickel, iron, and nickel-iron) into the precursor prior LIG formation significantly enhances its electrical and electrochemical properties[11]. However, special care should be taken when considering these doping species, not to significantly impair the sustainability of the process. In the specific case of supercapacitors, manganese oxide is a dopant as it has been regarded as an environment friendly metal oxide[107,108].

(b) Process atmosphere control

In addition to substrate pre-treatments, in situ modification can also be accomplished by employing various processing atmospheres during LIG formation. For instance, laser scribing in different atmospheres, such as argon (Ar), nitrogen (N_2), hydrogen (H_2), or other gas mixtures, can yield diverse outcomes in the structure and composition of the resulting LIG. Some precursors can be turned into LIG successfully only in an inert atmosphere, while others can form LIG even in a non-inert atmosphere, such as ambient air with the presence of oxygen (O_2)[65]. The composition of the atmosphere is crucial for controlling the degree of graphitization and LIG properties for different substrates. This is particularly important for bio-derived materials, which are more sensitive to higher temperatures and can burn more easily.

Inert atmospheres facilitate more efficient substitution of oxygen moieties and result in more stable surfaces. Conversely, the presence of oxygen in the air can lead to increased combustion and oxidation, resulting in higher volatile formation and porosity. This is specially significant where inert atmospheres are essential for LIG synthesis using CO_2 lasers[109].

2.4.1.3.2 Post-treatment

This modification involves applying additional processing steps to LIG after its initial formation. Although LIG exhibits defects, these can be particularly favorable for post-treatment methods, incorporating additional materials or layers into its surface or bulk (e.g., introducing conductive ink, functional elements, or metal nanoparticles), which effectively adjusts the properties of LIG.

Plasma treatment, such as fluorine plasma, oxygen plasma, and air plasma, is a convenient surface post-treatment technique for adjusting the hydrophilic/hydrophobic nature of LIG. Generally, treating LIG with fluorine plasma enhances hydrophobicity, whereas oxygen/air plasma treatment increases hydrophilicity[70].

Additionally, electrodeposition onto the interior or surface of LIG with polymers (e.g., polyaniline), metal oxides like iron oxyhydroxide (FeOOH) and manganese dioxide (MnO_2) can be accomplished to create opportunities to enhance LIG properties and functionalities, thereby expanding its potential applications across various fields[110]. Electroless plating serves as another surface post-treatment method for adjusting the electrical and electrochemical properties of LIG. Heteroatom doping can also provide additional sites for electrochemical reactions, which facilitate efficient ion transfer across a range of electrochemical processes[111]. For instance, the emerging and rapidly developing field of flexible electronics, including wearable electronics, robotics, smart clothing, and electronic skins, demands the integration of flexible sensors for activity monitoring and energy devices for power storage or harvesting. The application of advancements in LIG technology enables the fabrication of intricate and precisely designed porous carbon-based structures on flexible substrates, tailored to create specific sensors and energy devices.

Consequently, LIG technology has attracted considerable interest and is poised to significantly propel the development of flexible electronics and related fields. These efforts underline the continuously evolving nature of the rich field of laser-induced graphene synthesis, which enables the competitive development of actual graphene-based products, for active electrode and sensing materials, such as biosensors[112–114], physical sensors[115,116], supercapacitors[65,117,118], batteries[119,120], TENGs[121–124], transistors[125–127], among others. A section summary is presented in Figure 15.

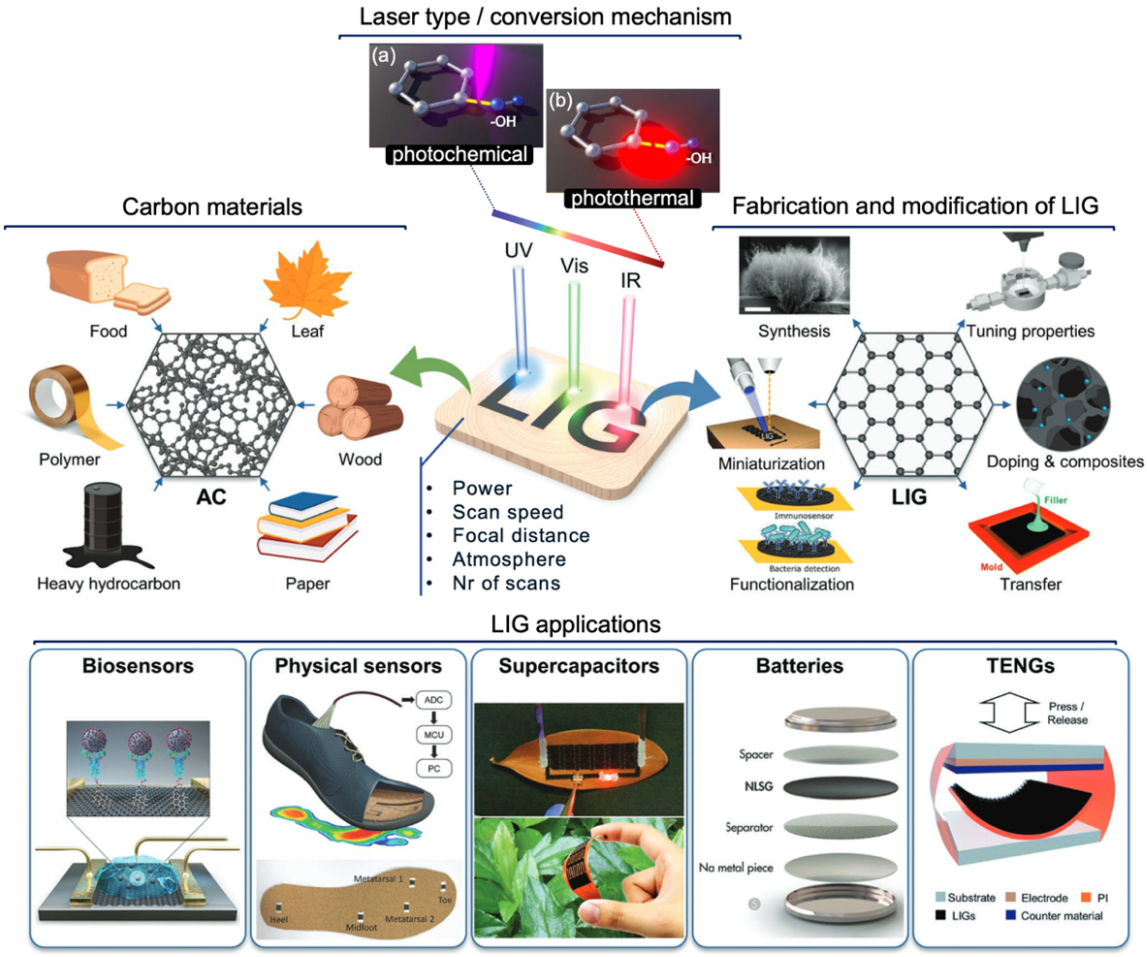

Figure 15. Schematic of the fabrication of LIG using various carbon precursors and lasers, inducing different types of conversions: (a) photothermal (thermal breakage of C and -OH bonds) and photochemical (photo-induced dissociation of bonds between C and -OH). Under laser irradiation, the carbon precursors are rapidly converted to amorphous carbon (AC), graphite, and graphene via carbonization, graphitization, and exfoliation processes, respectively. Direct laser writing (DLW) allows for easy fabrication and flexible modification of LIG patterns with desired structures and properties. These patterns can be used in advanced applications, including biosensors, physical sensors, supercapacitors, batteries, and triboelectric nanogenerators (TENGs), adapted with permission from [72,75,85]. Copyright (2020) AIP Publishing.

2.4.2 LIG applications

Researchers have invested considerable resources to refining the manufacturing processes of LIG to broaden its use across diverse domains. This subsection aims to delve into the principles of device engineering toward LIG's applicability within these technological contexts. The potential of LIG is explored, ranging from its application as an active material in electronic devices to its incorporation in sensing technologies, providing a comprehensive understanding of the effective integration of LIG into sustainable platforms.

2.4.2.1 LIG as an active electrode material

Widespread adoption of portable electronic devices and electric vehicles propelled the development of energy storage devices, particularly focusing on batteries and supercapacitors. Progress in this area primarily relies on the properties of electrode materials, with a strong focus on their porosity, which has resulted in extensive investigation of LIG as an active electrode material for supercapacitors. However, for other components such as transistors and conductive lines, different morphologies may be required.

2.4.2.1.1 In Supercapacitors

Energy storage devices emerged as one of the earliest demonstrated applications of LIG from synthetic precursors and remains a primary focus in approximately one-third of all LIG-related publications today[55]. Supercapacitors (SCs) play a key role as energy storage devices in electronic systems that require high charging/discharging rates, long-term cyclability, and high-power densities[128,129]. Based on their working mechanisms, supercapacitors can be categorized into three types: electrical double-layer capacitors (EDLCs), pseudo capacitors (PCs), and hybrid capacitors (Figure 16).

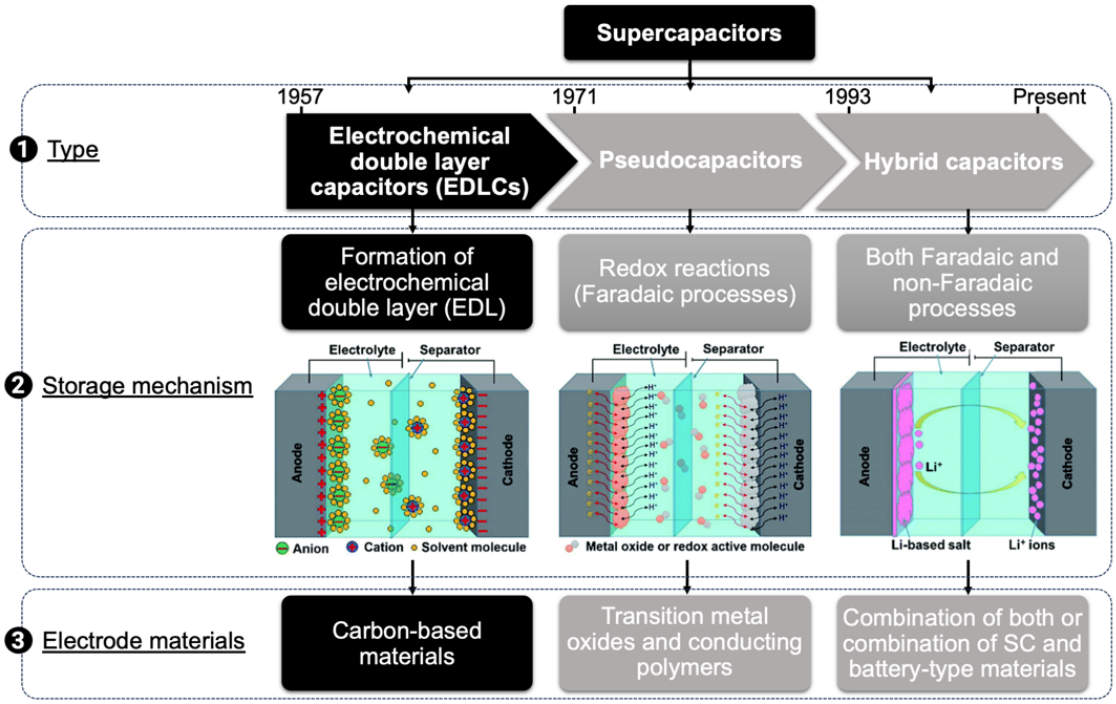

Figure 16. Summary of the types of supercapacitors, their mechanisms, and the main electrode materials used. Adapted with permission from [128,130]. Copyright (2022) RSC Publishing.

EDLCs store electrical energy by the electrostatic accumulation of negative (anions) and positive (cations) charges at the electrode-electrolyte interface, forming an electrical double

layer (EDL). Unlike traditional capacitors, the larger surface area, specific pore size, and volume of the electrodes promote electrolyte penetration at near surface. Thus, enables EDLCs to store a greater amount of charge, resulting in higher capacitance values. Additionally, the energy storage mechanism is purely electrostatic, involving the adsorption and desorption of the ions at the electrode surface, which allows for an intrinsically rapid and efficient charge-discharge process[131]. In contrast, pseudo capacitors store energy through fast and reversible faradaic redox reactions occurring between the electrode materials (mainly at surface) and ions in the electrolyte[128]. Hybrid capacitors combine the characteristics of the first two types, integrating the properties of an electric double-layer capacitor alongside with a pseudocapacitive or battery-like behavior[132].

The device architecture is a significant variable concerning SCs. The most common include the sandwich configuration, comprising two electrodes stacked with an electrolyte layer in between, and the planar (interdigitated) configuration, featuring arrays of in-plane electrode fingers.

LIG, serving as an active electrode material and current collector, is particularly attractive for EDLCs due to its properties: (a) an inherently low resistance that enables efficient electron transfer, (b) tailored wettability that promotes fast ion transfer within the electrode, and (c) a large accessible surface area with porous structure that offer concise transport pathways for the diffusion of the electrolyte ions to the interior surface of the electrode[133,134]. These features usually lead to high specific capacitances and enhanced electrochemical performances.

2.4.2.2 LIG as active sensing materials

Materials that exhibit immediate responses (signals) to environmental changes (including pressure, temperature, humidity, and others) play a significant role in our daily electronics. Among the various sensing materials, LIG has been extensively studied as the sensing unit in piezoresistive sensors.

2.4.2.2.1 For piezoresistive sensors

Strain sensors, which are also referred to as tactile and pressure sensors, play a significant role in a wide range of fields, particularly in the realm of healthcare applications (e.g., monitoring heart rate, pulse, and plantar pressure), environmental monitoring (e.g., temperature detection, gas sensing, and surveillance of pressure and humidity levels), and the realm of robotics and human-machine interfaces (e.g., for tactile sensing, manipulation based on gestures, sound recognition, proximity detection, and spatial orientation) [10].

Piezoresistive sensors are a major category of these sensors and often use LIG due to its effectiveness as a sensing element.

The piezoresistive effect of LIG structures is based on the variation of resistance under pressure or deformation. This change occurs because when an external force is applied or released, the walls of the graphene pores are pushed closer together, resulting in a denser contact between the composite sheets, reducing the resistance. This phenomenon, termed piezo resistivity, is essentially a material's response to strain varying its electrical resistance, which can be attributed to changes in lattice structure and electronic band structure[29].

LIG for piezoresistive sensors should exhibit a rapid response (i.e., change in resistance) to external stimuli with a notable sensitivity and a significant gauge factor (GF), according to $GF = (\Delta R/R)/\varepsilon$, where $\Delta R/R$ represents the normalized resistance and ε denotes the mechanical strain/pressure. Furthermore, possessing a broad sensing range, a linear behavior between strain and resistance, rapid response/recovery times, as well as robust durability are crucial characteristics for a sensing material.

In practical applications, LIG structured layering and unique micro-architectures provide excellent sensitivity across a wide range of pressures.

To increase their adaptability and durability, these graphene structures are often paired with flexible and elastic polymers like polyimide (PI), polyurethane (PU) or polydimethylsiloxane (PDMS). These polymers act as support structures, fillers, and coatings, expanding the sensors' applications without sacrificing their essential properties[135,136].

Moreover, manufacturing these sensors is streamlined by directly forming electrode patterns on flexible substrates or using transferring strategies of the LIG electrodes to a flexible polymer, which cuts costs and simplifies production. The inherent properties of LIG, such as its strong tensile strength and natural piezoresistive behavior, play a crucial role in enhancing the overall device performance.

3

GREEN LASER-INDUCED GRAPHENE: MATERIALS AND METHODS

The following chapter explores the production of green laser-induced graphene (gLIG) from natural bioderived sources, focusing on improvements in terms of their accessibility and sustainability. It outlines their properties and discusses the distinct conversion pathways involved for different precursors. Moreover, this chapter provides a thorough description of the substrate's preparation used in this thesis, such as paper, lignin-enriched paper, and cork materials. It details the experimental methodologies used to optimize and fabricate gLIG structures on these substrates for electrode purposes. Furthermore, it outlines the characterization techniques employed to evaluate the graphitization outcomes of gLIG synthesized from different precursors.

Some of the results shown herein were adapted and reproduced from:

- C. Claro, P. I., Pinheiro, T., **Silvestre, S. L.**, Marques, A. C., Coelho, J., Marconcini, J. M., Fortunato, E., C. Mattoso, L. H., & Martins, R. (2022). Sustainable carbon sources for green laser-induced graphene: A perspective on fundamental principles, applications, and challenges. *Applied Physics Reviews*, *9*(4). **DOI**:10.1063/5.0100785

- **Paper I: Silvestre, S. L.**, Pinheiro, T., Marques, A. C., Deuermeier, J., Coelho, J., Martins, R., Pereira, L., & Fortunato, E. (2022). Cork derived laser-induced graphene for sustainable green electronics. *Flexible and Printed Electronics*, *7*. **DOI**:10.1088/2058-8585/ac8e7b

- **Paper II: Silvestre, S. L.**, Morais, M., Soares, R. R. A., Johnson, Z. T., Benson, E., Ainsley, E., Pham, V., Claussen, J. C., Gomes, C. L., Martins, R., Fortunato, E., Pereira, L., & Coelho, J. (2024). Green Fabrication of Stackable Laser-Induced Graphene Micro-Supercapacitors under Ambient Conditions: Toward the Design of Truly Sustainable Technological Platforms. *Advanced Materials Technologies*, 2400261.
  DOI:10.1002/ADMT.202400261

- **Paper III (Under preparation): Silvestre, S. L.**, Morais, M., Silva, R. R. A., Martins, R., Fortunato, E., Pereira, L., Coelho, J. (2025) Piezoresistive Sensors via Laser-Induced Graphene on Cork for Energy Harvesting Systems

3.1 Introduction

Sustainability is now the driving force for a greener and more technologically advanced future, in line with the global goals set out by the United Nations 2030 agenda[137]. Therefore, to facilitate the transition to a sustainable world and to meet the increasing demand to reduce global dependence on fossil fuels and electronic waste (e-waste), it has become crucial to explore the potential of abundant and renewable materials[138–140]. In addition to their environmental benefits, these materials offer several advantages over traditional polymeric substrates, including cost effectiveness, ease of handling, and improved customization for a wide range of electronic applications, including disposable wearable electronics, paper-based circuits, and packing solutions[141]. However, not all cellulose-based electronics are straightforward in terms of complexity[142]. For example, paper-based electronics typically involve complex processes such as inkjet-based deposition, lithography, and spray coating, among others[143]. While these approaches enable the creation of innovative electronic functionalities on sustainable substrates, they still raise concerns in terms of complexity, limited design flexibility, and time required to manufacture specific devices[1].

The application of laser technology has proven to be an impressive solution to overcome these challenges, offering a simpler, faster, and more controlled methodology[144].

This cost-effective approach not only enables the large-scale conversion of natural, abundant, and renewable resources into gLIG structures with ease, but it also offers environmental advantages over conventional LIG fabricated on commercial materials such as polyimide[25,64,144]. Bio-derived precursors have been tested for green LIG production ranging from raw materials directly obtained from natural sources, such as wood, leaves, cork, and husks, to processed parts of it or byproducts from the wood and paper industries, such as lignin and cellulose.

While raw materials offer obvious advantages due to their availability and low cost, they pose challenges because of their inhomogeneity and large structural and compositional variability from different sources. These inconsistencies make them less suitable for use in LIG-based devices and difficult to integrate into complete electronic systems. In contrast, processed materials, although more expensive due to the extensive processing and refining, can be fine-tuned to achieve the desired properties and forms (e.g., sheet/thin films with homogeneous composition)[65]. Examples include paper substrates with varying amounts of cellulose, lignin-rich composites, cork agglomerated sheets, among others, making them more suitable for LIG production and device integration.

These materials can be divided into three main classes: lignocellulosic substrates (e.g., wood, leaves, and cork), cellulose (e.g., paper and nanocellulose) and lignin, as illustrated in Figure 17.

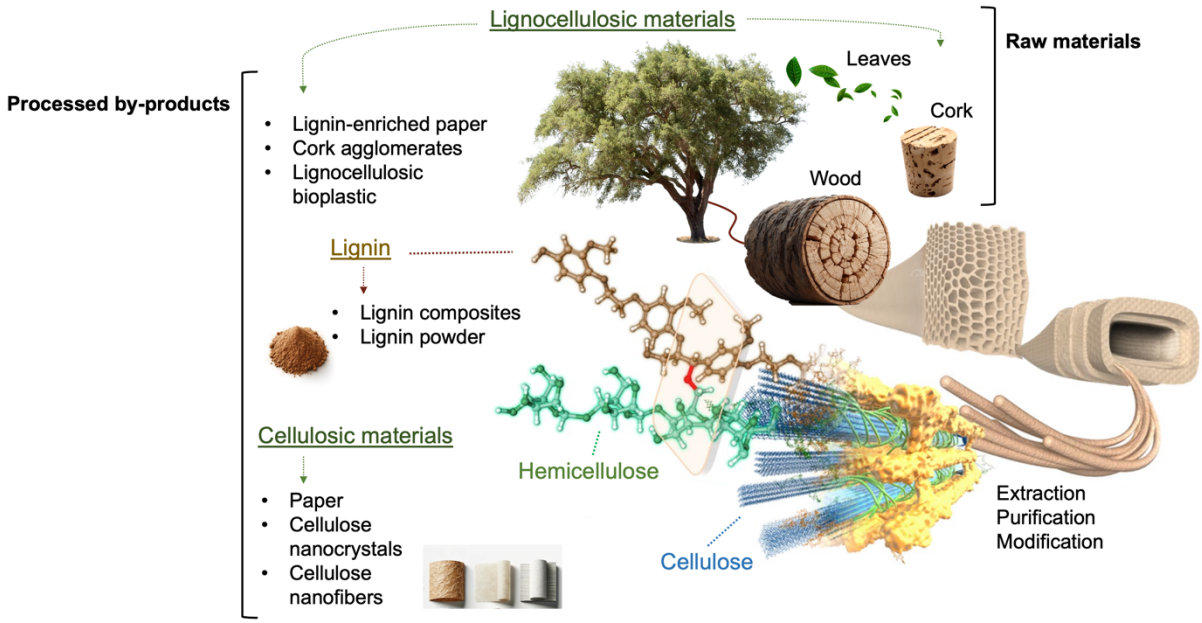

Figure 17. Schematic illustration of the distinct categories of precursors for gLIG synthesis, from raw materials to processed by-products obtained from these natural sources. Adapted with permission from[145]**. CC BY 4.0 license, https://creativecommons.org/licenses/by/4.0/.**

Lignocellulosic materials are naturally found in trees, including their bark and leaves, as well as in other plant sources. These materials are composed of lignin, which is rich in aromatic compounds, and cellulose and hemicellulose, both of which are types of polysaccharides, characterized by their aliphatic chemical structures. These three polymeric components—cellulose, hemicellulose, and lignin—can be seen as the precursors for LIG. They differ in their repetitive units and structure, affecting the carbonization pathways and efficiency of various natural materials. Wood, a common source of lignocellulosic materials, typically is composed of approximately 40−45% cellulose, 15−35% hemicelluloses, and 20−30% lignin[146,147].

The varying quantity of cellulose, hemicellulose, and lignin in wood are key factors in defining its structural, mechanical, and thermal properties of these substrates. Cellulose and lignin primarily contribute to the strength and rigidity to the wood, while hemicellulose enhances flexibility and elasticity. Each plays a distinct structural role within the wood matrix.

Cellulose, a linear polysaccharide, forms the primary structural framework of wood fibers. Its strength and rigidity come from a crystalline structure reinforced by strong hydrogen bonds, which make it rigid, insoluble, and resistant to solvents. These bonds between cellulose molecules are stronger than those between cellulose and hemicellulose, making cellulose

microfibrils the main load-bearing elements of the cell walls. Hemicellulose, a branched and amorphous polymer, binds cellulose and lignin, supporting structural cohesion while adding elasticity and flexibility. It acts as a matrix that embeds cellulose microfibrils, providing the flexibility required for cell walls to deform under stress. However, the amorphous nature of hemicellulose and its weaker hydrogen bonding compared to cellulose make it thermally less stable, introducing lower stability during thermal processing[148]. Lignin, an aromatic polymer filling spaces between cellulose fibers, enhances mechanical rigidity and hydrophobicity. Its high carbon content and aromatic structure play a key role in determining the quality of LIG derived from wood. Additionally, the natural fiber orientation in wood, aligned with its growth direction, introduces complex anisotropic characteristics that influence its mechanical performance, including tensile strength and bending flexibility[149–151]. Although this variability offers a wide range of options for specific applications, it also poses challenges in achieving consistent and repeatable electrical properties in LIG production. For instance, the different decomposition behaviors of cellulose, hemicellulose, and lignin during thermal treatments can lead to heterogeneous graphitization, affecting surface morphology and conductivity[152]. In contrast, leaves have a slightly different composition, with an estimated 47% of their weight consisting of aliphatic compounds and 39% consisting of aromatic compounds[153].

Cork substrate, harvested from the bark of cork oaks (*Quercus Suber L.*), is a unique lignocellulosic material, being one of nature's most extraordinary and versatile materials in the world[154]. Its core components are suberin (≈45%), lignin (≈20%), and polysaccharides (cellulose and hemicellulose) (≈12%)[155]. Like a beehive, cork has cells with pentagonal and hexagonal hollow structures, which provides a large surface area to induce porous 3D structures[156,157]. Furthermore, it presents extraordinary properties, such as lightweight, biodegradability, compressibility, impermeability, resistance to high temperatures, and thermal insulation[154,158].

Cork can be classified into two types: natural cork and agglomerated processed cork. Natural cork, depending on the harvesting stage (virgin tree, first-reproduction, second-reproduction, or successive), exhibits distinct characteristics in terms of structure, thickness, porosity, density, and strength. Agglomerated processed cork consists of a composite material, made from the agglomeration of processed native cork granules with binding agents, resulting in different size grains being compressed into each other while adhering together[159].

Using agglomerated cork instead of pristine cork brings scalability for industrial use, being currently one of the most marketable materials in the world, allowing the production of multiple substrate shapes, from millimeter sheets to bulky pieces. Also, being a composite material with

sophisticated properties can be beneficial for the desired type of application, especially for flexible platforms[155].

Within the cellulosic materials, cellulose is isolated during the pulp and paper production process, which consist of two main parts. The first part, known as pulping, involves converting lignocellulosic material into pulp by removing as much lignin as possible. The second part involves the steps required to produce the final product, which is paper. While wood is often the starting material, other sources such as rags, flax, cotton linters, and bagasse (a sugar cane residue) can also be used[146].

Paper was one of the first bioderived materials converted into LIG. Using paper as a substrate for devices offers a good balance between cost and performance. Paper is not only cheap, lightweight, flexible, and generally hydrophilic, with a high loading capacity important for many applications, but it is also recyclable and biodegradable, which are important for sustainability. Additionally, paper is easily available in various types, sizes, thicknesses, and finishes, allowing it to be tailored to specific applications[160].

Lignin, an extracted low-value waste by-product of the paper industry, is the most abundant naturally occurring aromatic polymer, mainly made up of different monolignols concentrations, which vary across different bioderived precursors, leading to diverse chemical and physical properties[161].

Unlike polysaccharides, lignin has a high carbon-to-oxygen ratio and excellent thermal stability, making it an ideal precursor for LIG production[162]. Lignin can be processed in powder form and converted into films facilitating its use in various applications. However, due to its poor mechanical properties, particularly brittleness, lignin is often combined with synthetic polymers or recycled paper to produce practical substrates. Some methods to create lignin-based substrates include making lignin films with PVA, doping substrates with lignin solutions, and embedding lignin into PDMS154,155.

Expanding the exploration of green LIG has shown that it fulfills essential and desired electrode requirements, including high electrical conductivity and surface area. These properties are primarily due to the inherent nature of the substrates, which results in a highly porous structure with a substantial surface area. Furthermore, the high defect density in the structure of gLIG enhances its electroactivity and catalytic potential for various electrochemical applications[65]. Therefore, the promising properties of gLIG have led to its use in a variety of fields, including the fabrication of biosensors[104,164,165], supercapacitors[78,155,159,166–168], humidity sensors[169], mechanical sensors[169,170], among others. Figure 18 illustrates examples of various bioderived substrates with practical applications based on green LIG.

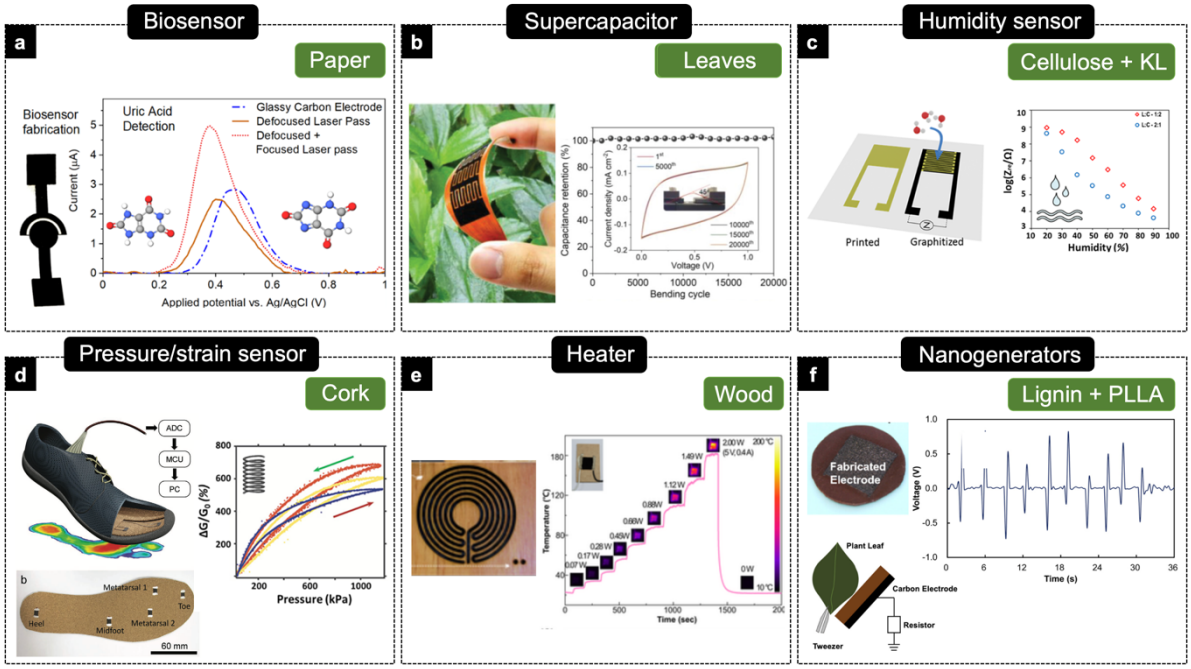

Figure 18. Overview of examples of applications from different bioderived LIG precursors: (a) biosensor, (b) supercapacitor, (c) humidity sensor, (d) pressure/strain sensor, (e) heater, and (f) nanogenerator. (a) Electrochemical biosensor using paper-based LIG electrodes for uric acid detection, reproduced with permission from[112]. CC BY 4.0 license, https://creativecommons.org/licenses/by/4.0/. (b) Interdigital microelectrodes based on LIG obtained from fallen leaves used in flexible supercapacitor., reproduced with permission from[153]. Copyright (2021) Wiley - VCH GmbH. (c) Humidity sensor from lignin (LS)/cellulose-derived LIG, reproduced with permission from[171]. CC BY 4.0 license, https://creativecommons.org/licenses/by/4.0/. (d) Piezoresistive pressure sensor from cork-derived LIG, reproduced with permission from[170]. Copyright (2020) Wiley - VCH GmbH. (e) Joule heating-based LIG heater on recycled wood, reproduced from[151]. (f) Triboelectric nanogenerator based on LIG from lignin/poly(l-lactic acid) (PLLA) composites for power generation, reproduced with permission from[172]. Copyright (2023) American Chemical Society.

Given the unique properties of these natural substrates, this dissertation explores the potential of paper, lignin-enriched paper, and agglomerated cork to produce gLIG. The subsequent section will detail the preparation of these substrates, the methodologies employed for optimizing gLIG properties, and the characterization techniques carried out in this research.

3.2 Materials preparation

3.2.1 Materials/substrates

- Whatman paper 1 (Whatman International Ltd., Floram Park, NJ, USA);
- Agglomerated cork (Corticeira Amorim SGPS, S. A, Mozelos, Portugal);
- Lignin-enriched paper (provided by Eric Benson, E. Ainsley and Veronica Pham, University of Illinois, IL, USA).

3.2.2 Substrates pre-treatments

3.2.2.1 Wax pre-treatment (Paper I – Chapter 5)

Agglomerated cork sheets with 2 mm thickness were pre-treated with a yellow wax-based ink (ColorQube 8870/8880 Yellow Solid Ink, Xerox Europe, Limited, Dublin, Ireland). Wax was melted on a hot plate at 125 °C for 20 s. After that, cork was placed on top of the melted wax layer, until it was absorbed throughout its volume. Finally, waxed cork was removed from the heating plate and allowed to cool down to room temperature and solidify.

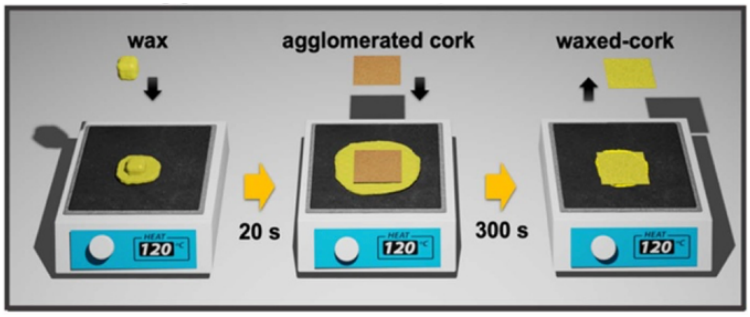

Figure 19. Schematic representation of the agglomerated cork wax pre-treatment. Reproduced with permission from [155]. CC BY 4.0 license, https://creativecommons.org/licenses/by/4.0/.

3.2.2.2 Flame-retardant (Paper II & Paper III – Chapter 5 and Chapter 6)

Whatman paper 1, lignin-enriched paper, and cork substrates were treated with borax, a flame-retardant agent, before undergoing laser irradiation under non-inert atmosphere (ambient conditions and room temperature). Typically, in a normal procedure, the substrates were soaked in an aqueous solution of sodium tetraborate decahydrate (0.1 M, ≥99.5%; CAS: 1303-96-4, Thermo Fisher Scientific, MA, USA) for ten minutes and then left to dry overnight.

3.2.3 Laser-induced graphene process optimization

For the LIG optimization process, a study was performed to compare and evaluate different types of laser systems, different environment conditions and laser conditions. To ensure consistency, all substrates were levelled and gently tapped on a glass surface prior to laser irradiation.

3.2.3.1 Under inert atmosphere (Nitrogen)

Using a IR CO_2 and a fiber laser – (Paper I – Chapter 5 and Chapter 6): For the conversion of cork substrates into LIG structures under a nitrogen atmosphere, a 10.6 µm CO_2 IR (VLS3.5 Laser Platform, Universal Laser Systems, Vienna, Austria) and a 1.06 µm Nd:YAG fiber laser (PLS6MW Multi-wavelength Laser Platform, Universal Laser Systems, Vienna, Austria), both equipped with 2.0” lens (focal length (FL) of 50.8 mm), were used. The CO_2 laser equipment

(Figure 20a) has a wavelength of 10.6 μm and a spot size of 0.13 mm, while the fiber laser (Figure 20b) operates at a wavelength of 1.06 μm and a spot size of 0.03 mm. LIG was engraved in 5×5 mm^2 squares and then silver ink contacts were placed on the ends of the squares. To identify the optimal laser system and conditions that produced the best results, a systematic study was performed, varying laser parameters such as (i) power (adjustable up to 50 W in both lasers), (ii) speed (adjustable up to 1.27 m s^{-1} on CO_2 laser and up to 1.78 m s^{-1} on fiber laser), and (iii) focal point defocus (from 0.76 mm above focal point to 1.52 mm below). A fixed 1000 pulses-per-inch (PPIs) was established for the CO_2 laser, while a fixed frequency of 100 kHz and 1000 PPIs were established for the fiber laser. The optimal conditions for cork-LIG (cLIG) formation were achieved at a laser power 5% and a speed of 4% (equivalent to 2.5 W @ 0.05 m s^{-1}), positioned 0.76 mm above the focal point for the CO_2 laser, and a laser power 11% and a speed of 1% (equivalent to 5.5 W @ 0.02 m s^{-1}), positioned 1.52 mm below the focal point for the fiber laser. Following the electrode requirements tailored to specific applications, the laser system and its parameters were meticulously selected. A fiber laser was selected to fabricate electrodes (operating at a laser power of 11% and a speed of 1% (equivalent to 5.5 W, 0.02 m s^{-1}), positioned 1.52 mm below the focal point onto waxed cork. These conditions were reproduced for the fabrication of electrodes with a view for micro-supercapacitors application, as elaborated in Chapter 5 of this thesis.

3.2.3.2 Under non-inert atmosphere (Ambient conditions)

Using a CO_2 laser – (Paper II – Chapter 5): To selectively convert various renewable substrates, including paper, lignin-enriched paper, and cork, into laser-induced graphene structures under ambient conditions and room temperature, a CO_2 IR (Fusion M2, Epilog Laser, Golden, CO, USA) was used.

An infrared (IR) laser was selected for this study, as it aligned with the focus of our experimental setup and was readily available in the lab. Additionally, it allowed for meaningful comparisons with previous work. The laser equipment (Figure 20c) operated with a wavelength of 10.6 μm, with a focal length of 50.8 mm and a spot size ranging from 0.10 to 0.17 mm. LIG squares designed in CorelDraw, each measuring 5×5 mm^2, were submitted to the laser-controlling program and scribed onto the treated substrates. This was achieved through the systematic variation of significant laser parameters, including (a) power (adjustable up to 75 W), (b) speed (adjustable up to 3.05 m s^{-1}), and (c) defocus distance. A frequency of 100 kHz and a resolution of 1200 dots-per-inch (DPI) were maintained throughout all experiments. After optimizing all laser parameters, the optimal conditions for fabricating paper and lignin-enriched paper electrodes were obtained at a laser power of 4% and a speed of 13% (equivalent to 3

W @ 0.40 m s^{-1}). Similarly, for the cork substrate, optimal LIG electrode formation was achieved at a laser power of 4% and speed of 6% (equivalent to 3 W @ 0.18 m s^{-1}). Additionally, positioning the laser beam 2 mm below the focal point for all substrates has been set as an optimal parameter. Further details regarding the fabrication of electrodes with these laser conditions for micro-supercapacitor applications are provided in Chapter 5 of this thesis.

Using a fiber laser – (Paper III – Chapter 6): The fiber laser (Figure 20b) was selected to fabricate electrodes, operating at 21% laser power and 2% speed (equivalent to 10.5 W @ 0.04 m s^{-1}), with the laser beam positioned 2 mm below the focal point. The power and speed were subsequently increased to achieve a faster and more efficient process, while the electrodes maintained excellent sheet resistance. A fixed frequency of 100 kHz and 1000 PPIs were used. These conditions were reproduced for electrode fabrication, aimed at piezoresistive sensor and TENG nanogenerator applications, as elaborated in Chapter 6 of this thesis.

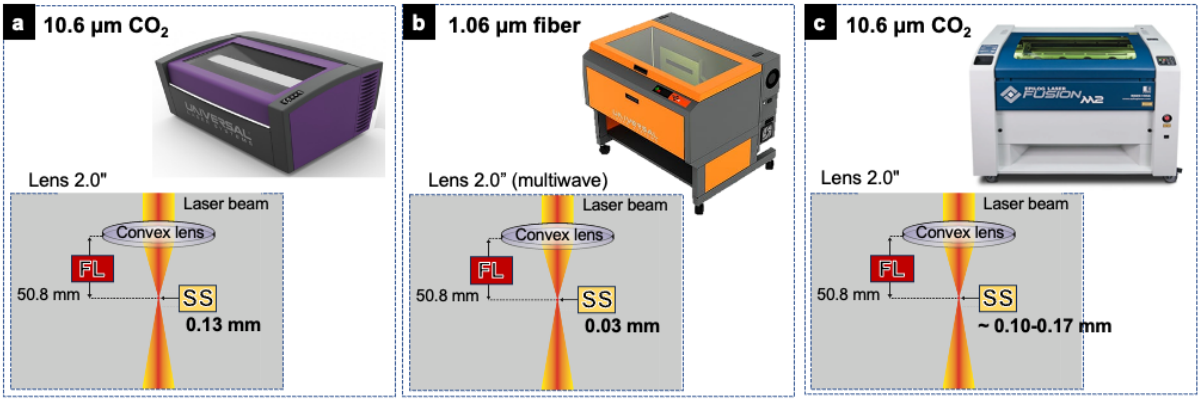

Figure 20. (a) CO_2 and (b) fiber laser cutting and engraving machine available at CENIMAT-i3N; and (c) CO_2 laser available at Iowa State University, each equipped with corresponding standard lens.

All the substrates, pre-treatments, type of laser and LIG processing atmosphere explored in this thesis so far are summarized in Figure 21.

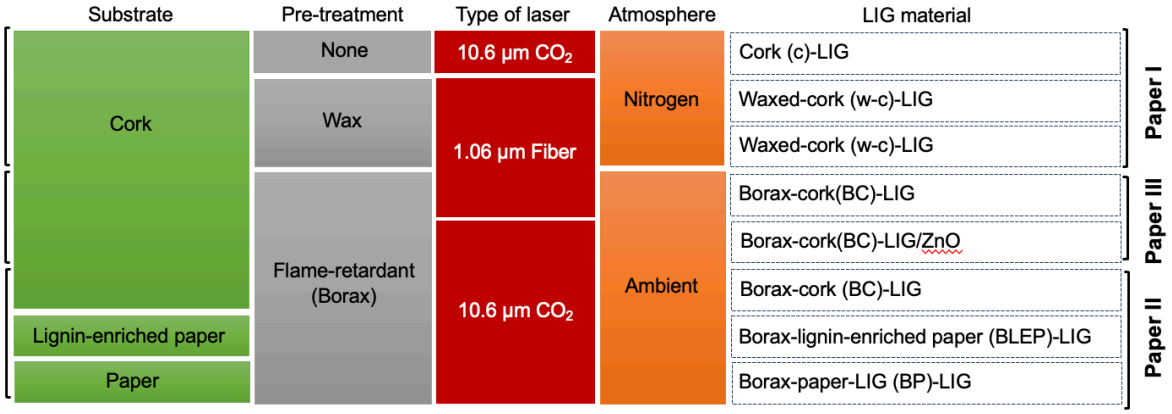

Figure 21. Overview of substrates, pre-treatments, type of laser, atmospheric conditions, and resultant LIG materials for subsequent sections.

3.3 LIG characterization

The structure, morphology, and cross-sectional analysis of the produced LIG were analyzed using a Hitachi TM 3030Plus Tabletop workstation with Scanning Electron Microscopy (SEM), while carbon and oxygen content was evaluated by Energy Dispersive Spectroscopy (EDS).

Raman spectroscopy served as a crucial tool in exploring the electrode composition. Its mechanism relies on the phenomenon of Raman scattering, based on the inelastic scattering of photons to determine the vibrational modes of molecules. In this thesis, Raman spectroscopy is used to identify the hybridization information within carbon structures.

Raman microscopy was carried out with a Renishaw® inViaTM Qontor® confocal Raman microscope equipped with a Renishaw Centrus 2957T3 detector. Excitation was carried out at 532 nm with a 10 mW green laser, focused via a 50× Olympus objective lens. For every measurement, three scans were undertaken, each with a 10-second exposure to laser.

Moreover, beyond material composition, the bonding arrangements, and the relative abundance of each element within the LIG matrix are observed through the analysis of X-ray Photoelectron Spectra.

X-ray Photoelectron Spectroscopy (XPS) was performed using a Kratos Axis Supra instrument, with monochromatic Al Kα and Al Lα sources, to analyze the chemical composition of the LIG substrates. The Al Kα source was running at 150 W and detailed scans were recorded with 5 eV pass energy. The Al Lα source was running at 300 W and the respective detailed scans were recorded with 40 eV pass energy. For data analysis, CasaXPS software was used.

For electrical characterization, LIG was engraved in 5×5 mm^2 squares and then silver ink contacts were placed on the ends of the squares. A multimeter was used for preliminary

assessments of the sample's conductance, followed by resistivity measurements using BioRad HL5500 apparatus at room temperature to determine LIG sheet resistances. All measurements were taken in triplicate for electrical characterization to ensure precision and reproducibility. LIG surface wettability was evaluated through contact angle (CA) measurements with Dataphysics OCA15 plus using the sessile drop method. Briefly, 3 µL of electrolyte (PVA-H_2SO_4) droplets were placed on the substrate surface and CAs were measured for 15 minutes, to assess the spreadability of the droplet. PVA-H_2SO_4 was specifically chosen for the MSCs work, making it essential to study its contact angle behavior on the substrate. The CA analysis was performed with embedded software (SCA 20) using Laplace-Young approximation model with at least three measurements per sample. Data analysis was performed using OriginPro (2022b Academic, MA, USA). Results are reported as mean ± standard deviation from at least three independent experiments. All figures were also plotted in OriginPro (2022b Academic, MA, USA).

4

GREEN LIG-BASED ELECTRODE OPTIMIZATION

This chapter provides an overview of the developments in the production of green laser-induced graphene (gLIG) through the direct conversion of various bioderived substrates, including paper, lignin-enriched paper, and cork. An in-depth investigation and optimization of the laser parameters tailored to each specific material and a thorough characterization of the resulting LIG is performed to support its potential application as electrode material, which will be further explored in Chapter 5 and Chapter 6.

The experimental analysis evaluates LIG structures, elemental composition, and electrical properties using various techniques, such as Raman spectroscopy, X-ray photoelectron spectroscopy (XPS), scanning electron microscopy (SEM), and Hall effect sheet resistance measurements, among others.

Some of the results herein were reproduced and adapted from:

- **Paper I: Silvestre, S. L.**, Pinheiro, T., Marques, A. C., Deuermeier, J., Coelho, J., Martins, R., Pereira, L., & Fortunato, E. (2022). Cork derived laser-induced graphene for sustainable green electronics. *Flexible and Printed Electronics*, *7*. **DOI:**10.1088/2058-8585/ac8e7b

- **Paper II: Silvestre, S. L.**, Morais, M., Soares, R. R. A., Johnson, Z. T., Benson, E., Ainsley, E., Pham, V., Claussen, J. C., Gomes, C. L., Martins, R., Fortunato, E., Pereira, L., & Coelho, J. (2024). Green Fabrication of Stackable Laser-Induced Graphene Micro-Supercapacitors under Ambient Conditions: Toward the Design of Truly Sustainable Technological Platforms. *Advanced Materials Technologies*, 2400261.

DOI:10.1002/ADMT.202400261

- **Paper III (Under preparation): Silvestre, S. L.**, Morais, M., Silva, R. R. A., Martins, R., Fortunato, E., Pereira, L., Coelho, J. (2025) Piezoresistive Sensors via Laser-Induced Graphene on Cork for Energy Harvesting Systems

4.1 Green LIG: optimization and fabrication

This chapter presents the optimization and fabrication of gLIG electrodes using the direct laser writing technique on sustainable materials. The laser conversion process to produce gLIG from various renewable materials has been extensively studied[25]. Furthermore, this chapter deals with the investigation and comparison of the conversion process for bioderived substrates, including paper, lignin-enriched paper, and cork, under different atmospheric conditions (inert and non-inert) and using different types of laser systems (CO_2 and fiber lasers). Recognizing the importance of selecting the most appropriate precursor for each target application, this research thoroughly investigates the tuning of LIG production from these substrates, thus providing the flexibility to tune the LIG electrode properties and architecture.

Due to the highly flammable nature of these materials, this chapter explores the application of a flame-retardant pre-treatment (borax) onto the substrates, with the procedure outlined in section 3.2.2.2. The purpose of this measure is to protect the substrate from thermal degradation and to prevent undesirable outcomes, including substrate ablation and the formation of fragile LIG structures. Similar issues have been previously observed in studies with other cellulosic substrates[78,104]. In addition, borax pre-treatment is a crucial step in the process, especially when these natural substrates are converted into LIG in a non-inert atmosphere [25]. After impregnating the substrates with a flame-retardant to fine-tune the LIG properties, different laser conditions such as the laser defocus, power, and speed were investigated, demonstrating the importance of precise laser settings to achieve distinct LIG properties, which have a direct impact on the performance of various LIG-based applications[173,174].

4.1.1 Under inert atmosphere (Nitrogen)

Agglomerated cork sheets were used as the substrate for LIG production. This composite material is made from the agglomeration of cork granules with binding agents, which results in different size grains being compressed into each other while adhering together. Figure 22 shows the substrate morphology, and as expected, coming from a natural source to a processed sheet, different dimensions of granules are observed.

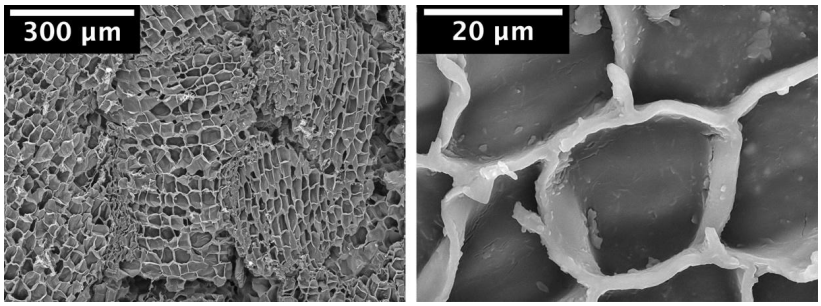

Figure 22. SEM image of the pristine agglomerated cork morphology. Reproduced with permission from [155]. CC BY 4.0 license, https://creativecommons.org/licenses/by/4.0/.

Natural cork presents different cork granules randomly oriented, and its cellular structure is composed of hexagonal and pentagonal structures as confirmed in the SEM micrographs (Figure 22)[175,176]. It can also be observed that the alveoli walls of the agglomerates are ~1.1 µm thick. The characteristic morphology of the cork is of utter importance, as it enables the production of 3D porous LIG exhibiting high surface area (inside the cork cells and even on the walls). These properties are highly advantageous for electrochemical applications, as the increased available surface area allows greater charge storage in the LIG electrodes, thereby improving energy storage performance.[177].

Optimization of the cLIG synthesis started with a systematic study of the laser system, by varying parameters such as power, speed, and focal plane defocus on cork substrate. Two laser-systems were used: a CO_2 laser, with a 10.6 µm wavelength, which has already been used for LIG conversion on cork substrates[93,178], and a fiber laser, with a 1.06 µm wavelength, reported for the first time, to the best of the author's knowledge, for LIG production on cork. First, the laser was focused on the substrate's surface at its focal point to identify the conditions of power and speed that result in a homogeneous LIG formation. As reported in the literature, higher laser powers increase LIG thickness, and lower laser speeds result in better quality LIG exhibiting an improved electrical conductivity[179,180]. With these considerations in mind, the laser conditions applied on the cork substrate were studied and optimized by combining the lowest speed possible with the highest power for the photothermal conversion to occur.

A complete conversion of a LIG square on the substrate is mandatory to carry out sheet resistance measurements using four-point probe measurements. For this reason, LIG conductivity of the uniform patterns was first verified with a multimeter.

The results shown in Figure 23 suggest that laser power cannot be increased too much at lower scanning speed since it results in undesirable outcomes such as laser ablation, thermal damage of the surrounding zones of established pattern, and formation of brittle powder LIG. For lower power and higher scanning speed, no changes were visually identified on the substrate or LIG formation did not occur on the entire surface of the defined square. This can

be explained by the low energy density delivered to the substrate unable to induce a photothermal conversion[59]. For this reason, the conditions selected for cLIG formation, under inert atmosphere, were 2.5 W at 0.05 m s^{-1} for CO_2 laser and 5.5 W at 0.02 m s^{-1} for fiber laser.

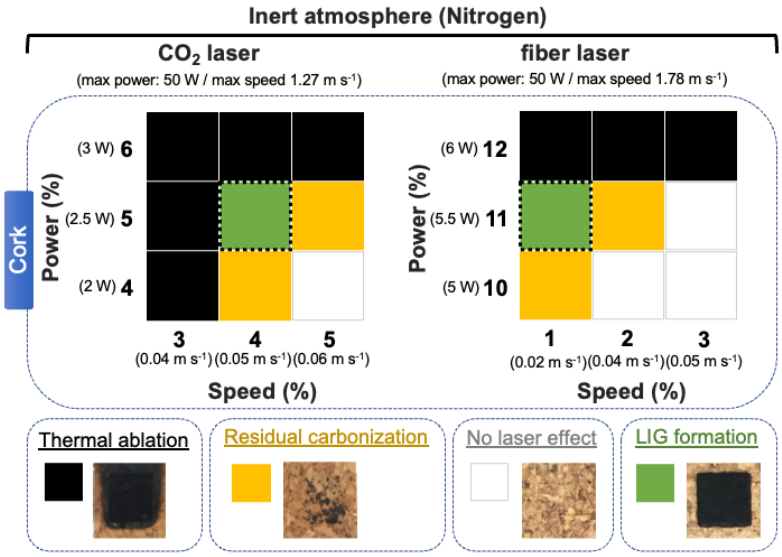

Figure 23. Optimization matrix for LIG formation onto cork by laser irradiation under inert atmosphere, with representative pictures.

After establishing the proper power and speed conditions for each laser wavelength, a study on the influence of focal point defocus on LIG synthesis by irradiation of cork substrate was performed. As reported by Chyan et al.[93], when the laser beam is in a defocused position, the spot size increases, subsequently laser spots overlap, and a multiple lasing effect can be achieved[169]. The multiple lasing method suggests that in some cases LIG formation occurs by two steps: conversion of a carbon precursor into amorphous carbon followed by a conversion to graphene upon subsequent lasing[180,181]. Using the defocusing method, the process is simplified by only one laser passage, resulting in multiple exposures in the overlapping area[84]. Thus, the effects of defocusing on the characteristics of LIG were explored in this work.

The structures obtained by defocusing the laser, from 0.76 mm above 1.52 mm below the focal plane, were characterized through SEM, as shown in Figure 24. Variations in defocusing distances and laser wavelengths result in clearly different LIG morphologies.

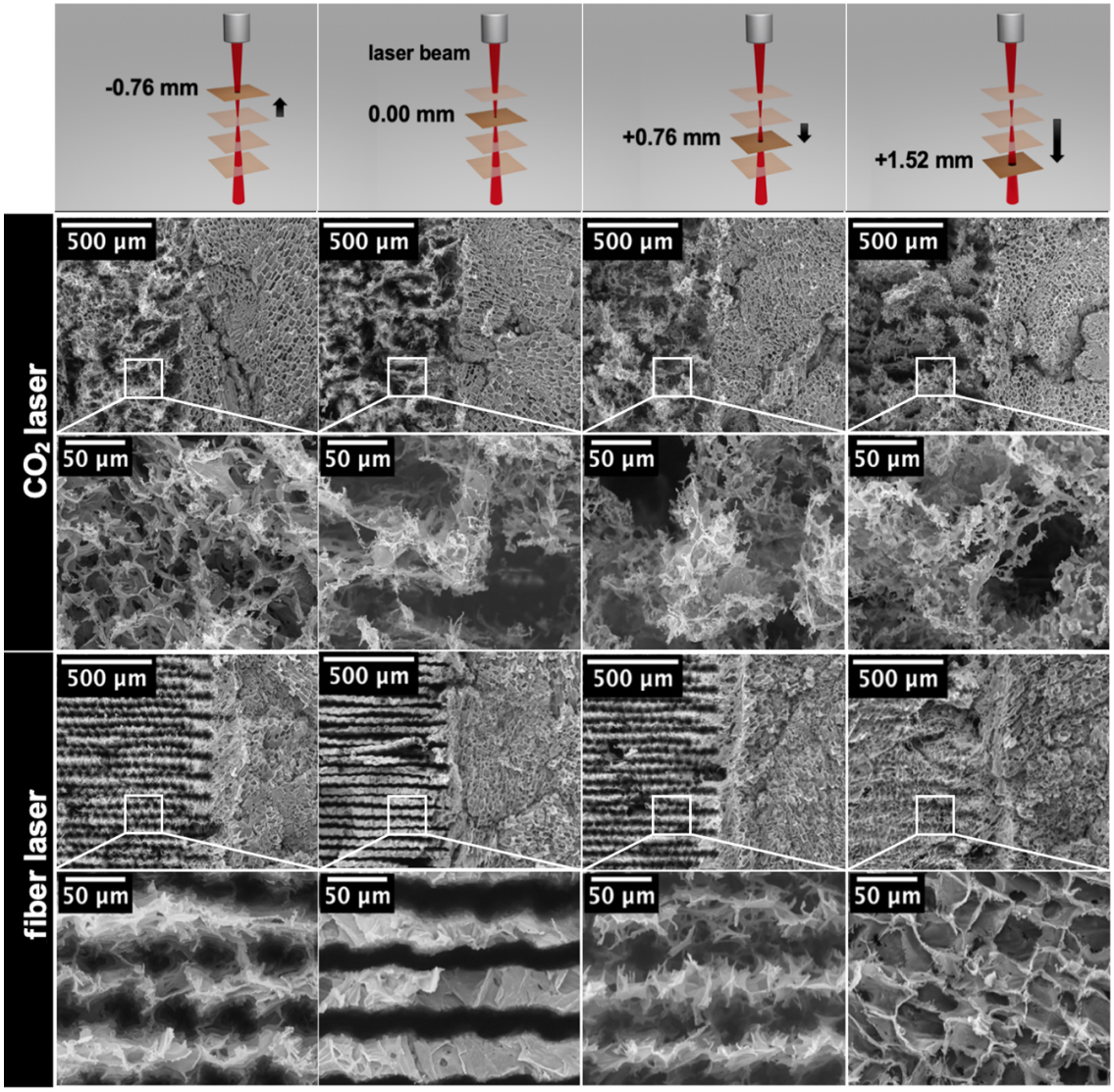

Figure 24. SEM images of substrate morphology with laser defocus variation. Top images show the interface lased (left) and agglomerated cork (right) interface. Reproduced with permission from [155]. CC BY 4.0 license, https://creativecommons.org/licenses/by/4.0/.

These results suggest that cork photothermal conversion into cLIG is in good agreement with the above explanation about the defocusing method. At the focal plane (Z = 0.00 mm) cork substrates receive a larger amount of energy per unit area, which results in a porous cLIG broken structure (using CO_2 laser) and depth powerful engravings (using fiber laser), which are undesirable results.

By moving the substrate far from the focal plane, in both positive and negative directions of the Z plane, the laser spot size expands over a larger area. This leads to an overlapping of the laser spots with a multiple lasing effect, resulting in better quality LIG[182,183].

Regarding the laser wavelength influence, as already reported, infrared lasers mainly result in photothermal conversion, which means that covalent bond breaking occurs by local high

temperature induction. Thus, the laser spot size and laser pulse duration influence the LIG formation[83,184]. These outcomes vary using lasers with different wavelengths, in which a higher resolution laser, as the fiber laser, reflects in a smaller spot size and a shorter pulse duration than the CO_2 laser[109]. Therefore, LIG morphology obtained with 10.6 µm CO_2 and 1.06 µm fiber lasers should be quite different as shown in Figure 23. In samples produced in the fiber laser a less ablative effect is observed, and better uniformity is achieved, contrarily to the fragile and powdery cLIG microstructure obtained from the CO_2 laser. In addition, by defocusing 1.52 mm below the focal point, it produces less depth of focus, and the initial porous honeycomb flake structure of cork (Figure 22) prevails even after irradiation (Figure 24). Thus, conferring the porous cLIG a hexagonal and pentagonal structure with an extensive accessible surface area for posteriorly electrochemical reactions.

Furthermore, analysis of Raman spectra and sheet resistance measurements as function of the laser used and defocus of the focal plane were correlated with SEM images on Figure 25.

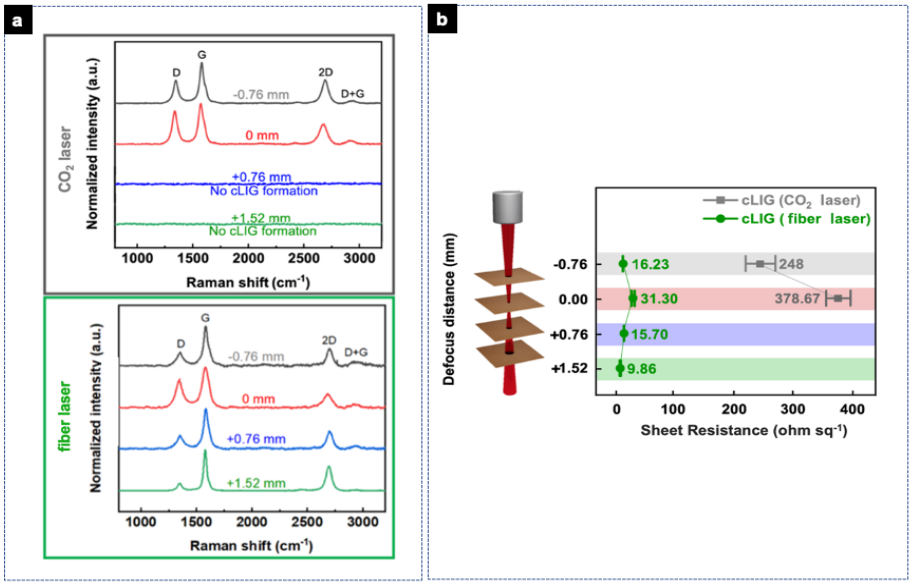

Figure 25. (a) Raman spectra and (b) sheet resistances using different laser systems and focal distances. Reproduced with permission from [155]. CC BY 4.0 license, https://creativecommons.org/licenses/by/4.0/.

All Raman spectra obtained (Figure 25) show the three prominent peaks of graphitic materials, ranging from 1000 to 3000 cm^{-1}. Two distinctive first-order peaks are presented at ~1350 cm^{-1} (D peak) and ~1580 cm^{-1} (G peak), and a second-order 2D peak is presented at ~2700 cm^{-1}, showing the presence of graphitic carbon[164]. The D band can be related to the formation of defects, vacancies and bent sp^2 bonds, while the G band results from the first-order inelastic scattering process being highly sensitive to the number of layers present in the LIG[185]. The 2D band corresponds to the second-order Raman peak, which results from two photon lattice vibrational process[186]. When relating the SEM images with Raman spectra and sheet

resistances, there is a correlation between Raman peaks intensity, the conductivity of the cLIG and structural morphology obtained. For both lasers, by defocusing substrate from the focal plane, cLIG samples show a decrease in D peak relative intensity, meaning that fewer defects are induced during LIG conversion, which is in accordance with previously reported works[93,187]. Hence, by defocusing the distance from the focal plane cLIG conductivity improves significantly using both lasers. Albeit, for CO_2 laser defocus below its focal point (i.e. Z= +0.76mm; Z= +1.52 mm), no cLIG formation was observed due to the insufficient energy for photothermal conversion on cork substrate.

In terms of sheet resistance, for LIG induced by IR (10.6 µm), visible (450 nm) and UV lasers (355 nm) on cork, there are reported values in the range 46-115 ohm sq^{-1} [178,187,188]. The current study using a fiber laser (1.06 µm), for the first time in this type of substrate, has attained an incredible enhancement in LIG quality with a sheet resistance almost 10 times lower (Rs ~9.86 ± 0.12 ohm sq^{-1}). This significant improvement, as already mentioned, is essentially due to the combination of the type of laser with different wavelengths used and the laser conditions applied.

XPS characterization was performed to characterize cork prior laser irradiation and after LIG conversion by the two different lasers (CO_2 and fiber), supporting the results above (Figure 26). Figure 26a shows C 1s spectra of cork prior to laser irradiation, with the presence of characteristic carbon bonds, O-C=O, C=O, C-O and sp^3. Figure 26b and Figure 26c corresponds to the C 1s spectrum of the LIG produced under the optimized laser conditions of the CO_2 and fiber laser, respectively. After the photothermal conversion of cork to LIG, the presence of sp^2 carbon bonds related to graphene structures is observed at 284.14 eV (for LIG produced by CO_2 laser) and 283.95 eV (for LIG produced by fiber laser). Although these results show a predominant sp^3 peak and a small sp^2 peak, it is not a representative measure of the entire LIG as a bulk, due to the high surface sensitivity of XPS.

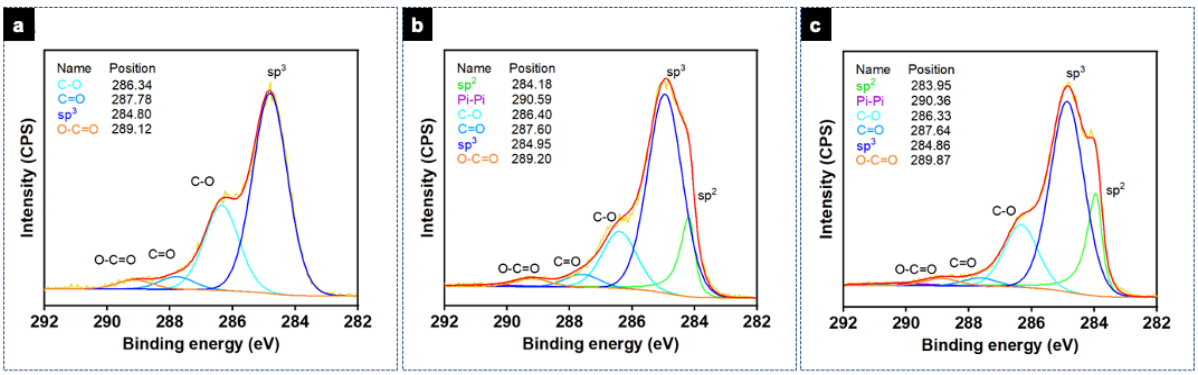

Figure 26. High resolution C 1s XPS data. (a) XPS spectra for cork prior laser irradiation and cLIG induction. (b) C 1s spectra of cork-based LIG produced by CO_2 laser (using optimized conditions). (c) C 1s spectra of

cork-based LIG produced by fiber laser (using optimized conditions). Reproduced with permission from [155]. CC BY 4.0 license, https://creativecommons.org/licenses/by/4.0/.

Regarding high-resolution spectrum of the C 1s, cLIG produced by both lasers revealed the presence of graphene structures. Regarding the variability of the XPS spectra and partial oxidation observed in both samples, a factor to be considered is the influence of the place where the measurement is performed. For the spectra shown in Figure 27, two X-ray sources were used: one comparatively sensitive to the surface (Al Kα) and one with about twice the energy, which allows to extract information from deeper-lying regions of the sample (Al Lα).
XPS data indicate greater oxidation on the sample surface and the existence of fewer C-O bonds towards the bulk of the sample. This can be verified by the shape of the C1s peaks (Figure 27a) and in the quantification table (Figure 27b), comparing the data obtained with the two X-ray sources. This qualitative comparison confirms that the sp^3 and oxidized carbon bonds are mainly located at the surface, and it is shown that in fact the most superficial zones of the sample are more oxidized, while an inner zone results in a LIG with lower oxygen content.

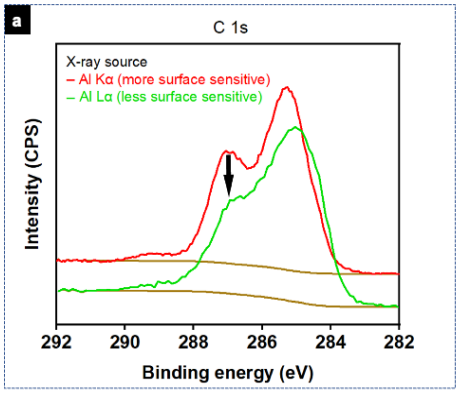

X-ray source	O 1s	C 1s
Al Kα	19.34	80.66
Al Lα	15.12	84.88

Figure 27. (a) C 1s spectra of cork-based LIG (produced by fiber laser with optimized conditions) obtained using different X-ray sources: Al Kα and Al Lα. (b) Oxygen and carbon quantification (per atomic percentage) table from detailed scans. Reproduced with permission from [155]. CC BY 4.0 license, https://creativecommons.org/licenses/by/4.0/.

In this study, fiber laser shows its promising application for converting carbon-based materials into LIG, taking advantage of its interaction with the substrate. The type of cork substrate used can also influence LIG production, due to its composition, different grain sizes and density.
A summary of the best conditions defined for each laser and resultant LIG properties are schematically shown in Figure 28. In Figure 28a-b it is visible a significant difference in the LIG

morphology produced with different lasers' wavelengths. LIG induced on cork present structures similar to porous and powdery honeycomb flakes, as previously described, in which the LIG thickness was 100 µm and 150 µm for CO_2 and fiber laser, respectively. It seems that cLIG produced in the fiber laser is thicker, exhibiting a continuous and uniform layer, with a less defective appearance compared to the LIG produced by the CO_2 laser. This can be supported and confirmed with the Raman spectra and ratios from Figure 28c-d. As already mentioned, the D peak corresponding essentially to the formation of defects, decreases when switching from the CO_2 to the fiber laser.

Therefore, for the remainder of this work, the most promising cLIG was obtained and used using the fiber laser at 1.52 mm below the focal plane. cLIG quality and the low sheet resistance makes this material attractive for circuit conductive tracks, electrodes, sensors, or even full devices. Subsequently, waxed-cork LIG prepared under optimized conditions was characterized to be used in Chapter 5 to develop a proof-of-concept flexible and sustainable micro-supercapacitor.

4.1.1.1 Waxed-cork LIG (w-cLIG) characterization

Adopting the methodology on section 3.2.2.1, a wax-based ink can be absorbed throughout the entire cork bulk volume when heated, occupying the free spaces between the granules. Wax being essentially paraffin, is a carbon-based material, and not only served as a binding element between agglomerated cork granules when pre-treatment was carried out, but also made possible the w-cLIG production.

This wax-based pre-treatment was performed to tailor hydrophobic properties for the LIG and substrate surface. To assess the effectiveness of the pre-treatment described in this work, it was important to characterize the wettability of substrate, before and after wax pre-treatment, and consequent cLIG.

Based on literature, cork is an impermeable material (macroscopically), presenting in its composition a hydrophobic substance (suberin)[189,190]. For this reason, it was already expected that cork would instantly present low permeability to liquids.

In the first minute, contact angles higher than 110º were obtained on untreated cork, sustaining the initial hydrophobic characteristic of cork mentioned in literature. However, in Chapter 5 during micro-supercapacitor fabrication, it was observed that over time, electrolyte droplets were gradually absorbed by the cork. Thus, presenting an intermediate behavior, between a hydrophobic and hydrophilic character. Also, pre-treated cork showed a hydrophobic behavior, with contact angles around 136.0 ± 1.8º. After 15 minutes, the sample remains hydrophobic, with a tendency to gradually lose this character, which means it will stay on the surface longer

during the electrolyte drying process. This wetting phenomenon could be influenced by the substrate texture, chemical composition (including adhesive and grain binding agents), grain size of the agglomerated cork and the type of liquid and volume used.

After cLIG production on untreated cork, the substrate becomes fragile, instantly absorbing the liquid droplet when it touches its surface (hydrophilic character). This interaction of the electrolyte with the active zone is not ideal, due to the electrolyte being absorbed by the entire volume of the substrate, without remaining longer on its surface, and consequently on engraved electrodes. Also, it overlaps the interdigitated silver contacts area. To develop an MSC with good performance, the drying process is an important step. A complete contact and adhesion between electrolyte and electrodes need to be ensured.

cLIG produced on waxed-cork demonstrated contact angles at the first instance around 143.4 ± 1.3º with a gradual and slow decrease over time (Table 2).

Table 2. Contact angles obtained for the different substrates: untreated and pre-treated cork (waxed), and resultant LIG (cork-LIG and waxed-cork-LIG). Reproduced with permission from[155]. CC BY 4.0 license, https://creativecommons.org/licenses/by/4.0/.

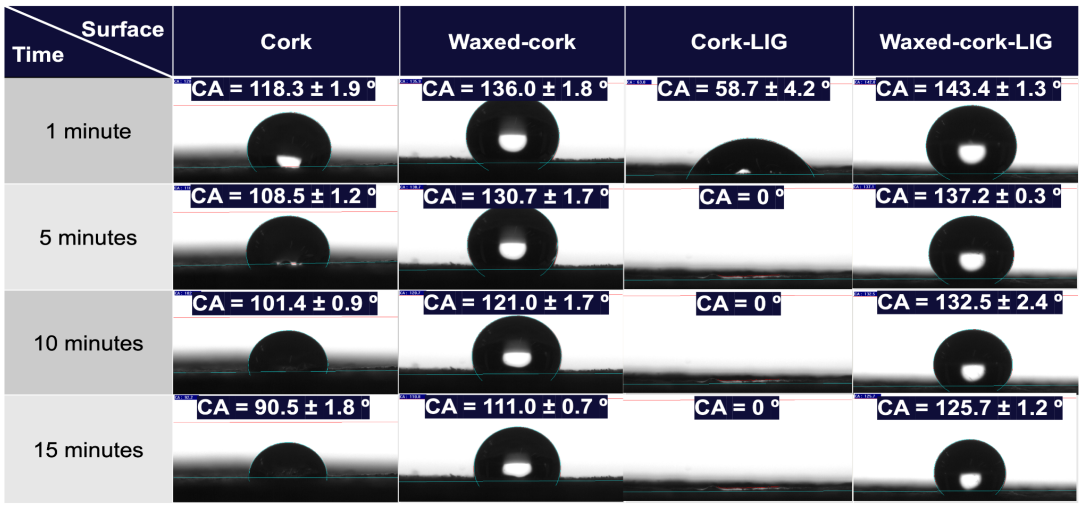

Figure 28 suggests that waxed-cork LIG (w-cLIG) hydrophobicity is mainly due to its structural morphology. The w-cLIG seems to adopt smaller pores, a sponge-like structure, which means it will have more contact points when a liquid is placed on top.

Therefore, the uncontrollable electrolyte spreading over the entire surface and substrate volume is solved without the need for masks or other complex methods. Also, it is guaranteed that over time as the electrolyte dries, a greater amount of electrolyte is concentrated on the surface and LIG structure and consequently in greater contact with the active area of the cLIG. Moreover, it was also verified that using wax pre-treatment does not produce significant variations in LIG quality compared with the above results, maintaining the characteristic Raman peaks of graphitic materials. Raman spectra of the waxed-cork LIG have similar

relative peak intensity as the LIG obtained without any pre-treatment done to the cork. Only a minimal and almost imperceptible increase is observed in D peak, which means that more defects occur when using waxed-cork. This observation can be explained by the photothermal effect on the substrate which, being composed of more residual species from the carbonization (different types of carbon) has more reactions occurring and subsequently more defects when irradiated, resulting in a higher surface area, increasing the number of conductive paths, like a formation of LIG bridges.

For the electrochemical performance of MSC, this means that enhanced surface area will facilitate electrolyte diffusion in the LIG electrodes area[191,192].

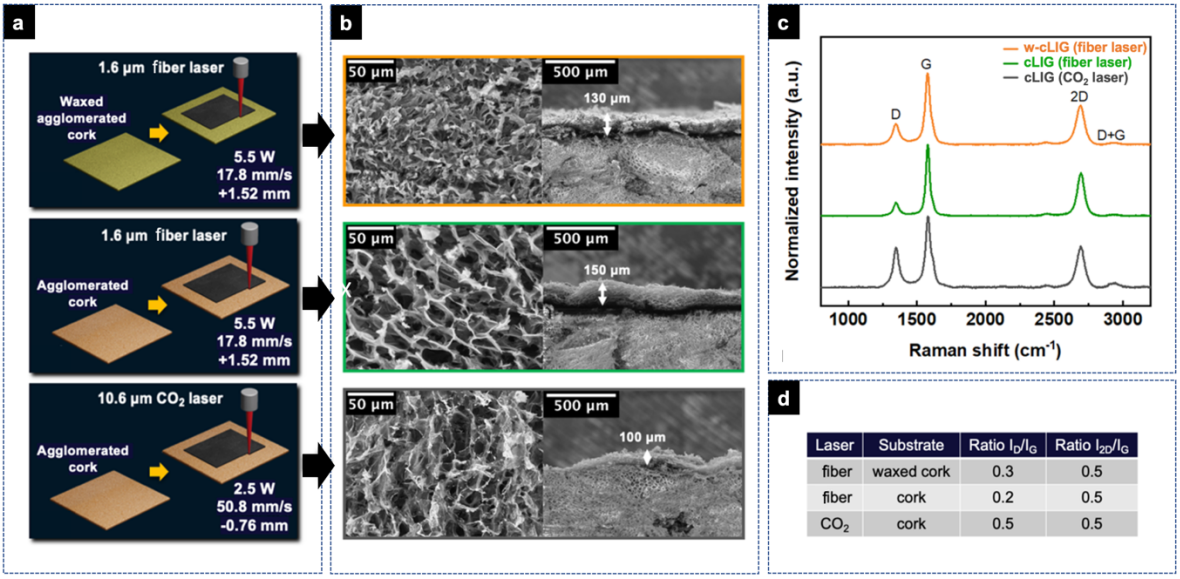

Laser	Substrate	Ratio I_D/I_G	Ratio I_{2D}/I_G
fiber	waxed cork	0.3	0.5
fiber	cork	0.2	0.5
CO_2	cork	0.5	0.5

Figure 28. (a) Schematic representation of optimized processes conditions, (b) SEM images, (c) Raman spectra of the resultant LIG, and (d) table with LIG ratios obtained in Raman spectra. Reproduced with permission from[155] CC BY 4.0 license, https://creativecommons.org/licenses/by/4.0/.

In Figure 29 a brief comparison is presented between sheet resistances of the already described samples, where the lowest value was attained with waxed-cork LIG produced using fiber laser, with an Rs of approximately 7.5 ohm sq^{-1}. Only a minimal reduction in sheet resistance was observed using the pre-treatment using fiber laser, which proves that this step is not relevant for conductivity improvement but an important approach for MSC assembly.

As mentioned above, although the wax treatment was not originally intended to improve the intrinsic properties of the LIG, it indirectly contributed to maintaining its conductivity and overall quality, while improving aspects such as the hydrophobicity of the substrate and the adhesion of the electrolyte to the LIG structure. By applying this wax pre-treatment to cork, the electrolyte was prevented from being immediately absorbed into the volume of the substrate, ensuring that it remained confined to the surface of the substrate and consequently to the LIG film. This

approach facilitated better adhesion of the electrolyte to the surface LIG network during drying, improving its interaction with the active electrode area. EDS analysis of the different samples was performed to compare elemental composition present in each one. As expected, all the LIG samples revealed an increased carbon content compared to agglomerated cork, due to the graphenization process (Figure 29b). This confirms the effective transformation of the substrates into LIG, containing a residual amount of oxygen.

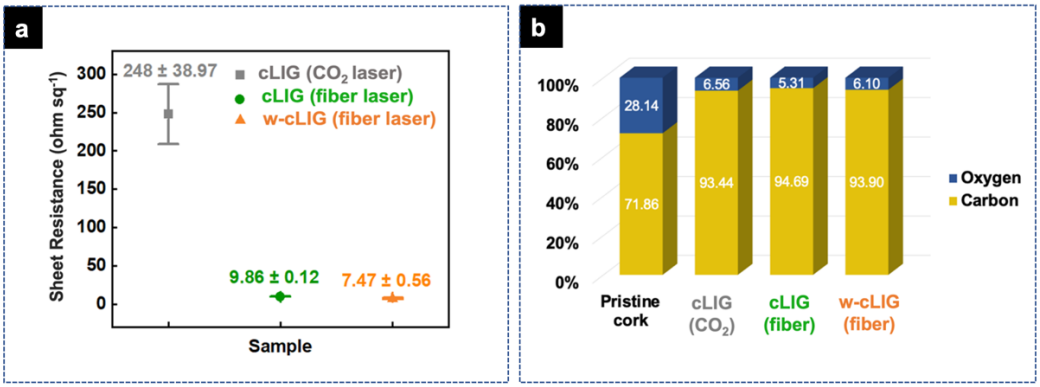

Figure 29. (a) Sheet resistance and (b) EDS analysis of the optimized cLIG produced with CO2 laser, and cLIG and w-cLIG produced with fiber laser. Reproduced with permission from [155] CC BY 4.0 license, https://creativecommons.org/licenses/by/4.0/.

The wax pre-treatment on cork resulted in a hydrophobic interaction between a liquid and the surface of the substrate for prolonged time, solving the uncontrolled spread of liquids. Furthermore, compared with untreated substrate, only a minimal reduction in sheet resistance was observed with an Rs of approximately 7.5 ohm sq^{-1}, proving that this step is not relevant for conductivity improvement but an important approach for micro-supercapacitors application, which will be further explored in the following chapter. Porous w-cLIG with excellent properties was achieved with greater electrical conductivity and fewer defects.

4.1.2 Under non-inert atmosphere (Ambient)

This part of the thesis aims to study and compare the conversion of three cellulosic substrates: paper, lignin-enriched paper, and cork.

Recognizing the importance of selecting the most appropriate precursor for each target application, this research thoroughly investigates the tunning of LIG production from these substrates, thus providing the flexibility to tune the LIG electrode properties and architecture.

Due to the highly flammable nature of the materials used, the substrates were impregnated with a borax fire retardant solution prior to laser exposure, followed by a drying process. This measure is intended to protect the substrate from thermal degradation and prevent undesirable

effects such as substrate ablation and the formation of fragile LIG structures. Similar issues have previously been observed in studies with other cellulosic substrates[78,104].

Some reports show that the use of boric acid in substrate pretreatment can lead to a boron doping effect during electrode fabrication[193–195]. As far as we are concerned, sodium tetraborate was not used as a doping agent but rather as a fire retardant to facilitate the formation of LIG on these highly sensitive substrates. However, it cannot be excluded that some boron doping may occur in the prepared samples.

In this study, it was not possible to compare the properties of LIG on treated substrates with those on untreated samples, as untreated samples tend to be destroyed during lasing. Consequently, the extent and importance of boron to overall energy storage process wasnot assessed, and further characterization was not pursued. To better investigate the effect of boron on the samples, a more detailed analysis using X-ray photoelectron spectroscopy would be valuable in the future. This analysis could help to identify the characteristic peaks of boron and determine whether it is structurally incorporated into the LIG. Additionally, other complementary characterizations would be required to better understand whether boron can be considered a true doping element impairing specific properties to LIG, or whether it merely acts as an intermediary to facilitate the production process.

After impregnating the substrates with a flame-retardant to fine-tune the LIG properties, different laser conditions such as the laser defocus, power and speed were investigated, demonstrating the importance of precise laser settings to achieve distinct LIG electrode properties that have a direct impact on different LIG applications[173,174].

By first optimizing the defocus, a foundation was established for the subsequent adjustments to power and speed, as the defocus conditions study helped to initiate the optimization process and minimize potential issues of overheating and substrate damage. Additionally, LIG electrical conductivity was also preliminarily verified using a multimeter under the laser conditions that resulted in carbonization (Figure S1).

In Figure 30, a correlation of the defocus distance versus resultant LIG sheet resistance is demonstrated for all substrates. For instance, adjusting the defocusing distance from its focal point leads to changes in the energy distribution across the area that undergoes LIG conversion, which affects the substrate carbonization rate and LIG formation, homogeneity, thickness, porosity, conductivity, crystallinity, among other factors[25,59,93].

On these natural and highly sensitive substrates prone to ablation, such optimization becomes significantly more challenging and sensitive to variations in laser conditions. To address this, the defocus adjustment was adopted as the strategy to avoid ablation, considering it has been reported in several prior studies[104,155].

Therefore, a laser beam position of 2 mm below the focal point was set as the optimum parameter for all substrates. This setting results in the lowest sheet resistance, as shown in Figure 30.

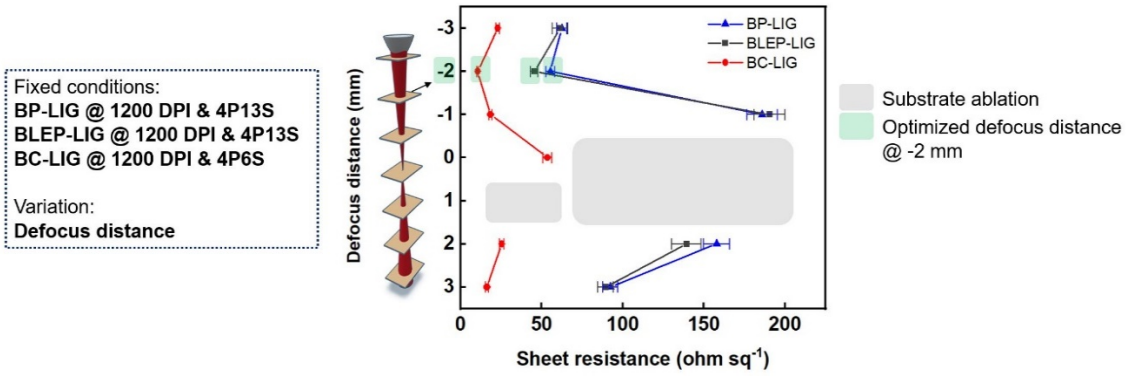

Figure 30. Sheet resistances of all substrates using different laser focal distances. Fixed conditions were used: 4P13S and 1200 DPI for Borax-Paper and Borax-Lignin-Enriched Paper, and 4P6S and 1200 DPI for Borax-Cork. P = power, S = speed, i.e., 4P13S is 4% power and 13% speed. Reproduced with permission from[196]. CC BY 4.0 license, https://creativecommons.org/licenses/by/4.0/.

This property has previously been highlighted as one of the most important aspects to improve when fine-tuning LIG electrode fabrication to meet the electrical conductivity criteria for desired electronic applications. While it is possible that other defocus adjustments could prevent ablation under varying power and speed conditions, the quality of the resulting LIG may not reach the achieved under the optimized parameters explored in this work.

Therefore, the optimized defocus distance was consistently maintained throughout the subsequent work, proving to be an effective strategy to avoid simultaneous changes in multiple parameters.

Continuing the evaluation of the LIG from different substrates, the analysis was extended to assess their morphology and surface topology. Figure 31a shows a comprehensive analysis of the correlation between variations in power and speed applied during laser irradiation and the resulting changes in LIG sheet resistance values for all substrates.

This matrix not only shows the sheet resistance values but also discloses the influence of the laser parameters on the electrical properties of each substrate. The matrix values are presented in percentage, considering that the maximum power and raster speed of the CO_2 laser system are 75 W and 3.05 m s^{-1}, respectively.

In addition to the matrix of sheet resistance values, Figure 31b complements the analysis by featuring top-view and cross-section SEM images of the three different LIG substrates fabricated under optimal laser settings. The scale was adjusted to match with the sample dimensions, aiming for a higher resolution in the cross-section images. These images provide

valuable morphological information regarding the surface topography, layering, and thickness of the LIG. This morphological information can help correlate the LIG microstructure with its conductivity.

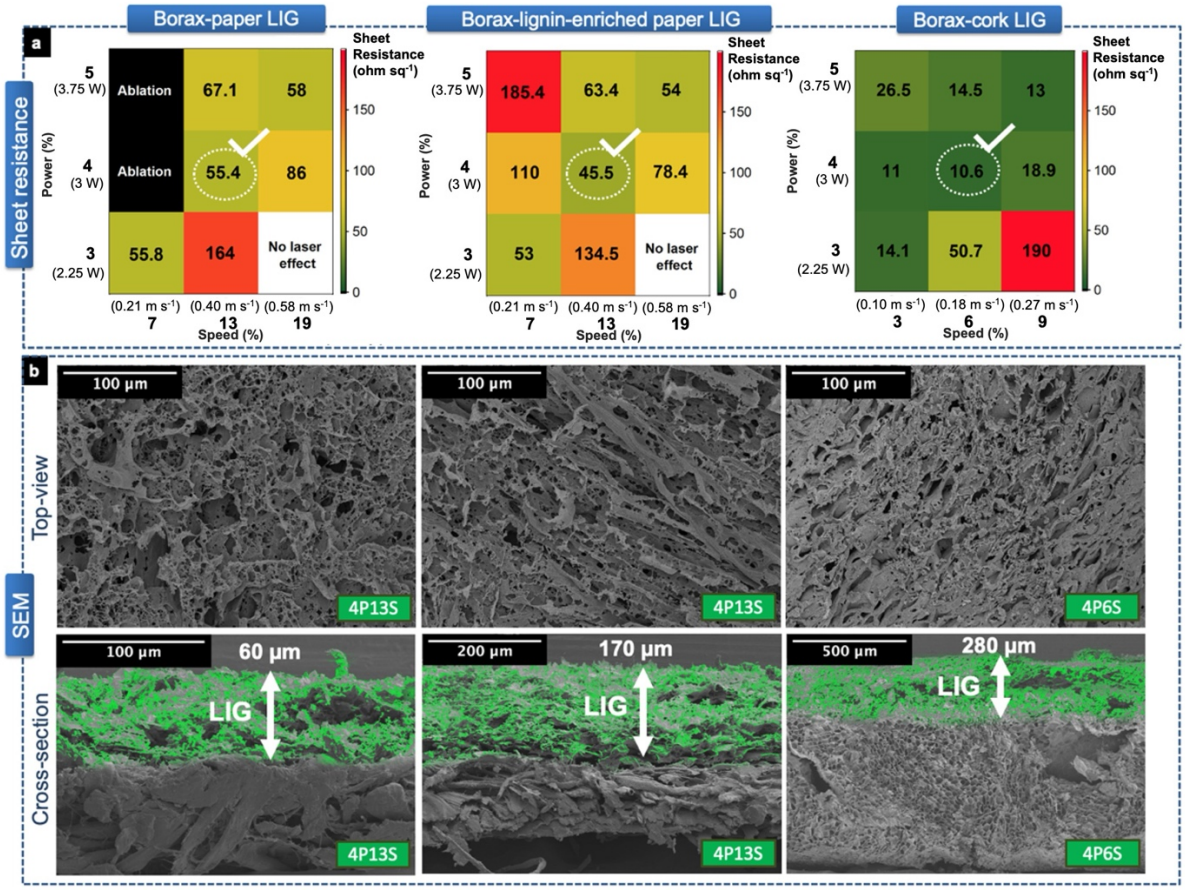

Figure 31. (a) Matrix of sheet resistance values for different laser settings (in percentage) and (b) SEM images of borax-paper, borax-lignin-enriched paper, and borax-cork laser-induced graphene fabricated using the optimal laser settings corresponding to the lowest sheet resistance. Reproduced with permission from[196]. CC BY 4.0 license, https://creativecommons.org/licenses/by/4.0/.

The observed reduced sheet resistance values, traced along the diagonal of each matrix, are in accordance with existing literature[78,104,155]. For the paper and lignin-enriched paper substrates, optimal conditions were obtained at a laser power of 4% and a speed of 13% (3 W @ 0.40 m s^{-1}) resulting in sheet resistances of 55.4 ± 2.8 ohm sq^{-1} (for paper) and 45.5 ± 2.3 ohm sq^{-1} (for lignin-enriched paper), respectively. Similarly, for the cork substrate, the optimal LIG electrode formation was achieved at a laser power of 4% and a speed of 6% (3 W @ 0.18 m s^{-1}), yielding a sheet resistance of 10.6 ± 0.5 ohm sq^{-1}. Notably, a higher degree of graphitization of the substrates with higher lignin content is observed. When comparing paper and lignin-enriched paper with cork, it becomes apparent that cork exhibits more tolerance and thermal resistance to laser irradiation, thereby preserving its structural integrity even at lower

processing speed. This arises from paper substrates being more susceptible to rapid heating and combustion during laser irradiation due to their lower thermal conductivity (0.05 W mK^{-1}) compared to cork (0.036-0.38 W mk^{-1}). As reported in literature, the thermal conductivity values are approximately 0.076 W m^{-1} K^{-1} and 0.045 W m^{-1} K^{-1}, for cellulose paper and cork, respectively[197,198]. This fact highlights the importance of the substrate composition and its inherent characteristics before laser conversion, which are determinants for the successful formation of conductive LIG. Notably, cork's sheet resistance values are significantly lower than those of paper and lignin-enriched paper while maintaining the underlying substrate's integrity. The susceptibility of sensitive substrates to ablation, despite flame-retardant pre-treatment, is a common phenomenon[78,104]. Nonetheless, this issue can be effectively addressed by applying higher processing speeds, and in this study, a speed two times higher for paper and lignin-enriched paper than the cork substrate was employed. This approach minimized the potential ablative effect on these substrates while still enabling the production of LIG with good electrical properties [11,28]. Sheet resistance can also be influenced by the morphology of LIG obtained. As evidenced by existing literature[80,99,199], it is well-established that LIG morphological structure can directly affect its electrical conductivity. Therefore, Figure 31b presents surface and cross-sectional views of the LIG samples produced from the different substrates, that yielded the lowest and optimal sheet resistance values. The images show a uniformly interconnected and porous LIG network for all substrates, which plays a pivotal role in the efficient charge transport within its framework. When examining the relationship between LIG's thickness and its sheet resistance, thicker LIG derived from cork presents a distinctive advantage in terms of electrical conductivity compared to LIG derived from paper and lignin-enriched paper. This characteristic may appear contradictory because thicker films usually exhibit lower conductivity when compared to thinner layers. Thinner layers offer a higher density of conductive pathways within the LIG matrix, often leading to improved conductivity[199]. However, when thicker LIG possesses a well-connected network of conductive pathways, it can provide an increased abundance of graphene layers and charge carrier pathways. Consequently, this offers a multitude of routes for charge carriers to move within its structure, ultimately promoting higher electrical conductivity.

To further understand the properties and potential applications of the fabricated LIG, the samples were studied by Raman spectroscopy. As depicted in Figure 32, the obtained spectra suggest the successful formation of LIG on paper, lignin-enriched paper, and cork substrates.

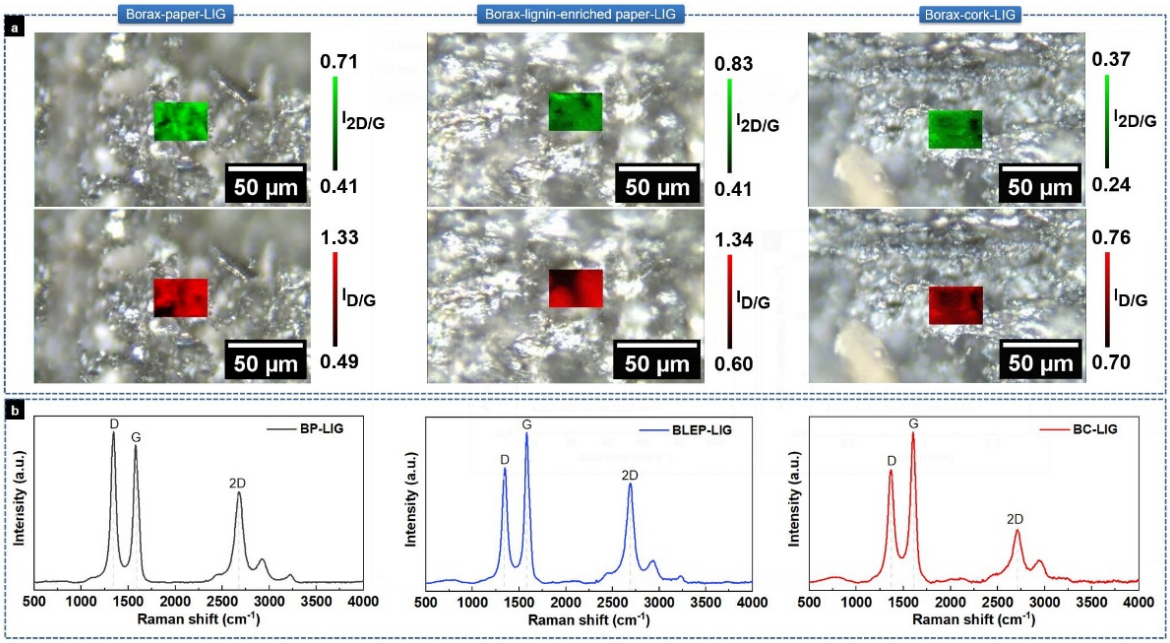

Figure 32. Raman (a) mapping and (b) spectra of borax-paper (BP), borax-lignin-enriched paper (BLEP), and borax-cork (BC) LIG. Reproduced with permission from[196]. CC BY 4.0 license, https://creativecommons.org/licenses/by/4.0/.

In Figure 32a, Raman mapping provides insights into the structural variations of LIG produced on these natural substrates along their surface. The I_{2D}/I_G and I_D/I_G ratios were evaluated by tracking the characteristic graphitic peaks measured at different locations on the samples and by assessing their intercorrelation. In Figure 32b, the peaks show the formation of LIG in all samples with characteristic Raman peaks identified. These include peaks D (approximately 1350 cm^{-1}), G (approximately 1580 cm^{-1}), and 2D (approximately 2700 cm^{-1})[25,65]. The color variations in each mapping result from increased or decreased peak intensity, which provides valuable information about the material's composition and quality.

Lower I_D/I_G ratios indicate the presence of higher-quality graphene domains with a lower density of defects in the formed graphitic structures[150]. This characteristic is prominently observed on lignin-enriched paper and cork substrates, where the D peak intensity is notably reduced. In contrast, when using a pure paper substrate, a prevalence of the D peak over the G peak is observed, indicative of a higher density of defects, and consequently, lower-quality LIG. The phenomenon of reduced D peak intensity has been reported for substrates with higher lignin content, resulting in an increased degree of graphitization. This consistent with the decreasing trend in sheet resistance, which follows the order: BP-LIG (~55.4 ohm sq^{-1}), BLEP-LIG (~45.5 ohm sq^{-1}), and BC-LIG (~10.6 ohm sq^{-1})[200]. Upon correlation with SEM images, borax-cork LIG appears to be thicker than paper-based LIG and exhibits a more

uniform and interconnected lattice structure. Consequently, cork-based LIG exhibits a lower sheet resistance than paper-based LIG.

Conversely, the presence of the 2D peak indicates the formation of graphitic material, and the I_{2D}/I_G ratios are often used as criteria to identify the number of graphene layers[25,201]. Therefore, the higher intensity of 2D peaks identified in paper-based LIG compared to cork-LIG, along with higher I_{2D}/I_G ratios, is mainly attributed to fewer graphene layers in the material.

To support the results above, XPS characterization was conducted, which showed the distinct presence of graphene structures[25,78,155]. Figure 33 shows this confirmation, derived from an analysis of the high-resolution spectrum of the C 1s in all samples, deconvoluted into five characteristic peaks: C=C sp^2, C-C sp^3, C-O, O-C-O and pi-pi* [25].

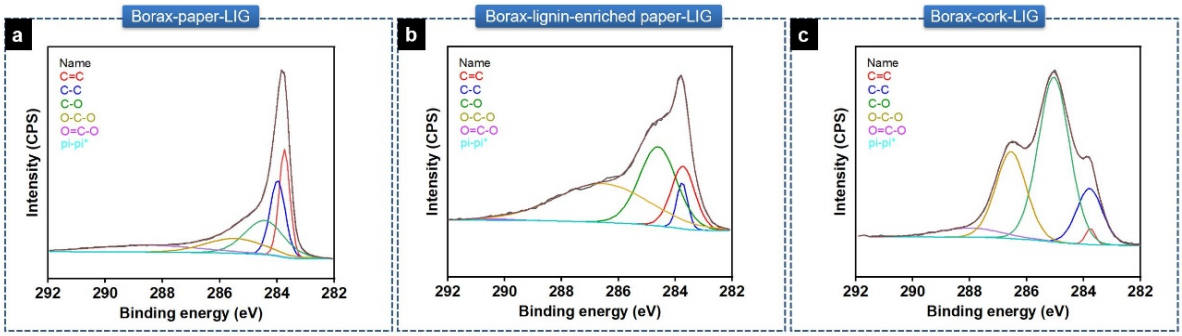

Figure 33. High resolution C 1s XPS data. XPS spectra of (a) BP, (b) BLEP, and (c) BC-LIG, produced by CO_2 laser using optimized conditions, reproduced with permission from[196]. CC BY 4.0 license, https://creativecommons.org/licenses/by/4.0/.

In Chapter 6, the laser conversion of the cork substrate was performed using the conditions optimized in the first part of this thesis (11P1S), employing a fiber laser under an inert atmosphere. However, as part of the continuous improvement of the methodology, cork samples were treated with borax. The fire retardant eliminated the need for an inert atmosphere, allowing a more efficient processing. This treatment enabled the cork to be converted using increased applied power and a higher processing speed. Specifically, using 21% power and a faster process at 2% speed, the sheet resistance of the LIG remained similar, with a value of ≈ 11 ohm sq^{-1}. Additionally, LIG produced in cork with ZnO precursor solution, using the same optimized conditions, as described in Chapter 6, the resistance remained unchanged, demonstrating the robustness of the process.

4.2 Summary

The study of LIG formation on bioderived precursors underscores the significant potential of renewable materials like paper, lignin-enriched paper, and cork for developing sustainable electronics. To optimize LIG properties, several variables can be adjusted, including using precursors with different chemical compositions, pre-treatment with fire-retardants, different laser systems and operating parameters, and the atmosphere during laser scribing. By adjusting the mentioned variables allows LIG from bioderived materials to match or even surpass the performance of LIG from traditional polymers.

This work shows that using different laser systems and substrates, under specific conditions, yield excellent LIG characteristics in terms of morphology, structure, conductivity, and quality. Cork stands out due to its excellent electrical properties (7.5-10.6 ohm sq^{-1}), high lignin content, and natural porosity. It can be processed in both inert and non-inert atmospheres,

Furthermore, it is an ideal substrate for LIG production for applications requiring a large surface area electrode, such as energy storage and chemical sensing.

Conversely, cellulosic materials like paper require a combination of additional fire-retardant treatment, an inert atmosphere, multistep scribing, or extra lignin to convert to LIG due to cellulose's poor thermal stability. The high temperatures reached during laser-induced pyrolysis necessitate these additional steps to improve carbonization.

Overall, the use of bioderived materials offers an eco-friendly alternative and opens new avenues for advancing green technology. LIG from these sources not only provides sustainable solutions but also maintains or exceeds the performance of traditional polymers. Beyond electrical properties, factors such as surface area, electroactive area, pore dimensions, and wettability are crucial for various LIG applications.

Under inert atmosphere conditions, a simple, eco-friendly, and efficient method for fabricating LIG electrodes using cork was demonstrated. The LIG structure was induced and controlled by DLW technique, a one-step, maskless, scalable and cost-effective process. Using a fiber laser on cork with specific tuned conditions yielded the best LIG characteristics. A systematic characterization of the LIG induced on untreated agglomerated cork was investigated. Therefore, using a fiber laser on cork substrate with tuned conditions of 5.5 W, 17.8 mm s^{-1} and a laser distance of 1.52 mm below the focal point, resulted in the best LIG characteristics in terms of morphology, structure, conductivity, and quality. Wettability tuning was demonstrated.

Under non-inert atmosphere conditions, the incorporation of fire retardants and systematic optimization of laser parameters ensured efficient electrode production, preventing combustion and substrate ablation, with cork exhibiting the lowest sheet resistance (≈10.6 ± 0.5 ohm sq^{-1})

compared to paper (≈55.4 ± 2.8 ohm sq^{-1}) and lignin-enriched paper (≈45.5 ± 2.3 ohm sq^{-1}). This is due to inherent material properties such as thermal resistance and lignin content. This highlights the inherent advantages of bio-derived materials in sustainable electronics.

5

GREEN LIG-BASED SUPERCAPACITORS: FABRICATION AND CHARACTERIZATION

In this chapter, materials prepared in Chapter 3 and fully optimized in Chapter 4 are employed with particular focus on their suitability for energy storage applications. The applicability of the green electrodes was successfully demonstrated through the production of planar and sandwiched LIG-based micro-supercapacitors. The electrochemical characterization demonstrated that these electrodes can be implemented as flexible and environmentally friendly energy storage devices, thus opening a novel route for the development of sustainable platforms.

Results shown herein were reproduced from:

- **Paper I: Silvestre, S. L.**, Pinheiro, T., Marques, A. C., Deuermeier, J., Coelho, J., Martins, R., Pereira, L., & Fortunato, E. (2022). Cork derived laser-induced graphene for sustainable green electronics. *Flexible and Printed Electronics*, *7*.
  DOI:10.1088/2058-8585/ac8e7b

- **Paper II: Silvestre, S. L.**, Morais, M., Soares, R. R. A., Johnson, Z. T., Benson, E., Ainsley, E., Pham, V., Claussen, J. C., Gomes, C. L., Martins, R., Fortunato, E., Pereira, L., & Coelho, J. (2024). Green Fabrication of Stackable Laser-Induced Graphene Micro-Supercapacitors under Ambient Conditions: Toward the Design of Truly Sustainable Technological Platforms. *Advanced Materials Technologies*, 2400261.
  DOI:10.1002/ADMT.202400261

5.1 Introduction

As introduced in Chapter 2, the evolution of electronics is closely tied to electrochemical energy storage technologies. As society advances, the global demand for environmentally friendly technology continues to grow. Exploring the integration of LIG into the development of sustainable platforms presents promising opportunities. To maximize the benefits of these innovations, it is essential to focus on refining energy storage solutions within these platforms. Although renewable energy sources, such as sunlight and wind, are becoming increasingly appealing for power generation, their intermittent nature emphasizes the importance of effective energy storage systems. These systems are crucial for maintaining a stable energy supply, while ensuring the efficiency and security of stored energy. Hence, the development of efficient and reliable energy storage solutions remains a challenge[202].

Traditional power sources, such as lithium-ion batteries (LIBs), are typically designed using brittle materials, which limits their applicability in flexible electronics. For example, in conventional LIBs, the electrode active materials are typically coated onto metal current collectors, primarily aluminum for the positive electrode and copper for the negative. Such coatings may readily detach from the underlying surface and exhibit limited resilience when subjected to bending[203]. For flexible power sources to be brought to practical applications, each component must be made from shape-conformable, highly efficient, non-flammable, non-toxic, and scalable materials that are also cost-effective[204]. Additionally, due to the rigid configuration and intrinsic mechanisms of LIBs, adapting them to flexible architectures is challenging. Moreover, these systems rely on hazardous electrolytes, which present significant safety risks to the user if not properly encapsulated[205]. In contrast, MSCs offer distinct advantages for flexible electronics. MSCs can be fabricated on flexible substrates, enabling them to bend, stretch, and conform to various shapes, making them ideal for integration into wearable devices, smart textiles, soft robotics, and large-scale flexible electronics[206]. As electronic devices become smaller and more integrated, the ability to produce compact, efficient energy storage solutions becomes increasingly important. MSCs can be fabricated in very small sizes while still providing adequate power. Batteries, for instance, tend to lose electrochemical performance when scaled down to micrometric dimensions. Furthermore, MSCs offer several advantages over other storage devices, including high power density, rapid charging and discharging, and long cycle life[207,208]. The possibility of widespread adoption of green laser-induced graphene electrodes in novel flexible and smart devices could lead to the further development of self-sustainable platforms.

Herein, we explore a sustainable production path for eco-friendly technical components, namely electrodes and conductive tracks. By using for the first time, to the best of the author's knowledge, a 1.06 μm wavelength laser to convert cork into LIG, promising results were achieved by exploring it as an alternative to a CO_2 laser (10.6 μm wavelength), which is the most used system for LIG preparation. Fiber laser emits radiation near to infrared radiation, which means it works on the same principle as CO_2 laser, inducing thermochemical reactions in the substrate to convert into LIG. However, combining its fast galvo scanning system and photon energy irradiated with meticulously controlling laser parameters, it allows a tunning of LIG composition, porosity, and morphology. Considering the fiber laser ultra-short duration pulses, it also presents high-resolution patterning, lower thermal degradation, and a high potential for large-scale LIG production. With promising graphitization efficiency in these natural substrates, a proof of concept was developed, with cLIG-based flat MSC successfully produced and characterized.

Different gLIG-MSC configurations have been developed in deferent substrates, exhibiting different ranges of specific capacitance and overall electrochemical performance. Although LIG production is a straightforward method, it often results in materials with diverse morphologies and properties, making the comparison between devices and substrates a cumbersome process[25].

This chapter follows the recent discoveries in the development of micro-supercapacitors and presents a sustainable approach to producing green electrodes for energy storage applications. Key considerations include the choice of substrate for electrode production and the selection of laser type and fabrication conditions.

Using a 1.06 μm wavelength fiber laser to convert cork into green laser-induced graphene under inert atmosphere conditions yielded promising results. This approach also explored the advantages of utilizing the fiber laser as an alternative to the traditional CO_2 laser. As a proof of concept, planar and flexible LIG-based micro-supercapacitors were successfully fabricated and comprehensively characterized.

Furthermore, this chapter also presents the synthesis of green LIG using a CO_2 laser under non-inert atmosphere conditions for integration into sandwich-shaped micro-supercapacitors. Initially, optimization of the laser writing process was conducted on various substrates (including paper, lignin-enriched paper, and cork) and under different laser conditions to enhance electrical conductivity and ensure the production of high-quality LIG. This optimization was inspected through Raman spectroscopy by mapping and examining the characteristic graphitic peaks. This research distinguishes itself by exploring sustainable and abundant substrates while also investigating the contribution of lignin substrates to enhancing LIG

production. Following this, MSCs were assembled to understand the influence of LIG properties derived from the different substrates on the electrochemical performance of the devices.

It also demonstrates a novel capability to interconnect individual sandwich MSC units in both series and parallel configurations. This distinctive adaptability significantly enhances the overall capacitance of the system, enabling tailored applications. Moreover, an environmentally conscious approach was introduced in the energy field by developing green LIG MSCs.

This work emphasizes the high potential and practical utility of the produced devices, positioning our work as a pioneering contribution in the realm of LIG-based energy storage platforms.

5.2 Materials and methods

5.2.1 Design and fabrication of green MSCs

For the development of MSCs, the procedures outlined in the respective papers (Paper I and Paper II) detailed in this thesis were followed. The process begins with substrate preparation, followed by LIG synthesis, and subsequent MSC fabrication/characterization, as described below.

5.2.1.1 Substrates preparation

For in-planar MSCs (Paper I):

For the in-planar MSCs development an extra process (illustrated in Figure 34) was added prior to LIG synthesis and subsequent MSC fabrication/characterization. Agglomerated cork sheets with 2 mm thickness were pre-treated with a wax-based ink, as described in section 3.2.2.1.

For sandwich MSCs (Paper II):

Whatman paper 1, and lignin-enriched paper, and cork substrates were treated with borax, a flame-retardant agent, before undergoing laser irradiation, as described in section 3.2.2.2.

5.2.1.2 LIG synthesis and electrode preparation

The LIG synthesis and patterning were conducted as previously described (see Chapter 4). Two different architectures were designed to fabricate in-planar and sandwiched micro-supercapacitors, as described below.

In-planar MSCs electrodes (Paper I):

The detailed optimization study of laser-induced graphene is available in Chapter 4, corresponding to LIG produced from cork substrates. After all laser parameters optimization, electrodes were scribed onto waxed-cork substrates using a 50 W PLS6MW Fiber laser (1.06 μm Nd:YAG Multi-wavelength Laser Platform, Universal Laser Systems, Vienna, Austria), under inert atmosphere (Nitrogen), equipped with a 2.0" lens.

A frequency of 100 kHz and a resolution of 1200 dots-per-inch (DPI) were maintained throughout the LIG production process. After optimizing all laser parameters, the optimal conditions for fabricating waxed-cork electrodes were obtained at a laser power of 11% and a speed of 1% (equivalent to 5.5 W @ 0.02 m s^{-1}). Additionally, positioning the laser beam 1.52 mm below the focal point has been set as an optimal parameter.

Six interdigitated electrodes were designed and patterned with fixed dimensions: lines with a width of 2 mm and a gap of 0.6 mm between them. Additionally, two finger pads were defined for the negative and positive electrodes.

Sandwich MSCs electrodes (Paper II):

Detailed LIG optimization study is available in Chapter 4, corresponding to LIG prepared from paper, lignin-enriched paper, and cork. After all laser parameters optimization, electrodes were scribed using a 75W Fusion M2 CO_2 laser (10.6 μm wavelength - Epilog Laser, Golden, CO, USA), under non-inert atmosphere (ambient conditions). A resolution of 1200 dots-per-inch (DPI) was fixed. After optimizing all laser parameters, the optimal conditions for fabricating paper and lignin-enriched paper electrodes were obtained at a laser power of 4% and a speed of 13% (equivalent to 3 W @ 0.40 m s^{-1}). Similarly, for the cork substrate, optimal LIG electrode formation was achieved at a laser power of 4% and a speed of 6% (equivalent to 3 W @ 0.18 m s^{-1}). Additionally, positioning the laser beam 2 mm above the focal point for all substrates has been set as an optimal parameter. Hexagonal designs were created using CorelDraw and laser patterned onto the substrates encompassing an area of 1 cm^2, using the optimized conditions. The current collector's conductor pads were coated with silver ink (silver-vinyl CI-1001, Engineering Materials Systems, OH, USA), then cured for 10 minutes at 90 °C.

5.2.1.3 Preparation of electrolytes

Electrolytes solutions of potassium sulfate (K_2SO_4), poly(vinyl alcohol)/sulfuric acid (PVA-H_2SO_4) and poly(vinyl alcohol)/phosphoric acid (PVA-H_3PO_4) were prepared and employed in the MSCs.

In the standard procedure, K_2SO_4 (0.5 M) electrolyte was prepared by dissolving K_2SO_4(4.35 g, ≥98 %, CAS 7778-80-5, Carl Roth, Karlsruhe, Germany) in deionized water (50 ml, Millipore) with stirring. PVA-H_2SO_4 (1M) electrolyte was prepared by dissolving PVA (Paper I/1 g, 98.0-98.8% hydrolyzed, M_w ~ 61000, CAS 9002-89-5, Merck KGaA, Darmstadt, Germany; Paper II/1 g, 99+% hydrolyzed, M_w ~ 89000-98000, CAS 341584, Thermo Fisher Scientific, MA, USA) in deionized water (10 ml, Millipore). Once the PVA was dissolved at 85°C under gentle agitation, H_2SO_4 acid (Paper I/0.5 ml, 95.0-97.0%, CAS 7664-93-9, Honeywell GmbH, Offenbach, Germany; Paper II/0.5 ml, 95.0-97.0%, CAS 7664-93-9, Thermo Fisher Scientific, MA, USA) was added and vigorously stirred for 1 hour. For the preparation of PVA-H_3PO_4 (1M) electrolyte, the PVA was first prepared as previously described (Paper I), and then the respective acid, H_3PO_4 (0.5 ml, 85.0-90.0 %, CAS 7664-38-2, Honeywell GmbH, Offenbach, Germany), was added and vigorously stirred for 1 hour.

5.2.1.4 MSCs Preparation and Assembly

In-planar MSCs (Paper I):

Electrolytes (for detailed formulation, see section 5.2.1.3) were applied to the active area of the devices using drop-casting method. Following the application of electrolytes, the devices were left to dry overnight at room temperature.

Sandwich MSCs (Paper II):

The PVA-H_2SO_4 electrolyte (for detailed formulation, see section 5.2.1.3) was applied to the active area of the devices. To enhance electrolyte penetration within the LIG matrix, the devices were subjected to a vacuum environment (approximately -60 mPa) for 10 minutes. Subsequently, MSCs in a sandwich configuration were assembled by carefully pressing the electrodes together with the electrolyte layer and a Whatman 1 paper separator in between. After assembling, the devices were left to dry overnight at room temperature, and then their electrochemical performance was assessed.

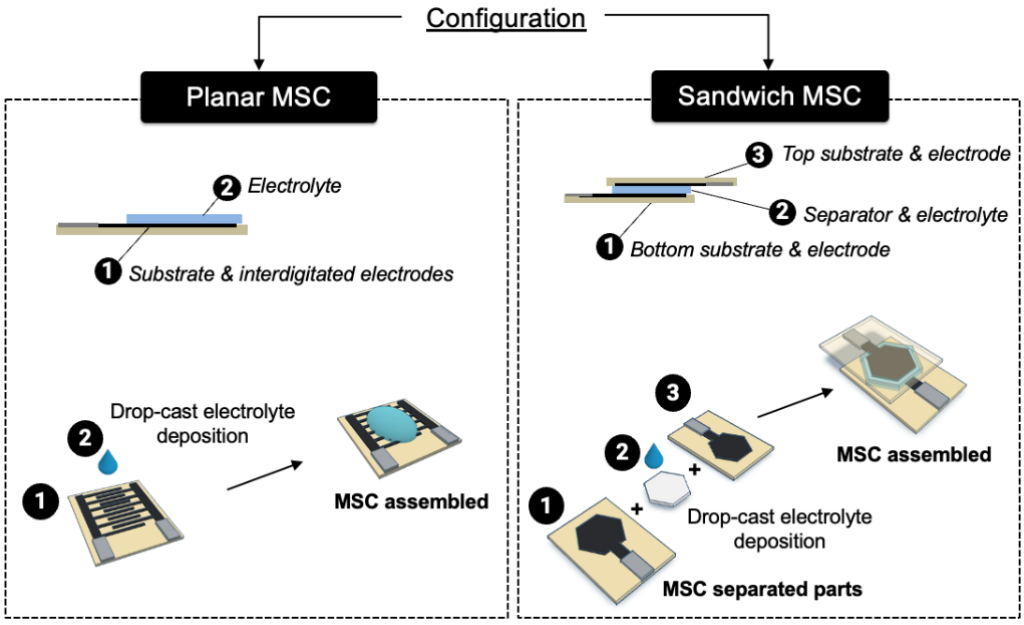

Figure 34. Schematic representation of the in-planar and sandwich configurations of MSCs used in this study, adapted from [155,196]. CC BY 4.0 license, https://creativecommons.org/licenses/by/4.0/.

5.2.2 Electrochemical characterization

The MSCs were connected to a PalmSens 4.0 Potentiostat/Galvanostat workstation (PalmSens Compact Electrochemical Interfaces, Netherlands) using silver pads under ambient conditions. Their electrochemical performance was evaluated through cyclic voltammetry (CV) conducted at various scan rates: from 5 to 500 mV s^{-1} for the **in-planar** MSCs (Paper I), and from 5 to 100 mV s^{-1} for the **sandwich** MSCs (Paper II), with a potential range of 0 to 0.8 V to avoid water decomposition at higher potentials.

Galvanostatic charge-discharge (GCD) tests were performed on a PalmSens 4.0 Potentiostat/Galvanostat workstation (PalmSens Compact Electrochemical Interfaces, Netherlands) for the **in-planar** MSCs (Paper I), using current densities from 0.005 to 0.1 mA cm^{-2}. For the **sandwich** MSCs (Paper II), the tests were conducted using a CH Instruments Electrochemical Analyzer (CHI7081E model, CH Instruments, Inc., Austin, TX, USA), with current densities ranging from 0.01 to 0.2 mA cm^{-2}. The potential window for both configurations ranged from 0 to 0.8 V.

Electrochemical impedance spectroscopy (EIS) was carried out on a PalmSens 4.0 Potentiostat (PalmSens Compact Electrochemical Interfaces) using an AC voltage amplitude of 10 mV at the open circuit condition and a frequency range from 10 mHz to 1 MHz (Paper II).

The areal capacitance (C_A) was determined using Equation S1 and Equation S2 based on CV and GCD measurements. The volumetric capacitance (C_V) was calculated using Equation S4.

Additionally, the areal energy density (E_A) and power density (P_A) of the devices were calculated according to Equation S4 and Equation S5, while the volumetric energy density (E_V) and power density (P_V) were determined using Equation S6 and Equation S7, respectively. These equations were applied following the methods outlined by Béguin et al. [209] and Lin et al. [55].

For the capacitance retention test, 10000 cycles were obtained from GCD curves at a current density of 0.05 mA cm^{-2} for the **in-planar** MSCs (Paper I), and 5000 cycles were obtained from GCD curves at a current density of 0.08 mA cm^{-2} for the **sandwich** MSCs (Paper II).

5.2.3 Data analysis

Data analysis was performed using OriginPro (2022b Academic, MA, USA). Results are reported as mean ± standard deviation from at least three independent experiments, and experimental designs were a completely randomized study. All figures were also plotted in OriginPro (2022b Academic, MA, USA).

5.3 Results and discussion

5.3.1 MSCs fabrication

In-planar MSCs (Paper I):

After the optimization process, cLIG (cork-LIG) was used to design interdigitated electrodes for MSC applications. However, during MSC preparation it was verified a random spreading when the electrolyte was drop casted onto the MSCs' active area. Hence, there was no control in defining the active area where the electrolyte should be deposited nor was it guaranteed that the electrolyte dried on the substrate surface where the electrodes were engraved. Consequently, a proper assessment of the device electrochemical properties was not possible. To circumvent this issue, a wax-based pre-treatment on cork was performed. In the Chapter 4 is described a brief characterization of the LIG induced into waxed-cork substrate.

After this process, MSC electrodes based on w-cLIG were patterned and integrated in flexible MSCs. A schematic representation of the flexible MSC fabrication process is shown in Figure 35.

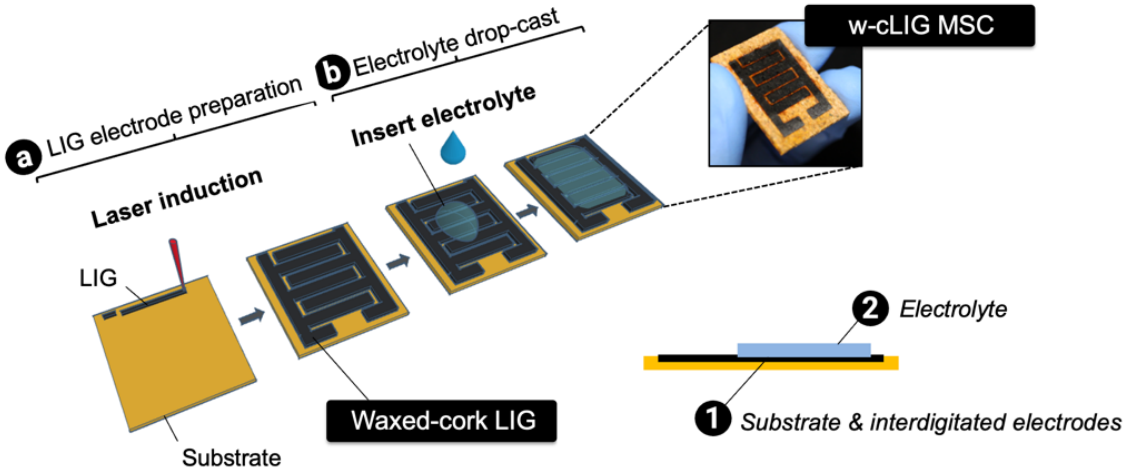

Figure 35. Schematic representation of a planar LIG-MSC fabrication process, from (a) electrode preparation to (b) electrolyte deposition, adapted with permission from [155]. CC BY 4.0 license, https://creativecommons.org/licenses/by/4.0/.

Sandwich MSCs (Paper II):

The fabrication process for the single-device MSCs is visually illustrated in Figure 36. This process involved three distinct steps: (a) electrode fabrication via laser-inducing technique, subsequent (b) deposition of the electrolyte, and the final (c) assembly of the components into functional MSCs. The solid PVA-H_2SO_4 electrolyte was carefully deposited onto the LIG electrodes through a drop-casting technique (Figure 36b). Next, a vacuum process was employed for 10 minutes. This additional step aimed to promote increased electrolyte penetration into the LIG structure, enhancing the contact area between the electrolyte and electrode. A paper separator was used to prevent device short-circuiting problems and retain the electrolyte within the desired area.

The adoption of the sandwich configuration over the interdigitated one aimed to fulfill the energy-related targets set forth for systems that require enhanced energy and power density, efficient electrode-electrolyte interaction, and integration in compact formats.

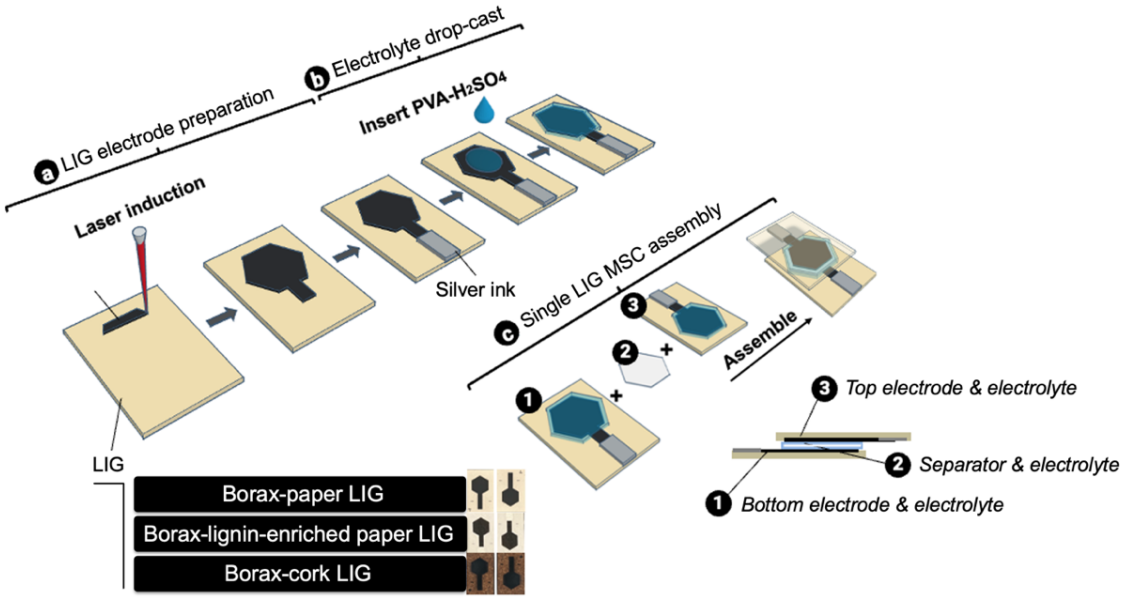

Figure 36. Schematic illustration of a single sandwich LIG-MSC fabrication process from (a) electrode preparation, (b) electrolyte deposition, and (c) device assembly, reproduced with permission from [196]. CC BY 4.0 license, https://creativecommons.org/licenses/by/4.0/.

For multiple connected LIG electrodes, a single-step patterning approach of multiple electrodes was initially considered. However, this approach has drawbacks, including limited independence from each individually fabricated MSC and potential short-circuit issues. An alternative strategy emerged: patterning distinct electrodes separately to create single MSCs and then assembling them one by one. This method allows for the integration of the desired number of MSCs, achieved by gently connecting each unit through their silver pads, as seen in Figure 37.

This strategy enhances the control over the final energy storage device as it enables individual replacement of MSC, the addition or removal of units for specific application needs, adaptability across diverse applications, and reusability. Integration of stacked MSCs offers significant benefits to the energy storage system, including increased energy and power density, enhanced total capacitance, improved energy efficiency, and customization flexibility[210,211]. Consequently, this strategy was subjected to exploration and is depicted in Figure 37, which presents single MSC and stacked MSCs arrangements arranged in series and parallel configurations, thereby demonstrating the reliability of the assemblies for compact energy storage solutions.

The subsequent section presents a comparative analysis of the electrochemical performance of various configurations and the number of employed MSC units. It highlights the stacked configuration's capability to meet diverse energy storage requirements.

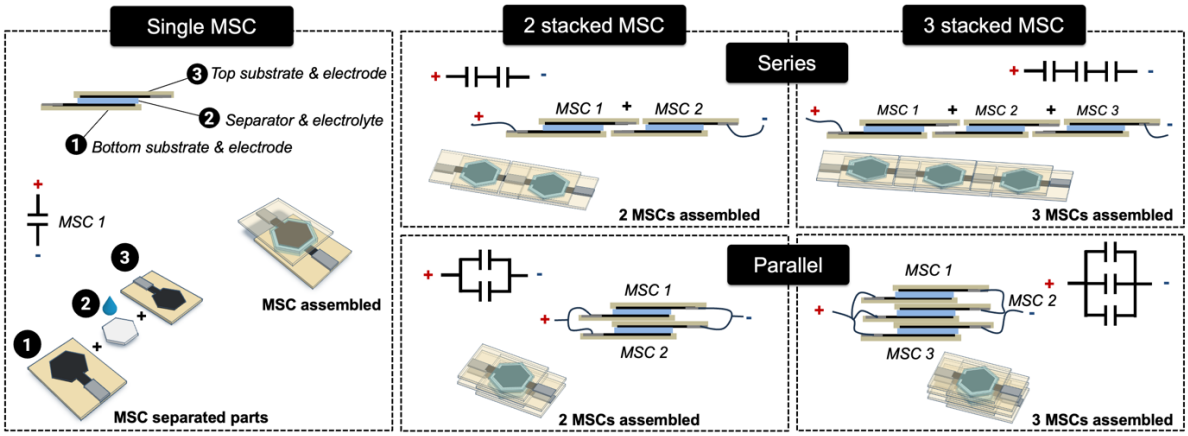

Figure 37. Illustration of single MSC alongside stacked MSCs in both series and parallel arrangements., reproduced with permission from [196]. CC BY 4.0 license, https://creativecommons.org/licenses/by/4.0/.

5.3.2 Electrochemical performance of in-planar and sandwich MSCs

In-planar MSCs (Paper I):

For the electrochemical performance assessment, w-cLIG flexible MSCs were fabricated and tested using different electrolytes.

Comparison of the correspondent areal and volumetric capacitances in function of scan rate (from 5 to 500 mV s^{-1}), obtained from CV curves are shown in Figure 38.

Although using the same electrode dimensions for all the MSCs produced, different CV curves were obtained suggesting different electrolyte-LIG electrodes interaction. By increasing the scan rates, 'quasi-rectangular' to a 'fish' shape curves are identified for all devices produced, which is more prominent on w-cLIG MSCs with PVA-H_2SO_4. This electrolyte is well-known to remain a viscous gel with an apparent higher water content upon drying, which enhances the electrochemical performance for graphene based MSCs[212,213].

Figure 38d-e show the areal and volumetric capacitance calculated using Equation S1 and Equation S3.

A gradual decrease in MSCs capacitance is observed with the scan rate. This phenomenon can be explained by the ion diffusion mechanism in the LIG-MSC.

Areal capacitances of 1.35 mF cm^{-2}, 0.41 mF cm^{-2}, and 0.23 mF cm^{-2} were measured for MSCs tested with PVA-H_2SO_4, PVA-H_3PO_4 and K_2SO_4, respectively (at a scan rate of 5 mV s^{-1}). Volumetric capacitances of 103.63 mF cm^{-3}, 32.06 mF cm^{-3}, and 17.57 mF cm^{-3} were measured for MSCs tested PVA-H_2SO_4, PVA-H_3PO_4 and K_2SO_4, respectively (at a scan rate of 5 mV s^{-1}).

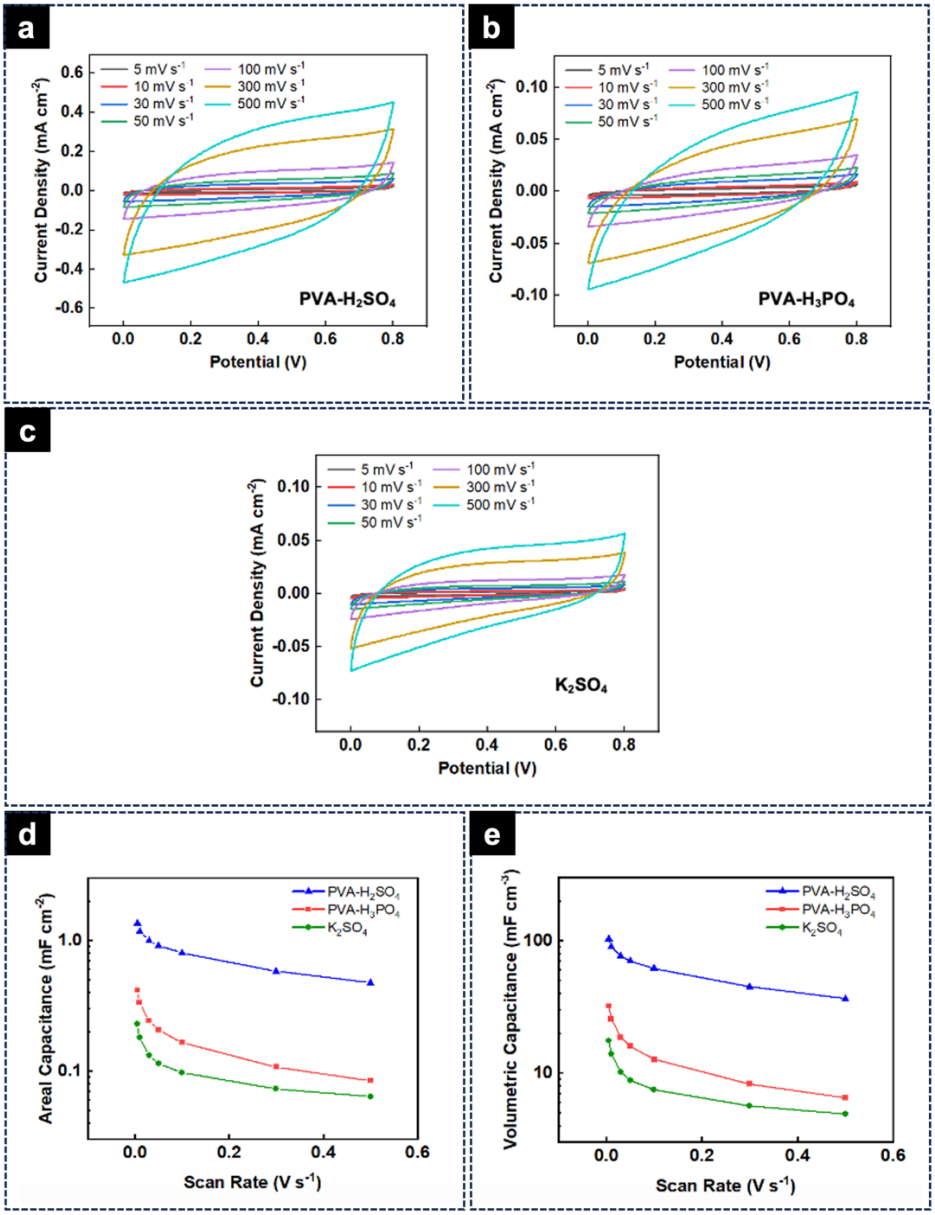

Figure 38. Electrochemical performance of MSCs fabricated using w-cLIG electrodes. Cyclic voltammograms measured at different scan rates using (a) PVA-H_2SO_4, (b) PVA-H_3PO_4 and (c) K_2SO_4 electrolyte. Comparison of the different electrolytes (d) areal and (e) volumetric capacitances in function of scan rate obtained from CV curves, reproduced with permission from [155]. CC BY 4.0 license, https://creativecommons.org/licenses/by/4.0/.

Since the PVA-H_2SO_4 electrolyte rendered w-cLIG MSC the best electrochemical performance among the tested electrolytes, further characterization is shown in Figure 39. The GCD curves of the MSC at different current densities of 0.005, 0.01, 0.02, 0.05 and 0.1 mA cm^{-2} were measured to determine the electrochemical performance of the device over time (Figure 39b).

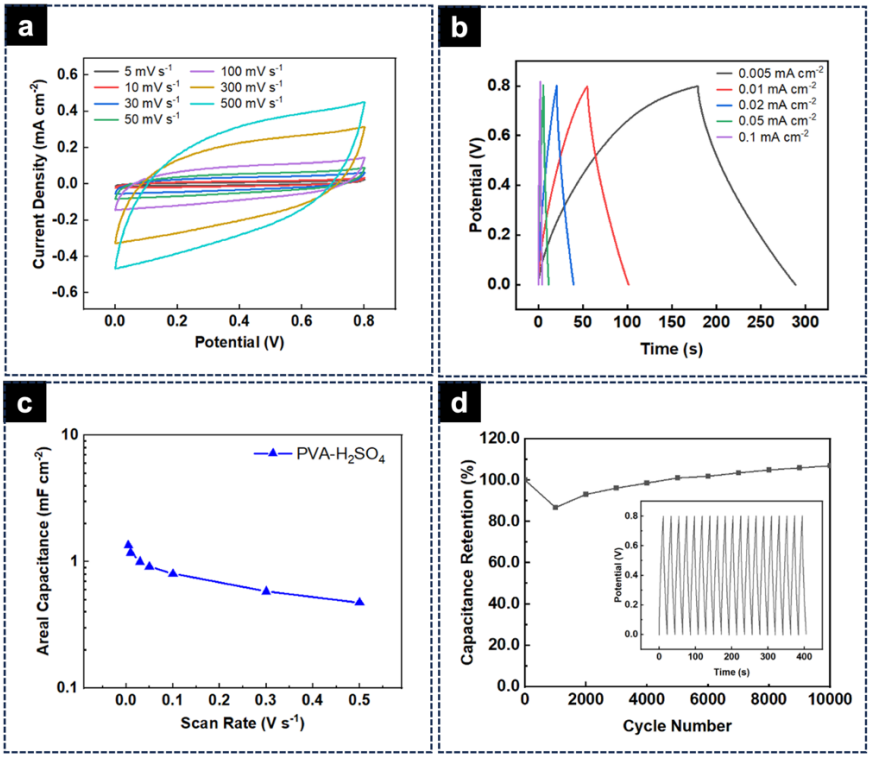

Figure 39. Electrochemical characterization of a w-cLIG MSC using PVA-H_2SO_4 electrolyte. (a) Cyclic voltammograms measured at different scan rates (in the 5-500 mV s^{-1} interval). (b) galvanostatic charge and discharge (GCD) curve of the device with a current density of 0.005, 0.01, 0.02, 0.05 and 0.1 mA cm^{-2}. (c) Areal and volumetric capacitances in function of scan rate obtained from CV curves. (d) Capacitance retention versus cycle number obtained from CGD curves at a current density of 0.05 mA cm^{-2}. Insets: representative GCD curves of the first cyclability for the same MSC, reproduced with permission from [155]. CC BY 4.0 license, https://creativecommons.org/licenses/by/4.0/.

Pseudo symmetrical response curves were observed, which means that its potential changes linearly with time due to its stable and reversible properties.

In Figure 39c, a gradual decrease in MSCs capacitance is observed with the scan rate, where the maximum areal capacitance (C_A) reached was 1.35 mF cm^{-2} (with a corresponding C_V of 103.63 mF cm^{-3} for w-cLIG 130 µm thick) at a scan rate of 5 mV s^{-1}, respectively.

This phenomenon can be explained by the ion diffusion mechanisms in the LIG-MSCs. At lower scan rates, electrolyte ions have more time to move and to penetrate deeply into the available pores in the LIG structure, which results in a higher areal capacitance [214]. At higher scan rates, a loss of efficiency of ions to infiltrate the LIG occurs, leading to a reduction on capacitance [215–217]. Therefore, Figure 39d shows the capacitance retention of the MSCs using PVA-H_2SO_4, which confirmed device excellent stability after 10 000 cycles at a current density of 0.05 mA cm^{-2}. During the cyclability test, it was observed a slight increase in capacitance retention with a tendency to stabilize over operation time like already reported[218]. A loss of MSC capacity is observed mostly due to irreversible electrochemical processes that occur in

the first phase of the cyclability test, such as electrolyte decomposition, gas or byproduct formation, and irreversible interactions of electrolyte ions with the electrode surface or their penetration into porous structures. Over several cycles, the electrodes adapt, and the pores open within its structure. This enhances the wettability of the electrolyte within the LIG structure, promoting greater activation of the ionic diffusion paths and electrochemical reactions. Therefore, throughout the charge and discharge process of the device, a gradual increase of the capacitance retention is observed. This is not a common electrode behavior, however it was already observed in other nanomaterials systems [219,220]. For this reason, w-cLIG electrodes exhibit long-term cyclical stability, which proves to be an excellent material with promising functionality in MSC applications.

To study the flexibility of the device and corresponding electrochemical performance, bending tests were carried out as presented in Figure 40.

Comparing the flat and bent MSC (with 35 ° angle), an increase in charge-discharge time in the GCD curve is observed. This behavior can be related with the deformation submitted to its structure and an opening of the spongy pores, which suggests an enhancing of the charge storage performance with expansion of the active area [221]. Also, when the MSC is bent, it benefits from the infiltration of the electrolyte through longer paths leading to a better charge carrier distribution.

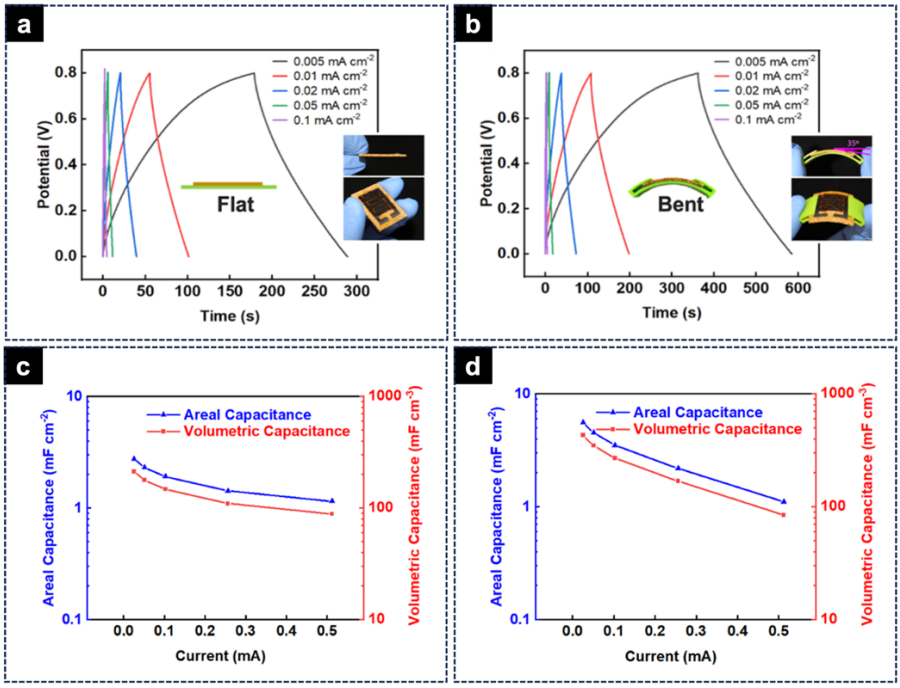

Figure 40. The galvanostatic charge and discharge (GCD) curve of (a) flat and (b) bent w-cLIG MSC with a current density of 0.005, 0.01, 0.02, 0.05 and 0.1 mA cm^{-2}. GCD curve comparison of (c) flat and (d) bent w-

cLIG MSC areal and volumetric capacitance calculated from GCD data, reproduced with permission from [155]. CC BY 4.0 license, https://creativecommons.org/licenses/by/4.0/.

In Figure 40c-d, the areal and volumetric capacitances were plotted at different current densities, calculated from the GCD curves according to Equation S2 and Equation S3.
Flat conformation yields a C_A of 1.43 mF cm^{-2} at 0.1 mA cm^{-2} (C_V corresponding to 109.62 mF cm^{-3}) and bent MSC resulted on a C_A of 2.20 mF cm^{-2} at 0.1 mA cm^{-2} (C_V corresponding to 169.23 mF cm^{-3}). These values confirm the suggestions above, where it was mentioned that a bent conformation increases LIG paths and facilitate ionic diffusion, consequently yielding a better capacitance.
In addition, areal and volumetric energy, and power densities of the flat and bent MSCs were evaluated, and the Ragone plots are shown in Figure 41.

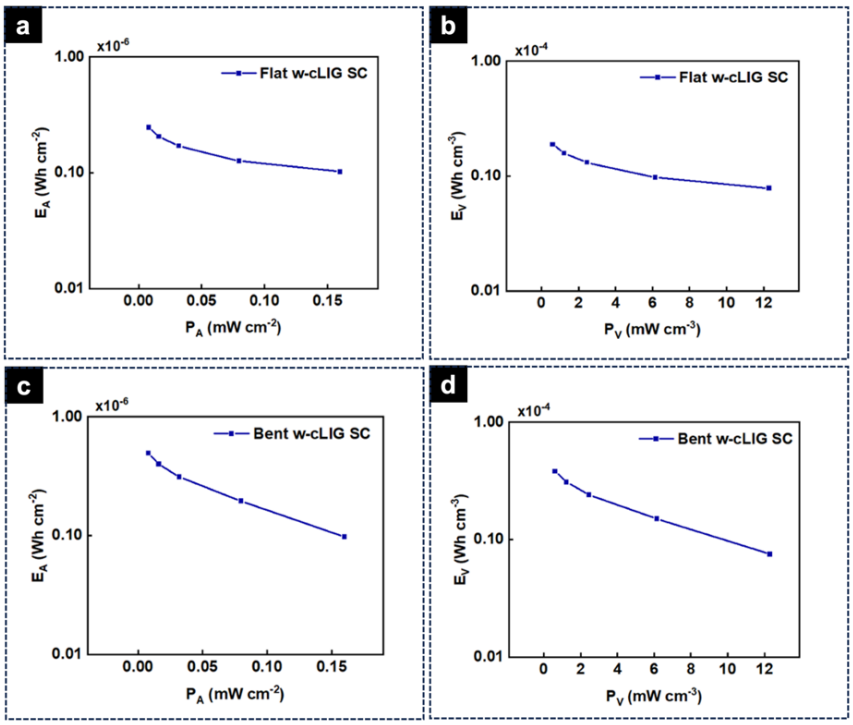

Figure 41. Ragone plots of w-cLIG MSCs (a) areal and (b) volumetric energy densities in flat conformation, and (c) areal and (d) volumetric energy densities in bent conformation, reproduced with permission from [155]. CC BY 4.0 license, https://creativecommons.org/licenses/by/4.0/.

Greater areal and volumetric capacitances obtained with the bent MSC reflect in better energy-power characteristics, which is in accordance with results demonstrated above. Flat w-cLIG MSC exhibits an E_A of 0.13 μWh cm^{-2} and an E_V of 9.74 μWh cm^{-3} at the current density of 0.1 mA cm^{-2}. For the bent conformation, the MSC was able to deliver the highest E_A of 0.20 μWh cm^{-2} and an E_V of 15.04 μWh cm^{-3} at the same current value. The areal power densities

resulting from flat and bent conformation reached 80 μW cm^{-2} and a corresponding P_V of 6154 μW cm^{-3} at the same current value.

By focusing this work on the sustainability and simplicity of the processes used, it is shown that exploring the use of renewable materials to develop electronics can achieve equally good or even better performances than what is currently found in the literature (Table 3). Similar works have already reported the conversion of natural carbon substrates into LIG electrodes, using laser sources ranging from UV to IR wavelengths. Thus, the properties of LIG can be manipulated according to each target application, achieving tailored electrical, physical, chemical resistance, and structural properties. However, different substrates can have limitations in terms of compatibility radiation absorption for specific wavelength lasers. This work introduces the importance of exploring the application of an alternative laser source (Fiber) for LIG synthesis in an agglomerated cork, without the need to use doping strategies or pre-treatments on the substrate. In contrast with that, the properties of the electrodes vary and, a porous w-cLIG with excellent properties was achieved with greater conductivity and fewer defects. Also, the optimized laser conditions, the electrodes design/geometry can also influence LIG properties. Overall, LIG electrodes induced on cork substrates with a fiber laser have the potential for low-cost MSCs electrodes fabrication compared to previous LIG reports produced on natural substrates by DLW, with similar electrochemical performances. It is important to highlight the fact that different lasers used on similar substrates do not always achieve the same results and therefore, the obtain metrics and consequent comparisons are not always straightforward.

Table 3. Comparison of planar LIG-based flexible MSCs capacitances from literature, using DLW method on natural based-substrates, reproduced with permission from [155]. CC BY 4.0 license, https://creativecommons.org/licenses/by/4.0/.

Electrode	Laser	Electrolyte	Capacitance	Capacitance retention	Energy and Power Density	Ref.
LIG/waxed cork	1.06 μm NIR (Fiber)	PVA-H_2SO_4	1.35 mF cm^{-2} @ 5 mV s^{-1} 1.43 mF cm^{-2} @ 0.1 mA cm^{-2}	106% (>10 000 cycles @ 0.05 mA cm^{-2})	0.13 μWh cm^{-2} and 80 μW cm^{-2} @ 0.1 mA cm^{-2}	This work
LIG/natural cork	450 nm UV	PVA-H_2SO_4	1.56 mF cm^{-2} @ 0.1 mA cm^{-2}	91% (>10 000 cycles @ 0.02 mA cm^{-2})	1.7 μWh cm^{-2} and 55.7 μW cm^{-2} @ 0.05 mA cm^{-2}	[159]
LIG/kraft lignin	10.6 μm IR (CO_2)	PVA-H_2SO_4	0.88 mF cm^{-2} @ 10 mV s^{-1}	91% (>10 000 cycles @ 0.02 mA cm^{-2})	31.3 μWh cm^{-2} and 138 μW cm^{-2} @ 0.01 mA cm^{-2}	[166]
LIG/phenolic resin	405 nm UV	-	0.78 mF cm^{-2} @ 500 mV s^{-1}	93.8% (>2000 cycles @ 1 mA cm^{-2})	-	[79]
LIG/wood	10.6 μm IR (CO_2)	PVA-H_2SO_4	1 mF cm^{-2} @ 1 mA cm^{-2}	-	-	[150]

MSC development on cork substrates is just one example of one possible application for LIG. It holds a great potential for future technology not only due to the simplicity of optimizing the electrodes but also due to the intrinsic properties of the substrate itself. Additionally, these metrics can be translated to other systems, such as transistors, sensors and general circuitry or conductive paths. Additionally, it is still possible to explore multiple lasing and doping strategies and other pre-treatments to the cork substrate to obtain better quality LIG, with enhanced properties adapted to the desired application. With this work, it is shown that LIG is to be a good candidate for further technological advances in electronics, due to its low sheet resistance, adaptability, low cost, and simplicity.

Sandwich MSCs (Paper II):

A comprehensive assessment of the sustainable MSCs was conducted to explore their energy storage and delivery capabilities. This evaluation involved the examination of cyclic voltammetry (CV) and galvanostatic charge-discharge (GCD) analyses performed across all devices. In Figure 42a-b is observed the presence of leaf-like shaped CV curves for MSCs derived from borax-paper and borax-lignin-enriched paper. In contrast the borax-cork MSC (Figure 42c) exhibits a quasi-rectangular shape, which is indicative of the typical electrical double layer (EDL) capacitive behavior[222].

Figure 42 illustrates the impact of varying scan rates on the diffusion of ions within the electrode. At lower scan rates, ions have more time to diffuse and penetrate the deeper pores of the electrode, leading to enhanced areal capacitance. As the scan rate increases from 5 to 100 mV s^{-1}, the distinct leaf-like shaped CV curves become more pronounced due to constrained ion diffusion. This is typically observed when the available time for ion diffusion is reduced at higher scan rates[207]. The borax-cork MSCs benefit from inherent substrate characteristics, including greater porosity, increased LIG thickness, and a larger surface area[159]. These attributes contribute to maintaining quasi-rectangular CV curves even at higher scan rates, highlighting the cork electrode's capability to withstand more challenging conditions. This resilience is crucial for applications requiring rapid charge and discharge cycles.

The GCD graphs demonstrate near-symmetrical triangular curves across all devices, in accordance with the typical EDL behavior observed in the CV analysis. The observed asymmetry in the LIG-derived MSCs' charge and discharge times can be attributed to ion kinetics within the porous electrode structure. This is influenced by electrochemical reactions occurring at the electrode-electrolyte interface[155]. Factors such as porosity, thickness, and the presence of surface functional groups within the electrode matrix contribute to variations in ion

transport rates[25,65]. Despite the observed variations, all devices exhibit relatively similar behavior, suggesting that the overall electrochemical performance remains consistent across all devices.

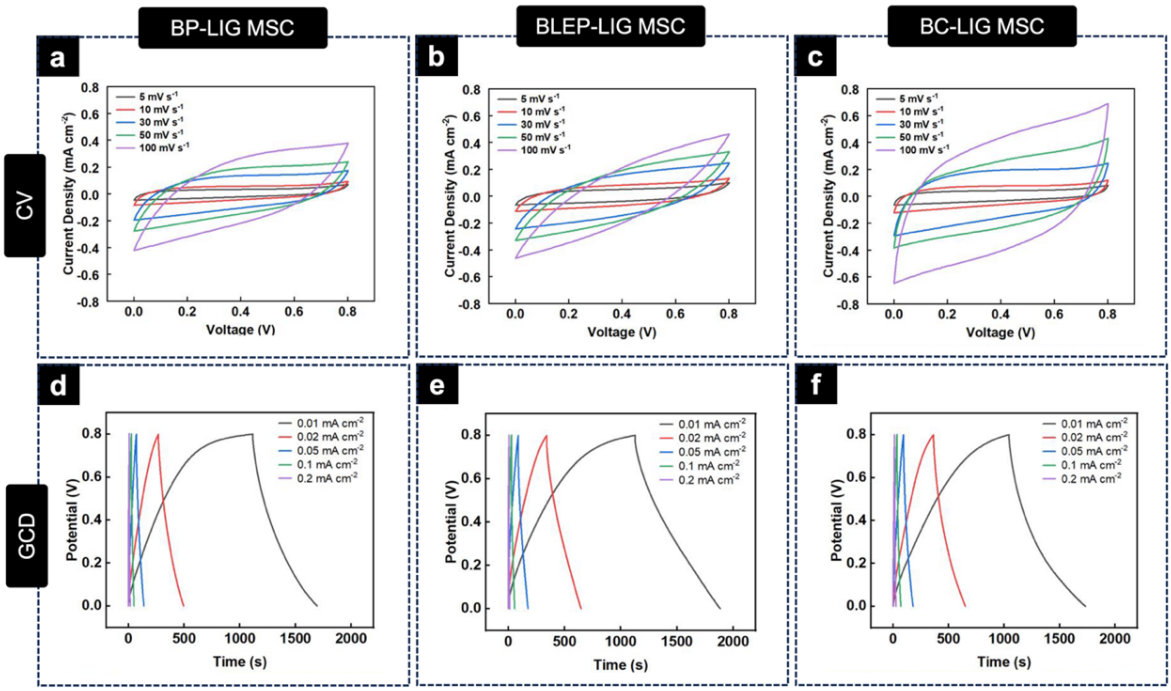

Figure 42. Cyclic voltammograms of (a) borax-paper (BP), (b) borax-lignin-enriched paper (BLEP), and (c) borax-cork (BC) based LIG MSCs and respectively galvanostatic charge and discharge curves on (d)-(f), reproduced with permission from[196]. CC BY 4.0 license, https://creativecommons.org/licenses/by/4.0/.

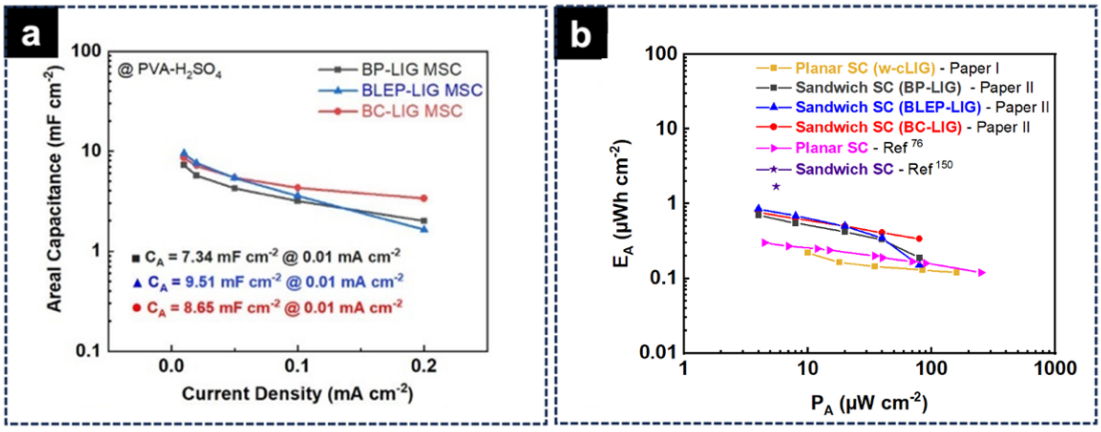

Figure 43. (a) Areal capacitance from galvanostatic charge-discharge analysis, reproduced with permission from [196]. CC BY 4.0 license, https://creativecommons.org/licenses/by/4.0/. (b) Ragone plot of all devices including similar devices from the literature.

Figure 43a presents a summary of the calculated areal capacitance values of all devices as the current density increases from 0.01 to 0.2 mA cm^{-2}, as extracted from the charge-discharge curves.

At a current density of 0.01 mA cm^{-2}, the highest capacitance (C_A) of 7.34 mF cm^{-2} was achieved for BP MSC, 9.51 mF cm^{-2} for BLEP MSC, and 8.65 mF cm^{-2} for BC MSC.

Table 4 compares the performances of gLIG and polyimide based LIG MSCs, in addition to the values obtained from this work.

Table 4. Comparison of LIG-based MSCs capacitances from literature, using direct laser writing method[196].

Electrode	Design	Laser	Electrolyte	Capacitance	Energy and Power Density	Ref.
LIG/Borax-paper LIG/Borax-lignin-enriched paper LIG/Borax-cork	Sandwich	CO_2	PVA-H_2SO_4	(BP) 7.34 mF cm^{-2} (BLEP) 9.51 mF cm^{-2} (BC) 8.65 mF cm^{-2} @ 0.01 mA cm^{-1}	0.73 µWh cm^{-2} (BP), 0.85 µWh cm^{-2} (BLEP), µWh cm^{-2} 0.77 (BC) & 4 µW cm^{-2} @ 0.01 mA cm^{-2}	This work
LIG/Natural Cork	Sandwich	UV	PVA-H_2SO_4	4.13 mF cm^{-2} @ 0.05 mA cm^{-2}	1.7 µWh cm^{-2} & 55.7 µW cm^{-2} @ 0.05 mA cm^{-2}	159
LIG/Kraft Lignin	Sandwich	CO_2	PVA-H_2SO_4	2.51 mF cm^{-2} @ 0.01 mA cm^{-1}	31.3 µWh cm^{-2} & 138 µW cm^{-2} @ 0.01 mA cm^{-2}	166
LIG/Waxed-cork	In-planar (interdigitated)	Fiber	PVA-H_2SO_4	1.43 mF cm^{-2} @ 0.1 mA cm^{-2}	0.13 µWh cm^{-2} and 80 µW cm^{-2} @ 0.1 mA cm^{-2}	155
LIG/Borax-paper	In-planar (interdigitated)	CO_2	PVA-H_2SO_4	4.6 mF cm^{-2} @ 0.015 mA cm^{-2}	0.30 µWh cm^{-2} & 4.5 µW cm^{-2} @ 0.01 mA cm^{-2}	78
LIG/Polyimide	In-planar (interdigitated)	CO_2	PVA-H_2SO_4	4 mF cm^{-2} @ 0.2 mA cm^{-2}	-	55
LIG/Polyimide	Sandwich	CO_2	PVA-H_2SO_4	9 mF cm^{-2} @ 0.02 mA cm^{-2}	-	223

The inclusion criteria considered a range of factors, including electrode designs, laser types, substrate type, optimized laser conditions, and those with the highest relevance and closest similarity to the presented study.

The capacitances of the best-performing devices in this work, when compared with those reported in the literature, suggest reliability in the obtained results. This contributes to a growing body of knowledge around gLIG as a promising alternative for energy storage devices.

In this part of the work, the sandwich configuration was chosen over the interdigitated, primarily motivated by the aim to prioritize a larger effective surface area for the electrode-electrolyte interface, following reports that demonstrated improved capacitance[159].

While certain applications may lean towards prioritizing high packing density, often favored by interdigitated designs, others may prioritize a greater effective surface area, favored by a sandwich configuration. Nevertheless, exploring the most suitable configuration requires a careful balance of multiple factors, including electrode thickness, electrolyte used, ion diffusion

paths, application-specific needs, among others[207,222]. These considerations are essential for optimizing the overall performance and efficiency of the supercapacitor system.

Furthermore, this study aimed to assess the suitability and versatility of renewable materials in the practical development of micro-supercapacitors. All devices showed relatively similar electrochemical performances (Figure 43). However, under higher current densities, borax-cork MSC consistently demonstrated superior performance. This resilient behavior suggests a notable capacity to sustain performance under increased current densities, making it particularly intriguing and promising candidate for applications that demand stable electrochemical performance.

The Ragone plot in Figure 43b confirms the high-energy and high-power density achieved for all devices and highlights the key differences between planar and sandwich-type SCs in terms of energy density and power density. At low power densities (0.01 mA cm^{-2}), the sandwich-type SCs demonstrated higher energy densities, reaching 0.73 μWh cm^{-2}, 0.85 μWh cm^{-2}, and 0.77 μWh cm^{-2} for BP-LIG, BLEP-LIG, and BC-LIG MSCs, respectively, compared to the planar configuration reported previously. When compared with other studies in literature that also use paper and cork substrates, the results presented here are in line with reported values. For instance, Coelho et al.[78] reported energy densities of 0.30 μWh cm^{-2} with a power density of 4.5 μW cm^{-2}, and 0.12 μWh cm^{-2} at a significantly higher power density of 255.4 μW cm^{-2}. Similarly, Imbrogno et al.[159] achieved an energy density of 1.7 μWh cm^{-2} and a power density of 55.7 μW cm^{-2} at a discharge rate of 0.05 mA cm^{-2}. While higher power densities have been reported, they are often achieved at the cost of reduced energy density. This trade-off between energy and power density remains a common challenge in optimizing MSC performance. The results obtained in this work demonstrate a promising energy storage capability while maintaining a stable power output, which is especially relevant for applications requiring consistent performance at low current densities.

The superior performance observed in sandwich-type SCs can be attributed to the larger electrode/electrolyte interface area, which enhances charge storage capacity. In contrast, planar SCs tend to exhibit lower energy densities at comparable power outputs, likely due to the limited surface area and increased ion diffusion resistance[159].

Nevertheless, planar configurations may still be advantageous for applications requiring simpler MSC assembly process and design. This comparison underscores the energy-power balance achievable with sandwich-type SCs, particularly when optimized electrode and substrate materials are employed, as demonstrated in this work.

A stability evaluation was conducted through 5000 cycles of charge-discharge (Figure 44) at a current density of 0.5 mA (0.08 mA cm^{-2}).

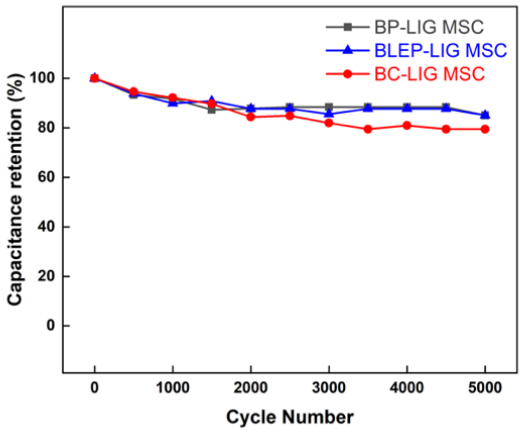

Figure 44. Comparison of the capacitance retention versus cycle number obtained from GCD curves of BP-LIG, BLEP-LIG, and BC-LIG MSC at a current density of 0.08 mA cm^{-2}, reproduced with permission from [155]. CC BY 4.0 license, https://creativecommons.org/licenses/by/4.0/.

During the cyclability test of all devices, it was observed that the paper based MSCs demonstrated slightly better capacitance retention (approximately 85% of initial capacitance) compared to the cork MSCs (approximately 80% of initial capacitance). This capacitance loss upon cycling is not ideal, but it is not uncommon. Some residual species resulting from the LIG processing, non-graphitic carbon, are likely to exhibit irreversible reactions or poorly bound particles that degrade the capacitance during the first measurement cycles. Other authors also report that during the charge/discharge cycles of these devices, the observed loss of capacitance can be attributed to factors such as corrosion of electrode and substrate materials, decomposition of electrolyte water, and formation of gases in electrode pores, among others. Nevertheless, it is observed that after 3000 cycles, the MSCs capacitance tends to stabilize over time as expected, which is consistent with the literature[78,155].

While the observed performance provides valuable insight into the potential applications of these devices, it is also crucial to also consider material stability and electrode-electrolyte interaction under demanding conditions over extended cycles. Compared to cork, paper substrates are typically thinner and more fragile, which may limit their suitability for prolonged use, particularly when using harsh electrolytes such as standard PVA-H_2SO_4, leading to substrate degradation over time. Nevertheless, borax-cork MSCs demonstrate robustness and longevity, making them more suitable for energy storage applications in real-world scenarios, despite slightly lower capacitance retention compared to other materials.

The Nyquist plots in Figure 45a provide important insights into the electrochemical performance of the BP-LIG MSC, BLEP-LIG MSC, and BC-LIG MSC devices. The high-frequency intercepts on the Z' axis correspond to the equivalent series resistance (ESR), with values of 222.4 Ω, 248.9 Ω, and 159.8 Ω for BP-LIG MSC, BLEP-LIG MSC, and BC-LIG MSC,

respectively. The values indicate relatively low internal resistance for this type of devices, consistent with literature values, as reported by Coelho et al. (~120 Ω) and Tariq et al. (~102.2 Ω) [78,224].

The absence of prominent semicircles in the high-to-mid-frequency region indicates a negligible charge-transfer resistance (*R*ct), typical for EDLCs, where the primary working mechanism relies on the physical separation of charges at the electrode-electrolyte interface, with no faradaic electron transfer occurring. Any minor contributions to *R*ct observed may arise from the presence of functional groups on the LIG surface, such as those introduced during the LIG process[117].

At low frequencies, the plots exhibit nearly vertical trends, which are indicative of efficient capacitive behavior. Deviations from the ideal vertical line, particularly in BLEP-LIG MSC and BC-LIG MSC, suggest diffusion limitations within the hydrogel-based PVA-H_2SO_4 electrolyte. This could be due to restricted ion mobility in the electrolyte or differences in the porosity and surface properties of the electrodes.

The ESR is a critical parameter as it directly impacts energy losses, charging/discharging efficiency, voltage fluctuations, and heat accumulation within the devices. Factors contributing to ESR include the intrinsic conductivity of the electrode materials, the ionic conductivity of the electrolyte, the electrode configuration (planar or sandwich), the separator, and the quality of electrical contacts[225].

Although the LIG was not doped, previous studies have demonstrated the presence of functional groups on its surface, which can be minimized through post-treatment processes such as nitric acid cleaning[226]. Further reductions in ESR could also be achieve by optimizing the LIG production conditions (e.g., using an inert atmosphere to reduce functional groups) and improving electrode-electrolyte interface.

The equivalent circuit model shown in Figure 45b provides a framework to analyze these results. The circuit consists of (i) *R*s (series resistance), representing the total internal resistance, including electrode and electrolyte, (ii) *R*ct (charge-transfer resistance), that accounts for resistance at the electrode-electrolyte interface, (iii) *C*dl (double-layer capacitance), describing the charge storage at the electrode surface, and (iv) *Z*w (Warburg element), which accounts for ion diffusion. The low ESR and negligible *R*ct observed for BC-LIG MSC highlight its efficient charge transport and capacitive performance, making it a promising candidate for energy storage applications. The importance of a low ESR lies in its direct impact on power delivery, energy efficiency, and the overall performance of the MSCs, particularly in applications demanding fast charge-discharge cycles.

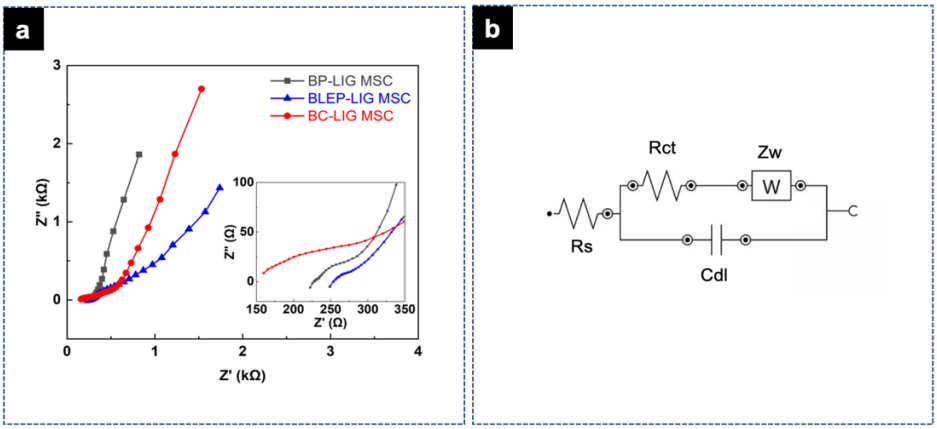

Figure 45. (a) LIG-MSCs Nyquist plots, reproduced with permission from[196]. CC BY 4.0 license, https://creativecommons.org/licenses/by/4.0/. The inset highlights the high-frequency region, providing a closer view of the impedance response for each device. (b) Equivalent circuit model used to interpret the electrochemical impedance spectroscopy (EIS) data.

As demonstrated by Syugaev et al., higher ESR values (similar to our work) can be obtained for MSCs produced with hydrogel electrolytes[227]. This was demonstrated by comparing hydrogel PVA-H_2SO_4 electrolyte with a liquid electrolyte, showing that inherent properties of the electrolyte and their interaction with LIG structure can influence EIS measurements. Since hydrogel electrolytes present noticeably lower ionic conductivity compared to liquid electrolytes, ion diffusion is hindered, and greater resistance is encountered when penetrating the LIG pores. Thus, the capacitance decreases in the high-frequency range, manifesting as resistive behavior in the initial part of the EIS curve. This behavior is primarily attributed to a high ESR, resulting from factors such as limited conductivity and slower ion transport within the hydrogel electrolyte. The linear segment observed at lower frequencies reflects diffusion limitations, which become more pronounced as the frequency decreases. Additionally, the ESR values can be influenced by the physical configuration of the system, such as the distance between electrodes in a sandwich assembly, which can be optimized through adjustments in the design or assembly process. To sum up, the present EIS spectra, are typical of porous materials, deviating from the ideal case scenario (semi-infinite diffusion condition). As such, our LIG-MSCs behave like non-ideal capacitors due to non-homogeneities throughout the structure. One may also consider that the angles of Warburg diffusion can also be influenced by the different porosity of the samples, leading to different levels of electrolyte impregnation[227,228].

Modular assembly characterization– stacked and sandwiched MSCs

To supply energy for practical applications, a single MSC is insufficient to power a system, so MSCs should be integrated into series or parallel configurations. This is essential to overcome the inherent limitations of the capacity of a single device.

Figure 46a-c, GCD curves are presented, comparing a single device with two and three-stacked devices integrated into both series and parallel configurations. These experiments were conducted at a current density of 0.05 mA cm^{-2}.

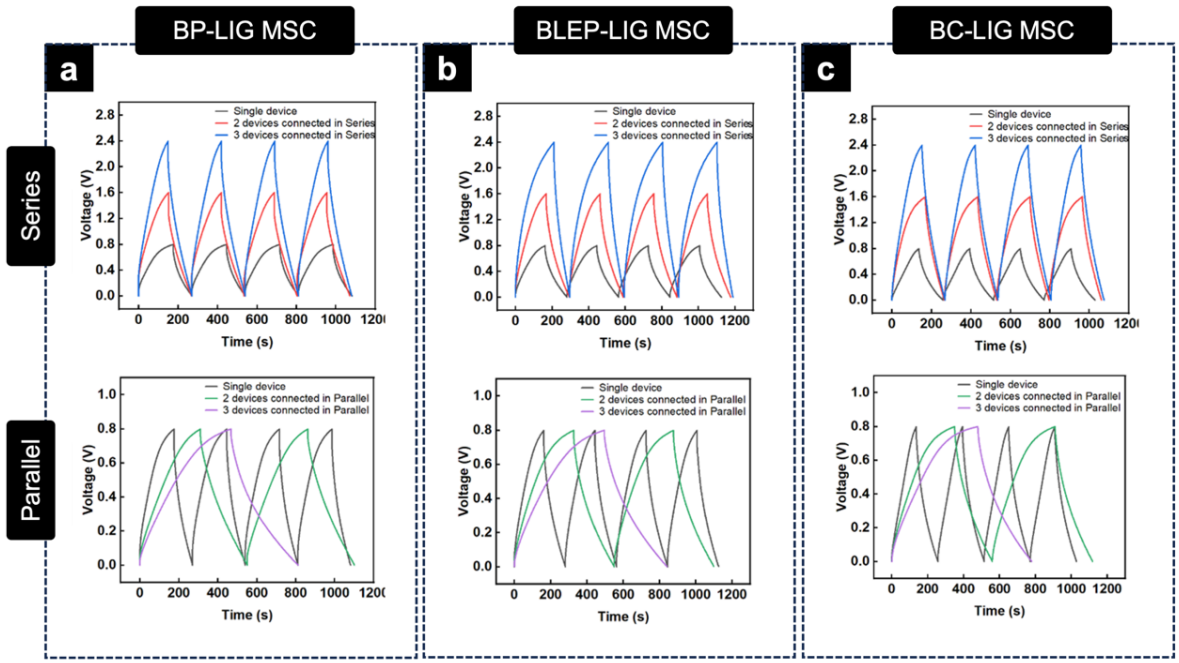

Figure 46. Electrochemical performances of single and stacked LIG-MSCs in series and parallel circuits. Galvanostatic charge and discharge curves comparing a single device to stacked series and parallel devices at a current density of 0.05 mA cm^{-2} in (a) BP, (b) BLEP, and (c) BC based LIG MSCs, reproduced with permission from [196]. CC BY 4.0 license, https://creativecommons.org/licenses/by/4.0/.

The GCD curves reveal the expected behavior of EDL capacitors, characterized by a quasi-triangular shape and a slight *iR* drop across all devices[209]. Nonetheless, these curves show distinct performances among the different configurations and quantities of stacked devices.

Compared to a single device, the stacked series MSC demonstrates a cumulative voltage, featuring a 2x higher working voltage window (1.6 V) for two devices and a 3x higher working voltage window (2.4 V) for three devices, respectively. In contrast, the stacked parallel configuration exhibits a 2x longer discharge time for two devices and a 3x longer discharge time for three devices at the same current density. Consequently, this results in an enhanced overall capacitance achieved by adding MSCs. The extended discharge times emphasize the potential for increased energy storage capabilities, making parallel configurations favorable for applications requiring prolonged power delivery at lower voltage[223]. Moreover, the basic

operational characteristics of both series and parallel connections are demonstrated by all MSCs, reinforcing the adaptability and feasibility of these configurations. Corresponding CV curves for stacked series and parallel MSCs can be found in the appendix (Figure S2 and Figure S3).

The versatility of integrating MSCs allows for tailored setups to meet specific application requirements, optimizing their performance for a diverse range of practical uses in electronic systems. As an example, and to validate their practicability, three borax-cork MSCs were stacked in series, highly extending the voltage window from 0.8 V up to 2.4 V. A practical demonstration (Figure 47) shows that the assembled MSCs were able to successfully power both a multicolor light-emitting diode (LED) with a typical forward voltage ranging from 2 V to 3.2 V and a humidity/temperature sensor with a forward voltage requirement of 1.5 V.

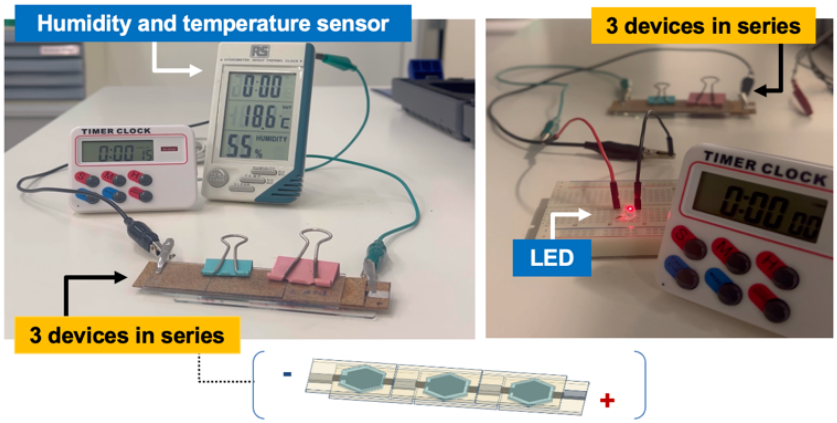

Figure 47. Humidity/temperature sensor and LED powered by three borax-cork LIG-MSCs in series, reproduced with permission from [196]. CC BY 4.0 license, https://creativecommons.org/licenses/by/4.0/.

This demonstration not only proved the capability and simplicity of stacking and connecting multiple MSCs according to specific voltage requirements but also emphasized their potential across different applications. The intermittent red, green, and blue (RGB) light-emitting diode (LED) was powered for approximately 30 seconds, while the humidity and temperature sensors were powered for roughly 3 minutes. The modular setup allows scalability, enabling the stacking of additional micro-supercapacitor units for increased energy storage and prolonged device operation. In principle, there is no limit to the number of micro-supercapacitors that can be connected in series and parallel. However, this *endless energy storage* capability would lead to an unpractical area for the micro-supercapacitors module. In the literature, there are very interesting ways to pack and fold the single cells and thus obtain a compact module[229,230]. For instance, Seol *et al.*, developed an all-printed supercapacitor array with vertical stacking based on Ag current collectors and a carbon mixture as active material[230]. In practical terms,

the authors showed that a 3x3 array exhibited an areal capacitance of 0.101 F cm^{-2}, areal energy density of 0.081 mWh cm^{-2}, and areal power density of 1.21 mW cm^{-2} (voltage window of 0 to 2.5 V). This type of configuration would be feasible on fixed smart house applications, but still too bulky for wearable applications. Regarding LIG, the processing area would be ultimately limited by the laser printing bed. However, considering that LIG can easily be peeled off from the substrate, foldable LIG based devices do not seem a feasible option unless proper encapsulation is used. In this case, micro-supercapacitors are usually designed by stacking individual devices or by just engraving the devices on the same substrate, as it has been shown on this thesis[78,230]. As such, for the time being, LIG based supercapacitors hold promises for energy-efficient, self-sustainable systems, particularly in low-power, low-resource, and remote sensing applications aiming at voltage windows of ~ 3.5 V. However, the field of supercapacitors consistently focuses on research and challenges to improve energy efficiency, capacitance, flexibility, and stability. For the devices under study, their maximum potential was already attained by optimizing the lasing conditions. Nevertheless, the field of supercapacitors remains committed to research and challenges aimed at enhancing energy efficiency, capacitance, flexibility, and stability. In the case of the devices under study, the maximum potential was already attained by optimizing the lasing conditions. Nevertheless, the electrochemical performance of the micro-supercapacitors can be enhanced by investigating the impact of alternative electrolytes. Polymer gel electrolytes, typically based on polyvinyl alcohol (PVA), are the most reported systems, allowing for maximum voltage windows of 2.0 V[231]. In contrast, non-aqueous electrodes based on ionic liquids enable voltage windows up to 3.5 V, which significantly enhances the energy density[232]. Furthermore, the parameter in question can also be enhanced through the introduction of foreign species, such as boron, into the LIG[233,234]. For instance, Yuan et al. designed a fluorine and boron-doped LIG supercapacitor, which delivered an areal-specific capacitance of 49.81 mF cm^{-2}, representing a 23-fold increase over the MSC from commercial polyimide (PI)-based LIG[234]. The addition of metal oxides has also been demonstrated to enhance MSC energy density. Abreu et al. employed a two-step process, whereby chromatography paper was first soaked in a solution of manganese tetraborate acetate, prior to the subsequent laser treatment. During the laser treatment, the paper fibers underwent a conversion process into LIG, while the precursor was simultaneously reduced onto manganese oxide. This resulted in a notable enhancement in capacitance, attributed to the pseudo-capacitive effect of the metal oxide[108]. Dos Santos Klem employed LIG on paper as viable electrodes for manganese oxide deposition[107]. By optimizing the deposition times, it was possible to obtain "sandwich" micro-supercapacitors with specific capacitances reaching as high as 90 mF.cm^{-2}. Finally, LIG can also be optimized by multi-

lasing approaches which increase the film's electrical conductivity. All the aforementioned LIG tailoring, results in an optimization of the capacitances, and as such, energy density. Higher energy densities will open the possibilities for new applications and reduce the size and/or number of devices on the modules. As such there are several venues to explore regarding the presented MSC optimization aiming at applications beyond IoT sensing.

5.4 Conclusions

5.4.1 In-planar MSCs (Paper I)

This work has successfully demonstrated a simple, eco-friendly, and efficient path for the fabrication of LIG electrodes using a renewable substrate as cork. The LIG structure was induced and controlled by a direct laser writing technique, a one-step, maskless, scalable and cost-effective process. A systematic characterization of the LIG induced on untreated agglomerated cork was investigated. Therefore, using a fiber laser on cork substrate with tuned conditions of 5.5 W, 17.8 mm s^{-1} and a laser distance of 1.52 mm below the focal point, resulted in the best LIG characteristics in terms of morphology, structure, conductivity, and quality. Additionally, for a MSC proof-of-concept, a pre-treatment with wax-based ink on cork led to a controlled deposition of electrolyte on the substrate, without the need for mechanical masks and complex processes. Thus, waxed-cork LIG electrodes were produced using the optimized conditions already established with untreated cork substrate, and showed great characteristics for MSC fabrication with an excellent sheet resistance of approximately 7.5 ohm sq^{-1}. The device was compared with other reports and showed an areal capacitance of 1.34 mF cm^{-2} at 5 mV s^{-1} and 1.43 mF cm^{-2} at 1 mA cm^{-2}. Furthermore, the w-cLIG MSC exhibited an energy density of 0.13 μWh cm^{-2} at a current density of 0.1 mA cm^{-2}, with the power density reaching 80 μW cm^{-2}, demonstrating a favorable balance between energy and power performance. Finally, the electrochemical performance of the w-cLIG electrodes is shown to render a great performance to fulfill the requirements for flexible energy storage devices to multiple other applications, which may hold great interest in future improvements. It was proved that it is possible to join sustainable materials and low-cost techniques for LIG electrodes production, representing a mandatory step for a clean and green future in self-sustainable electronics.

5.4.2 Sandwich MSCs (Paper II)

In summary, micro-supercapacitors were fabricated using green LIG electrodes were successfully fabricated on abundant, renewable, and non-toxic substrates, such as paper, lignin-enriched paper, and cork. The laser parameters were systematically optimized for each

substrate, and a flame-retardant was incorporated to ensure efficient electrode production while preventing combustion and substrate ablation. Cork exhibited the lowest sheet resistance (~10.6 ohm sq^{-1}), followed by lignin-enriched paper (~45.5 ohm sq^{-1}) and paper (~55.4 ohm sq^{-1}). This can be attributed to inherent material characteristics such as thermal resistance and lignin content.

The sustainable and stackable sandwich micro-supercapacitors demonstrated capacitance values of 7-10 mF cm^{-2}, which is consistent with prior research. At lower power densities (0.01 mA cm^{-2}), the sandwiched-type SCs exhibited higher energy densities 0.73 μWh cm^{-2}, 0.85 μWh cm^{-2}, and 0.77 μWh cm^{-2} for BP-LIG, BLEP-LIG, and BC-LIG MSCs, respectively, outperforming the planar configuration reported previously. This improvement highlights the effectiveness of the sandwich architecture in enhancing energy storage capabilities at low power densities.

The integration of these green LIG-based energy storage devices in various configurations offers potential for multifunctional platforms in renewable energy and off-grid technology. The study found out that cork is the preferred substrate material due to its natural resilience and durability, making it well-suited for prolonged operational periods in demanding conditions. Practical demonstrations, such as powering an LED and a humidity/temperature sensor with a series of three cork-based MSC units, demonstrate the feasibility of this approach.

This methodology offers simplified and cost-effective means to achieve comparable or superior performance in electronic devices. It has the potential to further improve in laser graphitization efficiency, electrode geometries, and electrochemical properties, contributing to a more sustainable and technologically advanced future.

6

EXPLORING FURTHER SUSTAINABLE APPLICATIONS THROUGH GREEN LIG-BASED SOLUTIONS

This chapter examines the development of promising applications for green LIG, with a particular emphasis on the adaptation of piezoresistive sensors for energy harvesting. Each component is optimized independently, and their integration is demonstrated to validate the performance of a self-sustaining system. The objective of this chapter is to demonstrate the efficacy and dependability of the discrete devices developed in this thesis, thereby substantiating their viability for practical applications.

Results shown herein were reproduced from:

- **Paper III (Under preparation): Silvestre, S. L.**, Morais, M., Silva, R. R. A., Martins, R., Fortunato, E., Pereira, L., Coelho, J. (2025) Piezoresistive Sensors via Laser-Induced Graphene on Cork for Energy Harvesting Systems

6.1 Introduction

LIG is a material with considerable potential for applications beyond those demonstrated in this thesis thus far. Indeed, the creation of a sustainable, flexible and modular platform is futile if only a single set of components can be manufactured. In this context, LIG demonstrates remarkable versatility. In addition to being a relatively low-cost, simple, and scalable process, LIG has opened a multitude of possibilities for a vast array of applications beyond micro supercapacitors, such as electrochemical sensors, water purification and desalination, catalysis and electrocatalysis, biomedical applications, electromagnetic interference (EMI) shielding, superhydrophobic and antibacterial coatings, actuators and soft robotics, photovoltaics and solar cells, among others[25,72,235]. This trend reflects the rapid advancements in electronics over recent years, which have resulted in an increased demand for devices that are not only high-performing but also sustainable and environmentally friendly[236]. In this context, LIG stand out as one of the most promising carbon-based materials. It should be noted, however, that the majority of LIG-based components utilized polyimide (PI or Kapton) as a substrate, which is not regarded as a sustainable option. In this work, cork—a natural, renewable, and biodegradable material and in - line with the MSC work — is used as the substrate for the development of both piezoresistive sensors and triboelectric nanogenerators. Piezoresistivity is the phenomenon where a material's electrical resistivity changes when subjected to mechanical strain[35]. This property has been extensively explored due to its broad applicability in cutting-edge sensing technologies.

Piezoresistive sensors have attracted significant attention in fields such as healthcare (e.g., monitoring heart rate, pulse, and plantar pressure), environmental monitoring (e.g., detecting temperature, sensing gases, and monitoring pressure and humidity levels), functional clothing, electronic skins, quality control monitoring, robotics (e.g., for tactile perception, gesture-driven manipulation, sound recognition, proximity detection, and spatial orientation), among others[115,237]. Their versatility makes them a key component in numerous IoT applications, offering innovative solutions for quality control, automation, and beyond.

LIG-based sensors have demonstrated exceptional sensitivity and reliability, due to their unique properties, including high surface area and excellent electrical conductivity. The porous, multi-layered structure of LIG plays a key role in boosting its piezoresistive efficiency, making it highly responsive to mechanical forces like stretching, bending, and compression. When subjected to strain, the structure of graphene deforms, inducing changes in its electrical resistance. These shifts are directly tied to the movement of charge carriers within the material. By quantifying the changes in resistance, LIG-based sensors can accurately detect and

quantify the level of strain applied, offering a precise and dependable way to monitor mechanical deformations[11,238].

The use of LIG on cork for piezoresistive sensing offers a unique blend of flexibility and sensitivity, enabling the sensor to effectively respond to mechanical deformations while preserving its structural integrity as already observed in previous reports[170].

Integrating these technologies into larger infrastructures, such as smart houses and smart cities applications, highlights their importance in addressing the growing demand for sustainable, low-power electronic systems.[4,239,240]

Since current piezoresistive sensors are still predominantly powered by external batteries, extensive research has been conducted on triboelectric nanogenerators (TENGs) as self-powered sensors and alternative power sources for electronic devices[241]

TENGs present a promising avenue for energy harvesting in everyday activities, such as walking, vehicle movement, or wind interactions with urban infrastructure, among others. Through the triboelectric effect, friction or contact between materials with differing electron affinities generates an electric charge. Therefore, by converting mechanical energy into usable power, TENGs offer an innovative solution for powering low-energy devices and can be integrated with piezoresistive sensors and micro-supercapacitors (MSCs), enabling both sensing and energy harvesting functions within a single system[124,242]. Although this system is relatively straightforward, it could represent a significant step toward realizing a simple, flexible self-powered LIG-based sensing platform developed on the same substrate. LIG-based TENGs enhanced performance can be attributed to the increased charge density on the dielectric surface, resulting from the lower barrier height for charge transfer and reduced interfacial contact impedance compared to traditional metal electrodes[124,243]. This makes LIG a highly efficient and sustainable choice for future sensor technology.

The integration of these technologies onto a flexible substrate, such as cork, paves the way for a multifunctional, lightweight platform that is both eco-friendly and capable of sustainable energy generation. Cork's natural flexibility, insulating properties, and durability make it an ideal substrate for these applications. LIG’s high electrical conductivity and surface area, combined with cork’s ability to withstand repeated mechanical deformations, create a compelling platform for developing next-generation, sustainable electronics[244]. Moreover, Cork’s compatibility with LIG enhances this effect, offering an efficient method for energy generation that aligns with global trends toward green technologies and circular economies[65,155].

A system like this is not only capable of monitoring mechanical deformations but can also harvest mechanical energy for powering small electronics, sensors, and potentially larger systems within smart cities.

This chapter covers the fabrication process of both piezoresistive and triboelectric devices. Detailed analysis of the electrical and mechanical performance of these systems is provided, highlighting the challenges and solutions encountered throughout the research. The potential for scaling these devices for broader applications is also discussed, with an emphasis on their eco-friendly nature and suitability for large-scale production. In conclusion, this chapter aims to demonstrate the potential of LIG-based devices on cork for advancing sustainable electronics beyond micro-supercapacitors. The work presented in this chapter not only provides insight into the technical aspects of these devices but also underscores the broader implications for integrating green electronics into future infrastructure, paving the way for smarter, more sustainable cities and portable electronics.

6.2 Materials and methods

6.2.1 Design and fabrication of electrodes for piezoresistive sensors and triboelectric nanogenerators

Device development begins with substrate preparation, followed by electrode fabrication, and then device fabrication/characterization as described below.

(i) LIG electrode synthesis via direct laser writing

The synthesis and patterning of LIG were carried out using the DLW technique as previously described in Chapter 4. Cork substrates were first treated with a boron-based flame-retardant chemical treatment, as described in section 3.2.2.2., to prepare them for LIG production.

The electrodes were fabricated on borax-cork substrates using a 50 W PLS6MW Fiber laser (1.06 μm Nd:YAG Multi-wavelength Laser Platform, Universal Laser Systems, Vienna, Austria), in ambient conditions. A 2.0” lens was used for precise focusing during laser scribing. Throughout the LIG production process, a frequency of 100 kHz and a resolution of 1000 PPIs were maintained. After optimizing the laser settings, the optimal fabrication conditions for borax-cork LIG electrodes were determined to be a laser power of 21% and a speed of 2% (equivalent to 10.5 W @ 0.04 m s^{-1}). Additionally, positioning the laser beam 2 mm below the focal point was identified as an optimal parameter for achieving high-quality LIG formation.

Recognizing that electrode geometry plays a crucial role in improving sensor performance, three distinct electrode designs - snake, honeycomb and square (all with an area of 0.6 cm^2) -

were tested to determine the optimal pattern for sensing capabilities. Among these, the square design was found to provide the best response to external stimuli and was therefore selected for further development.

To further expand the potential of these electrodes for energy harvesting applications, particularly as triboelectric nanogenerators (TENGs), an in-situ formation of LIG/ZnO composite was fabricated. This was achieved by irradiating cork substrates pre-treated with a ZnO precursor solution, forming ZnO nanostructures within the LIG during laser processing.

The LIG/ZnO electrodes were fabricated under the same optimized conditions as the standard LIG on borax-cork, using the square design.

(ii) Fabrication of commercial graphene ink electrodes via screen printing

For comparison, screen-printed square graphene electrodes (with an area of 0.6 cm^2) were fabricated on cork substrates for use as piezoresistive sensors. The electrodes were printed using a polyester screen mold with the following conditions: mesh model, 120–34; mesh count, 305 mesh/inch; aperture, 45 µm; thread diameter, 34 µm; opening, 30.5% and a fabric thickness of 52–57 µm. A 10 wt.% exfoliated graphene ink in water (Sigma-Aldrich, USA) was used. After printing, the ink was dried on a hot plate at 100 °C for 15 minutes in air. The surface of the substrate and printed layers were examined using scanning electron microscopy (SEM) with a Hitachi Regulus 8220 (Mito, Japan), equipped with an energy-dispersive X-ray spectroscopy (EDS) detector, to assess the homogeneity of the printed layer and its substrate coverage.

6.2.2 Preparation process of green LIG-based piezoresistive sensor and screen-printed graphene piezoresistive sensor

Piezoresistive Sensors and Screen-Printed Graphene Piezoresistive Sensors. The fabrication process of piezoresistive sensors based on LIG and screen-printed graphene ink electrodes is illustrated in Figure 50a and Figure 50b, respectively. To ensure the mechanical durability and long-term V_{oc} functionality of the electrodes, BC-LIG samples were encapsulated with Leukoplasti Fixomull medical-grade polyurethane tape, referred to as BC-LIG-Flix. These encapsulated sensors were compared with bare BC-LIG sensors, providing protection from environmental degradation while maintaining flexibility and mechanical stability. Additionally, encapsulating the sensors improves the electrical output of TENG, as the polyurethane tape acts as a dielectric material capable of accumulating electrical charges, thereby increasing the surface charge density and the electric potential. This will be discussed further in the following sections. Moreover, all the piezoresistive sensors produced demonstrated excellent robustness, withstanding bending and pressing without losing functionality.

6.2.3 Preparation process of green LIG-based TENG

The TENG device was assembled using a single-electrode configuration, as observed in Figure 50a. The LIG electrode (1x1 cm²) developed on a cork substrate was used as a single electrode of the TENG. The ZnO nanostructures within the LIG network, along with the thin polyurethane tape used to encapsulate the electrodes, serve as a dielectric material, acting as the tribo-negative layer when compared to the counterpart, i.e., wood (tribo-positive layer). In the initial state, before the contact of the tribo-pairs, there is no electric output due to the minimal electrical charge at the interfaces. When the wood counterpart comes into contact with the TENG, electrons are transferred to the polyurethane surface, which acquires a negative charge, while the wood surface gains a positive charge. As the applied force on the TENG is released, the tribo-pairs begin to separate, increasing the potential difference and driving a flow of electrons toward the ground through the resistive load. The current drops to zero once the force is fully released and reverses direction when compressive forces bring the tribo-layers back together, generating an alternating current in the output component.

6.2.4 Characterization methods

6.2.4.1 Electrical characterization of piezoresistive sensors

The electrical and mechanical properties of the piezoresistive sensors were preliminary measured by a Keysight Agilent 4155C parameter analyzer, with a constant applied voltage of 0.5 V. The devices were compressed using a custom-built flexible and stress machine controlled by an Arduino, which allowed control of the applied stress, bending deflection, and bending frequency (Figure 48).

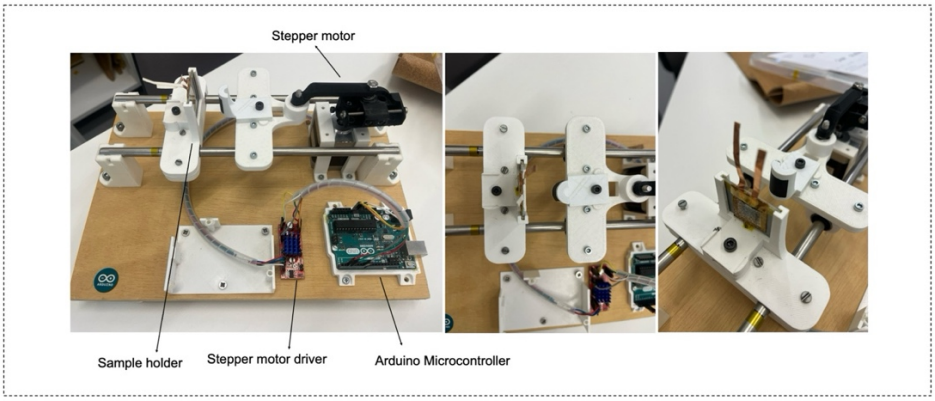

Figure 48. Photograph of the flexible and stress machine. The source Arduino code developed to run the machine is present in Appendix A.3.

Copper tape was used for electrical connections. The signal generated by external stimuli was monitored in real-time to measure the change in resistance of the device. This setup ensured

accurate and reliable measurements of the sensor's response to mechanical deformation, enabling detailed characterization of the device's behavior under various conditions.

For the keyboard application, a more practical approach was implemented. A microcontroller board was used to interrogate each sensor in a voltage divider configuration with a potentiometer. This configuration enabled the use of the microcontroller's internal analog-to-digital converted (ADC) to accurately capture changes in resistance in response to touch inputs. The keyboard itself was fabricated using the same process as the individual sensors but arranged in a 3x3 array grid, simulating a functional input device.

6.2.4.2 Electrical characterization of triboelectric nanogenerators

The open-circuit voltage and short-circuit current of the TENGs were measured by applying a controlled vertical mechanical stimulus using a custom-built pneumatic actuator load machine (Figure 49).

Since mechanical-to-electrical conversion is highly dependent on the type and intensity of mechanical stimuli, the electrical output varies accordingly. To effectively study and compare the performance of different devices, the pneumatic actuated load machine was used to precisely control the magnitude and frequency of the applied force, allowing for the establishment of a clear relationship between input intensity and output of the triboelectric devices.

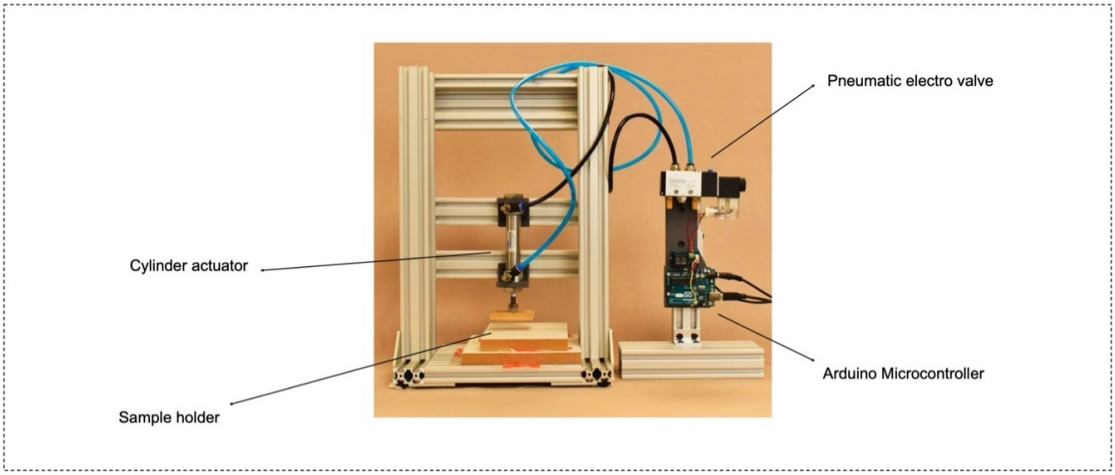

Figure 49. Photograph of the pneumatic actuator machine. The source Arduino code developed to run the machine is present in Appendix A.3.

The open-circuit voltage (V_{oc}) of LIG-based TENGs (1 cm²) was measured under mechanical loads ranging from 20 to 100 N, in 10 N increments at 2 Hz, using a pneumatic actuator. The pressure sensor's sensitivity to V_{oc} was determined from the slope of linear regression in both low (15–35 kPa) and medium-to-high (>35 kPa) pressure ranges applied on the TENG surface.

Copper tape was used for electrical connections, and data were recorded with a Tektronix TBS1000C oscilloscope at a sampling rate of 625 samples per second.

To evaluate the stability of LIG-based nanogenerators, V_{oc} was monitored over 10,000 cycles at 100 N and 2 Hz for devices with a dielectric layer. Charge transfer stability was assessed by comparing the short-circuit current (Isc) at 100 N and 2 Hz during the 1st and 100th cycles. The energy storage capability of the best-performing TENG was investigated by connecting the device to commercial capacitors with capacitances of 0.47 and 4.7 μF. The total stored charge was calculated by integrating the area under the capacitors' charging curve. Additionally, a COMSOL Multiphysics simulation was performed to verify the surface potential differences of the nanogenerators, with the simulation parameters provided in Table 5.

Table 5. Parameters utilized in COMSOL simulation.

Parameters	Value
Thickness of polyurethane (mm)	0.150
Relative permittivity of active layer	2.5
Relative permittivity of air	1
Thickness of electrode (LIG) (mm)	0.2
Width of polyurethane layer (mm)	100
Length of polyurethane layer (mm)	100
Gap distance between dielectric layers (mm)	0.4
Surface charge density of active layer (Cm^{-2})	$1x10^{-7}$

6.2.5 Data analysis

Data analysis was performed using OriginPro (2022b Academic, MA, USA). Results are reported as mean ± standard deviation from at least three independent experiments, and experimental designs were a completely randomized study. All figures were also plotted in OriginPro (2022b Academic, MA, USA).

6.3 Results and discussion

6.3.1 Design and fabrication of LIG-based sensors and nanogenerators

In order to further explore the potential applications of green LIG, two distinct devices were developed as part of this research project: a piezoresistive sensor and a triboelectric

nanogenerator. The initial objective was to develop high-performance electrodes for piezoresistive sensors. However, given the overarching goal of this thesis to enhance the versatility of LIG for self-sustaining systems, and with energy storage devices already established, it became evident that these electrodes could be extended for use in a triboelectric application with a view to energy harvesting. As such, for the piezoresistive sensors, it was crucial to produce electrodes with high electrical conductivity to efficiently transmit electrical signals with minimal resistance losses. This was essential for the accurate detection of resistance changes in response to mechanical deformation[170,245]. In the context of a triboelectric nanogenerator, the device was designed to maximize charge collection and transfer, thereby optimizing the conversion of mechanical energy into electrical energy. Additionally, since these devices are designed to be flexible, it is essential for the electrodes to withstand mechanical stresses such as compression and bending without degradation[121,123]. To meet these requirements, two distinct approaches were employed in the fabrication of the electrodes:

(i) Direct laser writing technique:

As described in previous chapters, this technique was used to produce green LIG electrodes directly onto borax-cork substrates. The DLW method offers precise patterning capabilities, enabling the production of conductive LIG structures with inherent flexibility and mechanical robustness. Furthermore, this technique was used to produce an in-situ LIG/ZnO composite, as shown in Figure 50a. By incorporating a ZnO precursor solution into the cork prior laser irradiation (Figure S4d), it was possible to convert the substrate itself along with the ZnO precursor solution, and by using a single-step approach it was possible to form ZnO nanostructures within the LIG matrix (Figure S4e). Following the demonstration of LIG's excellent and tunable conductive properties enabled by LIG synthesis, a flexible, stretchable polyurethane tape was used as an encapsulation layer to enhance durability and flexibility.

(i) **Screen-printing technique:**

In this approach, a commercially available graphene ink was used to screen-print electrodes onto cork substrates (Figure 50b). Screen printing is a well-established, scalable, and cost-effective technique suitable for mass production and offers the advantage of simplicity in fabrication. The inclusion of the screen-printing method alongside DLW was intended to enable a direct comparison between the performance of LIG-based electrodes and screen-printed graphene electrodes. Both fabrication methods are recognized for being eco-friendly and cost-effective, aligning with sustainable manufacturing practices and reducing environmental impact.

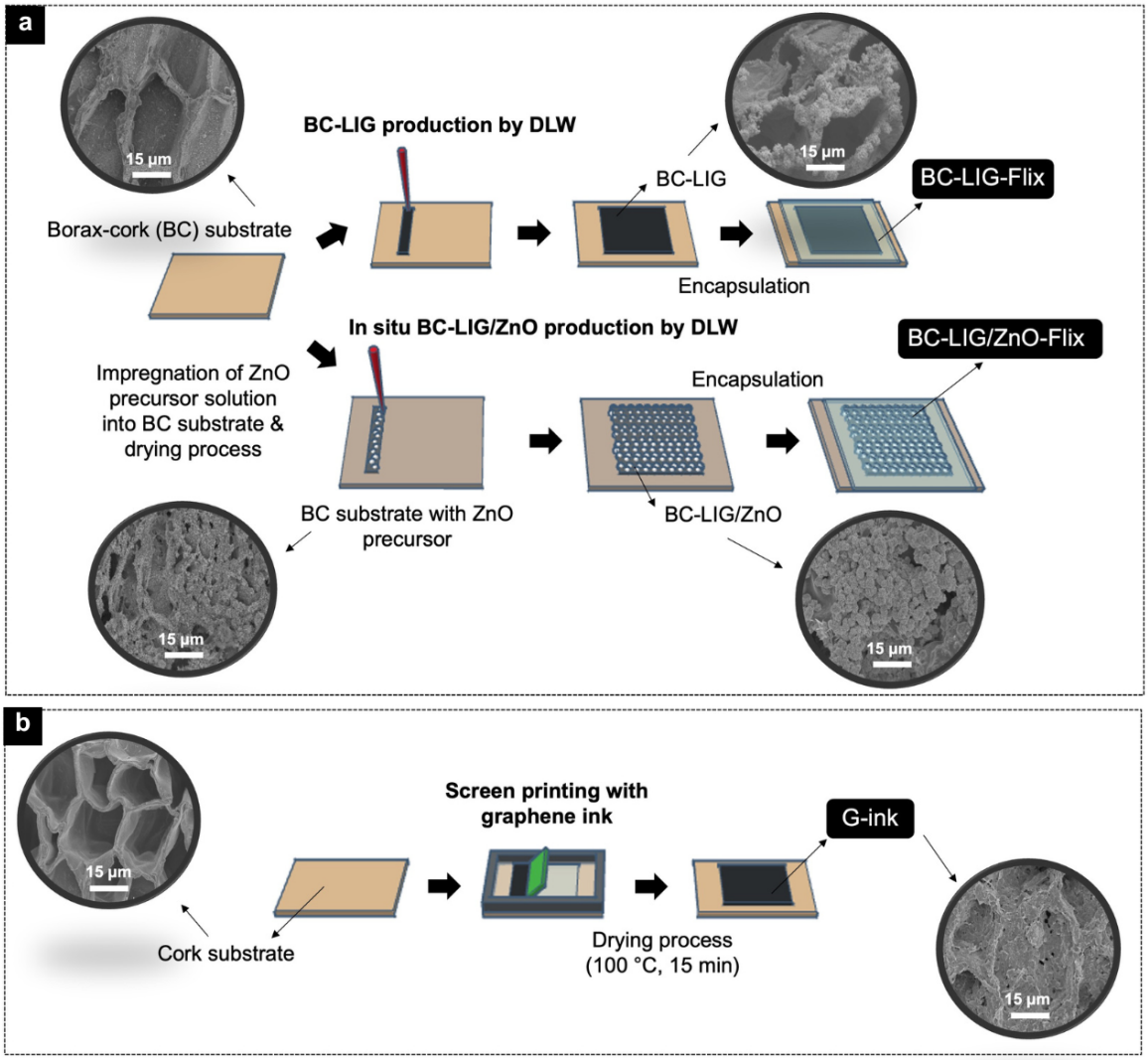

Figure 50. Schematic diagram of electrode preparation via (a) direct laser writing of LIG from borax-cork substrate and in-situ formation of the LIG/ZnO from the same substrate, and (b) screen printing of commercial graphene ink onto a cork substrate.

6.3.2 Performance evaluation of electrode designs

The sensing mechanism of a piezoresistive sensor relies on the material's piezoresistive effect, which is defined as the change in resistance relative to applied pressure or bending — an essential factor in evaluating sensor performance[245]. Given that sensor design plays a crucial role in determining how mechanical stress is distributed and converted into changes in electrical resistance, three LIG-based piezoresistive sensor geometries were explored: (A) snake, (B) honeycomb, and (C) square patterns, as illustrated in Figure 51a.

The piezoresistive response of these designs was assessed through three-point pressure and bending tests, with the setups and working principles illustrated in Figure 51b and Figure 51c, respectively. During the measurements, the sensors were subjected to periodic cycles of

loading and unloading, including both compression (Figure 51b) and bending tests (Figure 51c) while their resistance was continuously monitored. A custom-built flexible and stress machine (Figure 48) was used to simulate a finger touch, allowing for a qualitative assessment of each design's response to small mechanical deformations. The goal was to preliminarily identify the design that exhibited the greatest resistance variation in response to external stimuli.

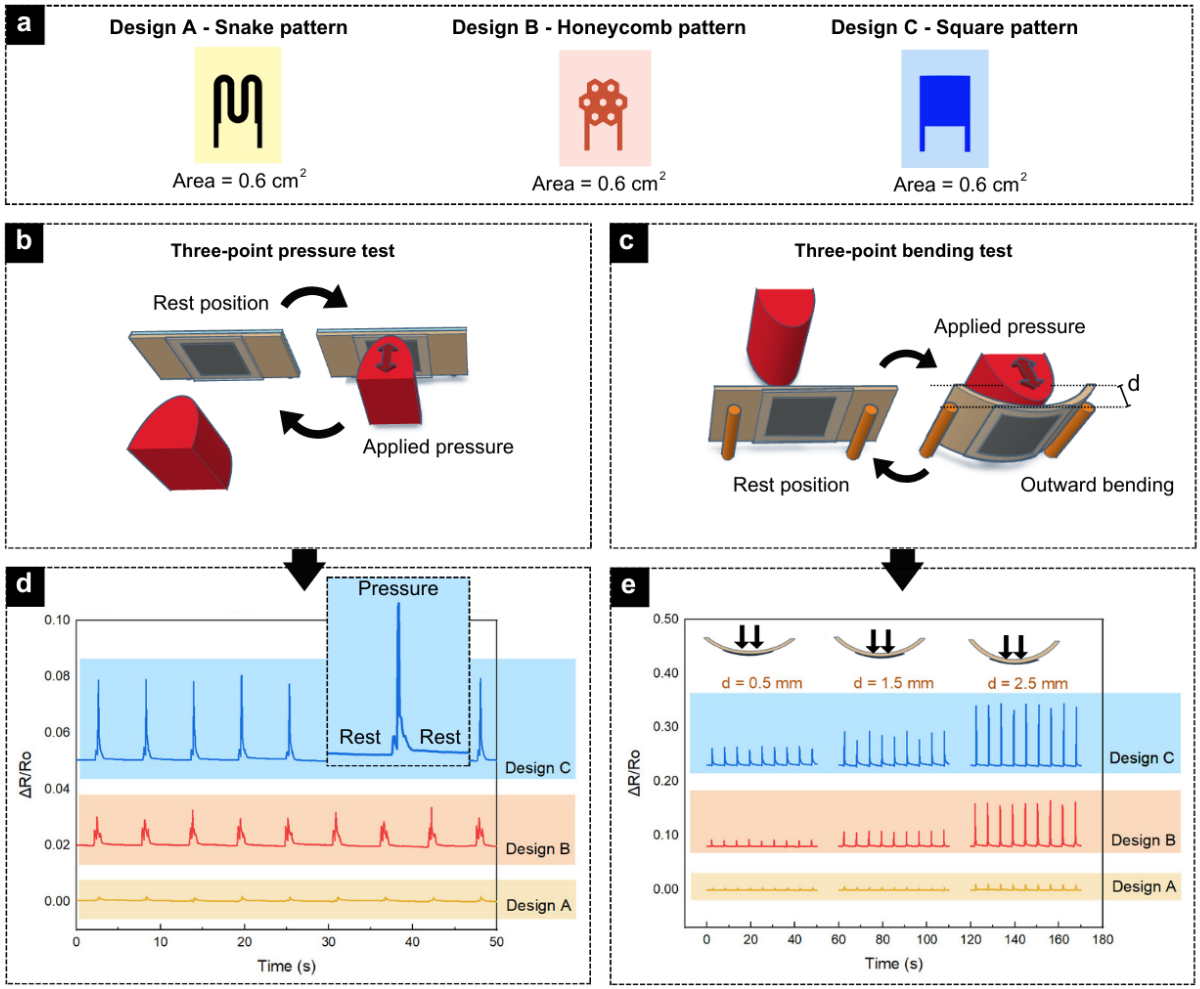

Figure 51. (a) Three distinct geometries tested for piezoresistive sensing, each with an area of 0.6 cm^2. (b) Schematic illustration of the pressure testing mechanism, and (c) bending test setup applied to the sensors. (d) Real-time monitoring of soft touch pressure responses for different BC-LIG-Flix electrode designs. (e) Real-time monitoring of bending deflections responses for different BC-LIG-Flix electrode designs.

All sensors showed an increase in relative resistances ($\Delta R/R = (R-Ro)/R$) under applied pressure, with a more pronounced response observed at higher bending deflections. Additionally, the sensor's response over time aligns with previous reports on cork-LIG-based sensors, showing a non-linear hysteretic behavior[170]. This behavior is not intrinsic to the sensor

itself but is largely influenced by the mechanical properties of the cork substrate. Cork's unique structure, characterized by its elasticity and near-zero Poisson's ratio, contributes to this non-linear response, allowing for high flexibility and durability but also leading to some hysteresis during mechanical loading and unloading[35,170]. Comparing the sensor's geometry, the square design demonstrated the highest relative resistance variation to applied pressure. This increased sensitivity can be attributed to several factors. First, the square design likely distributes mechanical stress more evenly across the sensor's surface, enhancing the piezoresistive effect and resulting in a more substantial change in resistance. Moreover, its larger contact area ensures that more material is directly impacted by the applied stress, which in turn contributes to a greater overall resistance change under pressure. In contrast, the honeycomb and snake design do not distribute strain as uniformly due to their geometry, which can lead to lower overall sensitivity. While these designs are preferred for LIG-based flexible applications, they absorb strain without inducing as large a change in resistance. For this reason, the square design was chosen for the fabrication of the other developed devices.

6.3.2.1 Comparing LIG-based piezoresistive sensor with a commercial graphene ink screen-printed piezoresistive sensor

The performance of the LIG-based piezoresistive sensors was compared to that of a commercially available screen-printed piezoresistive sensor using graphene ink. As observed in Figure 52, the LIG-based sensor demonstrated superior electrical performance over the screen-printed G-ink sensor. When comparing the two devices, the suggestion is that porous structure of LIG provides a greater surface area compared to G-ink electrodes, resulting in a stronger response to mechanical deformations such as pressure and bending.

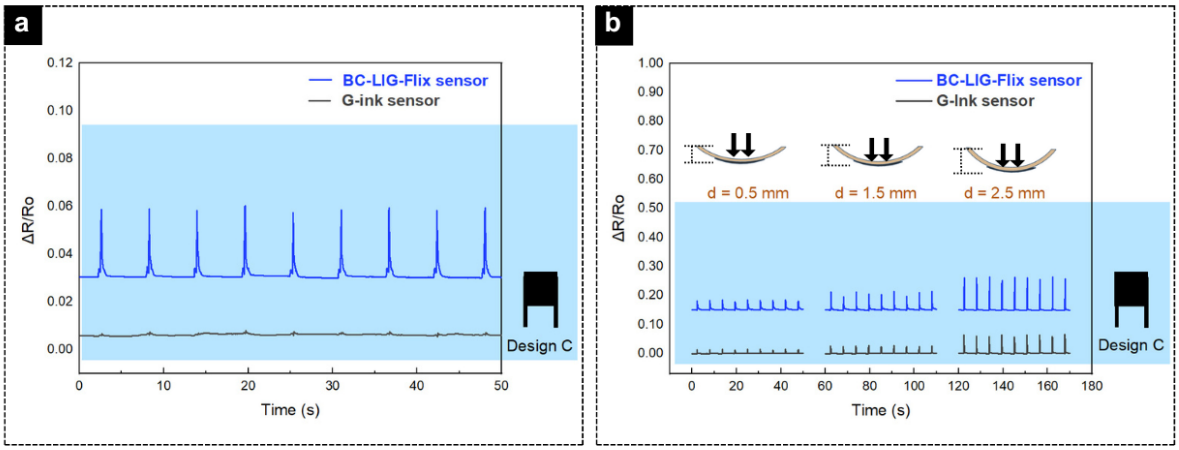

Figure 52. Comparison of BC-LIG-Flix sensor versus screen-printed G-ink sensor during (a) real-time monitoring of pressure responses and (b) real-time monitoring of bending deflection responses.

This is particularly important in applications requiring high precision, where detecting subtle changes in external stimuli is critical. In contrast, the screen-printed G-ink sensors, while functional, typically feature a 2D structure with less surface area, limiting their overall sensitivity. Moreover, the LIG fabrication process allows for more flexible and customizable sensor designs, enabling the creation of intricate patterns that optimize strain distribution and conductivity. On the other hand, the screen-printing process is more constrained by the limitations of the ink and cork substrate, which may not provide the same level of performance under varying mechanical conditions. Overall, the LIG-based piezoresistive sensor outperformed the screen-printed graphene ink sensor by showing enhanced electrical response to applied pressure and bending, greater mechanical robustness, and a simpler, maskless fabrication process.

As shown in Figure 53, the BC-LIG-Flix piezoresistive sensors demonstrated a clear distinction in relative resistance between soft, medium, and hard touches for faster tapping (Figure 53a) and slower tapping (Figure 53c).

The increase in resistance with increased touch intensity suggests that the sensor is highly sensitive to changes in pressure, making it suitable for applications requiring fine pressure detection. In Figure 53b the variation of resistance with changing touch frequency shows that the sensor maintains stable performance over time and suggests that the sensor can reliably detect both slow and rapid mechanical stimuli, a key feature for applications in dynamic environments.

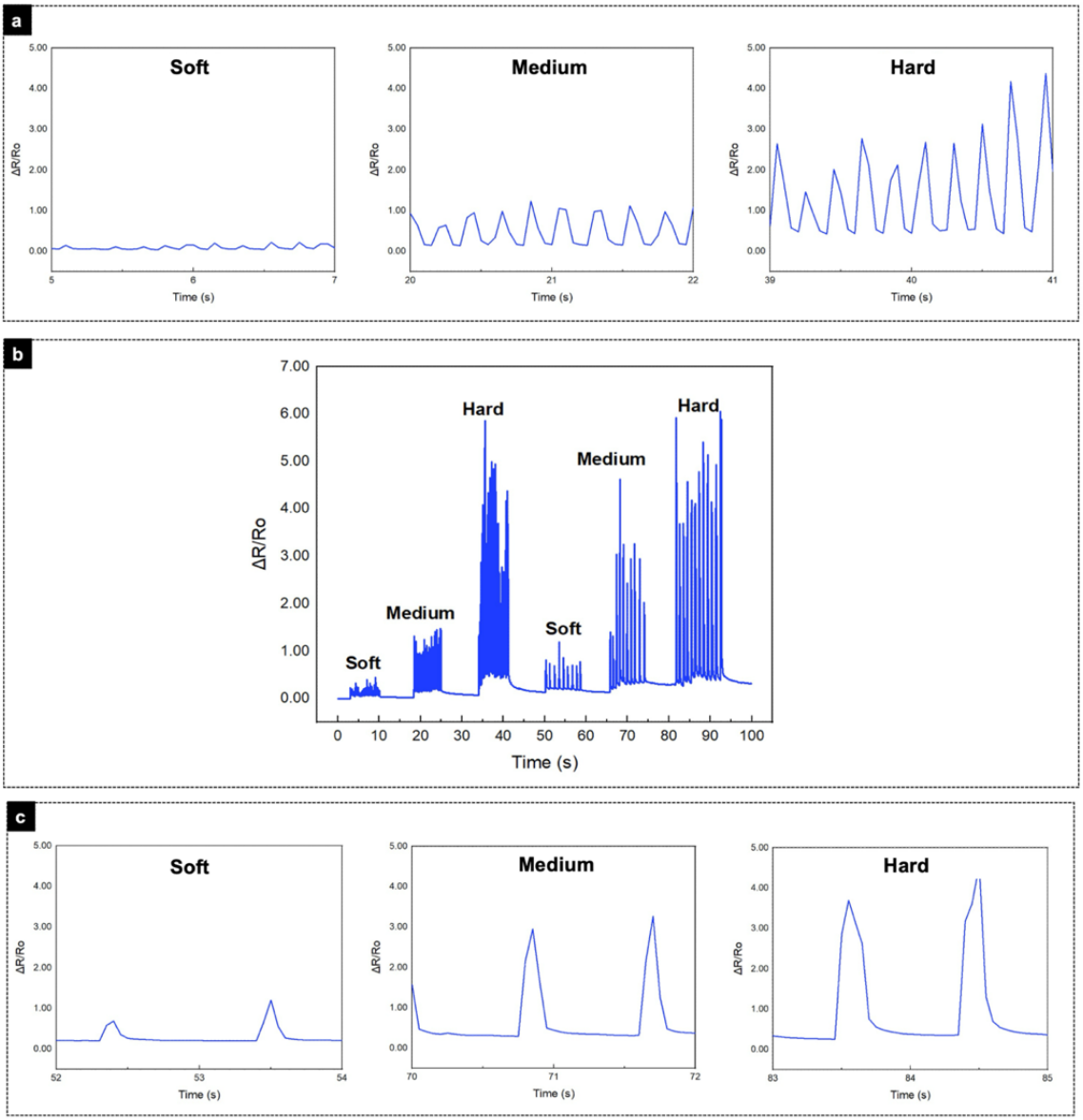

Figure 53. (a) Real-time monitoring of BC-LIG-Flix sensor response for faster tapping under different pressures. (b) Variation of resistance over time showcasing changes in touch pressure and frequency. (c) Real-time monitoring of BC-LIG-Flix sensor response for slower tapping under different pressures.

6.3.2.2 Practical application

The integration of piezoresistive sensors into grid matrix configurations demonstrates significant potential for various smart applications. In this study, to showcase the practical use of LIG-based piezoresistive sensors, an eco-keyboard was fabricated on a cork sheet in the form of a 3x3 sensor array.

Each key press applies simultaneous pressure and bending to the sensor through outerward motion in the empty space of the wooden separator, resulting in measurable resistance changes. These resistances changes are detected and processed by an Arduino

microcontroller. In Figure 54c is shown the real-time resistance variation of the LIG-based flexible sensors when different keys are pressed. The rising edge of each pulse corresponds to the touch of a specific key.

This practical demonstration confirmed that the assembled piezoresistive sensors effectively detected and responded to external stimuli, validating their functionality for smart device applications.

The versatility of these sensors for real-world applications highlights their potential integration into low-cost, flexible, and scalable electronics. The 3x3 grid, used in this case for a keyboard interface, illustrates how these sensors can be seamlessly integrated into interactive, touch-sensitive systems. This expands their application potential beyond wearable electronics to human-machine interfaces. Furthermore, the flexibility and scalability of these sensors make them ideal for use in smart home technologies, large interactive surfaces, and broader smart interface applications.

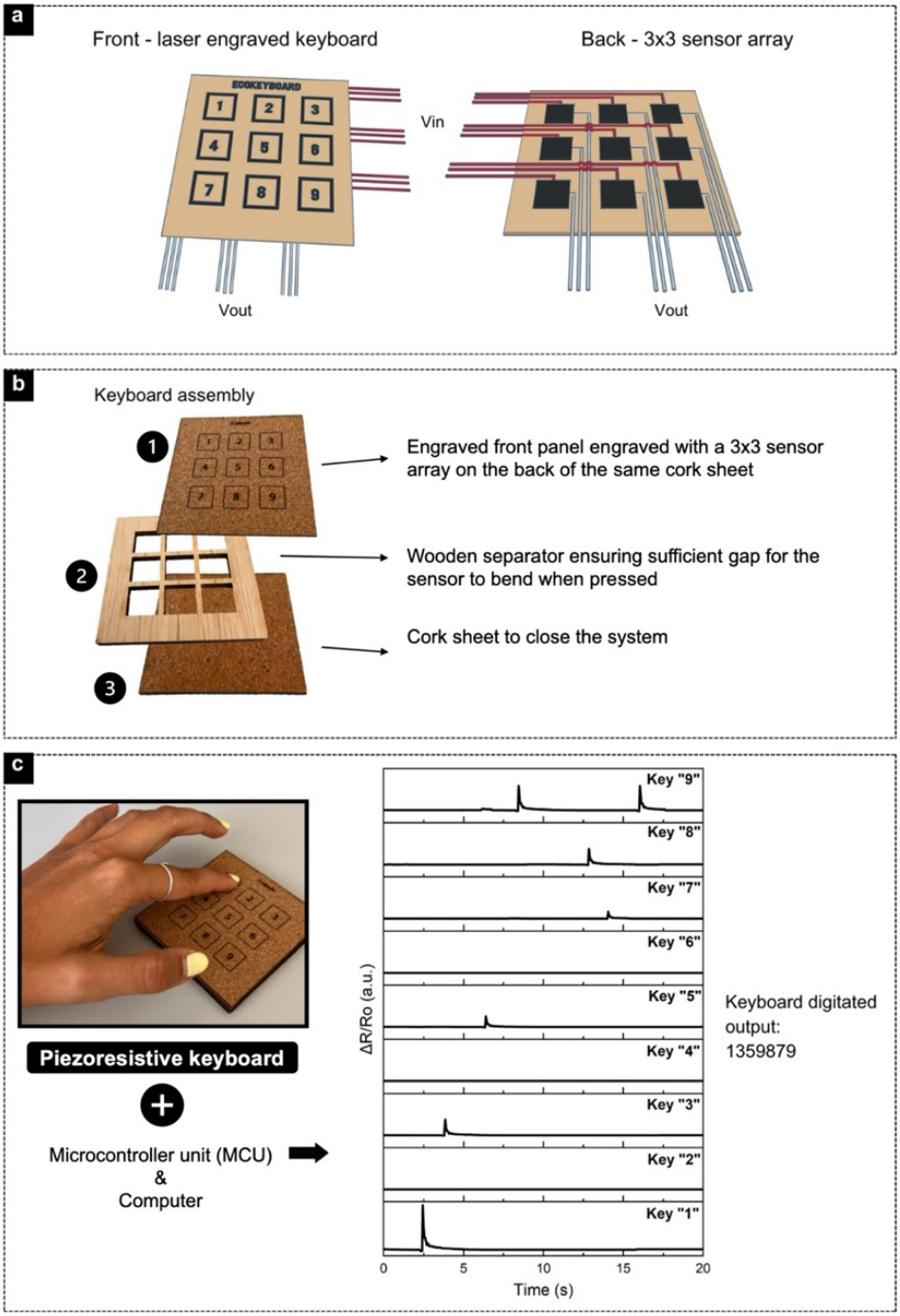

Figure 54. (a) Schematic of the eco-keyboard made from BC-LIG-Flix, showing the front of the cork sheet and the back panel with an engraved LIG 3x3 sensor array. (b) Schematic of the keyboard assembly. (c) Practical demonstration of the piezoresistive keyboard with corresponding signal output.

6.3.3 Enhanced LIG functionality with ZnO nanostructures

While the LIG-based piezoresistive sensors previously described can detect pressure and bending, this part of the work introduces ZnO nanostructures into the 3D porous LIG to enhance their mechanical response against pressure loading (Figure 55a) and bending (Figure

55b). The introduction of ZnO provides a dielectric material capable that can accumulate electrical charges, which boosts surface charge density and increases the electrical potential for LIG-based TENGs application.

When compared to the BC-LIG-Flix sensor, the electrodes with incorporated ZnO shows a larger increase in relative resistances, as observed in Figure 55.

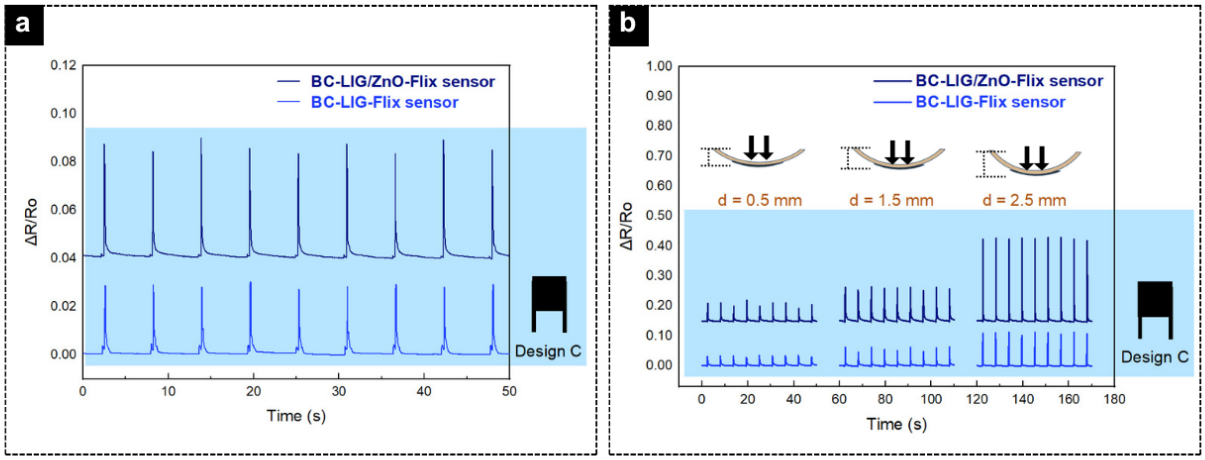

Figure 55. Comparison of BC-LIG-Flix versus BC-LIG/ZnO-Flix sensors during (a) real-time monitoring of pressure responses and (b) real-time monitoring of bending deflection responses.

The incorporation of ZnO is particularly interesting for triboelectric nanogenerators due to its unique properties. ZnO's high piezoelectric coefficient makes it ideal for improving electrical properties of sensors by increasing their sensitivity to mechanical deformation. Additionally, ZnO nanostructures offer a high surface area and exceptional charge-trapping capabilities, making them ideal for triboelectric nanogenerators. Their ability to generate surface charges through friction or contact significantly improves energy harvesting efficiency. The combination of LIG's conductivity and flexibility with ZnO's piezoelectric and triboelectric properties results in electrodes that are well-suited for flexible, high-performance sensing and energy harvesting devices.

6.3.4 Performance evaluation of a green LIG-based TENG

For this application, the printed sample was not tested due to their low response to external stimuli. Only the LIG-based devices were retained for the energy harvesting application.

The operational principle of LIG-based TENGs is illustrated in Figure 56a. Initially, both surfaces carry minimal electrical charges, leading to an almost negligible electric potential difference. Upon contact with the active surface of the TENG, the counter material (wood) induces charge separation due to differences in electronic affinity and Coulomb forces. For

instance, polyurethane attracts electrons from the wood, acquiring a negative charge, while the wood becomes positively charged (Figure 56a,i). As the separation process begins (Figure 56a,ii), an electrical potential imbalance develops due to previous charge transfer between the surfaces, driving electron flow from the ground through an external circuit until equilibrium is reached (Figure 56a,iii). Subsequently, mechanical triggering causes the surfaces to approach each other again, leading to electron movement in the opposite direction to restore electrical potential equilibrium (Figure 56a,iv), producing an alternating current[246,247].

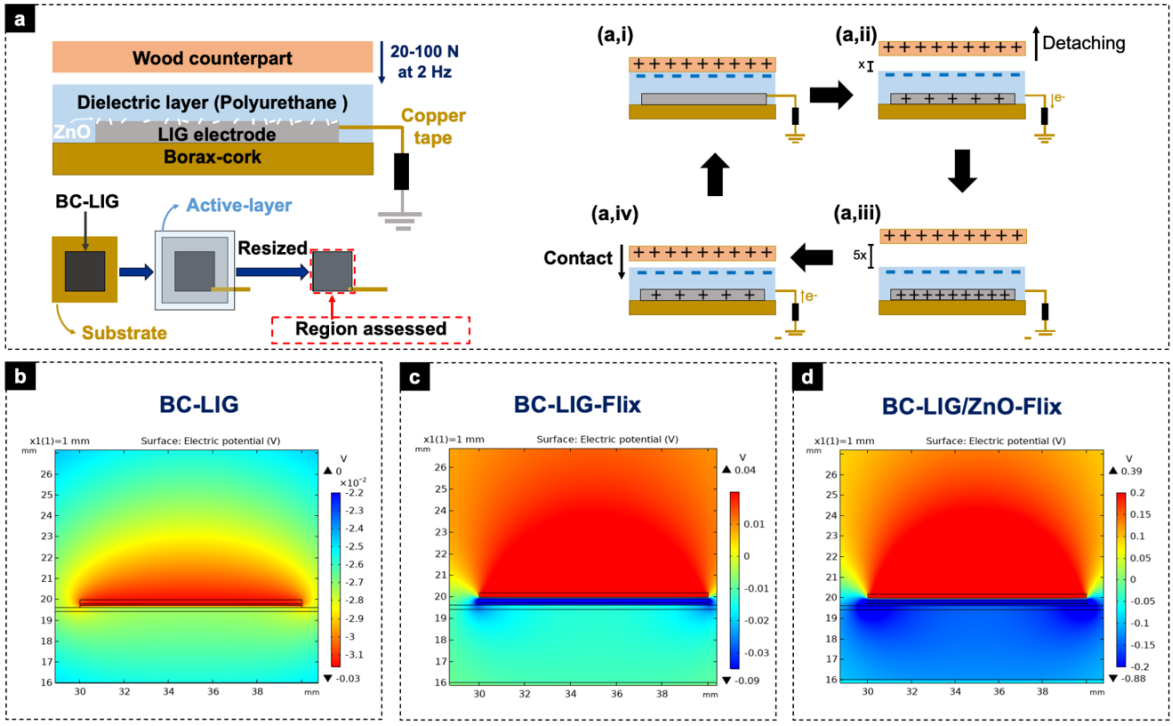

Figure 56. Illustration of the TENG working principle with a LIG electrode derived from cork in single electrode mode: (a,i) contact, (a,ii) detaching, (a,iii) detached, and (a,iv) pressing. Electric potential distribution from COMSOL simulations between the polyurethane layer with a BC-LIG (b), BC-LIG-Flix (c), and BC-LIG/ZnO-Flix (d) as the active layer.

A COMSOL Multiphysics simulation was performed to validate the surface potential difference between the nanogenerator devices (Figure 56b-d). The LIG used as the active layer exhibited the lowest electric potential, followed by BC-LIG-Flix, and BC-LIG/ZnO-Flix. Two main factors contribute to the higher electric potential difference observed in the BC-LIG/ZnO-Flix nanogenerators: (i) dielectric and piezoelectric contribution and (ii) Schottky junctions. In the first case, ZnO exhibits a high dielectric constant, enhancing charge buildup capacity, while its piezoelectric effect significantly increases the electric potential difference, especially under mechanical stress. The second factor involves the formation of a depletion layer, where electron depletion develops a region with fewer free carriers, and the Schottky barrier prevents

electron flow until the electrons gain sufficient energy to overcome it, thereby further increasing the potential difference.

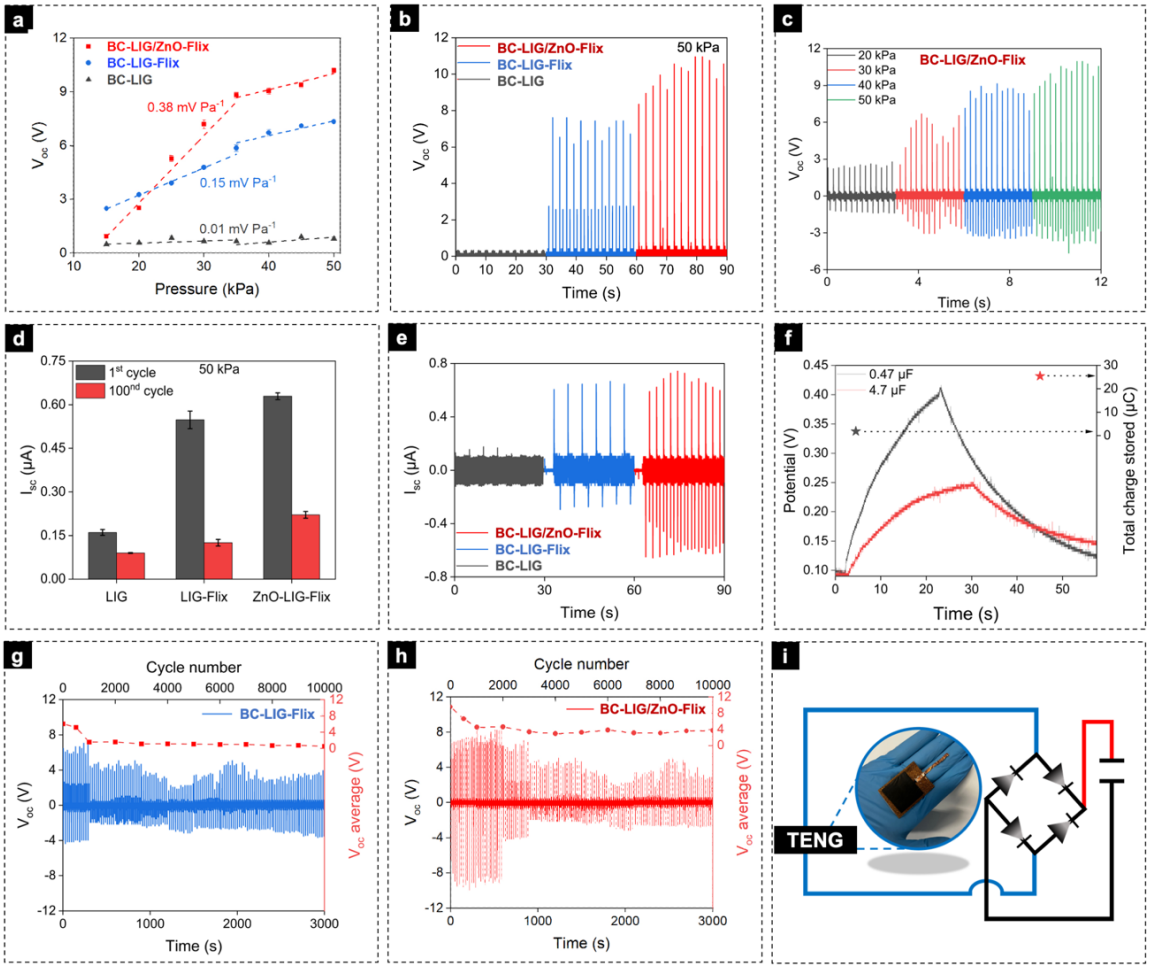

Figure 57. (a) Average V_{oc} of BC-LIG, BC-LIG-Flix, and BC-LIG/ZnO-Flix nanogenerators across 15–50 kPa, with corresponding pressure sensor sensitivities. (b) Open-circuit voltage (V_{oc}) peaks of BC-LIG, BC-LIG-Flix, and BC-LIG/ZnO-Flix nanogenerators under a 50 kPa drive. (c) V_{oc} peaks of the BC-LIG/ZnO-Flix nanogenerator under 20, 30, 40, and 50 kPa trigger. (d) Average short-circuit current (I_{sc}) of BC-LIG, BC-LIG-Flix, and BC-LIG/ZnO-Flix nanogenerators at the 1st and 100th cycles under 50 kPa, (e) and their corresponding peak values. (f) Charging of 0.47 and 4.7 μF capacitors by the BC-LIG/ZnO-Flix nanogenerators, along with the total charge stored. (g) Long-lasting stability of the for BC-LIG-Flix (h) and BC-LIG/ZnO-Flix nanogenerators over 10,000 cycles at 50 kPa. (i) Schematic illustration of the LIG-based TENG integrated with a rectifier circuit for capacitor charging.

To identify the optimal performance of TENGs as pressure sensors, sensitivity was evaluated in the 15-50 kPa range, with a focus on the low-pressure range (15-35 kPa) (Figure 57a). Although BC-LIG-Flix generated a higher initial V_{oc}, incorporating ZnO resulted in a more consistent stepwise V_{oc} increase, achieving the highest sensitivity (0.38 mV Pa^{-1}). This is likely due to ZnO's piezoelectric properties, which exhibit a positive correlation between mechanical tension and V_{oc}[248,249].

Table 6 presents the pressure sensor parameters, e.g., sensitivity and R^2, for each TENG. The higher initial V_{oc} of BC-LIG-Flix (2.5 V) compared to BC-LIG/ZnO-Flix (0.9 V) nanogenerators may be attributed to the greater contact area between the electrode and dielectric material (polyurethane), as ZnO growth reduces this interface area, compromising the electrical potential difference at low pressure. Wang et al.[246] demonstrated that an increased effective contact area between the electrode and dielectric material is crucial for achieving high TENG efficiency.

As pressure increases, the piezoelectric effect of BC-LIG/ZnO-Flix becomes more significant, contributing more to the V_{oc} increase than the triboelectric effect alone, as seen in BC-LIG-Flix nanogenerator. While the low-pressure sensitivity of LIG-based TENGs (0.01 mV Pa^{-1}) is likely due to different charge transfer mechanisms, where surface charge accumulation, as observed in dielectric materials, is reduced, limiting the electrical potential difference. At 50 kPa, V_{oc} increases sequentially from BC-LIG to BC-LIG-Flix and BC-LIG-/ZnO-Flix nanogenerators, reaching 0.33, 7.61, and 10.95 V, respectively (Figure 57b). The reproducibility of BC-LIG/ZnO-Flix V_{oc} peaks as pressure increases from 20 to 50 kPa at 2 Hz is also confirmed in Figure 57c.

Table 6. Pressure sensor parameters of triboelectric nanogenerators (TENGs) devices.

Device	Pressure region	Sensitivity (mV Pa^{-1})	R^2_{adj}
BC-LIG/ZnO-Flix	Low pressure (15-35 kPa)	0.376	0.981
BC-LIG-Flix		0.152	0.990
BC-LIG		0.011	0.620
BC-LIG/ZnO-Flix	Medium-to-high pressure (≥35 kPa)	0.089	0.909
BC-LIG-Flix		0.082	0.869
BC-LIG		0.028	0.303

Additionally, I_{sc} further corroborates the increasing electrical output efficiency in order of BC-LIG, BC-LIG-Flix, and BC-LIG/ZnO-Flix, resulting in 0.16, 0.55, and 0.63 μA, respectively (Figure 57d). Moreover, the devices appear to exhibit mechanical sensitivity for long-term applications, as indicated by the significant decrease in I_{sc} after 100 cycles. Despite this I_{sc} instability, the final I_{sc} stabilizes near the value observed for LIG nanogenerators (0.09 μA), which can be related to the electrode integrity. While the reproducibility of I_{sc} peaks for each nanogenerator is also confirmed in Figure 57e.

To expand the application of optimized TENGs, e.g., powering small electronics, the efficiency in charging 0.47 and 4.7 μF capacitors was demonstrated, reaching *V*peak in 23 and 30 seconds, respectively (Figure 57f). A schematic illustration of the LIG-based TENG integrated with a rectifier circuit for capacitor charging is demonstrated in Figure 57i. The total charge stored after charging these capacitors by mechanical triggering was 1.8 and 25.4 μC, confirming the potential of this technology for green energy harvesting. Moreover, to further evaluate the best-developed TENG, we assessed its mechanical stability in terms of V_{oc} over 10,000 cycles. The BC-LIG-Flix TENG showed higher V_{oc} instability (Figure 57g-h), with a 92% reduction in V_{oc}, compared to a 60% reduction in the BC-LIG/ZnO-Flix TENG (Figure 57h). This difference suggests that the BC-LIG/ZnO-Flix system has contributed to increase the structural stability and electrode integrity, since BC-LIG-Flix typically degrade over long mechanical cycles, and/or ZnO provides the higher piezoelectric performance under high mechanical pressure.

Despite the improvement caused by the in-situ ZnO growth in the BC-LIG electrode, the developed self-powered pressure sensor still shows considerable structural instability for long-term applications, particularly when considering the accuracy of pressure measurements over extended use. However, given the sustainable materials used in fabrication, this self-powered pressure sensor is well-suited for single-use applications. Although it could be a more sustainable option, its manufacuring significantly reduce carbon footprint and greenhouse gas emissions. Additionally, the simple fabrication process and ease of scalable production further highlight the commercial viability of this sustainable self-powered pressure sensor.

6.3 Conclusions

In conclusion, this work presents a sustainable approach to the development of LIG-based piezoresistive sensors and triboelectric nanogenerators (TENGs) using renewable materials. The piezoresistive BC-LIG-Flix devices exhibited significant potential for various sensing applications, such as integration into keyboard grids. A key innovation in this research was the incorporation of a ZnO precursor solution onto the substrate prior to laser irradiation, which enabled a novel single-step, in-situ process to enhance the functionality of LIG. The addition of ZnO nanostructures led to a more stable and sensitive voltage output, attributed to the piezoelectric properties of ZnO. This development expanded the application of green LIG electrodes beyond traditional uses, demonstrating their viability for energy harvesting in triboelectric nanogenerators. While the structural instability of LIG due to its intrinsic porosity remains a challenge for long-term applications, the TENGs developed in this work are particularly well-suited for single-use scenarios, where sustainability and low environmental

impact are critical. This emphasizes the need for future research to address the long-term mechanical stability of LIG-based devices, which could lead to their integration into smart infrastructures and more durable, continuous-use applications. Despite these challenges, the simplicity of the fabrication process and the scalability of production make these sustainable devices promising candidates for industrial applications. Nevertheless, more optimization is required to unlock the true potential of these devices. For instance, it should be assessed the optimal mass loading of ZnO and phase that maximizes the sensors properties. Even if these devices were developed as a starting point for applications beyond energy storage, very promising results were already obtained. The BC-LIG/ZnO-Flix TENG developed in this study exhibited exceptional sensitivity, achieving 0.38 mV Pa^{-1} at low pressure levels (15 kPa-35 kPa), and 0.286 mV Pa^{-1} at medium-to-high pressure (≥35 kPa). Additionally, to expand the broader applicability of these optimized TENGs, their efficiency in powering small electronics was tested by charging 0.47 and 4.7 μF capacitors, reaching peak voltages in approximately 23 and 30 seconds, respectively. These sensors also demonstrated effective energy harvesting capabilities, supporting their potential for sustainable and scalable green energy solutions. This further showcases the potential of LIG-based TENGs as a versatile solution for low-power, portable electronics, especially in the context of smart cities and Internet of Things (IoT) devices.

Overall, the findings of this work underscore the promise of using sustainable, cost-effective materials for the future development of sensing and energy harvesting technologies. By advancing the understanding and functionality of LIG-based systems, this research paves the way for environmentally friendly solutions in next-generation electronics, contributing to a greener, more sustainable technological future.

7

CONCLUSIONS AND FUTURE PERSPECTIVES

This chapter presents the key conclusions drawn from this research and outlines future perspectives for further development in this area.

7.1 Conclusions

The recent developments in manufacturing processes have led to a shift in focus from the complex and costly conventional methods of graphene fabrication to more environmentally sustainable approaches. This dissertation aimed to reduce the environmental footprint of electrode fabrication and to provide support for the development of sustainable technology. In this context, LIG has emerged as a material of particular interest due to its graphitic properties and straightforward production method. Substantial efforts have been made to expand the scope of LIG production, especially in synthesizing green LIG to promote a greener manufacturing practice by converting bioderived materials into valuable resources. This thesis explored various bioderived materials, particularly lignocellulosic and cellulosic substrates, for the development of green electronics. Paper, lignin-enriched paper, and cork were selected as precursors due for their environmental friendliness and capacity to produce high-quality LIG. Throughout this work, it was noted that selecting the appropriate precursor for specific applications is challenging due to numerous factors. Raw materials often offer limited customization, making it difficult to achieve consistent and repeatable electrical properties in LIG production. In contrast, by-products can be engineered to achieve the desired form factor, enhancing LIG production, performance, and applicability. First, using a CO_2 commercial laser system, optimal conditions were established for producing high-quality LIG on these substrates under both inert and non-inert atmospheres. Moreover, LIG production was achieved using different wavelength radiation. Notably, a 1.06 μm wavelength fiber laser successfully

produced porous 3D LIG on agglomerated cork substrates for the first-time, achieving low sheet resistance (7.5-10 ohm sq^{-1}), making it suitable for various applications.

These materials demonstrated the ability to produce LIG with properties comparable to, and in some cases superior to, synthetic LIG from commercial polymeric substrates. Notably, higher lignin content in the precursor resulted in a better conversion process and enhanced LIG quality. Cork's high recyclability potential makes it strategically important, particularly for Portugal, the world's leading cork producer. Pre-treatment with fire retardant was necessary for paper substrates or when working in non-inert atmospheres, due to the low thermal stability of cellulose compounds at the high temperatures during laser irradiation.

Bioderived LIG's high electrical conductivity and eco-friendly production method make these materials interesting for future technological applications. LIG-based electrodes offer high reproducibility, low-cost, and flexible design, easily adapting to various geometries and architectures to meet the evolving needs of the technology. While these devices may not meet the stringent requirements of high-end electronics, they are ideal for fast patterning and devices fabrication. This thesis also marks a turning point on LIG fundamental studies. It is clear that for LIG production Raman and XPS are tools enough for the characterization of the obtained materials. However, as substrates and applications become more complex further characterization is necessary. For instance, besides the analysis of C1s spectra, other orbitals need to be studied, namely the O1s spectra. As fire retardants and other species are used to maximize the LIG capabilities and substrates more fundamental and chemical analysis is required in order to understand the roles of the said species on LIG performance. As such, for further works these considerations should be taken with extreme care.

At device level, given the current global energy scenario, developing more efficient energy storage devices is essential. Micro-supercapacitors, with their fast charge-discharge capabilities and long cycling life, are particularly appealing. Chapter 5 focused on producing micro-supercapacitors using different LIG electrodes materials, electrodes geometries, electrolytes, and configurations.

While the observed performance of these MSC provides valuable insights, it is crucial to consider material stability and electrode-electrolyte interaction under demanding conditions over extended cycles. Cork MSCs demonstrated robustness and longevity, making them more suitable for real-world energy storage applications despite slightly lower capacitance retention compared to other materials. The electrochemical properties of cork for MSCs are promising, showing increased capacitance and long-term resistance compared to paper substrates. These LIG-based devices offer versatility, with adjustable voltage output through stacked and sandwich MSCs configurations, suitable for various large-scale applications. This study

demonstrates the feasibility of creating high-quality energy storage devices based on biodegradable materials. Implementing these electrodes in energy storage devices highlights LIG's potential in innovative, green, and self-sustaining platforms.

Eco-friendly, self-powered pressure sensors were developed on Chapter 6 using the DLW technique, showing great potential for applications beyond energy storage. The integration of ZnO into the LIG network enhanced the sensors' sensitivity and mechanical stability, particularly under higher pressures. These sensors also demonstrated effective energy harvesting capabilities, supporting their potential for sustainable and scalable green energy solutions.

Overall, the strategies proposed present a promising approach for the future of green flexible electronics, off-grid applications, and smart houses.

7.2 Outlook and future perspectives for green LIG – based devices

Throughout this thesis, it has been shown the development of a set of LIG based devices. While the applications of these emerging green LIG technologies are currently limited to the academic level, mainly because they have not yet reached the maturity of other graphene technologies and do not meet the stringent standards required for high-end electronics, there is significant potential for future development. As we have already seen with MSCs, there is much room for improvement in terms of device performance and potential applications. In addition, as LIG technologies are based on sustainable, biodegradable or recyclable substrates, they may become a viable option for some green electronics applications. LIG as a processing technique is also regarded as a virtually "zero waste" generation method. As such, the life cycle assessment (LCA) of LIG products should indicate a small environmental impact of through every phase of their life. However, for LIG, or graphene production in general, there is needed more accurate data for a proper life cycle assessment. Cossuta et al[250], presented a comparative LCA of different graphene production routes: electrochemical exfoliation of graphite. chemical oxidation of graphite with chemical or thermal reduction and chemical vapor deposition (CVD). Life Cycle Assessment (LCA) models were developed for each production method with the objective of quantifying the impacts on a "cradle-to-gate" basis, including activities from raw material extraction and processing to graphene manufacture. The findings of this study indicate that the material route with the least environmental impact is chemical oxidation, followed by thermal reduction, at both laboratory and industrial scales. To the best of my knowledge, no such studies have been conducted for

LIG. However, given that there is no need for the extraction of raw materials, sustainable substrates can be employed, and virtually no waste is generated, the environmental impact of LIG should be minimal. At the end of the device's life cycle, it can be readily incinerated, or the LIG can be recovered for further utilization, as the substrates can be recycled or safely disposed of. Regarding the issues of biocompatibility and toxicity, LIG has not been identified as a substance that is harmful. Consequently, it can be safely employed in medical applications, and an inadvertent release into the environment does not present a hazard. Although bioderived materials offer several advantages, they also face challenges such as poor reproducibility and incomplete characterization in some studies. In contrast, synthetic precursors, with their easily tunable atomic structure and morphology, often provide better performance but at higher costs and with less sustainable processes. Additionally, many of the substrates found in the literature and used in this work are by-products or waste materials from other processes and therefore lack the optimisation found in commercial products. In this respect, artificial intelligence could be very useful in identifying suitable substrates and how to process and characterize LIG more quickly and in a standardized manner. For example, LIG characterisation and optimization currently involves investigating different combinations of power, speed and laser defocus for each new substrate. This can be a cumbersome and time-consuming process, where AI could help identify the best conditions for laser processing and device optimization. The existence of optimized devices based on LIG can open opportunities for other device designs, fabrication, and commercialization. New devices usually face difficulties in entering the market due to general mistrust and lack of product testing.

Notwithstanding these shortcomings, the utilization of LIG is encouraging due to the minimal expense of the requisite precursor materials and the advantages of upcycling materials within a circular economy. As a technology still in its infancy, the potential of LIG remains largely underexplored. Bioderived LIG has the potential to play a significant role in the future of green electronic devices, thanks to its biodegradability, which opens the door to applications in edible and transient electronics. Furthermore, its intrinsic flexibility and expeditious production render it an appealing option for a multitude of applications. While LIG-based devices will not entirely supplant conventional technologies, they will undoubtedly assume a prominent role in domains where cost and ease of manufacture outweigh the importance of high-quality performance. Overall, the incorporation of bioderived materials in electronic applications aligns well with sustainability objectives and presents promising avenues for future research.

REFERENCES

1. Santato C, Alarco P. The Global Challenge of Electronics: Managing the Present and Preparing the Future. *Adv Mater Technol*. 2022;7(2). doi:10.1002/admt.202101265
2. Wang C, Xia K, Wang H, Liang X, Yin Z, Zhang Y. Advanced Carbon for Flexible and Wearable Electronics. *Advanced Materials*. 2018;1801072:1-37. doi:10.1002/adma.201801072
3. Wang P, Hu M, Wang H, et al. The Evolution of Flexible Electronics: From Nature, Beyond Nature, and To Nature. *Advanced Science*. 2020;7(20). doi:10.1002/advs.202001116
4. Scandurra G, Arena A, Ciofi C. A Brief Review on Flexible Electronics for IoT: Solutions for Sustainability and New Perspectives for Designers. *Sensors*. 2023;23(11):5264. doi:10.3390/s23115264
5. Tiwari SK, Mishra RK, Ha SK, Huczko A. Evolution of Graphene Oxide and Graphene: From Imagination to Industrialization. *ChemNanoMat*. 2018;4(7):598-620. doi:10.1002/cnma.201800089
6. Kim H, Ahn JH. Graphene for flexible and wearable device applications. *Carbon N Y*. 2017;120:244-257. doi:10.1016/j.carbon.2017.05.041
7. Dhinakaran V, Lavanya M, Vigneswari K, Ravichandran M, Vijayakumar MD. Review on exploration of graphene in diverse applications and its future horizon. *Mater Today Proc*. 2020;27:824-828. doi:10.1016/j.matpr.2019.12.369
8. Urade AR, Lahiri I, Suresh KS. Graphene Properties, Synthesis and Applications: A Review. *JOM*. 2023;75(3):614-630. doi:10.1007/s11837-022-05505-8
9. Yip TM, Tong GB. Fabrication Routes of Graphene. In: *Subramaniam, R.T., Kasi, R., Bashir, S., Kumar, S.S.A. (Eds) Graphene. Engineering Materials*. Springer; 2023:53-90. doi:10.1007/978-981-99-1206-3_4
10. Huang L, Su J, Song Y, Ye R. Laser-Induced Graphene: En Route to Smart Sensing. *Nanomicro Lett*. 2020;12(1). doi:10.1007/s40820-020-00496-0

11. Movaghgharnezhad S, Kang P. Laser-induced graphene: synthesis advances, structural tailoring, enhanced properties, and sensing applications. Published online 2024. doi:10.1039/d3tc04677j
12. Dreyer DR, Park S, Bielawski CW, Ruoff RS. The chemistry of graphene oxide. *Chem Soc Rev*. 2010;39(1):228-240. doi:10.1039/B917103G
13. Wallace PR. Erratum: The Band Theory of Graphite [Phys. Rev. 71, 622 (1947)]. *Physical Review*. 1947;72(3):258-258. doi:10.1103/PhysRev.72.258
14. Schafhaeutl C. Ueber die Verbindungen des Kohlenstoffes mit Silicium, Eisen und anderen Metallen, welche die verschiedenen Gallungen von Roheisen, Stahl und Schmiedeeisen bilden. *Journal für Praktische Chemie*. 1840;21(1):129-157. doi:10.1002/prac.18400210117
15. Dreyer DR, Ruoff RS, Bielawski CW. From Conception to Realization: An Historial Account of Graphene and Some Perspectives for Its Future. *Angewandte Chemie International Edition*. 2010;49(49):9336-9344. doi:10.1002/anie.201003024
16. Bianco A, Cheng HM, Enoki T, et al. All in the graphene family – A recommended nomenclature for two-dimensional carbon materials. *Carbon N Y*. 2013;65:1-6. doi:10.1016/j.carbon.2013.08.038
17. Geim AK, Novoselov KS. The rise of graphene. *Nat Mater*. 2007;6(3):183-191. doi:10.1038/nmat1849
18. Saidina DS, Zubir SA, Fontana S, Hérold C, Mariatti M. Synthesis and Characterization of Graphene-Based Inks for Spray-Coating Applications. *J Electron Mater*. 2019;48(9):5757-5770. doi:10.1007/s11664-019-07376-3
19. Toh SY, Loh KS, Kamarudin SK, Daud WRW. Graphene production via electrochemical reduction of graphene oxide: Synthesis and characterisation. *Chemical Engineering Journal*. 2014;251:422-434. doi:10.1016/j.cej.2014.04.004
20. Dasari BL, Nouri JM, Brabazon D, Naher S. Graphene and derivatives – Synthesis techniques, properties and their energy applications. *Energy*. 2017;140:766-778. doi:10.1016/j.energy.2017.08.048
21. Novoselov KS, Geim AK, Morozov S V., et al. Electric Field Effect in Atomically Thin Carbon Films. *Science (1979)*. 2004;306(5696):666-669. doi:10.1126/science.1102896
22. Geim AK. Graphene prehistory. *Phys Scr*. 2012;014003(T146). doi:10.1088/0031-8949/2012/T146/014003
23. Damien D, Sudeep PM, Narayanan TN, Anantharaman MR, Ajayan PM, Shaijumon MM. Fluorinated graphene based electrodes for high performance primary lithium batteries. *RSC Adv*. 2013;3(48):25702-25706. doi:10.1039/C3RA45377D

24. Graphene Flagship. Accessed May 4, 2024. https://graphene-flagship.eu
25. C. Claro PI, Pinheiro T, Silvestre SL, et al. Sustainable carbon sources for green laser-induced graphene: A perspective on fundamental principles, applications, and challenges. *Appl Phys Rev*. 2022;9(4). doi:10.1063/5.0100785
26. Tiwari SK, Sahoo S, Wang N, Huczko A. Graphene research and their outputs: Status and prospect. *Journal of Science: Advanced Materials and Devices*. 2020;5(1):10-29. doi:10.1016/j.jsamd.2020.01.006
27. Le TD, Phan H, Kwon S, et al. Recent Advances in Laser-Induced Graphene: Mechanism, Fabrication, Properties, and Applications in Flexible Electronics. *Adv Funct Mater*. 2022;32(48). doi:10.1002/adfm.202205158
28. Zhang Z, Zhu H, Zhang W, et al. A review of laser-induced graphene: From experimental and theoretical fabrication processes to emerging applications. *Carbon N Y*. 2023;214:118356. doi:10.1016/j.carbon.2023.118356
29. Sun Z, Fang S, Hu YH. 3D Graphene Materials: From Understanding to Design and Synthesis Control. *Chem Rev*. 2020;120(18):10336-10453. doi:10.1021/acs.chemrev.0c00083
30. Barkan T. Graphene: the hype versus commercial reality. *Nat Nanotechnol*. 2019;14(10):904-906. doi:10.1038/s41565-019-0556-1
31. Tuček J, Błoński P, Ugolotti J, Swain AK, Enoki T, Zbořil R. Emerging chemical strategies for imprinting magnetism in graphene and related 2D materials for spintronic and biomedical applications. *Chem Soc Rev*. 2018;47(11):3899-3990. doi:10.1039/C7CS00288B
32. Umar E, Ikram M, Haider J, Nabgan W, Imran M, Nazir G. 3D graphene-based material: Overview, perspective, advancement, energy storage, biomedical engineering and environmental applications a bibliometric analysis. *J Environ Chem Eng*. 2023;11(5):110339. doi:10.1016/j.jece.2023.110339
33. Gutiérrez-Cruz A, Ruiz-Hernández AR, Vega-Clemente JF, Luna-Gazcón DG, Campos-Delgado J. A review of top-down and bottom-up synthesis methods for the production of graphene, graphene oxide and reduced graphene oxide. *J Mater Sci*. 2022;57(31):14543-14578. doi:10.1007/s10853-022-07514-z
34. Tadyszak K, Wychowaniec JK, Litowczenko J. Biomedical applications of graphene-based structures. *Nanomaterials*. 2018;8(11). doi:10.3390/NANO8110944
35. Carvalho AF, Kulyk B, Fernandes AJS, Fortunato E, Costa FM. A Review on the Applications of Graphene in Mechanical Transduction. *Advanced Materials*. 2022;34(8). doi:10.1002/adma.202101326

36. Backes C, Abdelkader AM, Alonso C, et al. Production and processing of graphene and related materials. *2d Mater*. 2020;7(2):022001. doi:10.1088/2053-1583/ab1e0a
37. Madurani KA, Suprapto S, Machrita NI, Bahar SL, Illiya W, Kurniawan F. Progress in Graphene Synthesis and its Application: History, Challenge and the Future Outlook for Research and Industry. *ECS Journal of Solid State Science and Technology*. 2020;9(9):093013. doi:10.1149/2162-8777/abbb6f
38. Moosa AA, Abed MS. Graphene preparation and graphite exfoliation. *Turk J Chem*. 2021;45(3):493-519. doi:10.3906/kim-2101-19
39. Allen MJ, Tung VC, Kaner RB. Honeycomb Carbon: A Review of Graphene. *Chem Rev*. 2010;110(1):132-145. doi:10.1021/cr900070d
40. Zhang J, Gu M, Chen X. Supercapacitors for renewable energy applications: A review. *Micro and Nano Engineering*. 2023;21:100229. doi:10.1016/j.mne.2023.100229
41. Kumar N, Salehiyan R, Chauke V, et al. Top-down synthesis of graphene: A comprehensive review. *FlatChem*. 2021;27:100224. doi:10.1016/j.flatc.2021.100224
42. Edward K, Mamun K, Narayan S, Assaf M, Rohindra D, Rathnayake U. State-of-the-Art Graphene Synthesis Methods and Environmental Concerns. *Appl Environ Soil Sci*. 2023;2023:1-23. doi:10.1155/2023/8475504
43. Chua CK, Pumera M. Chemical reduction of graphene oxide: a synthetic chemistry viewpoint. *Chem Soc Rev*. 2014;43(1):291-312. doi:10.1039/C3CS60303B
44. Li Z, Young RJ, Backes C, et al. Mechanisms of Liquid-Phase Exfoliation for the Production of Graphene. *ACS Nano*. 2020;14(9):10976-10985. doi:10.1021/acsnano.0c03916
45. Xu Y, Cao H, Xue Y, Li B, Cai W. Liquid-Phase Exfoliation of Graphene: An Overview on Exfoliation Media, Techniques, and Challenges. *Nanomaterials*. 2018;8(11):942. doi:10.3390/nano8110942
46. Xu Y, Cao H, Xue Y, Li B, Cai W. Liquid-Phase Exfoliation of Graphene: An Overview on Exfoliation Media, Techniques, and Challenges. *Nanomaterials*. 2018;8(11):942. doi:10.3390/nano8110942
47. Abbas Q, Shinde PA, Abdelkareem MA, et al. Graphene Synthesis Techniques and Environmental Applications. *Materials*. 2022;15(21):7804. doi:10.3390/ma15217804
48. Chen D, Wang F, Li Y, et al. Programmed electrochemical exfoliation of graphite to high quality graphene. *Chemical Communications*. 2019;55(23):3379-3382. doi:10.1039/C9CC00393B

49. Mbayachi VB, Ndayiragije E, Sammani T, Taj S, Mbuta ER, khan A ullah. Graphene synthesis, characterization and its applications: A review. *Results Chem*. 2021;3:100163. doi:10.1016/j.rechem.2021.100163
50. Bhuyan MdSA, Uddin MdN, Islam MdM, Bipasha FA, Hossain SS. Synthesis of graphene. *Int Nano Lett*. 2016;6(2):65-83. doi:10.1007/s40089-015-0176-1
51. Brownson DAC, Banks CE. The electrochemistry of CVD graphene: progress and prospects. *Physical Chemistry Chemical Physics*. 2012;14(23):8264. doi:10.1039/c2cp40225d
52. Sun L, Yuan G, Gao L, et al. Chemical vapour deposition. *Nature Reviews Methods Primers*. 2021;1(1):5. doi:10.1038/s43586-020-00005-y
53. Saeed M, Alshammari Y, Majeed SA, Al-Nasrallah E. Chemical Vapour Deposition of Graphene—Synthesis, Characterisation, and Applications: A Review. *Molecules*. 2020;25(17):3856. doi:10.3390/molecules25173856
54. Li X, Cai W, Colombo L, Ruoff RS. Evolution of graphene growth on Ni and Cu by carbon isotope labeling. *Nano Lett*. 2009;9(12):4268-4272. doi:10.1021/NL902515K/ASSET/IMAGES/LARGE/NL-2009-02515K_0004.JPEG
55. Lin J, Peng Z, Liu Y, et al. Laser-induced porous graphene films from commercial polymers. *Nat Commun*. 2014;5(1):5714. doi:10.1038/ncomms6714
56. Wang M, Yang Y, Gao W. Laser-engraved graphene for flexible and wearable electronics. *Trends Chem*. 2021;3(11):969-981. doi:10.1016/J.TRECHM.2021.09.001
57. Nayak P, Kurra N, Xia C, Alshareef HN. Highly Efficient Laser Scribed Graphene Electrodes for On-Chip Electrochemical Sensing Applications. *Adv Electron Mater*. 2016;2(10):1600185. doi:10.1002/AELM.201600185
58. Samouco A, Marques AC, Pimentel A, Martins R, Fortunato E. Laser-induced electrodes towards low-cost flexible UV ZnO sensors. *Flexible and Printed Electronics*. 2018;3(4):0-21. doi:10.1088/2058-8585/aaed77
59. Ye R, James DK, Tour JM. Laser-Induced Graphene: From Discovery to Translation. *Advanced Materials*. 2019;31(1):1-15. doi:10.1002/adma.201803621
60. Scardaci V. Laser Synthesized Graphene and Its Applications. *Applied Sciences*. 2021;11(14):6304. doi:10.3390/app11146304
61. Jin H. Techno-economic assessment of laser-induced biomass graphene.
62. Yang W, Liu Y, Li Q, et al. In situ formation of phosphorus-doped porous graphene via laser induction. *RSC Adv*. 2020;10(40):23953-23958. doi:10.1039/D0RA03363D
63. Lee JU, Lee CW, Cho SC, Shin BS. Laser-Induced Graphene Heater Pad for De-Icing. *Nanomaterials*. 2021;11(11):3093. doi:10.3390/nano11113093

64. Le TD, Park S, An J, Lee PS, Kim Y. Ultrafast Laser Pulses Enable One-Step Graphene Patterning on Woods and Leaves for Green Electronics. *Adv Funct Mater*. 2019;29(33). doi:10.1002/adfm.201902771
65. Bressi AC, Dallinger A, Steksova Y, Greco F. Bioderived Laser-Induced Graphene for Sensors and Supercapacitors. *ACS Appl Mater Interfaces*. 2023;15(30):35788-35814. doi:10.1021/acsami.3c07687
66. Ye R, Tour JM. Graphene at Fifteen. *ACS Nano*. 2019;13(10):10872-10878. doi:10.1021/acsnano.9b06778
67. Pinilla S, Coelho J, Li K, Liu J, Nicolosi V. Two-dimensional material inks. *Nat Rev Mater*. 2022;7(9):717-735. doi:10.1038/s41578-022-00448-7
68. Leenen MAM, Arning V, Thiem H, Steiger J, Anselmann R. Printable electronics: flexibility for the future. *physica status solidi (a)*. 2009;206(4):588-597. doi:10.1002/pssa.200824428
69. Lan L, Ping J, Xiong J, Ying Y. Sustainable Natural Bio-Origin Materials for Future Flexible Devices. *Advanced Science*. 2022;9(15). doi:10.1002/advs.202200560
70. Laser-induced direct graphene patterning: from formation mechanism to flexible applications. *Soft Science*. 2023;3(1):4. doi:10.20517/ss.2022.26
71. Pinheiro T, Morais M, Silvestre S, et al. Direct Laser Writing: From Materials Synthesis and Conversion to Electronic Device Processing. *Advanced Materials*. Published online March 29, 2024. doi:10.1002/ADMA.202402014
72. Avinash K, Patolsky F. Laser-induced graphene structures: From synthesis and applications to future prospects. *Materials Today*. 2023;70:104-136. doi:10.1016/j.mattod.2023.10.009
73. Song C, Guan M, Jia Y, et al. Driving forces for ultrafast laser-induced sp2 to sp3 structural transformation in graphite. *npj Computational Materials 2023 9:1*. 2023;9(1):1-7. doi:10.1038/s41524-023-01035-2
74. Wang H, Zhao Z, Liu P, Guo X. Laser-Induced Graphene Based Flexible Electronic Devices. *Biosensors (Basel)*. 2022;12(2):55. doi:10.3390/bios12020055
75. Guo Y, Zhang C, Chen Y, Nie Z. Research Progress on the Preparation and Applications of Laser-Induced Graphene Technology. *Nanomaterials*. 2022;12(14):2336. doi:10.3390/nano12142336
76. Huang QM, Yang H;, Wang S;, et al. Laser-Induced Graphene Formation on Chitosan Derivatives toward Ecofriendly Electronics. *ACS Appl Nano Mater*. 2023;6(12):10453-10465. doi:10.1021/acsanm.3c01408

77. Yu W, Zhao W, Wang S, Chen Q, Liu X. Direct Conversion of Liquid Organic Precursor into 3D Laser-Induced Graphene Materials. *Advanced Materials*. 2023;35(9):2209545. doi:10.1002/ADMA.202209545
78. Coelho J, Correia RF, Silvestre S, et al. Paper-based laser-induced graphene for sustainable and flexible microsupercapacitor applications. *Microchimica Acta*. 2023;190(1):40. doi:10.1007/s00604-022-05610-0
79. Zhang Z, Song M, Hao J, Wu K, Li C, Hu C. Visible light laser-induced graphene from phenolic resin: A new approach for directly writing graphene-based electrochemical devices on various substrates. *Carbon N Y*. 2018;127:287-296. doi:10.1016/j.carbon.2017.11.014
80. Stanford MG, Zhang C, Fowlkes JD, et al. High-Resolution Laser-Induced Graphene. Flexible Electronics beyond the Visible Limit. *ACS Appl Mater Interfaces*. 2020;12(9). doi:10.1021/acsami.0c01377
81. Jelínková H, Šulc J. Laser characteristics. In: *Lasers for Medical Applications*. Elsevier; 2013:17-46. doi:10.1533/9780857097545.1.17
82. Chen Y, Long J, Zhou S, et al. UV Laser-Induced Polyimide-to-Graphene Conversion: Modeling, Fabrication, and Application. *Small Methods*. 2019;3(10):1-9. doi:10.1002/smtd.201900208
83. Wang L, Wang Z, Bakhtiyari AN. A Comparative Study of Laser-Induced Graphene by CO 2 Infrared Laser and 355 nm Ultraviolet (UV) Laser. Published online 2020.
84. Kulyk B, Silva BFR, Carvalho AF, et al. Laser-Induced Graphene from Paper by Ultraviolet Irradiation: Humidity and Temperature Sensors. *Adv Mater Technol*. 2022;7(7). doi:10.1002/admt.202101311
85. Li G. Direct laser writing of graphene electrodes. *J Appl Phys*. 2020;127(1). doi:10.1063/1.5120056
86. Lee Y, Low MJ, Yang D, et al. Ultra-thin light-weight laser-induced-graphene (LIG) diffractive optics. *Light: Science & Applications 2023 12:1*. 2023;12(1):1-33. doi:10.1038/s41377-023-01143-0
87. Lee Y, Low MJ, Yang D, et al. Ultra-thin light-weight laser-induced-graphene (LIG) diffractive optics. *Light Sci Appl*. 2023;12(1):146. doi:10.1038/s41377-023-01143-0
88. Wang S, Yang J, Deng G, Zhou S. Femtosecond Laser Direct Writing of Flexible Electronic Devices: A Mini Review. *Materials*. 2024;17(3):557. doi:10.3390/ma17030557

89. Weber R, Graf T, Berger P, et al. Heat accumulation during pulsed laser materials processing. *Optics Express, Vol 22, Issue 9, pp 11312-11324*. 2014;22(9):11312-11324. doi:10.1364/OE.22.011312
90. Hase M, Fons P, Mitrofanov K, Kolobov A V., Tominaga J. Femtosecond structural transformation of phase-change materials far from equilibrium monitored by coherent phonons. *Nature Communications 2015 6:1*. 2015;6(1):1-6. doi:10.1038/ncomms9367
91. Wang S, Yang J, Deng G, Zhou S. Femtosecond Laser Direct Writing of Flexible Electronic Devices: A Mini Review. *Materials 2024, Vol 17, Page 557*. 2024;17(3):557. doi:10.3390/MA17030557
92. Abdulhafez M, Tomaraei GN, Bedewy M. Fluence-Dependent Morphological Transitions in Laser-Induced Graphene Electrodes on Polyimide Substrates for Flexible Devices. *ACS Appl Nano Mater*. 2021;4(3):2973-2986. doi:10.1021/acsanm.1c00101
93. Tour JM, Li Y, Ye R, Chyan Y, Arnusch CJ, Singh SP. Laser-Induced Graphene by Multiple Lasing: Toward Electronics on Cloth, Paper, and Food. *ACS Nano*. 2018;12(3):2176-2183. doi:10.1021/acsnano.7b08539
94. Pinheiro T, Correia R, Morais M, et al. Water Peel-Off Transfer of Electronically Enhanced, Paper-Based Laser-Induced Graphene for Wearable Electronics. *ACS Nano*. 2022;16(12):20633-20646. doi:10.1021/acsnano.2c07596
95. Pinheiro T, Rosa A, Ornelas C, et al. Influence of CO2 laser beam modelling on electronic and electrochemical properties of paper-based laser-induced graphene for disposable pH electrochemical sensors. *Carbon Trends*. 2023;11:100271. doi:10.1016/J.CARTRE.2023.100271
96. Wang L, Wang Z, Bakhtiyari AN, Zheng H. A Comparative Study of Laser-Induced Graphene by CO2 Infrared Laser and 355 nm Ultraviolet (UV) Laser. *Micromachines (Basel)*. 2020;11(12):1-9. doi:10.3390/MI11121094
97. Gladush GG, Smurov I. *Physics of Laser Materials Processing*. Vol 146. Springer Berlin Heidelberg; 2011. doi:10.1007/978-3-642-19831-1
98. Minhas-Khan A, Nambi S, Grau G. Low-resistance laser-induced graphitic carbon by maximizing energy delivery and pulse overlap. *Carbon N Y*. 2021;181:310-322. doi:10.1016/J.CARBON.2021.05.037
99. Vivaldi FM, Dallinger A, Bonini A, et al. Three-Dimensional (3D) Laser-Induced Graphene: Structure, Properties, and Application to Chemical Sensing. *ACS Appl Mater Interfaces*. 2021;13(26):30245-30260. doi:10.1021/acsami.1c05614

100. Dallinger A, Keller K, Fitzek H, Greco F. Stretchable and Skin-Conformable Conductors Based on Polyurethane/Laser-Induced Graphene. *ACS Appl Mater Interfaces*. 2020;12(17):19855-19865. doi:10.1021/acsami.0c03148
101. Singh SP, Li Y, Zhang J, Tour JM, Arnusch CJ. Sulfur-Doped Laser-Induced Porous Graphene Derived from Polysulfone-Class Polymers and Membranes. *ACS Nano*. 2018;12(1):289-297. doi:10.1021/ACSNANO.7B06263
102. Lamberti A, Serrapede M, Ferraro G, et al. All-SPEEK flexible supercapacitor exploiting laser-induced graphenization. *2d Mater*. 2017;4(3):035012. doi:10.1088/2053-1583/AA790E
103. Ge L, Hong Q, Li H, Liu C, Li F. Direct-Laser-Writing of Metal Sulfide-Graphene Nanocomposite Photoelectrode toward Sensitive Photoelectrochemical Sensing. *Adv Funct Mater*. 2019;29(38):1904000. doi:10.1002/ADFM.201904000
104. Pinheiro T, Silvestre S, Coelho J, et al. Laser-Induced Graphene on Paper toward Efficient Fabrication of Flexible, Planar Electrodes for Electrochemical Sensing. *Adv Mater Interfaces*. 2021;8(22). doi:10.1002/admi.202101502
105. Qiu C, Jiang L, Gao Y, Sheng L. Effects of oxygen-containing functional groups on carbon materials in supercapacitors: A review. *Mater Des*. 2023;230:111952. doi:10.1016/J.MATDES.2023.111952
106. van der Veen I, de Boer J. Phosphorus flame retardants: Properties, production, environmental occurrence, toxicity and analysis. *Chemosphere*. 2012;88(10):1119-1153. doi:10.1016/J.CHEMOSPHERE.2012.03.067
107. klem M, Abreu R, Pinheiro T, Coelho J, Alves N, Martins R. Electrochemical Deposition of Manganese Oxide on Paper-Based Laser-Induced Graphene for the Fabrication of Sustainable High-Energy Density Supercapacitors. doi:10.2139/SSRN.4724436
108. Abreu R, dos Santos Klem M, Pinheiro T, et al. Direct laser writing of MnOx decorated laser-induced graphene on paper for sustainable microsupercapacitor fabrication. *FlatChem*. 2024;46:100672. doi:10.1016/J.FLATC.2024.100672
109. Mamleyev ER, Kudryashov V V., Heissler S, et al. Laser-induced hierarchical carbon patterns on polyimide substrates for flexible urea sensors. *npj Flexible Electronics*. 2018;3(1). doi:10.1038/s41528-018-0047-8
110. Li L, Zhang J, Peng Z, et al. High-Performance Pseudocapacitive Microsupercapacitors from Laser-Induced Graphene. *Advanced Materials*. 2016;28(5):838-845. doi:10.1002/ADMA.201503333

111. Li Z, Lin J, Li B, Yu C, Wang H, Li Q. Construction of heteroatom-doped and three-dimensional graphene materials for the applications in supercapacitors: A review. *J Energy Storage*. 2021;44:103437. doi:10.1016/J.EST.2021.103437
112. Bhattacharya G, Fishlock SJ, Hussain S, et al. Disposable Paper-Based Biosensors: Optimizing the Electrochemical Properties of Laser-Induced Graphene. *ACS Appl Mater Interfaces*. 2022;14(27):31109-31120. doi:10.1021/ACSAMI.2C06350/SUPPL_FILE/AM2C06350_SI_001.PDF
113. Meng L, Chirtes S, Liu X, Eriksson M, Mak WC. A green route for lignin-derived graphene electrodes: A disposable platform for electrochemical biosensors. *Biosens Bioelectron*. 2022;218:114742. doi:10.1016/j.bios.2022.114742
114. Gao P, Kasama T, Shin J, Huang Y, Miyake R. A Mediated Enzymatic Electrochemical Sensor Using Paper-Based Laser-Induced Graphene. *Biosensors (Basel)*. 2022;12(11):995. doi:10.3390/BIOS12110995/S1
115. Kaidarova A, Kosel J. Physical Sensors Based on Laser-Induced Graphene: A Review. *IEEE Sens J*. 2021;21(11):12426-12443. doi:10.1109/JSEN.2020.3034845
116. Zhu J, Huang X, Song W. Physical and Chemical Sensors on the Basis of Laser-Induced Graphene: Mechanisms, Applications, and Perspectives. *ACS Nano*. 2021;15(12):18708-18741. doi:10.1021/acsnano.1c05806
117. Reina M, Scalia A, Auxilia G, et al. Boosting Electric Double Layer Capacitance in Laser-Induced Graphene-Based Supercapacitors. *Adv Sustain Syst*. 2022;6(1). doi:10.1002/adsu.202100228
118. Banerjee R, Chowdhury AH, Kumar PS, Wang C, Goel S, Raj PM. Laser-induced graphene supercapacitors on flex substrates for package-integrated power supply. *2023 4th International Symposium on 3D Power Electronics Integration and Manufacturing, 3D-PEIM 2023*. Published online 2023. doi:10.1109/3D-PEIM55914.2023.10052332
119. Hasheminia F, Sadeghzadeh S. Laser-induced graphene in energy storage- batteries. *Nano-Structures & Nano-Objects*. 2024;40:101347. doi:10.1016/J.NANOSO.2024.101347
120. Shim H, Tran C Van, Kim A, Hyun S, In J Bin. Laser-Induced Graphene(LIG)-Based Anode Electrode for High-Rate Lithium-Ion Batteries. *ECS Meeting Abstracts*. 2022;MA2022-02(3):314. doi:10.1149/MA2022-023314MTGABS
121. Stanford MG, Li JT, Chyan Y, Wang Z, Wang W, Tour JM. Laser-Induced Graphene Triboelectric Nanogenerators. *ACS Nano*. 2019;13(6):7166-7174. doi:10.1021/acsnano.9b02596

122. Choi KH, Park S, Hyeong SK, et al. Triboelectric effect of surface morphology controlled laser induced graphene. *J Mater Chem A Mater*. 2020;8(38):19822-19832. doi:10.1039/D0TA05806H
123. Chen H, Yang W, Huang P, et al. A multiple laser-induced hybrid electrode for flexible triboelectric nanogenerators. *Sustain Energy Fuels*. 2021;5(14):3737-3743. doi:10.1039/d1se00819f
124. Xia SY, Long Y, Huang Z, et al. Laser-induced graphene (LIG)-based pressure sensor and triboelectric nanogenerator towards high-performance self-powered measurement-control combined system. *Nano Energy*. 2022;96:107099. doi:10.1016/J.NANOEN.2022.107099
125. Nazeri M, Ghalamboran M, Grau G. Laser-Induced Graphene Electrodes for Organic Electrochemical Transistors (OECTs). *Adv Mater Technol*. 2023;8(17):2300188. doi:10.1002/ADMT.202300188
126. Sun M, Zhang Y, Wang S, et al. Laser-induced graphene van der Waals contact-enabled high-performance 2D-materials-based field-effect transistor. *Carbon N Y*. 2024;225:119151. doi:10.1016/J.CARBON.2024.119151
127. Ren G, Fan H, Zhang L, et al. A laser-induced graphene-based flexible and all-carbon organic electrochemical transistor. *J Mater Chem C Mater*. 2023;11(14):4916-4928. doi:10.1039/D3TC00342F
128. Czagany M, Hompoth S, Keshri AK, et al. Supercapacitors: An Efficient Way for Energy Storage Application. *Materials*. 2024;17(3):702. doi:10.3390/ma17030702
129. Hawes GF, Rehman S, Rangom Y, Pope MA. Advanced manufacturing approaches for electrochemical energy storage devices. *International Materials Reviews*. 2023;68(3):323-364. doi:10.1080/09506608.2022.2086388
130. Lee JH, Yang G, Kim CH, Mahajan RL, Lee SY, Park SJ. Flexible solid-state hybrid supercapacitors for the internet of everything (IoE). *Energy Environ Sci*. 2022;15(6):2233-2258. doi:10.1039/D1EE03567C
131. Berrueta A, Ursua A, Martin IS, Eftekhari A, Sanchis P. Supercapacitors: Electrical Characteristics, Modeling, Applications, and Future Trends. *IEEE Access*. 2019;7:50869-50896. doi:10.1109/ACCESS.2019.2908558
132. Sagadevan S, Marlinda AR, Chowdhury ZZ, et al. Fundamental electrochemical energy storage systems. In: *Advances in Supercapacitor and Supercapattery*. Elsevier; 2021:27-43. doi:10.1016/B978-0-12-819897-1.00001-X

133. González A, Goikolea E, Barrena JA, Mysyk R. Review on supercapacitors: Technologies and materials. *Renewable and Sustainable Energy Reviews*. 2016;58:1189-1206. doi:10.1016/J.RSER.2015.12.249
134. Zhao J, Jiang Y, Fan H, et al. Porous 3D Few-Layer Graphene-like Carbon for Ultrahigh-Power Supercapacitors with Well-Defined Structure–Performance Relationship. *Advanced Materials*. 2017;29(11):1604569. doi:10.1002/ADMA.201604569
135. Wang W, Lu L, Li Z, et al. Fingerprint-Inspired Strain Sensor with Balanced Sensitivity and Strain Range Using Laser-Induced Graphene. *ACS Appl Mater Interfaces*. 2022;14(1):1315-1325. doi:10.1021/ACSAMI.1C16646
136. Zou Y, Zhong M, Li S, et al. Flexible Wearable Strain Sensors Based on Laser-Induced Graphene for Monitoring Human Physiological Signals. *Polymers (Basel)*. 2023;15(17):3553. doi:10.3390/polym15173553
137. United Nations. *Transforming Our World: The 2030 Agenda for Sustainable Development*.; 2015. Accessed September 6, 2023. https://sdgs.un.org/2030agenda
138. Silva JAP, Lima GG, Camilo-Cotrim CF, et al. Impact of E-Waste Toxicity on Health and Nature: Trends, Biases, and Future Directions. *Water Air Soil Pollut*. 2023;234(5):320. doi:10.1007/s11270-023-06328-2
139. Baldé CP, Forti V, Gray V, Kuehr R, Stegmann P. The Global e-Waste Monitor 2017: Quantities, Flows and Resources. Published online 2017.
140. Li W, Liu Q, Zhang Y, et al. Biodegradable Materials and Green Processing for Green Electronics. *Advanced Materials*. 2020;32(33). doi:10.1002/adma.202001591
141. Zhu H, Luo W, Ciesielski PN, et al. Correction To Wood-Derived Materials for Green Electronics, Biological Devices, and Energy Applications. *Chem Rev*. 2016;116(19):12650-12650. doi:10.1021/acs.chemrev.6b00576
142. Xu Y, Fei Q, Page M, et al. Paper-based wearable electronics. *iScience*. 2021;24(7):102736. doi:10.1016/j.isci.2021.102736
143. Khan SM, Nassar JM, Hussain MM. Paper as a Substrate and an Active Material in Paper Electronics. *ACS Appl Electron Mater*. 2021;3(1):30-52. doi:10.1021/acsaelm.0c00484
144. Park H, Park JJ, Bui PD, et al. Laser-Based Selective Material Processing for Next-Generation Additive Manufacturing. *Advanced Materials*. Published online 2023:2307586. doi:10.1002/ADMA.202307586
145. Nishimura H, Kamiya A, Nagata T, Katahira M, Watanabe T. Direct evidence for α ether linkage between lignin and carbohydrates in wood cell walls. *Sci Rep*. 2018;8(1). doi:10.1038/S41598-018-24328-9

146. Garcia-Maraver A, Salvachúa D, Martínez MJ, Diaz LF, Zamorano M. Analysis of the relation between the cellulose, hemicellulose and lignin content and the thermal behavior of residual biomass from olive trees. *Waste Manag*. 2013;33(11):2245-2249. doi:10.1016/J.WASMAN.2013.07.010
147. Kumar A, Jyske T, Petrič M. Delignified Wood from Understanding the Hierarchically Aligned Cellulosic Structures to Creating Novel Functional Materials: A Review. *Adv Sustain Syst*. 2021;5(5):2000251. doi:10.1002/ADSU.202000251
148. Mathura SR, Landázuri AC, Mathura F, Andrade Sosa AG, Orejuela-Escobar LM. Hemicelluloses from bioresidues and their applications in the food industry – towards an advanced bioeconomy and a sustainable global value chain of chemicals and materials. *Sustainable Food Technology*. 2024;2(5):1183-1205. doi:10.1039/D4FB00035H
149. Horikawa Y. Structural diversity of natural cellulose and related applications using delignified wood. *Journal of Wood Science*. 2022;68(1):1-9. doi:10.1186/S10086-022-02061-2/FIGURES/2
150. Ye R, Chyan Y, Zhang J, et al. Laser-Induced Graphene Formation on Wood. *Advanced Materials*. 2017;29(37). doi:10.1002/adma.201702211
151. Nam HK, Choi J, Jing T, et al. Laser-induced graphene formation on recycled woods for green smart furniture. *EcoMat*. 2024;6(4):e12447. doi:10.1002/EOM2.12447
152. Li H, Kulachenko A, Mathew AP, Stoltz RB, Sevastyanova O. Enhancing the Strength and Flexibility of Microfibrillated Cellulose Films from Lignin-Rich Kraft Pulp. *ACS Sustain Chem Eng*. 2023;11(47):16793-16805. doi:10.1021/ACSSUSCHEMENG.3C05086/ASSET/IMAGES/LARGE/SC3C05086_0006.JPEG
153. Le TD, Lee YA, Nam HK, et al. Green Flexible Graphene–Inorganic-Hybrid Micro-Supercapacitors Made of Fallen Leaves Enabled by Ultrafast Laser Pulses. *Adv Funct Mater*. 2022;32(20):2107768. doi:10.1002/adfm.202107768
154. Silva SP, Sabino MA, Fernandes EM, Correlo VM, Boesel LF, Reis RL. Cork: properties, capabilities and applications. *International Materials Reviews*. 2005;50(6):345-365. doi:10.1179/174328005X41168
155. Silvestre SL, Pinheiro T, Marques AC, et al. Cork derived laser-induced graphene for sustainable green electronics. *Flexible and Printed Electronics*. 2022;7. doi:10.1088/2058-8585/ac8e7b
156. Pereira H, M ER, Fortes MA. The cellular structure of cork from Quercus Suber L. *IAWA J*. 1987;8(3):213-218. doi:10.1163/22941932-90001048

157. Duarte AP, Bordado JC. Cork – a renewable raw material: Forecast of industrial potential and development priorities. *Front Mater*. 2015;2:116294. doi:10.3389/FMATS.2015.00002/BIBTEX
158. Costa A, Barbosa I, Miguel C, Graça J. Variation of cork porosity along the stem in harvested cork oak (Quercus suber L.) trees. *Ann For Sci*. 2021;78(2). doi:10.1007/s13595-021-01068-x
159. Imbrogno A, Islam J, Santillo C, et al. Laser-Induced Graphene Supercapacitors by Direct Laser Writing of Cork Natural Substrates. *ACS Appl Electron Mater*. 2022;4(4). doi:10.1021/acsaelm.1c01202
160. de Araujo WR, Frasson CMR, Ameku WA, Silva JR, Angnes L, Paixão TRLC. Single-Step Reagentless Laser Scribing Fabrication of Electrochemical Paper-Based Analytical Devices. *Angew Chem Int Ed Engl*. 2017;56(47):15113-15117. doi:10.1002/ANIE.201708527
161. Vanholme R, Demedts B, Morreel K, Ralph J, Boerjan W. Lignin biosynthesis and structure. *Plant Physiol*. 2010;153(3):895-905. doi:10.1104/PP.110.155119
162. Yang S, Ling Y, Wu Q, et al. Lignin-derived porous graphene for wearable and ultrasensitive strain sensors. *J Mater Chem C Mater*. 2022;10(32):11730-11738. doi:10.1039/D2TC00953F
163. Lei Y, Alshareef AH, Zhao W, Inal S. Laser-Scribed Graphene Electrodes Derived from Lignin for Biochemical Sensing. *ACS Appl Nano Mater*. 2020;3(2):1166-1174. doi:10.1021/acsanm.9b01795
164. Mendes LF, de Siervo A, Reis de Araujo W, Longo Cesar Paixão TR. Reagentless fabrication of a porous graphene-like electrochemical device from phenolic paper using laser-scribing. *Carbon N Y*. 2020;159:110-118. doi:10.1016/j.carbon.2019.12.016
165. Cantarella G, Madagalam M, Merino I, et al. Laser-Induced, Green and Biocompatible Paper-Based Devices for Circular Electronics. *Adv Funct Mater*. 2023;33(17). doi:10.1002/adfm.202210422
166. Mahmood F, Mahmood F, Zhang H, Lin J, Wan C. Laser-Induced Graphene Derived from Kraft Lignin for Flexible Supercapacitors. *ACS Omega*. 2020;5(24):14611-14618. doi:10.1021/acsomega.0c01293
167. Tan Y, Ren Y, Xu Z, Zhu Y, Li H. Highly Graphitized Porous Carbon Prepared from Biomass Waste Sunflower Shells for Supercapacitors. *J Electron Mater*. 2023;52(4). doi:10.1007/s11664-023-10223-1

168. Miyakoshi R, Hayashi S, Terakawa M. Simultaneous laser-based graphitization and microstructuring of bamboo for supercapacitors derived from renewable resources. *RSC Adv*. 2022;12. doi:10.1039/D2RA05641K
169. Kulyk B, Silva B, Carvalho A, et al. Laser-Induced Graphene from Paper for Mechanical Sensing. *ACS Appl Mater Interfaces*. Published online 2021. doi:10.1021/acsami.0c20270
170. Carvalho AF, Fernandes AJS, Martins R, Fortunato E, Costa FM. Laser-Induced Graphene Piezoresistive Sensors Synthesized Directly on Cork Insoles for Gait Analysis. *Adv Mater Technol*. 2020;5(12). doi:10.1002/admt.202000630
171. Edberg J, Brooke R, Hosseinaei O, Fall A, Wijeratne K, Sandberg M. Laser-induced graphitization of a forest-based ink for use in flexible and printed electronics. *npj Flexible Electronics*. 2020;4(1):1-10. doi:10.1038/s41528-020-0080-2
172. Funayama R, Hayashi S, Terakawa M. Laser-Induced Graphitization of Lignin/PLLA Composite Sheets for Biodegradable Triboelectric Nanogenerators. *ACS Sustain Chem Eng*. 2023;11(7):3114-3122. doi:10.1021/ACSSUSCHEMENG.2C07510/ASSET/IMAGES/LARGE/SC2C07510_0008.JPEG
173. Velasco A, Ryu YK, Hamada A, de Andrés A, Calle F, Martinez J. Laser-Induced Graphene Microsupercapacitors: Structure, Quality, and Performance. *Nanomaterials*. 2023;13(5). doi:10.3390/nano13050788
174. Ma W, Zhu J, Wang Z, Song W, Cao G. Recent advances in preparation and application of laser-induced graphene in energy storage devices. *Mater Today Energy*. 2020;18. doi:10.1016/j.mtener.2020.100569
175. Carvalho AF, Fernandes AJS, Martins R, Fortunato E, Costa FM. Laser-Induced Graphene Piezoresistive Sensors Synthesized Directly on Cork Insoles for Gait Analysis. *Adv Mater Technol*. 2020;5(12):1-8. doi:10.1002/admt.202000630
176. Lagorce-tachon A, Karbowiak T, Loupiac C, et al. The cork viewed from the inside. 2015;149:214-221. doi:10.1016/j.jfoodeng.2014.10.023
177. Li G. Direct laser writing of graphene electrodes. *J Appl Phys*. 2020;127(1). doi:10.1063/1.5120056
178. Stanford MG, Li JT, Chyan Y, Wang Z, Wang W, Tour JM. Laser-Induced Graphene Triboelectric Nanogenerators. *ACS Nano*. 2019;13(6):7166-7174. doi:10.1021/acsnano.9b02596

179. Samouco A, Marques AC, Pimentel A, Martins R, Fortunato E. Laser-induced electrodes towards low-cost flexible UV ZnO sensors. *Flexible and Printed Electronics*. 2018;3(4):0-21. doi:10.1088/2058-8585/aaed77
180. Pinheiro T, Silvestre S, Coelho J, et al. Laser-Induced Graphene on Paper toward Efficient Fabrication of Flexible , Planar Electrodes for Electrochemical Sensing. 2021;2101502:1-12. doi:10.1002/admi.202101502
181. Huang L, Su J, Song Y, Ye R. Laser-Induced Graphene: En Route to Smart Sensing. *Nanomicro Lett*. 2020;12(1). doi:10.1007/s40820-020-00496-0
182. Choi KH, Park S, Hyeong SK, et al. Triboelectric effect of surface morphology controlled laser induced graphene. *J Mater Chem A Mater*. 2020;8(38):19822-19832. doi:10.1039/d0ta05806h
183. Stanford MG, Zhang C, Fowlkes JD, et al. High-Resolution Laser-Induced Graphene. Flexible Electronics beyond the Visible Limit. *ACS Appl Mater Interfaces*. 2020;12(9):10902-10907. doi:10.1021/acsami.0c01377
184. Wang X, Zhang Q. Recent progress on laser fabrication of on-chip microsupercapacitors. *J Energy Storage*. 2020;(September):101994. doi:10.1016/j.est.2020.101994
185. Chen B, Johnson ZT, Sanborn D, et al. Tuning the Structure, Conductivity, and Wettability of Laser-Induced Graphene for Multiplexed Open Microfluidic Environmental Biosensing and Energy Storage Devices. *ACS Nano*. Published online 2021. doi:10.1021/acsnano.1c04197
186. Wall M. The Raman Spectroscopy of Graphene and the Determination of Layer Thickness. *Thermo scientific*. Published online 2011:5.
187. Carvalho AF, Fernandes AJS, Martins R, Fortunato E, Costa FM. Laser-Induced Graphene Piezoresistive Sensors Synthesized Directly on Cork Insoles for Gait Analysis. *Adv Mater Technol*. 2020;5(12):1-8. doi:10.1002/admt.202000630
188. Imbrogno A, Islam J, Santillo C, et al. Laser-Induced Graphene Supercapacitors by Direct Laser Writing of Cork Natural Substrates. *ACS Appl Electron Mater*. Published online March 30, 2022:acsaelm.1c01202. doi:10.1021/ACSAELM.1C01202
189. Chanut J, Wang Y, Dal Cin I, et al. Surface properties of cork: Is cork a hydrophobic material? *J Colloid Interface Sci*. 2022;608:416-423. doi:10.1016/j.jcis.2021.09.140
190. Correia VG, Bento A, Pais J, et al. The molecular structure and multifunctionality of the cryptic plant polymer suberin. *Mater Today Bio*. 2020;5(December 2019). doi:10.1016/j.mtbio.2019.100039

191. Fornasini L, Scaravonati S, Magnani G, et al. In situ decoration of laser-scribed graphene with TiO2 nanoparticles for scalable high-performance micro-supercapacitors. *Carbon N Y*. 2021;176:296-306. doi:10.1016/j.carbon.2021.01.129
192. Chen B, Johnson ZT, Sanborn D, et al. Tuning the Structure, Conductivity, and Wettability of Laser-Induced Graphene for Multiplexed Open Microfluidic Environmental Biosensing and Energy Storage Devices. *ACS Nano*. Published online 2021. doi:10.1021/acsnano.1c04197
193. Yuan G, Wan T, BaQais A, et al. Boron and fluorine Co-doped laser-induced graphene towards high-performance micro-supercapacitors. *Carbon N Y*. 2023;212. doi:10.1016/j.carbon.2023.118101
194. Peng Z, Ye R, Mann JA, et al. Flexible Boron-Doped Laser-Induced Graphene Microsupercapacitors. *ACS Nano*. 2015;9(6). doi:10.1021/acsnano.5b00436
195. Khandelwal M, Tran C Van, Lee J, In J Bin. Nitrogen and boron co-doped densified laser-induced graphene for supercapacitor applications. *Chemical Engineering Journal*. 2022;428. doi:10.1016/j.cej.2021.131119
196. Silvestre SL, Morais M, Soares RRA, et al. Green Fabrication of Stackable Laser-Induced Graphene Micro-Supercapacitors under Ambient Conditions: Toward the Design of Truly Sustainable Technological Platforms. *Adv Mater Technol*. Published online 2024:2400261. doi:10.1002/ADMT.202400261
197. Castro O, Silva JM, Devezas T, Silva A, Gil L. Cork agglomerates as an ideal core material in lightweight structures. *Mater Des*. 2010;31(1):425-432. doi:10.1016/j.matdes.2009.05.039
198. Dombek G, Nadolny Z, Przybylek P, et al. Effect of Moisture on the Thermal Conductivity of Cellulose and Aramid Paper Impregnated with Various Dielectric Liquids. *Energies (Basel)*. 2020;13(17):4433. doi:10.3390/en13174433
199. Le TSD, Phan HP, Kwon S, et al. Recent Advances in Laser-Induced Graphene: Mechanism, Fabrication, Properties, and Applications in Flexible Electronics. *Adv Funct Mater*. 2022;32(48):2205158. doi:10.1002/ADFM.202205158
200. Qu W, Zhao Z, Wang J, et al. Direct laser writing of pure lignin on carbon cloth for highly flexible supercapacitors with enhanced areal capacitance. *Sustain Energy Fuels*. 2021;5(14):3744-3754. doi:10.1039/D1SE00828E
201. Wall M. The Raman Spectroscopy of Graphene and the Determination of Layer Thickness. *Thermo scientific*. Published online 2011:5.

202. Zhang R, Wang B, Xiao T, Wang M, Wu Z, Xiao X. Laser induced flexible micro-supercapacitor for pressure sensing. Published online 2023. doi:10.1016/j.mset.2023.05.004
203. Jo H, Park JH, Choi D, Kim K, An S. Percolative Metal Microweb-Based Flexible Lithium-Ion Battery with Fast Charging and High Energy Density. *Advanced Materials*. Published online 2024:2407719. doi:10.1002/ADMA.202407719
204. Zhang Q, Gao XW, Liu X, et al. Flexible wearable energy storage devices: Materials, structures, and applications. *Battery Energy*. 2024;3(2):20230061. doi:10.1002/BTE2.20230061
205. Deng R, He T. Flexible Solid-State Lithium-Ion Batteries: Materials and Structures. *Energies 2023, Vol 16, Page 4549*. 2023;16(12):4549. doi:10.3390/EN16124549
206. Khalil N, Nadeem N, Zahid M, Rehan ZA, Zubair U. Freestanding carbonaceous cathodes for flexible supercapacitors – A comprehensive prospect on materials' composition & structure, and device configuration. *Synth Met*. 2024;301:117521. doi:10.1016/J.SYNTHMET.2023.117521
207. Velasco A, Ryu YK, Boscá A, et al. Recent trends in graphene supercapacitors: From large area to microsupercapacitors. *Sustain Energy Fuels*. 2021;5(5):1235-1254. doi:10.1039/d0se01849j
208. Wang M, Chen J, Lu K, Ma Y, Li H, Ye J. Preparation of high-performance flexible microsupercapacitors based on papermaking and laser-induced graphene techniques. *Electrochim Acta*. 2022;401:139490. doi:10.1016/j.electacta.2021.139490
209. Béguin F, Frąckowiak E. *Supercapacitors*. (Béguin F, Frąckowiak E, eds.). Wiley; 2013. doi:10.1002/9783527646661
210. Liu H, Zhang G, Zheng X, Chen F, Duan H. Emerging miniaturized energy storage devices for microsystem applications: from design to integration. *International Journal of Extreme Manufacturing*. 2020;2(4):042001. doi:10.1088/2631-7990/abba12
211. Lee K, Kim S, Kim M, et al. Folding the Energy Storage: Beyond the Limit of Areal Energy Density of Micro-Supercapacitors. *Adv Energy Mater*. 2023;13(20). doi:10.1002/aenm.202204327
212. Singh R, Charu Tripathi C. Study of Graphene based Flexible Supercapacitors with Different Gel Electrolytes. *Mater Today Proc*. 2018;5(1):943-949. doi:10.1016/j.matpr.2017.11.169
213. Chen Q, Li X, Zang X, et al. Effect of different gel electrolytes on graphene-based solid-state supercapacitors. *RSC Adv*. 2014;4(68):36253-36256. doi:10.1039/c4ra05553e

214. Mahmood F, Mahmood F, Zhang H, Lin J, Wan C. Laser-Induced Graphene Derived from Kraft Lignin for Flexible Supercapacitors. *ACS Omega*. 2020;5(24):14611-14618. doi:10.1021/acsomega.0c01293
215. Li T, Cao Y, Xue W, Sun B, Zhu D. Self-assembly of graphene-based planar micro-supercapacitor with selective laser etching-induced superhydrophobic/superhydrophilic pattern. *SN Appl Sci*. 2020;2(2). doi:10.1007/s42452-020-2000-4
216. Liang J, Mondal AK, Wang D wei, Iacopi F. Graphene-Based Planar Microsupercapacitors : Recent Advances and Future Challenges. 2019;1800200:1-38. doi:10.1002/admt.201800200
217. Bu F, Zhou W, Xu Y, Du Y, Guan C. Recent developments of advanced micro-supercapacitors : design , fabrication and applications. Published online 2020. doi:10.1038/s41528-020-00093-6
218. Gul H, Shah A ul HA, Bilal S. Achieving ultrahigh cycling stability and extended potential window for supercapacitors through asymmetric combination of conductive polymer nanocomposite and activated carbon. *Polymers (Basel)*. 2019;11(10). doi:10.3390/polym11101678
219. Zhang C (John), Liang M, Park SH, et al. Extra lithium-ion storage capacity enabled by liquid-phase exfoliated indium selenide nanosheets conductive network. *Energy Environ Sci*. 2020;13(7):2124-2133. doi:10.1039/d0ee01052a
220. Gul H, Shah A ul HA, Bilal S. Achieving Ultrahigh Cycling Stability and Extended Potential Window for Supercapacitors through Asymmetric Combination of Conductive Polymer Nanocomposite and Activated Carbon. *Polymers (Basel)*. 2019;11(10):1678. doi:10.3390/POLYM11101678
221. Yun X, Xiong Z, Tu L, Bai L, Wang X. Hierarchical porous graphene film: An ideal material for laser-carving fabrication of flexible micro-supercapacitors with high specific capacitance. *Carbon N Y*. 2017;125:308-317. doi:10.1016/j.carbon.2017.09.063
222. Huang J, Xie Y, You Y, et al. Rational Design of Electrode Materials for Advanced Supercapacitors: From Lab Research to Commercialization. *Adv Funct Mater*. 2023;33(14). doi:10.1002/adfm.202213095
223. Peng Z, Lin J, Ye R, Samuel ELG, Tour JM. Flexible and Stackable Laser-Induced Graphene Supercapacitors. *ACS Appl Mater Interfaces*. 2015;7(5):3414-3419. doi:10.1021/am509065d
224. Tariq H, Awan SU, Hussain D, et al. Enhancing supercapacitor performance through design optimization of laser-induced graphene and MWCNT coatings for flexible and portable energy storage. *Sci Rep*. 2023;13(1). doi:10.1038/s41598-023-48518-2

225. Zhang S, Li Y, Song H, et al. Graphene quantum dots as the electrolyte for solid state supercapacitors. *Sci Rep*. 2016;6(1). doi:10.1038/srep19292
226. Lan X, Chen X, Chen X, et al. Toxicity assessment of laser-induced graphene by zebrafish during development. *Journal of Physics: Materials*. 2020;3(3):034008. doi:10.1088/2515-7639/AB9522
227. Syugaev AV, Zonov RG, Mikheev KG, Maratkanova AN, Mikheev GM. Electrochemical impedance of laser-induced graphene: Frequency response of porous structure. *Journal of Physics and Chemistry of Solids*. 2023;181. doi:10.1016/j.jpcs.2023.111533
228. Kulyk B, Pereira SO, Fernandes AJS, Fortunato E, Costa FM, Santos NF. Laser-induced graphene from paper for non-enzymatic uric acid electrochemical sensing in urine. *Carbon N Y*. 2022;197. doi:10.1016/j.carbon.2022.06.013
229. Li J, Shao Y, Shi Q, et al. Calligraphy-inspired brush written foldable supercapacitors. *Nano Energy*. 2017;38:428-437. doi:10.1016/J.NANOEN.2017.06.013
230. Seol ML, Jones JM, Sadatian E, et al. All-printed supercapacitor array with vertical stacking. *J Power Sources*. 2023;576:233186. doi:10.1016/J.JPOWSOUR.2023.233186
231. Dennis JO, Shukur MF, Aldaghri OA, et al. A Review of Current Trends on Polyvinyl Alcohol (PVA)-Based Solid Polymer Electrolytes. *Molecules 2023, Vol 28, Page 1781*. 2023;28(4):1781. doi:10.3390/MOLECULES28041781
232. Dai H, Zhang G, Rawach D, et al. Polymer gel electrolytes for flexible supercapacitors: Recent progress, challenges, and perspectives. *Energy Storage Mater*. 2021;34:320-355. doi:10.1016/J.ENSM.2020.09.018
233. Khandelwal M, Tran C Van, Lee J, In J Bin. Nitrogen and boron co-doped densified laser-induced graphene for supercapacitor applications. *Chemical Engineering Journal*. 2022;428:131119. doi:10.1016/J.CEJ.2021.131119
234. Yuan G, Wan T, BaQais A, et al. Boron and fluorine Co-doped laser-induced graphene towards high-performance micro-supercapacitors. *Carbon N Y*. 2023;212:118101. doi:10.1016/J.CARBON.2023.118101
235. Zhang Z, Zhu H, Zhang W, et al. A review of laser-induced graphene: From experimental and theoretical fabrication processes to emerging applications. *Carbon N Y*. 2023;214. doi:10.1016/J.CARBON.2023.118356
236. Moon HR, Ryu B. Review of Laser-Induced Graphene (LIG) Produced on Eco-Friendly Substrates. *International Journal of Precision Engineering and Manufacturing-Green Technology*. 123AD;11:1279-1294. doi:10.1007/s40684-024-00595-y

237. Liu T. Research on flexible piezoresistive sensors based on nanocomposite materials. *Applied and Computational Engineering*. 2024;70(1):261-268. doi:10.54254/2755-2721/70/20241050
238. Zhao Y, Miao L, Xiao Y, Sun P. Research Progress of Flexible Piezoresistive Pressure Sensor: A Review. *IEEE Sens J*. Published online 2024. doi:10.1109/JSEN.2024.3443423
239. Weiland S, Hickmann T, Lederer M, Marquardt J, Schwindenhammer S. The 2030 agenda for sustainable development: Transformative change through the sustainable development goals? *Politics and Governance*. 2021;9. doi:10.17645/pag.v9i1.4191
240. Malik H, Niazi MBK, Miran W, et al. Wood as a green and sustainable alternative for environmentally friendly & flexible electronic devices. *Chemosphere*. 2023;336:139213. doi:10.1016/j.chemosphere.2023.139213
241. Chen X, Patil IG, Kou R, et al. Encapsulated Laser-Induced Graphene Flexible Piezo-resistive Sensors for Speech Recognition. *2023 IEEE International Conference on Sensors and Nanotechnology, SENNANO 2023*. Published online 2023:180-183. doi:10.1109/SENNANO57767.2023.10352566
242. Yan Z, Wang L, Xia Y, et al. Flexible High-Resolution Triboelectric Sensor Array Based on Patterned Laser-Induced Graphene for Self-Powered Real-Time Tactile Sensing. *Adv Funct Mater*. 2021;31(23):2100709. doi:10.1002/ADFM.202100709
243. Zhao P, Bhattacharya G, Fishlock SJ, et al. Replacing the metal electrodes in triboelectric nanogenerators: High-performance laser-induced graphene electrodes. *Nano Energy*. 2020;75:104958. doi:10.1016/j.nanoen.2020.104958
244. Harija H, Langer E, Prokopchuk A, et al. A Piezoresistive Cork-Based Sustainable and Robust Sensor for Force-Sensing Application. *IEEE Sens J*. Published online 2024. doi:10.1109/JSEN.2024.3448632
245. Zheng Q, Lee J hun, Shen X, Chen X, Kim JK. Graphene-based wearable piezoresistive physical sensors. *Materials Today*. 2020;36(June):158-179. doi:10.1016/j.mattod.2019.12.004
246. Zhou Y, Deng W, Xu J, Chen J. Engineering Materials at the Nanoscale for Triboelectric Nanogenerators. *Cell Rep Phys Sci*. 2020;1(8):100142. doi:10.1016/J.XCRP.2020.100142
247. Xu C, Zi Y, Wang AC, et al. On the Electron-Transfer Mechanism in the Contact-Electrification Effect. *Adv Mater*. 2018;30(15). doi:10.1002/ADMA.201706790

248. Li GY, Li J, Li ZJ, et al. Hierarchical PVDF-HFP/ZnO composite nanofiber–based highly sensitive piezoelectric sensor for wireless workout monitoring. *Adv Compos Hybrid Mater*. 2022;5(2):766-775. doi:10.1007/S42114-021-00331-Z
249. Ahmed R, Kumar P. Simulation study of ZnO nanorod geometry for the development of high-performance tactile sensors and energy harvesting devices. *Phys Scr*. 2024;99(2):025930. doi:10.1088/1402-4896/AD19BD
250. Cossutta M, McKechnie J, Pickering SJ. A comparative LCA of different graphene production routes. *Green Chemistry*. 2017;19(24):5874-5884. doi:10.1039/C7GC02444D

A

APPENDIX

A.1 Supplementary figures

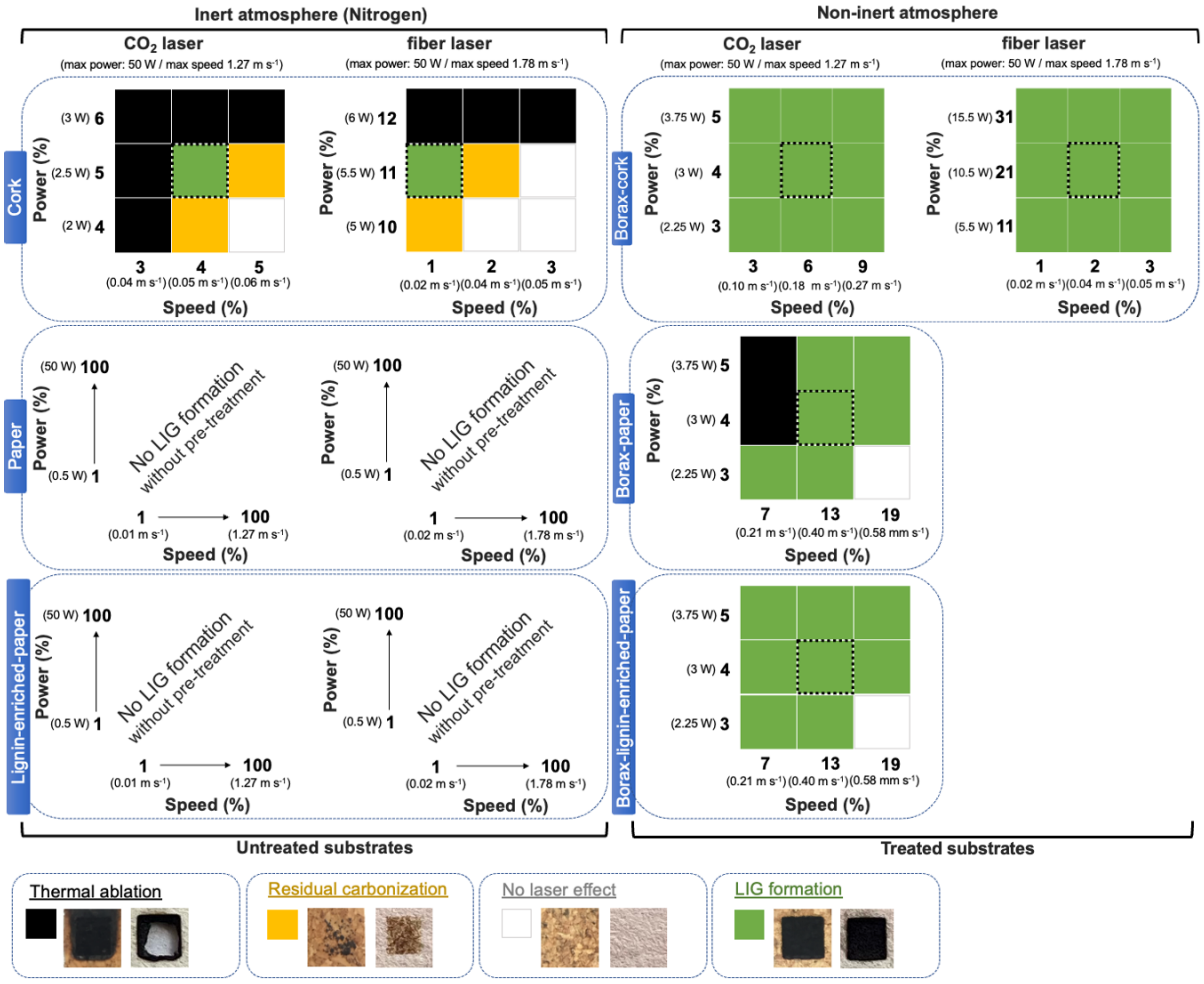

Figure S1. Optimization matrix for LIG formation onto paper, lignin-enriched paper, and cork by laser irradiation, using different laser systems and different atmospheres, with representative pictures.

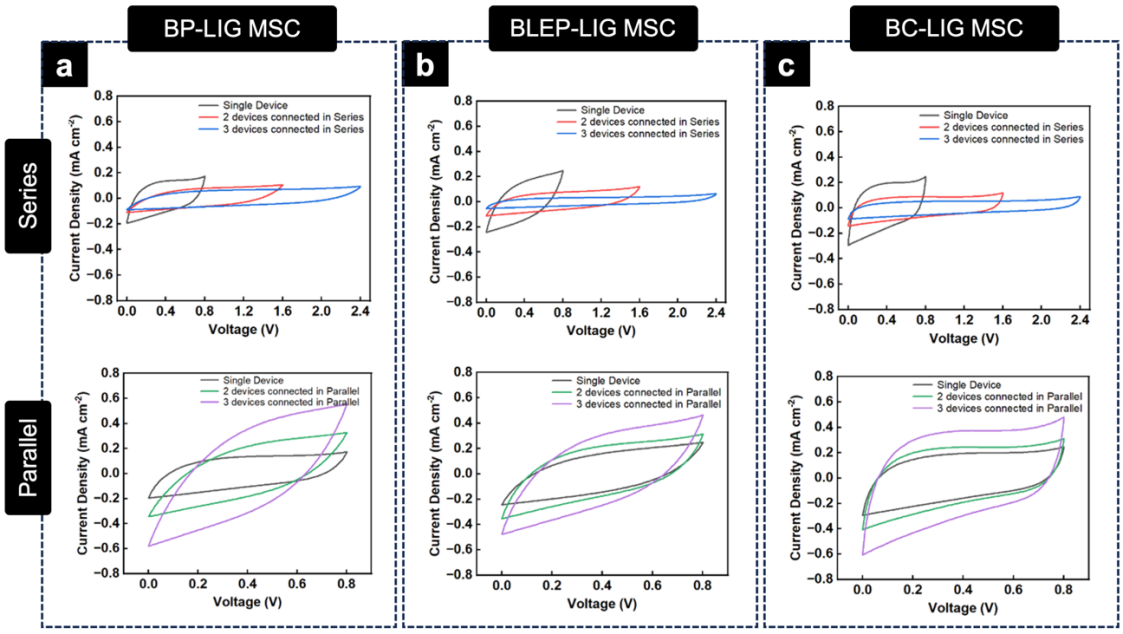

Figure S2. Cyclic Voltammetry curves of a single device and devices connected in series and parallel obtained at 30 mV s^{-1} in (a) borax-paper (BP), (b) borax-lignin-enriched paper (BLEP), and (c) borax-cork (BC) based LIG MSCs, reproduced with permission from [196]. CC BY 4.0 license, https://creativecommons.org/licenses/by/4.0/.

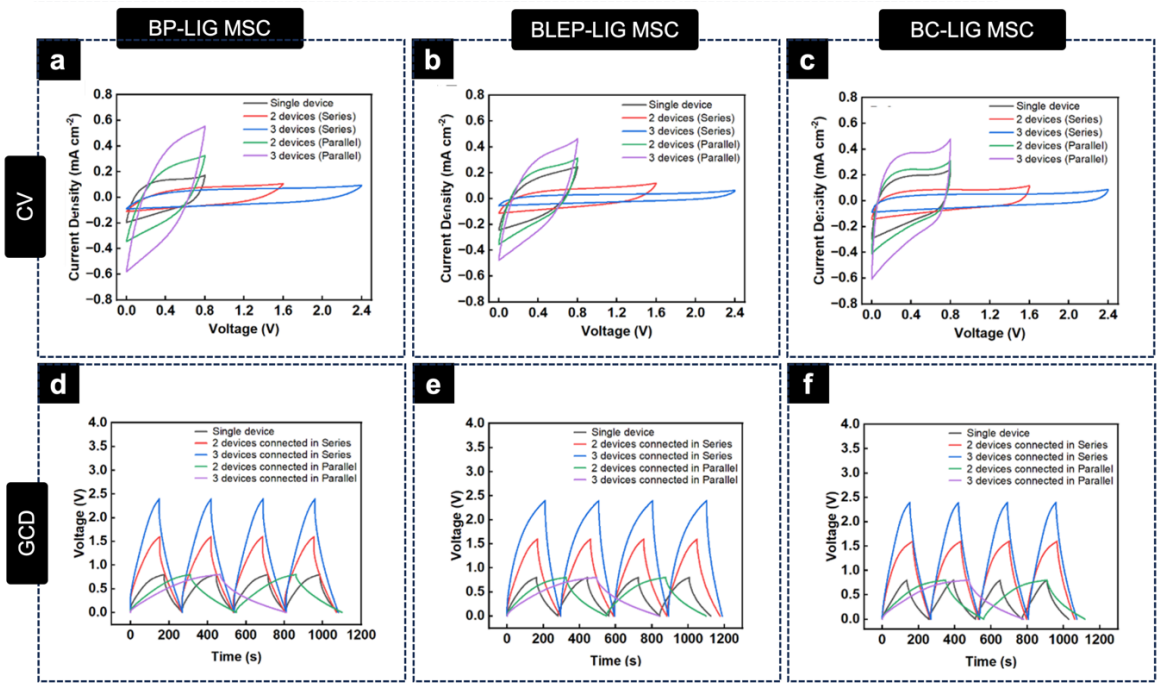

Figure S3. Cyclic voltammetry curves of a single device and devices connected in series and parallel obtained at 30 mV s^{-1} in (a) borax-paper (BP), (b) borax-lignin-enriched paper (BLEP), and (c) borax-cork (BC) based LIG MSCs, and corresponding (d)-(f) galvanostatic charge and discharge curves obtained at

0.05 mA cm^{-2}, reproduced with permission from [196]. CC BY 4.0 license, https://creativecommons.org/licenses/by/4.0/.

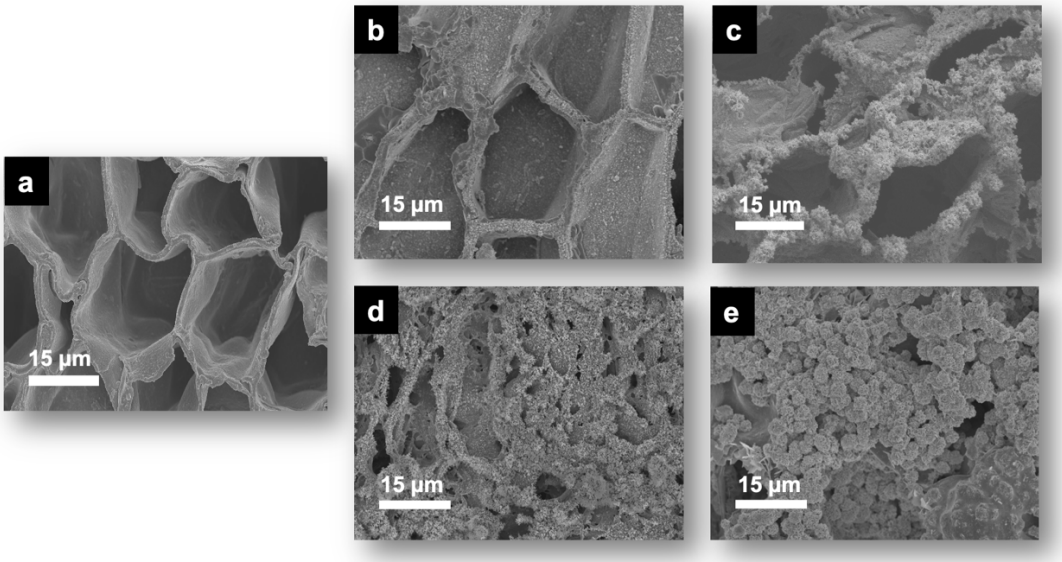

Figure S4. SEM images of (a) cork, (b) borax-cork (BC), (c) BC-LIG, (d) BC with ZnO precursor, and (e) BC-LIG/ZnO.

A.2 Supplementary equations

$$C_{\mathrm{A}} = \frac{1}{2 \times A \times \Delta V \times s} \times \int (V) dV$$

Equation S1. Equation used for calculating the areal capacitance (C_A), based on cyclic voltammetry (CV) measurements.

The areal capacitance, C_A, based on CV measurements, was calculated according to Equation S1, where A denotes the total active area of the electrodes (with 1.84 cm^2 for the **in-planar** devices produced in **paper I** and 1 cm^2 for the **sandwich** devices produced in **paper II**), ΔV represents the potential window (in V), s is the scan rate (in V s^{-1}) and $\int (V) dV$ is the integrated area of CV curve.

$$C_{\mathrm{A}} = \frac{I \times \Delta t}{A \times \Delta V} = \frac{I}{A \times \left(\frac{dV}{dt}\right)}$$

Equation S2. Equation used for calculating the areal capacitance (C_A), based on the charge-discharge (GCD) measurements.

The areal capacitance, C_A, based on the charge-discharge profiles, was calculated according to Equation S2. Here I represents the applied current (in A), Δt is the discharge in time (in s), and A denotes the active area of the MSC. In this equation, $\Delta V = V_2 - V_1$, where V_2 is the potential at the beginning of discharge, post the internal resistance (IR) potential drop, while V_1 stands for the potential at the end of discharge. Alternatively, the equation can also be expressed as $\frac{I}{\mathrm{A} \times \left(\frac{dV}{dt}\right)}$, where dV/dt represents the slope of galvanostatic discharge curves.

$$C_{\mathrm{V}} = \frac{C_{\mathrm{A}}}{d}$$

Equation S3. Equation used for calculating the volumetric capacitance (C_V).

The volumetric capacitance, C_V, was calculated based on Equation S3, where d represents the thickness of active materials used (in μm).

$$E_{\mathrm{A}} = \frac{1}{2} \frac{C_{\mathrm{A}} \times \Delta V^2}{3600}$$

Equation S4. Equation used for calculating the areal energy (E_A) density.

$$P_{\mathrm{A}} = \frac{E_{\mathrm{A}}}{\Delta t} \times 3600$$

Equation S5. Equation used for calculating the areal power (P_A) density.

The areal energy, E_A, and power, P_A, densities of the devices were calculated, according to Equation S4 and Equation S5, respectively, where 3600 is the conversion factor transforming Watt-seconds (Ws) into Watt-hours (Wh).

$$E_V = \frac{1}{2}\frac{C_V \times \Delta V^2}{3600}$$

Equation S6. Equation used for calculating the volumetric energy (E_V) density.

$$P_V = \frac{E_V}{\Delta t} \times 3600$$

Equation S7. Equation used for calculating the volumetric power (P_V) density.

The volumetric energy, E_V, and power, P_V, densities of the devices were calculated, according to Equation S6 and Equation S7, respectively, where 3600 is the conversion factor transforming Watt-seconds (Ws) into Watt-hours (Wh).

A.3 Source Arduino code used to program Flexible and Stress Machine

```
// Sara Silvestre, 2024 //

#define DIR_PIN 3
#define STEP_PIN 2
#define ENABLE_SM 7

void setup() {
  pinMode(DIR_PIN, OUTPUT);
  pinMode(STEP_PIN, OUTPUT);
  pinMode(ENABLE_SM, OUTPUT);
}

void loop(){
  long long int cycles = 500;   // Number of cycles (rotations)
  float rps = 1.5;                // Speed in rotations per second (rps) from 0.005 to 2
  int stopDelay = 5;           // Delay time in seconds after each cycle

  for(long long int i = 0; i < cycles; i++) {
    rotateDeg(360, 1/rps);       // Rotate one full rotation (360 degrees)

    delay(stopDelay* 1000);     // Wait for the specified time in seconds before the next cycle
  }

  digitalWrite(ENABLE_SM, HIGH); // Disable the motor after all cycles are completed
  while(1) { }                   // Stop the loop permanently
}

void rotateDeg(long long int deg, float speed){
  int dir = (deg > 0) ? HIGH : LOW;
  digitalWrite(DIR_PIN, dir);

  long long int steps = abs(deg) * (1 / 0.225);
  float usDelay = speed * 312.5;

  for(long long int i = 0; i < steps; i++){
    digitalWrite(STEP_PIN, HIGH);
    delayMicroseconds(usDelay);

    digitalWrite(STEP_PIN, LOW);
    delayMicroseconds(usDelay);
  }
}
```

A.4 Source Arduino code used to program Pneumatic Force Actuator Machine (PFAM)

```
/* Driver controller for Pneumatic Force Actuator Machine - PFAM */

int dataPin = 10; // set data output pin name
void setup() {
pinMode(dataPin, OUTPUT);
}

void loop() {
//Choose frequency: 1750 = 0.5Hz || 750 = 1Hz || 250 = 2Hz || 83 = 3 Hz
int a = 1750; // 0.5 Hz
int b = 750; // 1 Hz
int c = 250; // 2 Hz
int d = 83; // 3 Hz

digitalWrite(dataPin, HIGH); // turn on
delay(250); // in millisec
digitalWrite(dataPin, LOW); // turn off
delay(b);
}
```

2024

SARA ISABEL LAIGINHA SILVESTRE

SUSTAINABLE MATERIALS APPLIED TO FLEXIBLE ELECTRONICS USING A LASER-INDUCED MODULAR PLATFORM